

UNIVERSITY OF BREMEN

DOCTORAL THESIS

Large-scale Modelling of
Subglacial Hydrology

A thesis submitted in fulfillment of the requirements
for the degree of Doctor of Natural Sciences in the
DEPARTMENT OF GEOSCIENCES (FB5)

by

Sebastian Beyer

June 30, 2018

Date of doctoral colloquium: 6.12.2018

Supervisors: Prof. Dr. Angelika Humbert and Prof. Dr. Ian Hewitt

ABSTRACT

Subglacial hydrology is a key component in ice sheet dynamics and controls the sliding of ice sheets. Modelling the integrated system between ice dynamics and subglacial hydrology is essential for understanding current changes in the system and projecting future evolution of ice sheets and their contribution to sea level rise. The recent acceleration of mass loss of the Greenland ice sheet can be largely attributed to dynamic thinning at the ice margin, where hydrologic processes play a significant role in the speed-up of outlet glaciers. Models of subglacial hydrology recently have progressed to incorporate multiple components of the drainage system and are able to represent observed seasonal evolution of an efficient drainage system during the melt season, but the application of models on a continental scale remains a challenge. This doctoral thesis analyzes different approaches to model the subglacial hydrology and its interaction with the ice flow in respect to their ability to be applied to large domains. Two different models are developed and analyzed. A balance flux model coupled to the ice dynamics model SICOPOLIS is used to study the effect of subglacial water on the Eurasian ice sheet, applied to the simulation of future sea level contribution of Greenland where it reveals that the effect of subglacial discharge on submarine melting is comparable to increased ocean warming. Additionally, this model is utilized in the study of subglacial lakes at Recovery Glacier, Antarctica. The second model is an equivalent aquifer model which describes the water flow in a porous layer adapted to exhibit the properties of the complex drainage system. The evolution of the system is achieved by locally adjusting the transmissivity. It is shown that this approach leads to realistic pressure and discharge distributions which compare well with more sophisticated models, while keeping computational costs low.

ZUSAMMENFASSUNG

Subglaziale Hydrologie ist ein Schlüsselement in der Dynamik von Eisschilden, da es das basale Gleiten bestimmt. Die Modellierung eines gekoppelten Systems aus Eisdynamik und Hydrologie ist essenziell für das Verständnis der aktuellen und zukünftigen Veränderungen der Eisschilde und ihrem Beitrag zum globalen Meeresspiegelanstieg. Die in den letzten Jahren beobachtete Beschleunigung des Masseverlustes des Grönländischen Eisschildes wird großenteils durch das Dünnwerden des Eises an den Küsten und damit durch die Beschleunigung der Auslassgletscher verursacht, bei denen hydrologische Prozesse eine große Rolle spielen. Aktuelle numerische Modelle der subglazialen Hydrologie haben große Fortschritte erzielt und sind nun in der Lage die beobachtete saisonale Entwicklung des Drainagesystems während der Tauperiode zu reproduzieren. Die Anwendung auf kontinentaler Größenordnung bleibt jedoch eine Herausforderung. Diese Doktorarbeit untersucht verschiedene Ansätze die subglaziale Hydrologie und deren Interaktion mit dem Eis numerisch zu modellieren im Hinblick auf ihre Eignung, große Gebiete damit zu untersuchen. Es werden zwei verschiedene Modelle entwickelt und analysiert. Das erste Modell basiert auf dem balance flux Ansatz und wird mit dem Eisdynamik Modell SICOPOLIS gekoppelt. Dieses Modell wird verwendet, um damit den Effekt des subglazialen Wassers auf das Eurasische Eisschild zu untersuchen, um den zukünftigen Beitrag von Grönland zum Meeresspiegelanstieg zu ermitteln —wo sich herausstellt, dass der Effekt des basalen Wassers auf submarines Schmelzen vergleichbar mit dem Effekt des sich erwärmenden Ozeans ist. Außerdem wird das Modell genutzt, um in einer Studie des Recovery Gletschers in der Antarktis subglaziale Seen zu detektieren. Das zweite Modell verwendet den Ansatz eines äquivalenten Aquifers. Das Fließen des Wassers wird hierbei durch die Beschreibung von Wasserfluss durch ein poröses Medium angenähert, welches so angepasst wird, dass es die Eigenschaften des komplexen subglazialen Systems hat. Die Adaption des Systems wird durch das lokale Anpassen der Transmissivität erreicht. Es wird gezeigt, dass dieser Ansatz zu realistischen Verteilungen von Druck und Wasserfluss führt und dass die Ergebnisse mit denen von komplexeren Modellen vergleichbar sind, wobei der Rechenaufwand geringer ist.

VERSICHERUNG AN EIDES STATT / AFFIRMATION IN LIEU OF AN OATH

gem. § 5 Abs. 5 der Promotionsordnung vom 15.07.2015
according to § 5 (5) of the Doctoral Degree Rules and Regulations of 15 July, 2015

Ich / I, Sebastian Beyer, Römerstraße 27, 28203 Bremen, Matrikel Nummer: 3018450

versichere an Eides Statt durch meine Unterschrift, dass ich die vorliegende Dissertation selbständig und ohne fremde Hilfe angefertigt und alle Stellen, die ich wörtlich dem Sinne nach aus Veröffentlichungen entnommen habe, als solche kenntlich gemacht habe, mich auch keiner anderen als der angegebenen Literatur oder sonstiger Hilfsmittel bedient habe und die zu Prüfungszwecken beigelegte elektronische Version (PDF) der Dissertation mit der abgegebenen gedruckten Version identisch ist. *With my signature I affirm in lieu of an oath that I prepared the submitted dissertation independently and without illicit assistance from third parties, that I appropriately referenced any text or content from other sources, that I used only literature and resources listed in the dissertation, and that the electronic (PDF) and printed versions of the dissertation are identical.*

Ich versichere an Eides Statt, dass ich die vorgenannten Angaben nach bestem Wissen und Gewissen gemacht habe und dass die Angaben der Wahrheit entsprechen und ich nichts verschwiegen habe. *I affirm in lieu of an oath that the information provided herein to the best of my knowledge is true and complete.*

Die Strafbarkeit einer falschen eidesstattlichen Versicherung ist mir bekannt, namentlich die Strafandrohung gemäß § 156 StGB bis zu drei Jahren Freiheitsstrafe oder Geldstrafe bei vorsätzlicher Begehung der Tat bzw. gemäß § 161 Abs. 1 StGB bis zu einem Jahr Freiheitsstrafe oder Geldstrafe bei fahrlässiger Begehung. *I am aware that a false affidavit is a criminal offence which is punishable by law in accordance with § 156 of the German Criminal Code (StGB) with up to three years imprisonment or a fine in case of intention, or in accordance with § 161 (1) of the German Criminal Code with up to one year imprisonment or a fine in case of negligence.*

Ort / Place , Datum / Date

Unterschrift / Signature

CONTENTS

1	INTRODUCTION	1
1.1	Aims and objectives	4
1.2	Structure	4
2	SUBGLACIAL HYDROLOGY	7
2.1	Basal Conditions	7
2.1.1	Sliding-law	8
2.1.2	Connection between water and sliding	8
2.1.3	Water sources	9
2.2	The elements of the drainage system	9
2.2.1	Distributed Flow	11
2.2.2	Channelized Flow	11
2.2.3	Subglacial Lakes	13
3	MODELLING SUBGLACIAL HYDROLOGY	15
3.1	Introduction	15
3.2	Balance flux approach	16
3.2.1	Numerical Implementation	17
3.2.2	Depression filling and flat resolution	19
3.2.3	Coupling to the ice model	20
3.2.4	Assignment to glaciers	21
3.3	Channels and Network of Channels	23
3.4	Equivalent aquifer model	25
4	MISSING EVIDENCE OF WIDESPREAD SUBGLACIAL LAKES AT RECOVERY GLACIER, ANTARCTICA	27
4.1	Introduction	30
4.2	Methods	31
4.2.1	Subglacial-lake identification from modelling	31
4.2.2	Ice thickness from RES	34
4.2.3	Basal reflection coefficient	35
4.2.4	Subglacial-lake identification	37
4.2.5	Active lake identification from satellite altimetry	38
4.3	Results	38
4.3.1	Ice thickness and subglacial topography	38
4.3.2	Subglacial temperature distribution	40
4.3.3	Subglacial water flux and hydraulic potential	43

4.3.4	Active lakes from altimetry	45
4.3.5	Lake identification	45
4.3.6	Basal reflection coefficient	45
4.3.7	Combined Analysis	46
4.4	Discussion	52
4.4.1	Origin of missing basal reflections	52
4.4.2	Missing evidence in lake identification	53
4.4.3	Trustworthiness of basal reflection coefficient	54
4.4.4	Synthesis	56
4.5	Conclusion	57
4.6	Supplemental Information	58
5	EURASIAN ICE-SHEET DYNAMICS AND SENSITIVITY TO SUBGLACIAL HYDROLOGY	65
5.1	Introduction	68
5.1.1	Previous modelling studies	68
5.2	Modelling approach	69
5.2.1	Ice sheet model	69
5.2.2	Climate forcing	70
5.2.3	Subglacial hydrology	70
5.2.4	Basal sliding	71
5.2.5	Subglacial lakes	72
5.3	Model results	73
5.4	Discussion	77
5.4.1	Hydrology	77
5.4.2	Subglacial lakes	79
5.4.3	Water storage	79
5.5	Conclusions	80
6	SIMULATION OF THE FUTURE SEA LEVEL CONTRIBUTION OF GREENLAND WITH A NEW GLACIAL SYSTEM MODEL	81
6.1	Introduction	83
6.2	Ice sheet model for Greenland including ocean and outlet glaciers (IGLOO), ver- sion 1.0	87
6.2.1	Ice sheet model SICOPOLIS version 3.3	87
6.2.2	Subglacial hydrology model HYDRO	88
6.2.3	Meltwater plume model	89
6.2.4	Coupling of model components	89
6.2.5	Evaluating the data from the regional atmosphere model MAR	90
6.2.6	Past climate forcing and implied SMB of the GrIS	91
6.2.7	Future climate forcing of the GrIS	92
6.2.8	Future climate forcing of the plume model	93
6.3	Model initialization via palaeo-runs	93
6.4	Present-day Greenland ice sheet	97

6.5	Greenland glacial system projections	100
6.5.1	Projections of the GrIS's sea level contribution	100
6.5.2	Projections of the GrIS's total basal and surface runoff	102
6.5.3	Projections of submarine melt rate for the GrIS outlet glaciers Helheim and Store	102
6.6	Discussion	105
6.7	Conclusion	106
6.8	Appendix	107
6.8.1	Mass conservating scheme for ice thickness evolution	107
6.8.2	Adapting MAR data for the future simulations	108
7	MODELING THE RESPONSE OF GREENLAND OUTLET GLACIERS TO GLOBAL WARMING USING A COUPLED FLOWLINE-PLUME MODEL	111
7.1	Introduction	113
7.2	The coupled flowline-plume model	114
7.2.1	Glacier model	115
7.2.2	Plume model	116
7.2.3	Coupling between glacier and plume model	116
7.3	Model Input	117
7.3.1	The choice of glaciers	117
7.3.2	Glacier geometry	117
7.3.3	Subglacial discharge and glacier surface mass balance	118
7.3.4	Fjord temperature and salinity profiles: CTD measurement and Ocean Reanalysis data	121
7.4	Experimental setup	126
7.4.1	Selection of model parameters and model spin up	126
7.4.2	Future climate scenarios	126
7.5	Results	127
7.5.1	Present-day state	127
7.5.2	Future simulations	128
7.6	Discussion and Conclusions	134
8	A CONFINED–UNCONFINED AQUIFER MODEL FOR SUBGLACIAL HYDROLOGY AND ITS APPLICATION TO THE NORTH EAST GREENLAND ICE STREAM	137
8.1	Introduction	140
8.2	Methods	141
8.2.1	Confined–Unconfined Aquifer Scheme	141
8.2.2	Opening and closure	143
8.3	Experiments with artificial geometries	144
8.3.1	Parameter estimation and sensitivity	144
8.3.2	The benefit from treating unconfined aquifer	148
8.3.3	Seasonal channel evolution and properties	150
8.4	Subglacial hydrology of NEGIS, Greenland	152
8.5	Conclusions	157

8.6	appendix	158
8.6.1	Parametrization of evolution of transmissivity	158
8.6.2	Discretization	160
8.7	Acknowledgements	161
9	SHMIP THE SUBGLACIAL HYDROLOGY MODEL INTERCOMPARISON PROJECT	163
9.1	Introduction	165
9.2	The wide variety of subglacial hydrology models	166
9.2.1	Subglacial hydrology modelling	167
9.2.2	Sheet drainage	168
9.2.3	Channelised drainage	169
9.2.4	Porous layer drainage	170
9.2.5	Additional drainage elements	170
9.2.6	Coupling of components	171
9.3	Participating models	171
9.4	Intercomparison call and setup	176
9.4.1	Topographies	176
9.4.2	Boundary conditions	178
9.4.3	Parameters and optional tuning	178
9.4.4	Suite A: steady state	180
9.4.5	Suite B: localised input	180
9.4.6	Suite C: diurnal cycle	180
9.4.7	Suite D: seasonal cycle	181
9.4.8	Suite E: overdeepening of valley topography	181
9.4.9	Suite F: seasonal cycle on valley topography	182
9.5	Results	182
9.5.1	Suite A: steady state	184
9.5.2	Suite B: steady state with moulin input	184
9.5.3	Suite C: diurnal cycle	186
9.5.4	Suite D: seasonal cycle	188
9.5.5	Suite E: overdeepening of valley topography	189
9.5.6	Suite F: seasonal cycle on valley topography	191
9.6	Discussion	193
9.7	Conclusion	197
10	CONCLUSIONS	201
10.1	Achievements	201
10.1.1	Balance flux modelling	201
10.1.2	Equivalent aquifer model	202
10.2	Outlook and future work	203
	BIBLIOGRAPHY	205

1 INTRODUCTION

Climate change is one of this centuries gravest challenges for humanity. Higher global temperatures lead to sea-level rise, melting of glaciers and ice sheets, changes in large scale precipitation patterns, intensification of extreme weather events, floods, and draughts. The cryosphere with its large ice sheets in Greenland and Antarctica and many mountain glaciers plays an integral role in the climate system. Strong feedbacks link the cryosphere with the global climate and it exerts significant influence on the surface energy fluxes, precipitation as well as atmospheric and oceanic circulation. And it currently undergoes vigorous change. The water that is stored frozen in Antarctica and Greenland has the potential to rise the global sea level by a significant amount (Alley et al., 2005b). The Fifth Assessment Report of the Intergovernmental Panel on Climate Change (IPCC, 2013) states “with high confidence” that the Greenland mass loss has accelerated over the last 20 years, but future projections are in a “fairly early stage”. Therefore, it is of great importance to understand and quantify the dynamics of this system in order to predict its future evolution.

The mass loss of large ice sheets mainly takes place at the margins of the ice body, called *ablation zone*. While in the center of the ice sheet snow accumulates which drives the ice flow towards the margins, in the ablation zone the snow and ice at the surface melt and generate surface runoff. The total surface mass balance (SMB) is determined by the balance between accumulation and ablation and is one component of the total mass balance. The second component is ice discharge across the grounding line (often termed D), which controls the total mass loss of Antarctica. In Greenland, air temperatures are much higher during the summer, leading to extensive surface melt, which means that Greenlandic mass loss is determined to 60 % by its negative SMB (Broeke et al., 2016). From 1992 to 2010 the acceleration in ice loss was $21.9 \pm 0.1 \text{ Gt a}^{-2}$ for Greenland and $14.5 \pm 0.2 \text{ Gt a}^{-2}$ for Antarctica, resulting in a total acceleration of $36.3 \pm 0.2 \text{ Gt a}^{-2}$ (Rignot et al., 2011a). For Greenland this speedup can partly be attributed to ice streams, which channelize the flow at the coasts and can move a hundred to a thousand times faster than the average ice flow. Their fast flow is explained by ice-ocean interaction and enhanced sliding over the bedrock controlled by lubrication due to basal water and in some cases soft sediment. While there has been some recent discussion if basal sliding depends on frictional stress at the base, it is pretty clear that water and water pressure play a crucial role (Stearns and Veen, 2018).

Water at the base of the ice is long known to play an important role for sliding. It decreases the coupling between the ice and the bed, leading to faster flow. In Greenland, the meltwater that drains into the subglacial system leads to the seasonal acceleration of ice velocities during summer. Predicted increased summer melt (Hanna et al., 2013), already visible with e.g. the record melt year of 2012 (Nghiem et al., 2012), raises the question of how this may affect the future evolution of the Greenland ice sheet. If warmer temperatures lead to an increase of the annual mean velocities, then there would be a positive feedback loop, where faster ice flow would lower the elevation of the

1 Introduction

ice sheet and therefore increase melting, leading to even faster flow in turn. However, observations have shown that the relationship between melt, surface runoff and ice velocities is not that simple.

Higher melt intensity does in fact lead to faster ice flow in the beginning of summer, but later during the melt season the ice decelerates even though melt rates remain high. This is explained by the subglacial system adapting to the conditions and becoming more efficient in removing the water towards the ocean (Sundal et al., 2011). The same effect can even lead to slower mean ice velocities during winter, if the system does not return to its previous state (Sole et al., 2013). Moon et al. (2014) find that glaciers differ in their seasonal velocity evolution and identify different patterns which they use to classify the glaciers into three different types (see Fig. 1.1). While for the first type the fluctuations in speed correspond mainly to the terminus position, type 2 and type 3 are controlled by surface runoff. Glaciers of type 2 have a speedup that is synchronous with the surface runoff. The increase in speed coincides with the onset of the melt season and no drop in the velocities is observed before the runoff recedes. This suggests, that there is no switch in the subglacial system. Type 3 glaciers do exhibit a velocity decline in late summer, when the runoff is still high, which can be explained by the transformation of the subglacial drainage system into a more efficient one. These differences between different types of glaciers are attributed to varying geologic subglacial conditions and water availability, whereas type 2 glaciers do not receive as much water, due to a shorter melt season. In order to understand this behaviour and being able

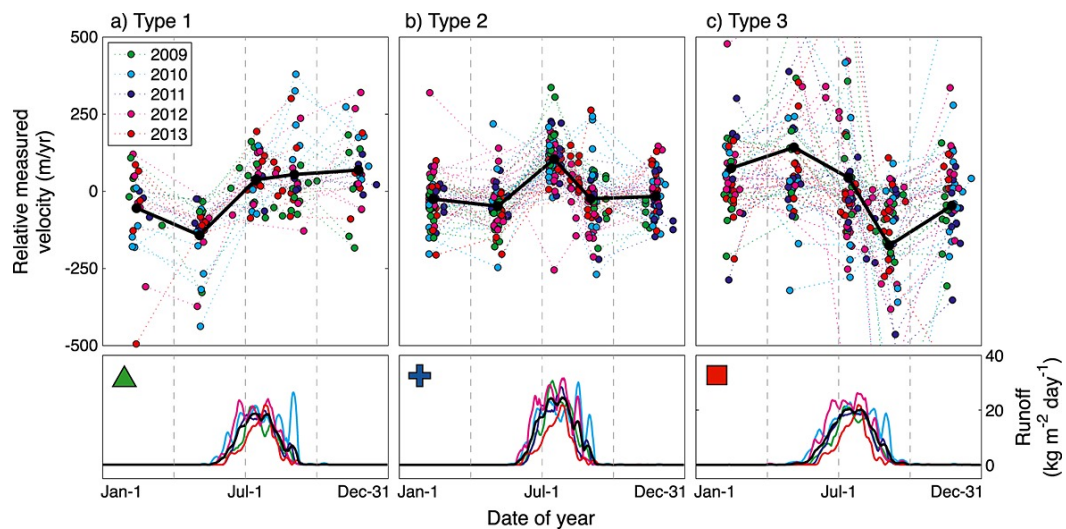


Figure 1.1: Different patterns of velocity modes for marine-terminating Greenland outlet glaciers. Top panels show velocity variation over the melt season with black lines indicating the mean velocity pattern. The bottom panels show the respective mean runoff (Moon et al., 2014).

to predict how a warmer climate will affect the development of glaciers, it is necessary to examine the components and mechanisms of the (subglacial) hydraulic system, also known as subglacial hydrology.

Since the beginning of glaciology as a modern research domain hydrology is known to play a major role in glacier flow (Clarke, 1987). Water in liquid form appears on the ice surface due to summer melt, forming channels and rivers which either form a supraglacial lake or disappear into

the glacier through moulines (vertical conduits that connect the surface to the base of the ice). In areas with a firn layer, the water does also flow through it, albeit very inefficiently. Meltwater lakes can form in topographic lows and grow over the season due to more water being collected, as well as a due to their darker color compared to the surroundings, which increases the absorption of solar energy, enhancing melt. Some lakes drain in very short time (hours) due to hydrofracturing opening a connection to the ice base, which is then rapidly enlarged by the water flow (Das et al., 2008). Depending on the pressure conditions and water availability, these connections can penetrate up to 1 km of ice and may stay open, draining more water to the base, as it arrives. At the base, the water flow is difficult to observe. Data has been collected of only a few parameters (pressure, velocity, flux) and only on limited points like boreholes and from measurements at the snout of glaciers. Still, there has been a lot of development in the theory of subglacial hydrology. A main feature of the subglacial water flow is, that there are two fundamentally different modes of drainage. There is inefficient drainage through thin water films or cavities, which operate at high water pressure, reducing the contact forces between the ice and the bedrock, thus, enhancing the ice flow. With increased water discharge, the flow enlarges passageways and localizes into large channels, which efficiently removing the water, lowering the water pressure which leads to slower ice flow. In Figure 1.2 the main components of the water system are shown.

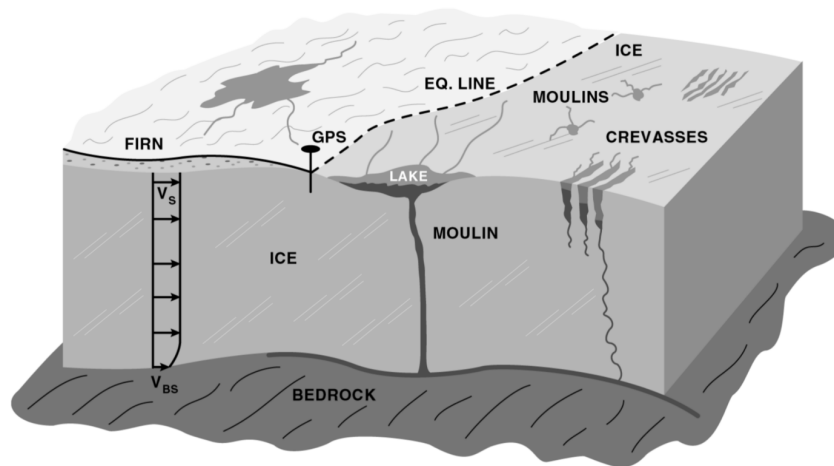


Figure 1.2: Elements of the hydraulic system. The equilibrium line is the boundary between the ablation and the accumulation zone. Shown are supraglacial lakes, moulines, crevasses and the basal water system (Zwally et al., 2002).

Numerical models can help to understand the dynamics and mechanisms of hydrological processes. Over the last years there has been newly sparked interest in modelling the subglacial hydrology and great progress has been made on the development of numerical models. A number of models is now able to reproduce the inefficient as well as the efficient system and the coupling between them (Schoof, 2010b; Hewitt, 2013; Werder et al., 2013; Fleurian et al., 2014; Fleurian et al., 2016; Pimentel and Flowers, 2010). They can reproduce the emergence of an efficient system over the melt season and some have even been coupled to an ice dynamics model, leading to realistic ice velocity patterns (Hewitt, 2013). Usually they use a continuum description for the inefficient flow and add a channel or a network of channels to that, coupling the two systems via

pressure or water flux. A major problem for these models is, that they require prior knowledge of where subglacial channels form. The solution to this problem is to have potential channels everywhere (usually at the edges of numerical grid cells), which then only form into real channels if certain conditions are met. While this solution works well, it requires high spatial resolution, leading to high computational cost. Fleurian et al. (2014) use a different approach, in that they approximate the drainage system with a two-layer equivalent aquifer model, describing not only the inefficient, but also the efficient system as a continuum. So far, most of these models have only been used on artificial test cases or small glaciers.

1.1 AIMS AND OBJECTIVES

The overarching aim of this thesis is to study different approaches to numerically modelling subglacial hydrology on a large scale. The main objective was therefore to implement different types of models, apply them to real geometries and evaluate their performance in detail. It is very important to understand the properties and qualities of a model and to know what it is capable of before it can be used in the context of future predictions.

This work is part of the “Greenland glacial system and future sea-level rise” (GreenRise) project, which had the goal of designing a computationally efficient intermediate complexity model suitable for performing large ensemble studies on the Greenland glacial system’s (GGS) response to climate change. It aimed at coupling different models of individual elements of the GGS, including a three-dimensional ice model, a regional climate model, an outlet glacier model and a model for subglacial hydrology, and contribute to the assessment of the risk of future sea-level rise. Therefore, it was necessary to quickly develop a simple drainage model that could be coupled to the ice dynamics model and produce water discharge volumes for the outlet glacier models. This was then supposed to be enhanced or replaced by more complex model that would also be capable of representing the specific properties of the seasonal evolution of subglacial drainage. My objectives were to:

- develop a first drainage model that can be used to determine water flow paths, be coupled to a large scale ice dynamics model and determine discharge into specific glaciers/fjords,
- apply and evaluate that model in different contexts,
- improve the model by including more complex physics in order to enable it to simulate the seasonal evolution of the Greenlandic subglacial hydrology system, and
- compare the model to other available models and assess the feasibility to use these kinds of simplistic models for large scale study of ice dynamics.

1.2 STRUCTURE

This thesis is based on six research papers, which are included as self contained chapters. Before, Chapter 2 gives an overview of the different components of the subglacial drainage system, explaining the main differences between the fundamental flow regimes of distributed and channelized flow and presents the connection between water and ice flow. In Chapter 3 the fundamental

concepts of using numerical models for subglacial hydrology are explained. It summarizes the ideas of different types of models and explains the equations.

The papers are:

- I Angelika Humbert, Daniel Steinhage, Veit Helm, Sebastian Beyer, and Thomas Kleiner, “Missing evidence of widespread subglacial lakes at Recovery Glacier, Antarctica”, Chapter 4
- II Eythor Gudlaugsson, Angelika Humbert, Karin Andreassen, Caroline C. Clason, Thomas Kleiner, Sebastian Beyer, “Eurasian ice-sheet dynamics and sensitivity to subglacial hydrology”, Chapter 5
- III Reinhard Calov, Sebastian Beyer, Ralf Greve, Johanna Beckmann, Matteo Willeit, Thomas Kleiner, Martin Rückamp, Angelika Humbert, and Andrey Ganopolski, “Simulation of the future sea level contribution of Greenland with a new glacial system model”, Chapter 6
- IV Johanna Beckmann, Mahé Perrette, Sebastian Beyer, Reinhard Calov, Matteo Willeit, and Andrey Ganopolski, “Modeling the response of Greenland outlet glaciers to global warming using a coupled flowline-plume model”, Chapter 7
- V Sebastian Beyer, Thomas Kleiner, Vadym Aizinger, Martin Rückamp, and Angelika Humbert, “A confined–unconfined aquifer model for subglacial hydrology and its application to the North East Greenland Ice Stream”, Chapter 8
- VI Basile de Fleurian, Mauro A. Werder, Sebastian Beyer, Douglas J. Brinkerhoff, Ian Delaney, Christine F. Dow, Jacob Downs, Olivier Gagliardini, Matthew J. Hoffman, Roger LeB Hooke, Julien Seguinot, Aleah N. Sommers, “SHMIP The Subglacial Hydrology Model Intercomparison Project”, Chapter 9

Each paper is preceded by a short “context” section, which explains the motivation and the significance for the thesis and the contributions from the author of this thesis are explained.

Finally, Chapter 10 summarizes the conclusions.

2 SUBGLACIAL HYDROLOGY

One of the biggest uncertainties in predicting future mass loss of large ice-sheets and sea-level rise originates from our incomplete understanding of the processes at the ice base. This chapter explains the connection between water at the ice base and the ice flow velocity and gives a compact overview of the components of the subglacial drainage system.

2.1 BASAL CONDITIONS

Ice flow and therefore ice discharge into the ocean and the resulting mass loss for the ice-sheets is governed by three major components, as depicted in Fig. 2.1. The total ice flow is comprised of sediment deformation, basal sliding and internal ice deformation. Internal deformation mainly drives the ice flow in the center of large ice-sheets and leads to a typical velocity–depth function that is parabolic with the fastest flow at the surface and slowest (or no) flow at the base. Sediment deformation can only occur when the glaciers rest on a soft deformable bed and adds up to the ice deformation. The high flow speeds at the edges of large ice masses, such as the many outlet glaciers around Greenland (Rignot and Mouginot, 2012) can only be explained by the third component, basal sliding. Basal sliding can determine up to 90 percent of the total ice surface velocity and often varies in time and space. The mixture of ice, bedrock, and possibly water saturated sediment at

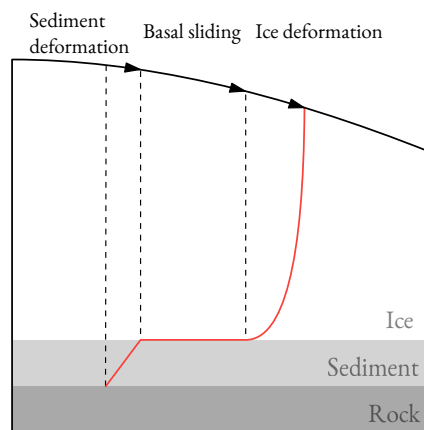


Figure 2.1: Components of ice flow.

the base lead to complex interactions. This makes it difficult to obtain a simple model that relates basal ice velocity to the various contributing factors, such as geometry, sediment properties, basal drag, water quantity and water pressure. Finding the correct parametrization, the optimal *sliding-*

2 Subglacial Hydrology

law, that is able to describe the spatial and temporal evolution of basal ice velocity is a challenging question for ice-sheet modelling.

2.1.1 SLIDING-LAW

A sliding-law, or sliding relation, parametrizes how the ice moves over its bed. It relates the basal ice velocity \mathbf{u}_b to a function of a multitude of factors. Early theoretical foundations have been laid out by Weertman (1957), Lliboutry (1958a), and Lliboutry (1958b) which have later revised and improved upon by Nye (1969), Nye (1970), Kamb (1970), Fowler (1981), Fowler (1986), Fowler (1987), Iken (1981), Gudmundsson (1997a), Gudmundsson (1997b), Schoof (2005), Gagliardini et al. (2007a), and Gagliardini et al. (2007b). Fowler (2010) gives a good historic overview of the development.

In the simplest incarnation the sliding law expresses how the average basal drag τ_b experienced by the ice while sliding over obstacles, simply depends on the ice velocity \mathbf{u}_b ,

$$\tau_b = f(u_b). \quad (2.1)$$

Herein, f rises with increasing \mathbf{u}_b and is often taken as $f(\mathbf{u}_b) = C\mathbf{u}_b^m$, where C and m are positive constants. It was Lliboutry (1958a) who first suggested that high water pressure below glaciers might play an important role, leading to the development of water-filled cavities at the lee side of basal protrusions. He proposed to change Equation 2.1 to

$$\tau_b = f(\mathbf{u}_b, N), \quad (2.2)$$

with N being the *effective pressure*, meaning the difference between the ice overburden pressure P_i and the water pressure P_w ,

$$N = P_i - P_w. \quad (2.3)$$

A smaller value of N means more water pressure, larger cavities and therefore, less basal drag.

In an attempt to incorporate this behaviour into ice dynamics, a lot of models use the modified Weertman model (Weertman, 1957; Weertman, 1966; Weertman, 1972),

$$\tau_b^p = \mathbf{u}_b N^q C, \quad (2.4)$$

with constant exponents p and q . So far they mostly relied on the height-above-buoyancy (Huybrechts, 1990) as an approximation for the effective pressure.

2.1.2 CONNECTION BETWEEN WATER AND SLIDING

In practice, this dependency of basal sliding on the water pressure comes into play, when there is a lot of water available. This is the case mostly on Alpine glaciers and in Greenland during the summer melt season. It has long been observed that during periods of summer melting, the ice flow at the coast of Greenland accelerates compared to the winter period. There is also an inter-annual correlation between the intensity of summer melt and the increase in ice velocity (Zwally et al., 2002). Shepherd et al. (2009) find a diurnal connection between surface melt and ice flow variations and associate a longer period variation with the drainage of supraglacial lakes. This

connection between drainage of supraglacial lakes and increased sliding has also been shown by Stevens et al. (2015) and Das et al. (2008). However, the speedup is limited in time and space, because the drainage system is able to adapt to larger inputs, transforming into a more efficient system (Wal et al., 2008; Sundal et al., 2011). Studies for land-terminating outlet glaciers even found that after a summer with faster flow, the following winter flow is slower and explain this with the more efficient drainage system prevailing after the melt season (Sole et al., 2013; Tedstone et al., 2013). Moon et al. (2014) show that the velocity evolution over the year differs between glaciers, recognizing different patterns that reveal differences in the way that the subglacial water systems evolve.

This overview shows that, in order to understand how the drainage works and how the water controls the ice flow, we need to understand the different types and components of drainage systems and also where the water comes from.

2.1.3 WATER SOURCES

Water at the base of the ice comes from two sources: Basal contribution, which is water that is directly produced by melting the ice at the base or within the ice body. This water is generated from melt through the geothermal flux and frictional heating at the base, as well as heating from the deformation of the ice. These mechanisms are the predominant source in Antarctica, where surface temperatures are low and are active independent of seasons. The second contribution is water from the surface which is available in much larger quantity on mountain glaciers and in Greenland. During the melt season, water flows along the ice surface forming *supraglacial streams* which collect the water in surface lakes, also known as *supraglacial lakes* (McMillan et al., 2007; Sundal et al., 2009). At the bottom of these lakes high pressure can cause hydro-fracturing, as described by e.g. Alley et al. (2005a), Veen (2007), and Das et al. (2008), where the resulting cracks can form connections to the base through up to 1000 m thick ice. These connections are called *moulins* and they are the most important mechanism for rapid water transport to the base of the ice. Figure 2.2 gives an overview on available water for Antarctica and Greenland. As described above, in Antarctica only basal melt is considered and is in the order of 5 mm a^{-1} (Fig. 2.2a). Basal melt in Greenland is comparable to Antarctica (Fig. 2.2b), but surface runoff is as high as 1000 mm a^{-1} (Fig. 2.2c). However, surface runoff is a seasonal effect that provides the largest amounts of water during the melt season in summer in Greenland. The fact that there is seasonally much more water available in Greenland leads to different possible drainage system configurations.

2.2 THE ELEMENTS OF THE DRAINAGE SYSTEM

The transport of water at the ice base can be divided into two fundamentally different flow regimes where the amount of available water controls which system prevails: At low water supply, inefficient *distributed* systems, where the water flow is laminar in a thin film form, whereas for large water masses, efficient *channelized* flow form, where a large amount of water is transported in discrete conduits. Their presence and configuration varies in space and time, depending mainly on the available water and geometry. While both systems can coexist at the same time, usually one dominates the water transport.

2 Subglacial Hydrology

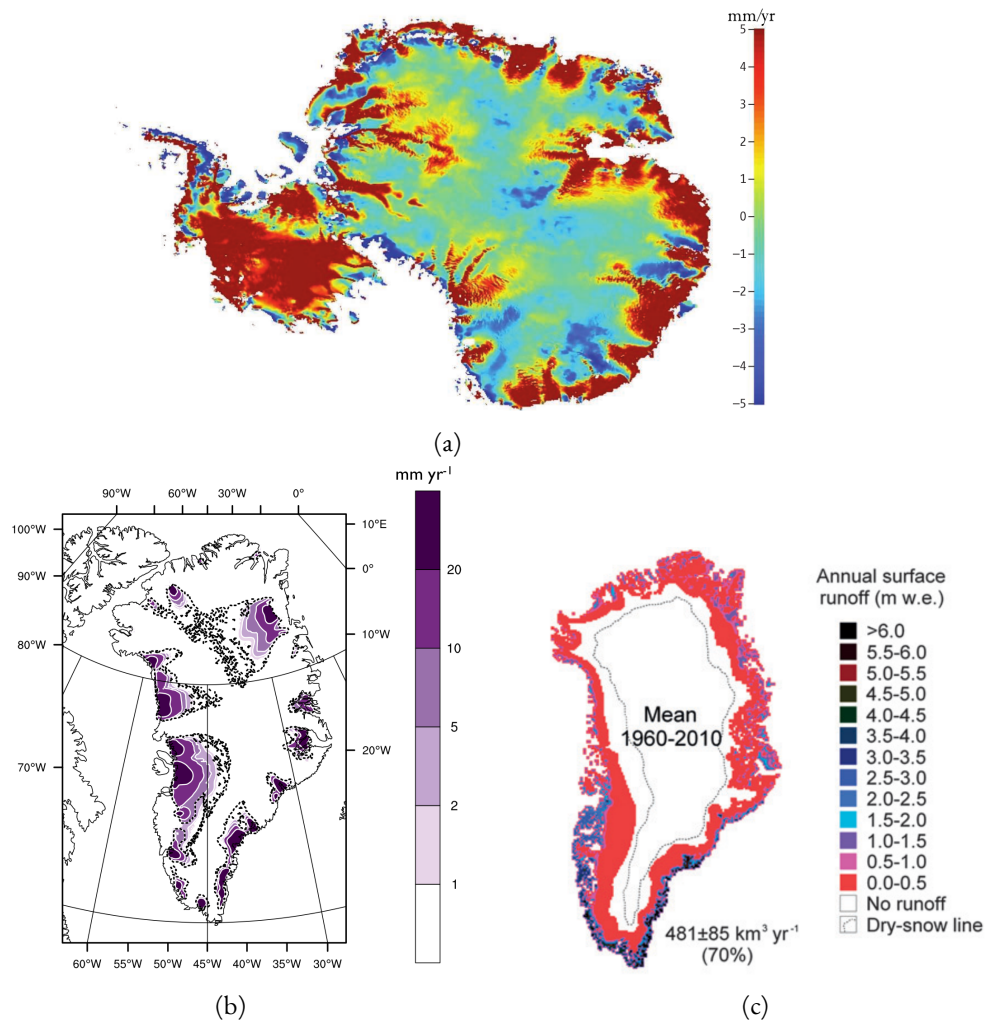


Figure 2.2: Available water in Antarctica and Greenland. (a) Basal melt rates in Antarctica (Tulaczyk and Hossainzadeh, 2011). (b) Greenland basal melt rates (Aschwanden et al., 2012). (c) Greenland surface melt (Mernild and Liston, 2012)

2.2.1 DISTRIBUTED FLOW

Distributed flow encompasses all forms of slow water movement that transport a small volume of water at low effective pressure. That includes linked cavities (Kamb, 1987), flow in a thin Sheet (Weertman, 1957) as well as flow through sediment. These systems prevail all year, as they are independent of large seasonal discharge that comes with summer melt.

Flow in a thin water sheet was one of the first descriptions of subglacial drainage and introduced by Weertman (1957) in his sliding theory, where he developed how sliding is enhanced around bedrock protrusions due to regelation. For this he used the theory of water flow between two rigid plates and assumed that the flux balances all water production. A sheet like this can only be of very few millimeter thickness, because any small perturbation would grow unstable and lead to unbound growth as shown by Walder (1982). This means that for large water supply, the sheet would probably collapse into a more efficient system, as depicted in Figure 2.3.

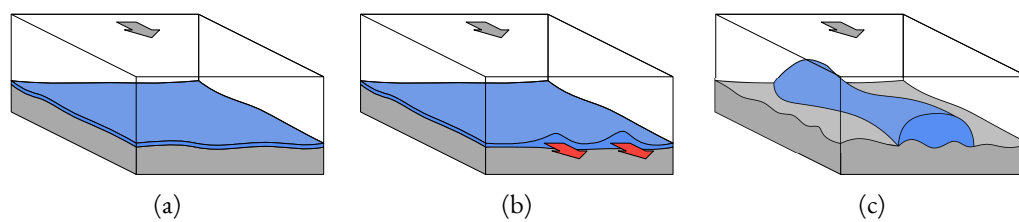


Figure 2.3: Sheet flow, as described by Weertman (1957). (a) Water flows in a millimeter thin film. (b) Small perturbations lead to instability and unstable growth. (c) The sheet collapses and a subglacial channel emerges. Grey arrows indicate flow direction of the ice. Illustrations after Hewitt (pers. communication).

Cavities develop when the ice moves over bedrock protrusions, separating the ice from the bedrock and were first described in the sliding theory of Lliboutry (1958a). They are assumed to be decimeters high and some meters wide, depending on the size of the obstacles. Walder (1986) expanded on this work and studied their hydraulic behaviour, assuming opening of the cavity space by sliding and closure due to ice creep. He described the main characteristics for cavity flow in that they can become unstable at low effective pressure (when creep closure is too small to counteract the opening) and that the water pressure increases with discharge. Therefore, they are stable to perturbations making them good candidates for a long-lived drainage system. The currently used description of cavities is however based on the works of Kamb (1987), who reached the same conclusions for a system of cavities that are connected by narrow ‘orifices’. An idealized configuration of these *linked-cavities* can be seen in Figure 2.4. An important addition is, that orifices can experience melt through dissipation of heat in the flow, which means that the system may grow unstable to small perturbations (of cavity size or effective pressure) if it becomes dominated by viscous heating. In this way the system can transition into an effective channelized system (see Fig. 2.5).

2.2.2 CHANNELIZED FLOW

Subglacial channels are water filled conduits within the ice and probably the most renowned features of subglacial hydrology. They represent the efficient or ‘fast’ drainage element and can transport huge amounts of water in short time. Mostly studied in mountain glaciers (Benn and Evans, 2014;

2 Subglacial Hydrology

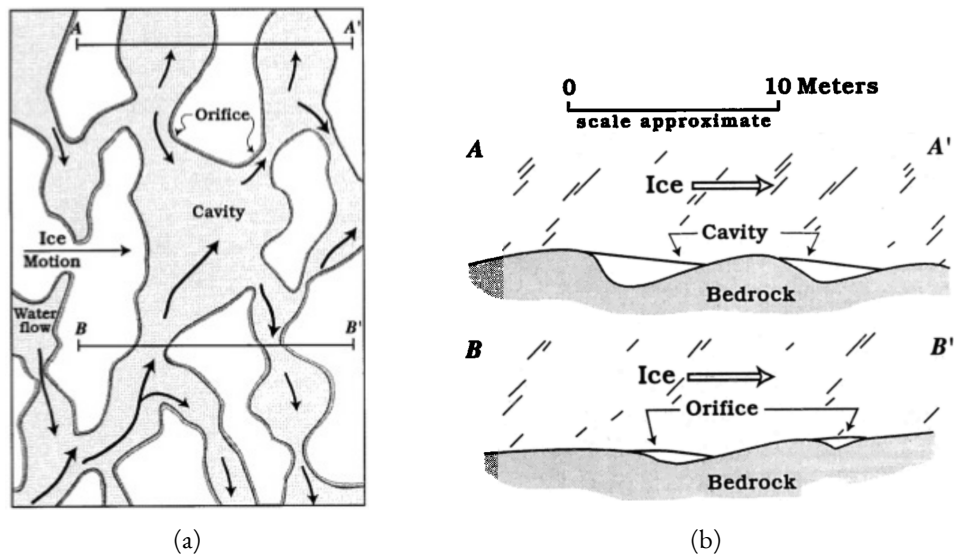


Figure 2.4: Illustration of linked cavities from Fountain and Walder (1998) In (a) the gray areas represent water-filled cavities, which are connected through narrow passages or orifices. Arrows indicate the water flow. (b) shows cross sections, emphasizing the 'throttling' effect of the orifices.

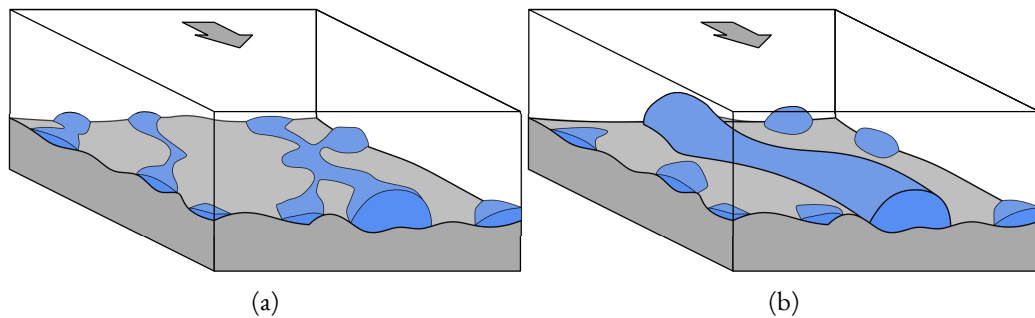


Figure 2.5: The linked cavity system as described by Kamb (1987) (a). While it is stable to small perturbations, large water flux can lead to large viscous heating and a transition to a channelized system (b). Illustrations after Hewitt (pers. communication).

Cuffey and Paterson, 2010), where they form inside the ice or bedrock (Röthlisberger, 1972; Nye, 1976), they have also been observed in Greenland. Assuming saturated flow in a conduit, the channel is controlled by the balance of melt through viscous dissipation and creep closure of the walls due to the weight of the overlaying ice. In contrast to cavities, increasing water flux leads to lower water pressure (higher effective pressure), which means that there is a positive feedback making channels inherently unstable (given enough water supply). Larger channels capture water from smaller ones, creating an arborescent network (Schoof, 2010b). As channels remove a lot of water in short time (operating at low water pressure), they reduce the effective pressure and therefore basal sliding, netting lower ice discharge in turn.

2.2.3 SUBGLACIAL LAKES

Subglacial lakes are bodies of water that form between the base of the ice and the bedrock. Liquid water accumulates in topographic hollows and forms reservoirs below the ice. They are very interesting due to their complete isolation of the atmosphere and extreme pressure and temperature conditions and the fact that microbes were found in samples, proofing that life exists in this hostile environment (Abyzov et al., 2001). In the context of ice dynamics however, it is their effect on sliding which makes them unique. Basal friction is zero above subglacial lakes leading to increased ice velocities, which can induce changes in ice viscosity temperature regime (e.g. Patryn et al., 2004; Gudlaugsson et al., 2016). Using radar and satellite remote sensing, more than a hundred lakes have been observed below Antarctica where they could play an important role for ice-stream genesis (Wright and Siegert, 2012).

3 MODELLING SUBGLACIAL HYDROLOGY

In this chapter I explain the fundamental ideas to modelling the subglacial hydrology. While I give an overview of the currently available methods, I concentrate on two concrete approaches —Balance Flux and Equivalent Porous Media— which I have implemented and used. I will shortly summarize the ideas and equations of channel networks, because they concentrate on an important mechanism of the drainage system and it is important to understand why they can not easily be used for continental scale modelling. I also ignore sediment channels and flow through sediment, because they are outside the scope of this work and refer to the excellent review of Flowers (2015) for an in-depth discussion of different subglacial hydrology models.

During my work I developed three different subglacial hydrology models:

(i) `HYDRO`, which is an implementation of the balance flux method in FORTRAN and coupled to the `Simulation COde for POLythermal Ice Sheets (SICOPOLIS)`. (ii) `CIDRE`, a second balance flux model, which is implemented in Python and Cython and is standalone application and also incorporates a simple method for matching the outflux to the different outlet glaciers and fjords of Greenland. (iii) `CUAS`, a Confined–Unconfined equivalent Aquifer System, which uses an equivalent porous media approach to include the representation of channelized flow (Python/Cython).

3.1 INTRODUCTION

Subglacial water systems are difficult to access and elude direct measurements. Observations are usually confined to single points, such as boreholes, dye tracing experiments at moulins or flux measurements at glacier snouts. Remote sensing can give some clues on the presence of subglacial water, such as surface uplift or certain features in radargrams, but the primary variables of the drainage system, pressure and flux, as well as the geometry is rarely known. This makes it necessary, but also difficult to use numerical modelling in order to get insight into subglacial processes. The following general recipe for drainage models is based on Flowers (2015), who give a great overview over the historic development of drainage models.

The basic requirements for any subglacial or englacial hydrology model are that the water flows down the hydraulic potential and that the water mass is conserved. This gives rise to the continuity equation,

$$\frac{\partial h}{\partial t} + \nabla \cdot \mathbf{q} = m, \quad (3.1)$$

assuming an incompressible water layer with an averaged thickness h (L), water flux q (L^2T^{-1}) and a source term m (LT^{-1}). Sources can be supraglacial, such as runoff from moulins, and englacial/subglacial, like melt from the geothermal flux or frictional heat flux arising from sliding, as well as melt from strain heating.

3 Modelling Subglacial Hydrology

For the computation of flux, most models use empirical relations (instead of deriving flow velocity from conservation of linear momentum and integrating over flow depth h). Such a relation has the general form:

$$\mathbf{q} = -Kh^\alpha(\nabla\phi)^\beta, \quad (3.2)$$

with K a rate factor, $\nabla\phi$ the gradient of the hydraulic potential and α and β exponents which determine the type of assumed flow. K can be a tensor $K_{i,j}(x, y, t)$, which accounts for anisotropy and heterogeneity (as used in Sec. 3.4). Using $\alpha = \beta = 1$, the equation represents laminar Darcy flow with K describing the conductivity. For turbulent flow often $\alpha = 5/4$ and $\beta = 1/2$ are used.

When applied to subglacial channels, Equation 3.2 changes to compute the discharge Q (L^3T^{-1}) instead of the flux q (L^2T^{-1}) and the height h is replaced with the cross section of the conduit S ,

$$Q = -KS^\alpha(\nabla\phi)^\beta. \quad (3.3)$$

In that case, K represents the properties of the assumed pipe, e.g. wall roughness and wetted perimeter.

The hydraulic potential describes the energy in an incompressible fluid and consists of the water pressure P_w and the elevation above a reference level z_b (Shreve, 1972):

$$\phi = \rho_w g z_b + P_w. \quad (3.4)$$

The gradient of this potential $\Phi = \nabla\phi$ is the main driver of water flow.

Some models do also allow for the drainage system do evolve,

$$\frac{\partial h}{\partial t} = \text{opening} - \text{closure}, \quad (3.5)$$

where the opening and closure terms depend on the particular system, but usually refer to melting of the ice, enlargement of conduits by sliding over obstacles and closure due to ice creep. The exact configuration differs in the various published models and a varying combination of different hydrology components is considered.

3.2 BALANCE FLUX APPROACH

One of the most simple concepts for a drainage system is the balance flux approach (Le Brocq et al., 2009; Budd and Warner, 1996; Quinn et al., 1991; Tarboton, 1997). It assumes that the system is always in a steady state, because compared to the slow changes of the ice flow, the subglacial water system reacts almost instantaneously. It further assumes that the water pressure is equal to the ice pressure ($N = 0$) and therefore computes the hydraulic potential (Eq. 3.4) as

$$\phi = \rho_w g z_b + P_i. \quad (3.6)$$

Taking the ice pressure as hydrostatic, the potential then reads

$$\phi = \rho_w g z_b + \rho_i g (z_s - z_b) \quad (3.7)$$

with ρ_i the density of ice and z_s the ice surface height.

It routes the available water along the potential, computing the flux for every model cell, but can not describe water pressure. This approach leads to a very easy and fast implementation which makes it a good candidate for continental scale modelling and coupling to ice sheet models.

Ignoring any change in the geometry of the water system, the continuity equation (3.1) simplifies to

$$\nabla \cdot \mathbf{q} = m. \quad (3.8)$$

Using the divergence theorem, this can be written in integral form

$$\iint_{\Omega} m \, dx dy = \int_{\partial\Omega} \mathbf{q} \cdot \mathbf{n} ds, \quad (3.9)$$

where \mathbf{n} is the outward pointing normal vector. This means that any water produced within the area Ω is balanced by the flux through the boundary $\partial\Omega$ of length s , hence the name balance flux. The balance flux is a volumetric scalar flux ($L^3 T^{-1}$) and can be written as the right-hand side of Eq. 3.9,

$$\Psi = \int_{\partial\Omega} \mathbf{q} \cdot \mathbf{n} ds. \quad (3.10)$$

3.2.1 NUMERICAL IMPLEMENTATION

While it is clear that the water has to follow the steepest gradient of the hydraulic potential, there are multiple possible ways of implementing this on a numerical grid. Three implementations which differ in the number of considered neighboring cells have been compared by Le Brocq et al. (2006): The algorithms of Budd and Warner (1996), Quinn et al. (1991), and Tarboton (1997). I have implemented all three variants in `HYDRO`, but I will only show the details of Quinn et al. (1991) here and refer to Le Brocq et al. (2006) for details on the other two. Quinn et al. (1991) is a multiple flow direction (MFD) algorithm, that—in contrast to single flow direction—allows for bifurcation and convergence of flow.

I have implemented the computation of the balance flux on a structured numerical grid with the grid spacing Δx and Δy . The flux out of a cell is the sum of the water that enters the system within the cell $m_{i,j}$ and the water that entered the cell from cells at a higher potential

$$\Psi_{i,j}^{(\text{out})} = m_{i,j} \Delta x \Delta y + \Psi_{i,j}^{(\text{in})}. \quad (3.11)$$

Using all 8 adjacent cells as possible donors, the flux that enters a receiving cell from a donor cell can be expressed as

$$\Psi_{i,j}^{(\text{receiver})} = \frac{\phi^{(\text{donor})} - \phi^{(\text{receiver})} r}{\sum \Delta\phi^{\text{downslope}}} \Psi_{i,j}^{(\text{donor})}, \quad (3.12)$$

where $\sum \Delta\phi^{\text{downslope}}$ is the sum of the hydraulic potential differences for all downslope cells and r the distance between cells ($r = \Delta x$ or $r = \Delta y$ for cardinal and $r = \sqrt{\Delta x^2 + \Delta y^2}$ for diagonal neighbors).

The flux has to be evaluated in descending order of the hydraulic potential in order to make sure that all contributions are considered. In `HYDRO` I achieve this with a recursive algorithm (from Le

Brocq et al. (2006)). In `CIDRE` I use a different approach that is based on a transfer matrix \mathbf{M} as in Schwanghart and Kuhn (2010) and Schwanghart and Scherler (2014).

The neighborhood relations of the hydraulic potential with n elements can be represented by an *adjacency matrix* $\mathbf{A}(\phi)$; a symmetric $n \times n$ matrix, with elements $a_{i,j}$ equal to one if the cell i is a neighbor of cell j (linear, rowwise increasing index). \mathbf{A} is sparse, allowing for efficient storage and operations and are therefore great for further analysis. An example for this is shown in Figure 3.1b.

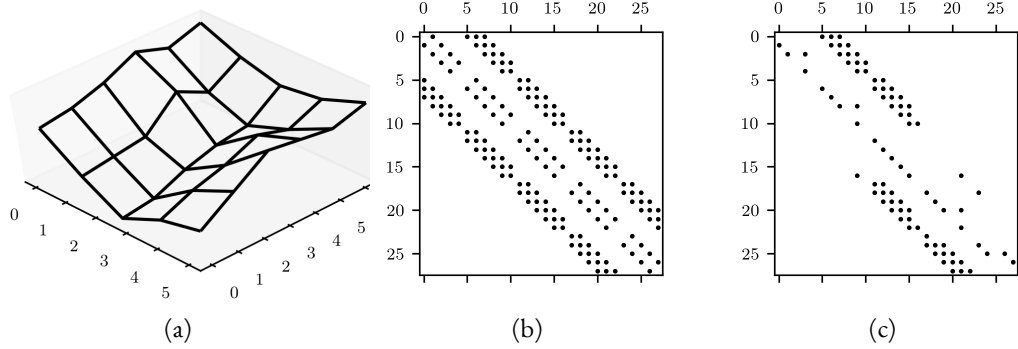


Figure 3.1: Example hydraulic potential (a) and sparsity patterns of adjacency and slope matrix (b) and transfer matrix (c). Black dots indicate nonzero entries of the sparse matrices.

It is now possible to compute the gradient of hydraulic potential and store it using the same structure:

$$\Phi_{i,j} = \frac{\phi_i - \phi_j}{r_{i,j}}, \quad (3.13)$$

where i is the row index and j the column index. Downstream neighbors can now easily be identified, because they correspond to positive values in Φ and the transfer matrix \mathbf{M} is generated by setting negative values of Φ to zero and normalizing each row to one (this is needed for mass conservation).

We can then denote the storage of water in a cell i with w_i and compute the $n \times 1$ vector $\mathbf{w}(k)$ which contains the storage at iteration step k as

$$\mathbf{w}(k) = \mathbf{M}^T \mathbf{w}(k-1), \quad (3.14)$$

where \mathbf{M}^T is the transpose of the transfer matrix \mathbf{M} . A hydrograph for a cell i can now be generated as the time series $w(0, 1, 2, \dots)_i$. It can be shown (Schwanghart and Kuhn, 2010) that the balance flux can be computed as the integral of the hydrograph, resulting in

$$\Phi = [\mathbf{I} - \mathbf{M}^T]^{-1} \mathbf{m}, \quad (3.15)$$

with \mathbf{I} as the identity matrix, a system of linear equations which can easily be solved.

An alternative approach is to understand \mathbf{M} in graph theoretic terms, where it resembles a weighted, directed acyclic graph (DAG). This means, by simply following the graph in descending

order of hydraulic potential and applying Equation 3.12 the balance flux can be computed easily and effectively, which is why I have it implemented in `CIDRE`.

Results for flux on an inclined plane can be seen in Figure 3.2. Cells can be marked as no-flow, where the water is not allowed to pass, e.g. where the ice base is frozen to the ground (Fig. 3.2f). This is easy to realize, because these cells can just be removed as donor/receiver cells from \mathbf{M} . In the same way the flux through arbitrary boundaries can be computed by marking cells boundary cells and then removing them as donor cells. This ensures, that the flux from one boundary cell to another boundary cell is counted, which is not flux over the boundary. In the recursive approach this is not as straight-forward to guarantee.

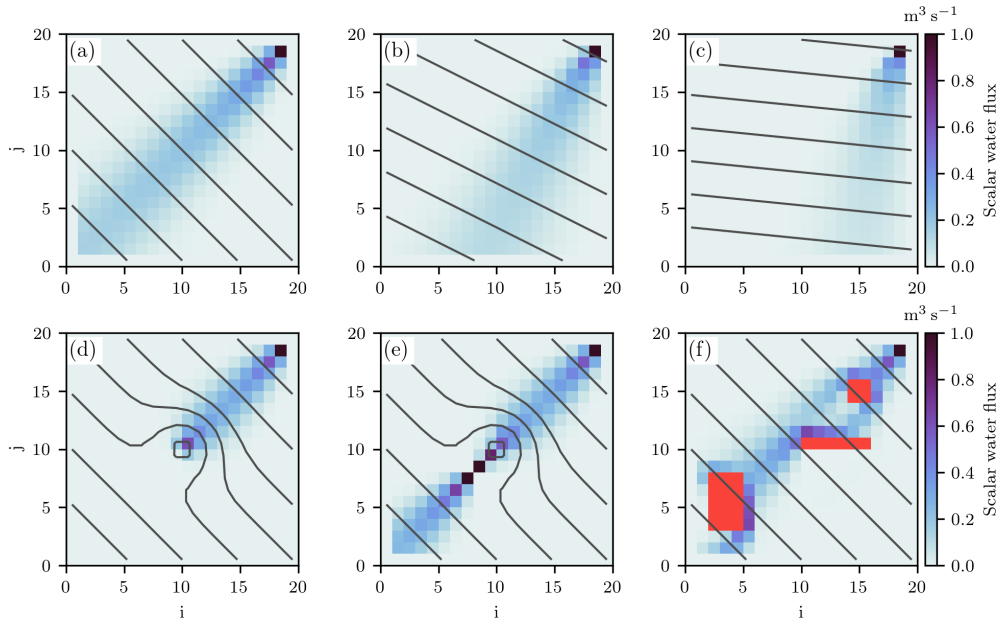


Figure 3.2: Scalar water flux computed via the balance flux approach. Shown here is the multiple flow direction scheme from Quinn et al. (1991). Hydraulic potential is shown as black isolines. The source is a single cell at the top right corner, where a flux of $1 \text{ m}^3 \text{ s}^{-1}$ is injected. Panels (a) to (c) show the influence of the grid orientation. In panel (d) the flow ends in a sink of the hydraulic potential, while in (e) the sink was filled and the water continues past. In (f) red color indicates areas where the water is not allowed to pass through, e.g. where the base is frozen.

3.2.2 DEPRESSION FILLING AND FLAT RESOLUTION

The computation of \mathbf{M} (or recursive evaluation of Eq. 3.12) is complicated by the fact that the flux routing algorithm requires that (i) each cell of the computed hydraulic potential has a defined flow direction and that (ii) by successively following these directions from cell to cell, the boundary of the grid is reached (Barnes et al., 2014b). The presence of flat areas and depressions within the potential surface violates these requirements and therefore, need to be resolved prior to the routing process. Depressions are local minima of the hydraulic potential and therefore have no outlet. Water that enters a depression is trapped inside which makes them possible locations for

subglacial lake locations. Given enough water supply, they would fill up with water and form a lake. In the balance flux approach, however, the flux does not change the geometry or hydraulic potential and depressions collect an infinite amount of water. This is unphysical and violates the assumptions for flux routing. The issue needs to be resolved by filling every depression prior to the routing. By simply filling the sink, flat areas are generated with no local gradient and the flow direction is not defined, which violates property (i), so an additional step is necessary to resolve these flat areas.

In HYDRO and CIDRE I implemented a Priority-Flood algorithm which fills depressions inwards from the edges of the potential surface using a priority queue and is optimal in terms of computational operations ($\mathcal{O}(n \log_2 n)$ for floating-point data Barnes et al. (2014b)). Flat areas are resolved using the algorithm described in (Barnes et al., 2014a): Cells with no defined flow direction are identified and then a gradient is added to direct flow away from the edges of a flat and towards the outlet. It has the benefit of altering the hydraulic potential in the smallest possible way and operates in $\mathcal{O}(n)$ time. Subjected to this treatment, the hydraulic potential is guaranteed to satisfy properties (i) and (ii). An example can be seen in Figure 3.2(d): There is a sink in the hydraulic potential (centered around $i = j = 10$) where the water vanishes. In 3.2(e) the depression has been filled and the water continues past.

3.2.3 COUPLING TO THE ICE MODEL

The balance flux does only compute a flux and no pressure, therefore it can not directly be used in a sliding law like the Weertman-type sliding shown in Equation 2.4. Kleiner and Humbert (2014) solve this problem by converting the balance flux to a water layer thickness (based on Weertman, 1972; Weertman, 1966)

$$h^* = \left(\frac{12\mu\Psi'}{\Phi} \right)^{1/3}, \quad (3.16)$$

with the water viscosity μ and the vector flux Ψ' ($\text{L}^2 \text{T}^{-1}$), which is given for a unit width in the direction of flow (see Le Brocq et al., 2006). The water layer thickness is then used to increase the basal sliding by adding a factor C_b into the sliding law

$$\mathbf{u}_b = -C_b |\tau_b|^{p-1} \tau_n^{-q} \tau_b, \quad (3.17)$$

where

$$C_b = (1 + f_w) C_b^0 \quad \text{and} \quad f_w = 9 \left[1 - \exp\left(-\frac{h^*}{h_0^*}\right) \right]. \quad (3.18)$$

Here, C_b^0 is a tuning constant and h_0^* is the typical scale of the water layer thickness (≈ 1 mm) and the equation ensures that the basal sliding can be enhanced up to ten-fold by the subglacial water.

In collaboration with Ralf Greve, I have coupled this simple hydrology model to the SICOPOLIS ice sheet model, as shown in Figure 3.3. At each time step SICOPOLIS supplies the hydrology module with the current ice geometry and water supply, which it uses to update the balance flux and layer thickness. The layer thickness is then given back to the ice dynamics model to modify basal sliding as in Equation 3.18.

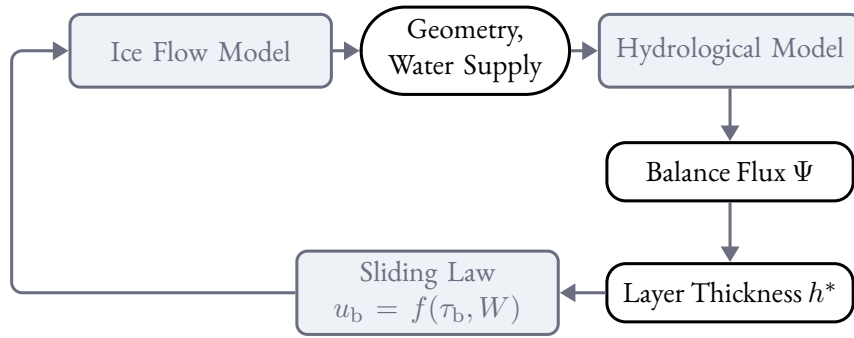


Figure 3.3: Model coupling via layer thickness.

3.2.4 ASSIGNMENT TO GLACIERS

The simplicity of the balance flux method makes it a good candidate for continental scale modelling of ice dynamics, but the computed flux is also interesting for other applications. One possible case is the computation of subglacial melt of outlet glaciers, such as the one by Beckmann et al. (2018). Submarine melt potentially drives glacier retreat and depends largely on the subglacial discharge. One-dimensional models for submarine melt, such as Beckmann et al. (2018), need the discharge not on a two-dimensional grid, but accumulated on a single point per outlet glacier. This requires some additional treatment of the data from the hydrology model.

For the work presented in Chapter 7, I chose a simple mapping of the water flux grid to individual glaciers that is simply based on distance. The position of any glacier is determined by its coastline, taken from the *MEaSURES Annual Greenland Outlet Glacier Terminus Positions from SAR Mosaics* dataset (Moon and Joughin, 2008), supplemented with glacier positions from Rignot and Mouginot (2012) where no data found in the MEaSURES dataset. Obviously the better approach would be to use grounding line positions, but those unknown for a lot of glaciers and I am not aware of any comprehensive dataset. Every cell that is at the edge of the ice mask is then associated with the closest coastline and the respective glacier and all cells matching the same glacier are summed up. Cells that are further than 50 km away from any glacier not assigned at all. The procedure can be seen for an example region in west Greenland in Figure 3.4, using the balance flux computed from basal melt and surface runoff as detailed in Chapter 7. This procedure results in a water flux dataset for every glacier which can be used to track the development over time as illustrated in Figure 3.5.

3 Modelling Subglacial Hydrology

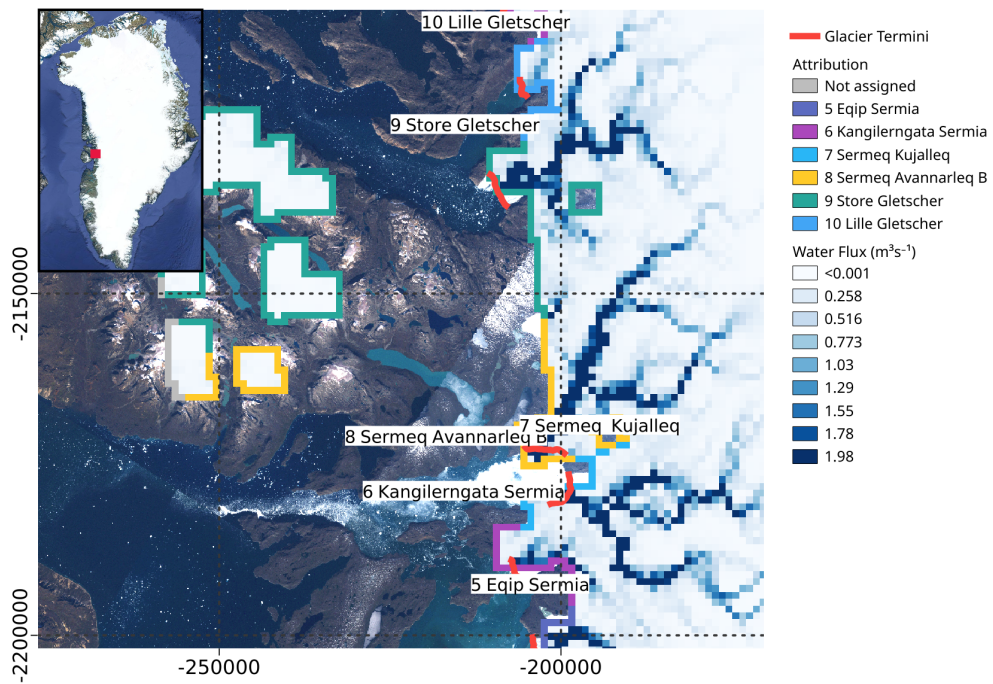


Figure 3.4: Assignment of the water flux to glaciers example in west Greenland with the water flux from August of the year 1900. Background image is the GIMP Landsat-7 mosaic (Howat et al., 2014).

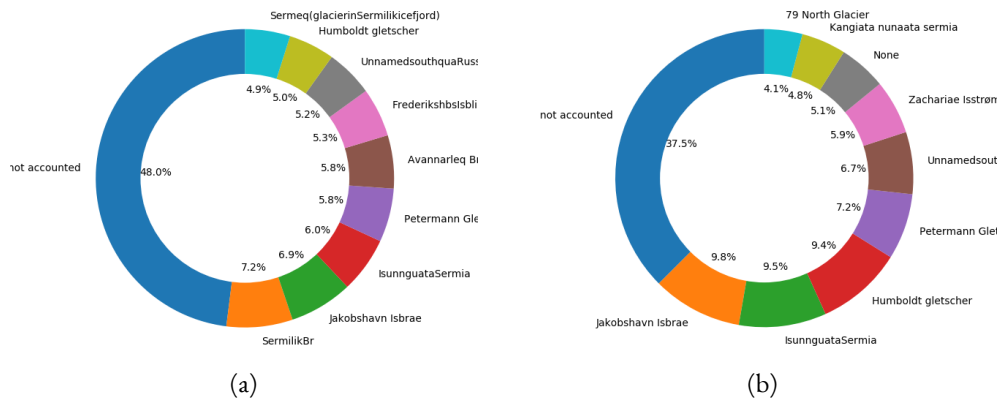


Figure 3.5: Top ten glaciers that receive the most water (runoff plus subglacial melt) for year 2000 (a) and year 2300 (b). The large share that is not accounted to any glacier is due to a lot of melt in the south of Greenland where no named glaciers are in the dataset.

3.3 CHANNELS AND NETWORK OF CHANNELS

Subglacial channels are large conduits that can form below the ice and transport a lot of water, often named ‘R-channels’. Their evolution is governed by the balance of opening due to dissipation of heat and closure by ice creep, as illustrated in Figure 3.6a. The governing equations have been described by Röthlisberger (1972) and Nye (1976) and the evolution of a channel with cross section S and length s can be written as

$$\frac{\partial S}{\partial t} = \underbrace{\frac{Q}{\rho_i L} \left(-\frac{\phi}{\partial s} - (1 - c_t \rho_w c_p) \frac{\partial P_w}{\partial s} \right)}_{\text{opening}} - \underbrace{2SA \left(\frac{P_i - P_w}{n} \right)^n}_{\text{closure}}, \quad (3.19)$$

with the discharge Q , latent heat of fusion L , hydraulic head ϕ , Clausius-Clapeyron slope c_t (change in melting temperature with pressure) specific heat capacity of water c_p , creep rate factor A and Glen’s exponent $n = 3$. The derivative of ϕ along the channel coordinate s (first term of the opening part) describes the energy that is available for melting due to the gravitational potential, while the second term of the opening part represents energy from pressure differential, lessened by the amount of heat necessary to keep the water temperature at pressure melting point. The latter effect is sometimes neglected, although it can reduce the available energy for melting by almost 30 % (assuming a horizontal channel, $\partial\phi/\partial s = 0$) (Flowers, 2015). Equation 3.19 together with the continuity equation (3.1) and a suitable flow law (3.3), such as Darcy-Weisbach or Manning flow, completes a one-dimensional channel model.

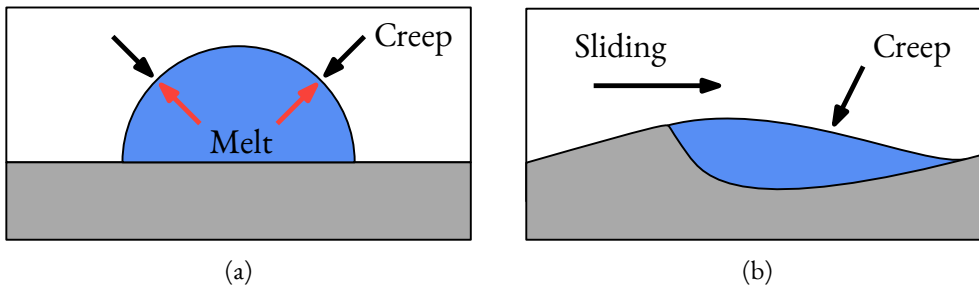


Figure 3.6: Processes governing opening and closure of channels (a) and cavities (b).

Various studies been motivated by the phenomenon of ice-dammed lake drainage and have used different implementations of the channel equations in combination with an additional inefficient system with great success (e.g. Flowers et al., 2004; Pimentel and Flowers, 2010), but the one dimensional nature somewhat limits its application. More recent advances use a network of channels in order to represent two-dimensional drainage systems. Herein, a two-dimensional numerical mesh is used as a network of potential channel locations as shown in Figure 3.7. Schoof (2010b) uses a single common equation for channels and cavities, where the balance between opening and closure determines if the element behaves as a channel or as a conduit. The individual conduits are coupled by enforcing mass conservation at nodal points and a network of channels forms, given sufficient water input. Werder et al. (2013) and Hewitt (2013) use a continuum sheet description for inefficient cavity flow, where the network of potential channels is defined along the edges

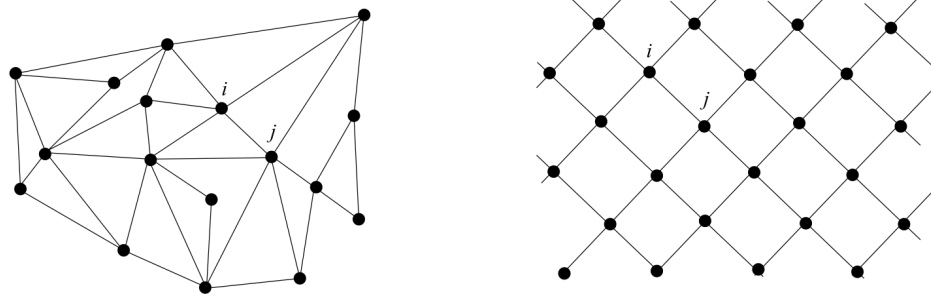


Figure 3.7: Channel network (Schoof, 2010b, SI)

of the continuum cells. These models are able to realistically predict the spontaneous evolution of channels networks and Hewitt (2013) additionally couples the model to the ice flow, successfully reproducing ice flow speedup during summer melt with the characteristic slowdown when the drainage system becomes efficient. However, these models are computationally expensive and therefore have not yet been used on continental scale modelling.

3.4 EQUIVALENT AQUIFER MODEL

Once established, channels are crucial for subglacial water flow but their location is usually unknown. Recent models solve this problem by using a network of potential channel locations, which are only developed when enough water is supplied. This adds a considerable amount of complexity and computational cost, which sparks the idea for a simpler approach: The subglacial drainage system can be classified into two basic states, inefficient drainage, such as a system of cavities or sediment flow on one end, and an efficient system of channels on the other end. Disregarding any specific details on the particular system, this can be viewed not as two different systems with distinct mechanisms, but as a uniform system with location dependent (heterogeneous) properties.

This idea has already been studied for the modelling of karst aquifers which are similar in their structure: formed by dissolution processes in carbonate rocks a network of preferential flow paths, conduits and fractures controls the water in the rock matrix. Flow in the rock matrix is usually laminar, while it is predominantly turbulent in fractures. Distribution of fractures and conduits is usually unknown, making it very difficult to use traditional models that require detailed data on the state and location of conduits. In this context, the attempt is called equivalent porous medium. It assumes that the bulk medium of the rock matrix and efficient network of cracks and connections can be approximated as a simple porous medium with a conductivity that is chosen such that it is equivalent to the original medium over a large enough area. This approach is also known as smeared conduit approach, heterogeneous continuum approach, or Single continuum porous equivalent (Ghasemizadeh et al., 2015). It has been shown that it leads to good results for groundwater flow on regional scale, but is not applicable for contaminant transport (Scanlon et al., 2003).

In the context of subglacial hydrology, Fleurian et al. (2014) employed the idea of an equivalent aquifer model, where they used two separate layers to reflect the two different types of drainage. They differ in their hydraulic properties, where the inefficient and efficient layer are characterised by low and high conductivity respectively. The efficient layer is only activated when the inefficient system is unable to remove the water alone. In Fleurian et al. (2016) an evolution for the thickness of the efficient layer is introduced, resembling the channel evolution as given in Equation 3.19. I took this idea one step further by only using a single layer and adapting its ability to transport water (transmissivity) according to Equation 3.19 (as shown in Fleurian et al. (2016)), which results in a very simple model that incorporates the different types of flow in a unifying manner.

In this context the continuity equation together with Darcy's law $q = -T\nabla h$, with the transmissivity $T = Kb$ and aquifer thickness b , leads to the groundwater flow equation

$$S \frac{\partial h}{\partial t} = \nabla \cdot (T\nabla h) + m, \quad (3.20)$$

with the Storage S , which describes how the porous matrix and fluid can be compressed, and water source m . Here, h is the hydraulic head, which consists of elevation head and pressure head and differs from the hydraulic potential ϕ by the factor $\rho_w g$,

$$h = \frac{P_w}{\rho_w g} + z_b. \quad (3.21)$$

3 Modelling Subglacial Hydrology

Since the transmissivity represents the effectivity of the system, it has to adjust according to the opening and closure terms for the channel and cavity equations. In this regard, the model is similar to the one by Schoof (2010b), as it does not distinguish between channels and cavities. The evolution equation for T reads

$$\frac{\partial T}{\partial t} = a_{\text{melt}} + a_{\text{cavity}} - a_{\text{creep}}, \quad (3.22)$$

in which

$$a_{\text{melt}} = \frac{g\rho_w K T}{\rho_i L} (\nabla h)^2, \quad (3.23)$$

with L as latent heat of fusion,

$$a_{\text{cavity}} = \beta |\mathbf{u}_b| K, \quad (3.24)$$

with β is a factor controlling the opening (accounting for geometry) and \mathbf{u} the basal ice velocity. The creep term reads

$$a_{\text{creep}} = 2An^{-n}|N|^{n-1}NT, \quad (3.25)$$

where A is the creep rate factor, N the effective pressure and n the exponent in Glen's flow law. The complete description is given in Chapter 8.

In order to couple this model to an ice dynamics model, a scheme like the one pictured in Figure 3.8 can be used. The ice flow model computes the geometry, water supply and the ice pressure, which the hydrology model uses to compute the water pressure. Then the water pressure together with the ice pressure determine the sliding for the ice base via effective pressure.

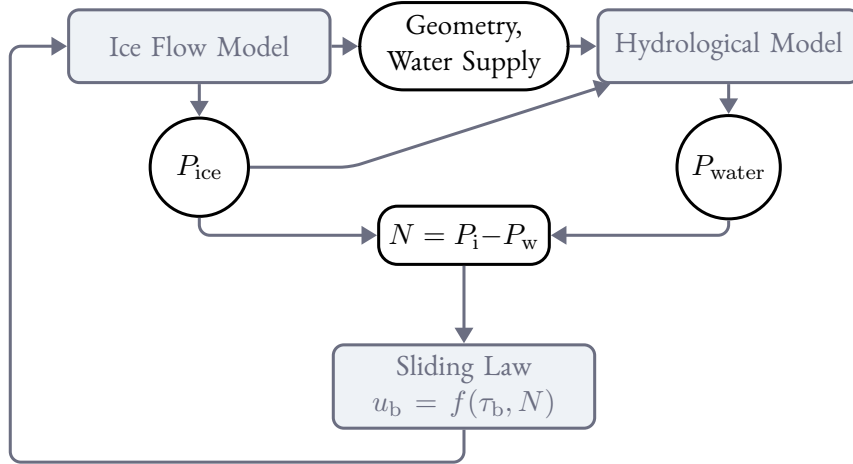


Figure 3.8: Model coupling via effective pressure.

4 MISSING EVIDENCE OF WIDESPREAD SUBGLACIAL LAKES AT RECOVERY GLACIER, ANTARCTICA

CONTEXT

Subglacial lakes are an important feature of the hydrology system beneath the Antarctic ice sheet. Compared to Greenland, in Antarctica there is a lot less water supply due to the lack of surface runoff, which makes a balance flux approach, as described in Section 3.2, a viable modelling approach. The Recovery Glacier drains a large part of the East Antarctic Ice Sheet and subglacial hydrology and lakes were suggested to play a role in the fast flow of the ice stream. For the modelling of the hydrology, it is important to have reliable data on the geometry (basal topography and ice thickness) and on the water supply into the system. The extensive radio-echo sounding dataset compiled over the area together with melt rates computed from the Parallel Ice Sheet Model (PISM) gives a unique opportunity to apply the model and compare its result with the additional information on subglacial conditions which were extracted from different sources.

The idea of this paper was to combine multiple approaches to lake identification and water detection in order to study the basal properties of the Recovery Ice Stream. The amplitude of the radar reflection at the ice–bed interface yields information on basal properties and can be used as a proxy for hydraulic and thermal conditions at the bedrock (see Section 4.2.3 in the paper). In order to analyze the reflection coefficient, temperatures computed by the ice model were used to determine radar absorption within the ice. Additionally, different schemes for lake identification were applied, based on basal reflectivity as well as on surface elevation changes derived from satellite data.

From the perspective of assessing the capabilities of the subglacial hydrology model `HYDRO`, it is important to apply the model on a non-artificial test case, where at least some information about the presence of water at the base is available. Observations to verify subglacial hydrology models are scarce and usually restricted to singular points. Radar data covering a large domain are a possibility to compare the modelled hydrology over an area. For large scale models, as targeted in this thesis, it is important to check their validity also on regional scales in order to determine their limits.

The hydraulic potential was computed using Equation 3.7 and then experiments with four different basal melt distributions (3 from PISM and one with basin wide constant melting) were performed, where the water was routed along the potential. The difference between the filled potential and the original potential (see Section 3.2.2) served as a starting point for potential lake locations, because water would be collected in topographic hollows of the potential. The resulting water pathways together with potential lake location were combined with the radar data and

additional lake indicators to discuss the presence of water and to examine previously suggested lake locations.

CONTRIBUTION

For this article, I computed the hydraulic potential and identified sinks as potential lake locations and used the newly developed subglacial hydrology model HYDRO to investigate the water pathways. I wrote the section on the subglacial water flux and hydraulic potential in the methods and the results part. Together with all authors, I reviewed the results and combined analysis and contributed to the discussion and conclusion. The synthesis was written by all authors.

AUTHORS AND AFFILIATIONS

Angelika Humbert^{1,2}, Daniel Steinhage¹, Veit Helm¹, Sebastian Beyer^{3,1}, and Thomas Kleiner¹,

¹*Alfred Wegener Institute, Helmholtz Centre for Polar and Marine Research, Bremerhaven, Germany*

²*Department of Geosciences, University of Bremen, Bremen, Germany*

³*Potsdam Institute for Climate Impact Research (PIK), Member of the Leibniz Association, Earth System Analysis, Potsdam, Germany*

ABSTRACT

Recovery Glacier, draining into Filchner Ice Shelf, reaches far into the East Antarctic Ice Sheet. Recent projections point out that its dynamic behaviour has a considerable impact on future ice loss (Golledge et al., 2017). Subglacial lakes were suggested to play a major role in the initiation of the rapid ice flow (Bell et al., 2007) and altimetry observations have suggested that several subglacial lakes underlie the main trunk, actively filling and draining (Smith et al., 2009). We present a study that aims to determine the geometry of the glacier and its basal properties by means of radio-echo sounding. Using ice-sheet modelling, we were able to constrain estimates of radar absorption in the ice, but uncertainties remain large. The magnitude of the basal reflection coefficient is thus still poorly known. However, the spatial variability, in conjunction with additional indicators, can be used to infer the presence of subglacial water. We do not find clear evidence for water at most of the previously proposed lake locations, especially locations where active lakes were reported do not exhibit lake characteristics in RES. The newly derived geometry was used for hydraulic modelling (flux routing), which reveals subglacial water paths and multiple lake locations in the main trunk. However, we argue that lakes far upstream the main trunk are not the cause for ice stream flow.

4.1 INTRODUCTION

Recovery Glacier drains an area of $\sim 996,000 \text{ km}^2$, corresponding to $\sim 8 \%$ of the area and $\sim 5 \%$ of the volume of the East Antarctic Ice Sheet (EAIS) (Rignot et al., 2008b). It has first been surveyed in 1957 by the Commonwealth Transantarctic Expedition (Lister and Pratt, 1959). The drainage basin is traversed by the main ice stream, Recovery Glacier, flanked to its west by the Shackleton Mountain Range and draining 1000 km from the interior EAIS to Filchner Ice Shelf, and fed by several tributaries including Ramp and Blackwall glaciers. Its drainage basin ranges nearly 1000 km (Figure 4.1). Gолledge et al. (2017) demonstrated that the majority of the future mass loss from the EAIS will originate from the Recovery basin, underlining the importance of understanding its dynamics and, in turn, the role subglacial water plays in influencing them. Previous studies based on surface structure, elevation change and radio echo sounding (RES) suggest prominent subglacial lakes exist beneath Recovery Glacier (Bell et al., 2007; Smith et al., 2009; Fricker et al., 2014). These lakes have been implicated in both the ice stream’s onset and its fast flow, although there remains a poor understanding of the processes by which subglacial lakes overall influence ice dynamics here and elsewhere across Antarctica (Ashmore et al., 2014; Siegert et al., 2014). Apart from lakes, basal water may occur either in form of a distributed layer —like a thin film— or as a network of channels, which both affect sliding.

Observations below the ice masses are limited by accessibility, which usually restricts analysis to indirect methods. However, significant differences in the dielectric properties of subglacial water and rock (or sediment) result in different reflection coefficients of radar waves, which can be analyzed in order to detect water at the reflection interface (and infer if the base of the ice is wet). It requires, however, a reasonable estimate of the absorption in the ice, which depends on the (unknown) temperature distribution in the ice. For this reason previous studies interpreted the variation of the reflection loss, rather than the absolute magnitude and combined that with an analysis of the hydraulic head (e.g. Langley et al., 2014) or basal roughness (e.g. Diez et al., 2018).

In the recent years, the detection of active lakes by means of altimetry has been challenged by findings of Siegert et al. (2014), which were missing evidence for a site on Institute Ice Stream in RES data. Wright et al. (2014) came to the same conclusion for eleven sites at Byrd Glacier catchment. Siegert et al. (2016a) carried out a study to examine the capability and limits of radar and remote sensing methods to infer location and dynamics of subglacial lakes which also challenged the current view on active lakes. Our study is continuing this route of a critical assessment of different methods. For this purpose and in order to increase the data coverage, in January 2014 an extensive airborne survey of Recovery Glacier and its drainage basin was carried out, surveying a total length of 22,700 km. Ice thickness, ice structure, and surface topography data were acquired, extending the region mapped by earlier surveys (Paxman et al., 2017; Diez et al., 2018; Forsberg et al., 2018) further south-east. Our survey aimed to accomplish two goals: (1) acquire extensive basic coverage of Recovery Glacier and its tributaries, Ramp Glacier and Blackwall Glacier (see Figure 4.1), and (2) collect data along flow lines of the main trunk and detailed coverage of the proposed lake areas. A surface velocity data set derived by Floricioiu et al. (2014) was used to compute flow lines prior to the survey. The resulting profiles are shown in Figure 4.1 together with the previously proposed lakes by Bell et al. (2007) and Smith et al. (2009) (referred to as LA–LD and Lakes R1–R11, respectively in the following).

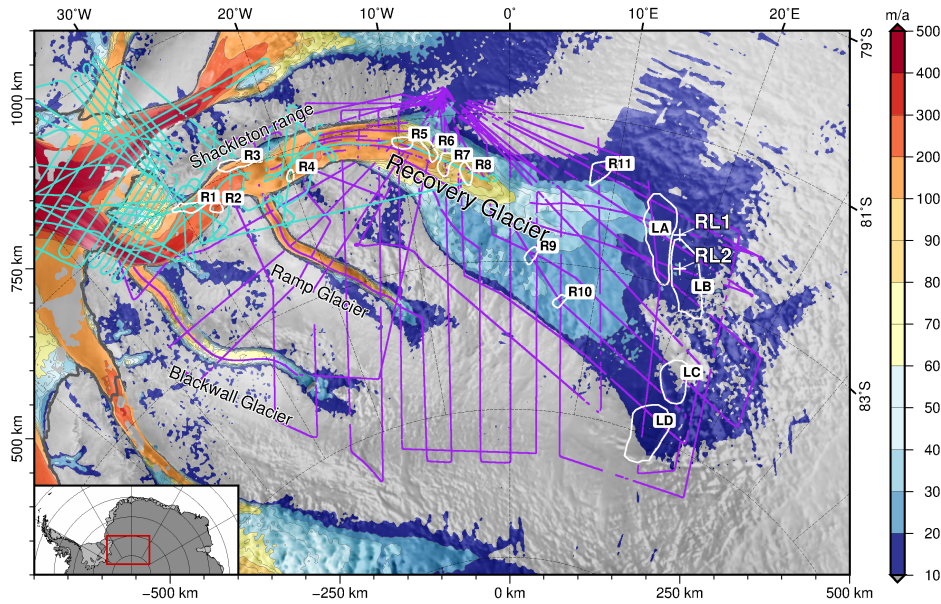


Figure 4.1: Map of the Recovery basin area with selected place names. Lakes observed by Bell et al. (2007) marked with LA–LD, and Smith et al. (2009) marked with R1–R11, both outlined in white. Dots indicate basal returns of the radio echo signal from this study (purple) and from OIB (Leuschen et al. (2010, updated 2017), turquoise). Surface velocities (blue to red) derived from satellite radar interferometry (Rignot et al., 2011b) are clipped at the 10 m a^{-1} lower limit. The thick grey line denotes the grounding line position. The background image in this and all subsequent maps is Ramp Antarctic Mapping Mission 1 mosaic (Jezek, 1999).

In our study, we examine the magnitude of the basal reflection coefficient and its determining factors and discuss the general ability and limits of this approach. The second part of our study uses the basal reflection coefficient in conjunction with additional parameters, such as modelling of subglacial hydrology, mapping surface elevation change, reflectivity and variability of reflection loss as a means of reviewing previously proposed lake locations. Furthermore, we discuss the nature and spatial variability of the bed of Recovery Glacier.

4.2 METHODS

The following sections summarize the modelling studies we conducted to study the subglacial properties of Recovery Glacier and its tributaries. We introduce the deployed radio-echo sounding (RES) system and present methods applied to obtain bed elevation and the approach to distinguish between wet or dry bed returns. Furthermore, the method used to determine active lakes based on ICESat altimetry is described.

4.2.1 SUBGLACIAL-LAKE IDENTIFICATION FROM MODELLING

Two different modelling studies were conducted to derive the thermal regime of the ice sheet and at the base as well as to calculate the hydraulic potential for and flux routing beneath the ice with

emphasis on the Recovery Glacier region. To improve the output of both modelling studies ice-thickness-data derived from our survey were integrated into the Bedmap2 data set.

ENGLACIAL AND SUBGLACIAL TEMPERATURE FIELDS

We engaged numerical ice flow modelling to derive a first-order estimate of the basal thermal regime across Antarctica. The simulated temperature-depth profiles at each grid location were also used to derive englacial attenuation in support of our RES analyses introduced in Section 4.2.2. This has been done also in previous studies e.g. Matsuoka et al. (2012), Wright et al. (2012) and Ashmore et al. (2014).

Here we used the Parallel Ice Sheet Model (PISM v0.6.2, Bueler and Brown, 2009; Winkelmann et al., 2011). PISM solves the non-sliding shallow ice approximation (SIA) and the shallow shelf approximation (SSA) for grounded ice, where the SSA solution acts as a sliding law, and only the SSA for floating ice. New ice-thickness data derived for this study (methods described in Section 4.2.2) were used for different simulations with varying data sets for boundary conditions as: surface temperature (Comiso (2000), Fortuin and Oerlemans (1990) and Wessem et al. (2014)), surface mass balance (Arthern et al. (2006), Berg et al. (2006) and Wessem et al. (2014)) and geothermal flux (Shapiro and Ritzwoller (2004), Fox Maule et al. (2005) and the update from Purucker (2012b) based on the method of Fox Maule et al. (2005)). The original data set of Fox Maule et al. (2005) was capped at a value of 0.07 W m^{-2} according to the recommendation for the SeaRISE-Antarctica set-up (Bindschadler et al., 2013). A summary of the selected data sets is given in Table 4.1.

PISM is in contrast to the ice sheet models used in Matsuoka et al. (2012) and Ashmore et al. (2014) not based on a balance velocities approach, where the vertical distribution of velocity is calculated based on shape functions (Pattyn, 2010; Leysinger Vieli et al., 2011). A major difference of our model setup to the flow model applied in Wright et al. (2012) is that the geothermal heat flux in our study is not spatially invariant.

In a series of successive grid refinements (all based on the initial 1 km present day geometry) using 40 km, 20 km and 10 km horizontal resolution and 41, 81 and 101 vertical layers, respectively, a present day state of the Antarctic Ice Sheet was computed for each combination of boundary conditions, with the restriction that RACMO2.3/ANT (Wessem et al., 2014) data for mean annual skin temperature and accumulation rate are used in conjunction for consistency. Thus, a combination of five different surface forcings for three different geothermal fluxes was used to build the ensemble.

In one group of simulations we applied PISM's flux-correction method, where the climatic mass balance was modified at each time step to obtain an ice sheet thickness in closer agreement with measurements (hereinafter referred to as *evoFT*). In this group we further prescribed the present day calving front position according to Bedmap2 (Fretwell et al., 2013). In a second group of simulations, the ice thickness and calving front position were allowed to evolve freely (hereinafter referred to as *evoSR*). In all simulations we applied the sub-grid grounding-line interpolation scheme (Feldmann et al., 2014) for a better grounding-line representation in the relatively coarse model, while other parameters correspond to the PISM's SeaRISE-Antarctica set-up (c.f. the Potsdam model in Nowicki et al., 2013). After initialisation (1 a), a short relaxation period (100 a) and a purely thermal spin-up with the geometry held fixed (200 ka) on the 40 km grid us-

ing only the non-sliding SIA, the model ran for 100 ka, 20 ka and 4 ka on the 40, 20 and 10 km grid, respectively, in the hybrid (SIA + SSA) mode for each set-up to reach the final temperature distribution used here.

The results of all model runs were analysed for the temperate ice area fraction (TIAF), as a temperate base is a prerequisite for subglacial water. TIAF was calculated as the ratio between the grounded temperate ice area and total grounded ice area in Recovery Glacier area. In addition, we computed the temperate ice volume fraction (TIVF) as the ratio between temperate ice volume and the total grounded ice volume. With the TIVF we have measured the amount of very warm ice (at pressure melting point) near the base that contributes to the attenuation of the radar signal.

SUBGLACIAL WATER FLUX AND HYDRAULIC POTENTIAL

The new ice geometry (ice thickness and ice base) together with the basal melt rates from ice modelling were used to estimate the water flux. Subglacial water flux and storage are governed by the hydraulic potential Φ , which depends on the elevation potential and the water pressure p_w (Shreve, 1972):

$$\Phi = \rho_w g h_b + p_w, \quad (4.1)$$

with the ice base h_b , acceleration due to gravity g and density of water $\rho_w = 1000 \text{ kg m}^{-3}$. The water pressure depends on the ice overburden pressure and the effective pressure N (normal stress at the bed minus water pressure):

$$p_w = \rho_i g H - N, \quad (4.2)$$

wherein $\rho_i = 910 \text{ kg m}^{-3}$ is the density of ice. Following previous authors such as Le Brocq et al. (2009) and Livingstone et al. (2013), we assumed the water flows as a thin (a few mm) and distributed water film. Under this premise, the water pressure and the ice overburden pressure are in equilibrium and therefore the effective pressure is zero. This enabled us to reformulate Equation (4.1) as

$$\Phi = \rho_w g h_b + \rho_i g H, \quad (4.3)$$

and then computing the water flux with a simple flux routing scheme as described by Le Brocq et al. (2006). This approach is only valid at large (km) scales and is not able to include local features such as channels. Also, lakes that are formed by ice dynamic mechanisms are not captured by this.

We interpolated the melt rates given by the PISM model onto a 1 km grid. The hydraulic potential was computed following Equation (4.1) before smoothing it with a 10 km radius box blur filter. This was done to make use of our high resolution ice surface while accounting for the averaged sheet flow assumption. Additionally, a version of the potential with only 2 km smoothing filter was generated as a basis for the identification of lake candidates from additional criteria (see Section 4.2.4). As the next step local sinks in the hydraulic potential were marked as expected positions for subglacial lakes. The flux routing method requires that every cell has a defined flow direction and that by successively following these directions, the boundary of the study area is reached. Therefore, local sinks and flat areas must be removed prior to applying the routing scheme. We accomplished this by using a Priority-Flood algorithm as described in Barnes et al. (2014b), which fills depressions in a single pass and then adds a small gradient to the resulting flats. The gradient generation follows Barnes et al. (2014a), adds a gradient towards the outlet of the depression and

ensures that the hydraulic potential is altered in the smallest possible way. This procedure is a very efficient way to guarantee that all water is drained into the ocean.

We calculated the hydraulic potential and resulting water flux for different melt rate distributions: catchment wide melting of 0.006 m a^{-1} and melt rates from the evoSR type simulations using $q_{\text{geo}}^{\text{S}}$, $q_{\text{geo}}^{\text{P}}$, $q_{\text{geo}}^{\text{F}}$. This allowed us to differentiate between flow paths that were theoretically possible and those that were likely developed with the available water.

Note that we only routed the water that was produced within the investigated area and not the entire Recovery drainage basin, since we were only interested in the general distribution pattern rather than the magnitude of the flux.

4.2.2 ICE THICKNESS FROM RES

SURVEY AND AWI-RES SYSTEM

To map the ice thickness and basal properties of the Recovery basin, we undertook an extensive RES survey in January 2014. The flight tracks, totalling 22,700 km in length and depicted in Figure 4.1, were designed to achieve a basic coverage across the Recovery catchment, while additionally targeting flow lines along Recovery Glacier and its tributaries including Ramp and Blackwall glaciers, and more detailed coverage across the proposed subglacial lakes from Bell et al. (2007) and Smith et al. (2009). flow lines were derived from Floricioiu et al. (2014).

We surveyed with the Alfred-Wegener Institute RES system (hereafter AWI-RES), operating at a carrier frequency of 150 MHz. Building upon the basic design reported by Nixdorf et al. (1999), the system deployed in 2014 used a new signal generator inside the transmitter and a completely revised receiver. The transmitted signals were generated by a programmable digital synthesizer which started each burst with the same phase. The new receiver was based on a 14-bit digitizer with 4 ns sampling interval, but retained the concept of different pre-amplifying and logarithmic detectors (Nixdorf et al., 1999). This setup covered a wide dynamic range (-105 to +10 dBm) but, critically, allowed for the determination of a basal reflection coefficient from the returned signal. The antenna hardware and signal handling between transmitter, receiver and antennas remained unchanged from that reported by Nixdorf et al. (1999).

The system was operated in mono burst mode, transmitting a long non-coherent pulse of $\tau = 600 \text{ ns}$. The received power was rectified and the envelope was recorded. Subsequently, shots were incoherently stacked 1024 fold for improving signal-to-noise ratio and then recorded at a rate of 15 Hz. The corresponding average shot separation was 6 m. The accuracy of the travel-time measurements was determined by the sample interval of 4 ns, corresponds to 0.34 m in ice. The recording time window was $64 \mu\text{s}$, allowing registration of reflections up to a maximum ice thickness of 5000 m, on a flight level of 600 m above ground. Processing of the data prior to evaluation comprised further stacking of shots (7 fold) and filtering. From this point on, two processing branches commence: one in which the amplitudes were scaled for picking the basal reflections in order to estimate ice thickness, and the second, which kept the amplitudes unscaled and was used for the analysis of the basal reflection power.

The AWI-RES system differs in some parameters from the systems deployed by other groups. The small bandwidth of 1,666 kHz ($= \tau^{-1}$) results in a vertical resolution of approximately 50 m and a radius of the first Fresnel zone of ca. 300 m (assuming 3000 m thick ice and a flight level of 600 m above ground). Radar waves are diffusively scattered at small facets (small with respect

to wavelength) within the first Fresnel zone. The width and intensity of the bedrock return is controlled by the number and size distribution of the corresponding scattering elements. For large Fresnel zones usually enough scattering elements are available to form intensity peaks with a similar width. However, the peak intensity will change from trace to trace by several dB, which is known as the radar speckle. Incoherent stacking along track reduces this speckle effect slightly. In consequence, the AWI-RES system with its long pulse duration is neither sensitive to small scale changes in bed roughness nor to specular surfaces, which has implications for our ability to detect subglacial lakes that we will discuss in detail below.

ICE THICKNESS AND SUBGLACIAL TOPOGRAPHY

To improve and densify the manual picked ice thickness retrievals as well as to evaluate the return power an automatic algorithm determining the basal reflection in a predefined time window on a shot to shot basis was developed. The algorithm generated a quality flag for each pick, based on the noise floor before and after the bed pick and, where the reported quality was low, we undertook manual picking. The resulting two-way travel times (twt) in ice were converted into thickness by using locally determined velocity depth functions. The appropriate velocities were calculated by computing depth-density profiles (Herron and Langway, 1980) using accumulation and temperature distribution of the regional atmospheric climate model RACMO2.3 (Wessem et al., 2014).

For the interpolation of direct ice-thickness measurements onto an ice-thickness grid we have first selected a polygon surrounding the data with a margin of approximately 50 km including only the grounded ice area. Within that polygon we have further incorporated Operation IceBridge (OIB) data from the years 2011/12 and 2012/13 (Leuschen et al., 2010, updated 2017) and the locations of known rock outcrops from Survey (2004). In addition to these point observations, gridded data from Bedmap2 (Fretwell et al., 2013) has been used outside the polygon towards the domain margin (see Figure 4.1 for domain extent). The ice-thickness data has been interpolated on an initial 5 km x 5 km grid using the continuous curvature splines in tension algorithm (Smith and Wessel, 1990) and resampled to the final 1 km resolution grid. After interpolation the data inside the polygon was stencilled out of the regional grid and incorporated into the Bedmap2 ice-thickness grid. We further subtracted this subset of the regional ice-thickness grid from the Bedmap2 surface topography for the basal topography, that we incorporated into the Bedmap2 bedrock grid. The Bedmap2 surface topography has been used to be consistent with the Bedmap2 bedrock topography.

4.2.3 BASAL REFLECTION COEFFICIENT

Previous studies have suggested that where englacial attenuation can be accounted for, the strength of the returned radar echo from the ice-bed interface, here termed the basal reflection coefficient, can be used as a proxy for the thermal condition of the ice bed (Gades et al., 2000; Rippin et al., 2006; Jacobel et al., 2010; Langley et al., 2011; Ross et al., 2012; Wright et al., 2012; Ashmore et al., 2014; Diez et al., 2018). We follow this principle by rearranging the radar equation (Bogorodsky et al., 1985) for the reflection loss ($L_R = |r|^{-2}$), where P_r denotes the power of the received RES signals, P_t the transmitted power, H the ice thickness, h the height of the aircraft above ground, G the antenna gain, q the refraction gain, λ the wavelength of the RES carrier frequency, L_K the ca-

ble losses of the RES system, L_T the transmission loss at the surface of the ice, and L_A absorption in the ice, it is possible to calculate the basal reflection coefficient:

$$L_R = \frac{P_t G^2 q \lambda^2}{(4\pi)^2 [2(H+h)]^2 L_K^2 L_T^2 L_A P_r} = \frac{C_1}{P_r} \frac{1}{L_A} = \frac{1}{r^2} \quad (4.4)$$

With the exception of L_A and L_R all parameters are measured for each shot, or are constants of the system and can be represented as a single constant C_1 . Thus, if L_A can be determined, it is possible to calculate basal reflection loss. However, if L_A is overestimated, r becomes > 1 , a non-physical value.

The received signal power P_r was obtained by selecting the maximum amplitude within a time window for each shot ranging -300 ns to +900 ns from the manually picked, as well as automatically detected, basal reflector, accounting for picking errors. In order to assess the maximum amplitude really represents a basal reflector, we compared the standard deviation of the amplitudes to the maximum amplitude found within this time window. Since the radar speckle was large (couple of dBs), Oswald and Gogineni (2008) suggested to use the integrated power (P_r^{ig}) across the whole bed return to minimize this spatial Fresnel zone variability. Thus, we integrated P_r across ± 800 ns of the bed peak position, a slightly larger and symmetrical zone around the bed peak position, for each shot to derive P_r^{ig} .

Subsequently, L_R^{ig} has been estimated taking Equation (4.4) and derived the full-width-half-maximum of the frequency distribution over moving windows of 2500 shots (~ 105 km). By correcting the returned power for geometric effects and using an average attenuation rate, the presence of only two different basal regimes — wet and dry — should result in a bimodal distribution in the histogram of the corrected return power (Oswald and Gogineni, 2008). However, this approach required that a significant portion of both classes were covered by the profile under examination.

In our analysis we used unstacked and stacked (along track) amplitudes as well as stacked integrated power, respectively. As previous studies (Langley et al., 2011, e.g.) have estimated the nature of the bed from assessing variability in $[P_r]_{\text{dB}} - [C_1]_{\text{dB}} + [L_A]_{\text{dB}}$, we also computed this quantity.

The total attenuation L_A integrated over the two-way travel path between the surface h_s and the base h_b can be written as (Matsuoka et al., 2010):

$$[L_A]_{\text{dB}} = 2 \left[\int_{h_b}^{h_s} A(z) dz \right]_{\text{dB}}, \quad (4.5)$$

where $A(z)$ is the local attenuation rate per unit path length (one-way) in vertical (z) direction. The local attenuation rate A (unit: dB m^{-1}) in ice depends on the permittivity $\epsilon' = 3.2$ and the conductivity σ of the ice. The permittivity is assumed to be constant (cf. MacGregor et al., 2007) while the conductivity varies with depth in the local ice column, thus (Zirizzotti et al., 2010; Matsuoka et al., 2012):

$$[A(z)]_{\text{dB}} = 8.686 \sqrt{\frac{\mu_0}{\epsilon_0 \epsilon'}} \frac{\sigma(z)}{2} = 914.63 \sigma(z), \quad (4.6)$$

where $\epsilon_0 = 8.8541878176 \times 10^{-12} \text{ F m}^{-1}$ and $\mu_0 = 1.25663706 \times 10^{-6} \text{ N A}^{-2}$ are the free-space dielectric permittivity and magnetic permeability. The conductivity $\sigma(z)$ depends on temperature following an Arrhenius model

$$\sigma(z) = \sigma_0 \exp \left[\frac{E}{k} \left(\frac{1}{T_r} - \frac{1}{T(z)} \right) \right], \quad (4.7)$$

where $E = 0.51 \text{ eV}$ is the activation energy, $k = 8.6173324 \times 10^{-5} \text{ eV K}^{-1}$ is the Boltzmann constant and σ_0 being a reference conductivity for pure ice. In general, the effect of impurities can be parameterized, however, as $\sigma(z)$ is dominated by the effect of temperature, in a study area of limited extent, we neglect the effect of impurities and use $\sigma_0 = 9.2 \mu\text{S m}^{-1}$ for pure ice conductivity at $T_r = 251 \text{ K}$ (Matsuoka et al., 2012).

Thus, the two-way attenuation could be calculated once the local temperature distribution in the ice is known. We derived the required temperature fields from the modelling introduced in Section 4.2.1. With this we estimated r and used this as one criterion for assessing the nature of the bed.

4.2.4 SUBGLACIAL-LAKE IDENTIFICATION

In our lake identification scheme we followed the procedure of Carter et al. (2007) (Carter scheme) and began with identifying lake candidates from the hydrology, which was required for defining an area over which quantities that we used to assess the characteristics of the potential lakes were averaged. For this purpose we estimated the hydraulic potential in along-track direction (1D), as well as used sinks in the hydraulic potential (2D, description of the hydraulic model follows below). For the 1D case, we strictly followed Carter et al. (2007). For the 2D approach we smoothed the potential with a box blur filter (2 km radius). Across these lake candidates, we engaged two criteria for assessing the existence of a lake based on RES:

- Basal reflectivity criterion: $\overline{PPC}_{lake} > 0.95$, where \overline{PPC}_{lake} is defined as the mean of all PPC values across the lake candidate.
- Relative power criterion: $\overline{L}_{R_{lake}} > \overline{L}_{R_{sur}} + 5\text{dB}$. $\overline{L}_{R_{lake}}$ is defined as the mean of all L_R values across the lake candidate and $\overline{L}_{R_{sur}}$ as the mean of all L_R values in the area before and after the lake candidate. By definition those areas have the same extent as the lake candidate, but are not larger than 20 km and not smaller than 3 km.

As discussed above, our RES system was not sensitive to specular surfaces. Therefore, we were unable to use the specularity, defined as the normalized standard deviation of the echo power of all shots within 200 m of a shot (Carter et al., 2007), for assessing the existence of lakes. A typical bed peak of AWI-RES had a skewed Gaussian shape with a half beam width of 300 ns. Therefore, we defined a new variable, the peak to peak correlation (PPC), instead of specularity, to estimate the similarity of bed reflections within the first Fresnel zone. If a thick water body was present, the roughness should have been small and all bed peaks should have been very similar in amplitude and shape, resulting in high PPC. In cases with strong radar speckle (thin water layers) or prominent small scale roughness, the bed peaks should have varied within the Fresnel

zone resulting in lower PPC. PPC was calculated in a running window along track for each auto-detected bed peak as follows:

$$PPC(i) = \frac{1}{n} \sum_{j=i-n/2}^{j=i+n/2} C_i C_j \quad (4.8)$$

where $C_i C_j$ is the cross correlation of two bed peaks centred at its maximum spreading of 1600 ns (twice the pulse length with 200 ns margin at both ends). The number of bed peaks n was chosen to cover the Fresnel zone of approximately 300 m and contains at least 20% automatically detected bed peaks of all shots within the Fresnel zone.

4.2.5 ACTIVE LAKE IDENTIFICATION FROM SATELLITE ALTIMETRY

In addition to our airborne survey we also drew on ICESat altimetry data to identify locations of potentially active lakes. To identify outlines of active lakes within our research area we slightly modified the along-track processing approach presented by Smith et al. (2009) and Fricker et al. (2014) using the ICESat data release 34. We mapped the ICESat tracks of the 17 laser campaigns acquired between 2003 and 2009 to a reference orbit. Since the tracks are offset to the reference orbit by up to 400 m it is necessary to account for topography and/or cross-track slope errors. Our approach is slightly different to the improved repeat track technique introduced by Fricker et al. (2014) but gave very similar results. Instead of estimating linear trends in sub-swaths to correct for across-track slope we used a reference DEM of Helm et al., 2014 to derive the topographic correction. In both cases all ICESat tracks of the different campaigns are projected to the reference orbit to be able to estimate elevation change.

To determine active lakes a mean elevation profile along the reference orbit track was derived. For each of the 250 m along track positions we averaged all topographically corrected data within 1 km distance. Subsequently, the elevation difference to the mean elevation profile for each of the 17 laser campaigns was calculated, producing similar Gaussian shaped elevation anomalies over active lakes as previously presented by Smith et al. (2009) and Fricker et al. (2014). In a final step we separately integrated all positive and negative anomalies along the reference orbits and interpolated the data to two grids with a 1 km pixel spacing using inverse distance weighting within a 5 km search radius.

4.3 RESULTS

4.3.1 ICE THICKNESS AND SUBGLACIAL TOPOGRAPHY

Figure 4.1 shows all points where ice-thickness data were obtained. Along the main trunk of Recovery Glacier, just upstream from the junction with Ramp Glacier, almost no basal reflections could be obtained, neither along or across flow direction. No reflections were recovered east of LB, across LC, or across the southern extent of LD. Elsewhere, the coverage was good, with basal reflections achieved for 74 % of RES profiles. The new ice-thickness and subglacial-topography DEMs are shown in Figure 4.2.

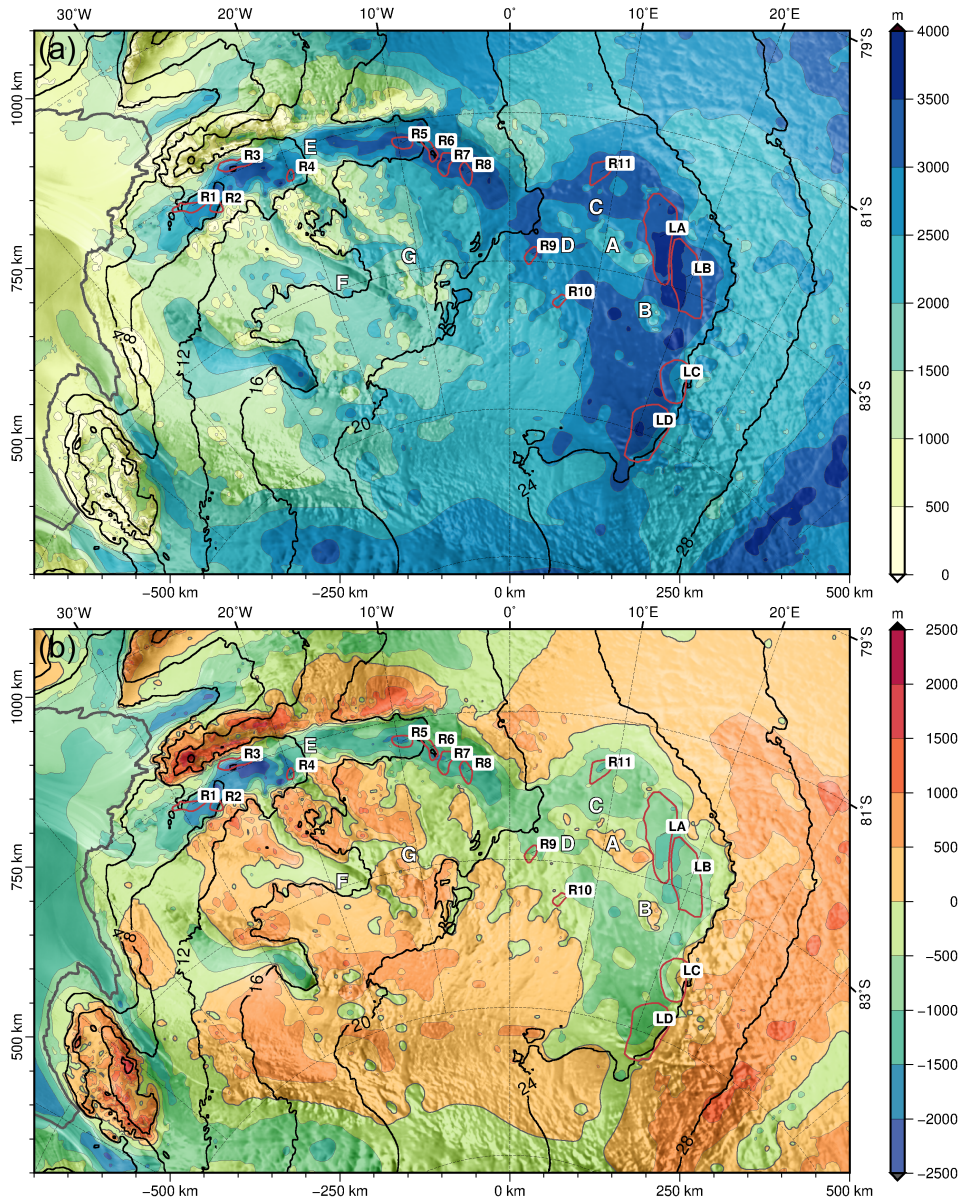


Figure 4.2: New ice-thickness data generated using the methods outlined in Sect. 4.2.2 and 4.2.2 (a) and basal topography based on the ice-thickness grid shown in (a) and Bedmap2 surface topography (Fretwell et al., 2013) (b). Superimposed are previously proposed lake outlines (Bell et al., 2007; Smith et al., 2009) in red and contours of the hydraulic potential annotated every 4 MPa. Feature names A–G are used in the main text. The thick grey line denotes the present-day grounding line position.

The thinnest ice, with a minimum of just 67 m, drapes across the Shackleton Range (Figure 4.2), marking the north-western boundary of Recovery Glacier’s main trunk. Transecting the Shackleton Range at approximately S 81° W 005° is a region of thicker ice, ~2500 m deep, beneath

which the subglacial reflector at < 1000 m elevation is very smooth. This bears the characteristics of an ice-stream tributary, but which is currently shut down according to surface ice velocities (Floricioiu et al., 2014). Diez et al. (2018) also imaged this feature and termed it the “Recovery-Slessor Gate”. Upstream of this point, the mountain range continues but shrouded beneath ice that increases in thickness until reaching the vicinity of subglacial lakes LA–LD. Lakes LA–LD and R9–R11 sit within a subglacial basin with ice ~ 3000 – 3500 m thick resting atop a bed ~ 500 – 1000 m below sea level (Figure 4.2). A region of higher bed, with two subglacial peaks reaching > 500 m above sea level (marked A and B in Figure 4.2) forms a ridge within the main upstream basin, possibly a further inland subglacial extension of the Shackleton Rang. The mountain at ‘B’ was also found by Diez et al. (2018) and Forsberg et al. (2018).

Following the main trunk from R9 downstream, the ice thickness is more or less similar, with about 3000 – 3500 m in the centre down to the area denoted with E in Figure 4.2a. At E the base is higher elevated forming a ridge, about 1000 m higher than the surroundings and covered with about 1000 m thinner ice than upstream and downstream. This is also found by Diez et al. (2018) and Forsberg et al. (2018). Immediately downstream from this ridge, and evidenced in the surface imagery (Figure 4.1) and subglacial topography (Figure 4.2b), a tributary joins the trunk from the west. Further downstream, at the junction with Ramp Glacier, the subglacial reflector deepens to > 2000 m below sea level, below ice > 3000 m thick. Downstream again, ~ 150 km upstream from the grounding line, the eastern shear margin ends, and Recovery Glacier becomes wider and turns eastwards. Here, the ice decreases to < 1500 m deep, with the bed lying below sea level at both margins. The western shear margin remains to just upstream of the grounding line, where the tributary Blackwall Glacier converges with Recovery Glacier, which together discharge ice ~ 1200 m thick into Filchner Ice Shelf.

Ramp Glacier does not show any significant ice-thickness variations along its main trunk. In its lower part Ramp Glacier cuts through valleys of both thin ice and high elevated bed, as typical for an outlet glacier. However, neither the ice thickness nor the basal topography varies considerably in the upstream area marked with F. The sharp western margin of Ramp Glacier is thus unlikely topographically controlled and might be driven by a change in sliding regime. In its vicinity, area G, does show a change in ice thickness of more than 500 m, but appears in radar imagery like an ice filled valley with a smooth surface.

In contrast to Ramp Glacier’s relatively flat profile, Blackwall Glacier varies considerably in ice thickness. It is thickest at its onset region, thinning downstream to match the thickness of Recovery Glacier where the two glaciers converge. We did not sound a basal reflector in the onset region, limiting a detailed interpretation of subglacial topography there, but in the vicinity is a deep subglacial basin. The main trunk of Blackwall Glacier has sharp shear margins imaged in the RES, but appears not to follow a topographically-defined route (Figure 4.2b).

In general, there are differences of more than 2000 m in bedrock topography between the modelled basal topography based on balance flux assumption and ice surface topography given by Le Brocq et al. (2008).

4.3.2 SUBGLACIAL TEMPERATURE DISTRIBUTION

In general, the TIVF was very small, but locally the basal temperate ice layer thickness reached several 100 metres (Figure S1 in the supporting information). The results of all model runs are

summarised in Table 4.2. The TIAF ranges from 17.6 % for the lowest geothermal flux ($q_{\text{geo}}^{\text{P}}$) to 85.3 % for the strongest geothermal flux ($q_{\text{geo}}^{\text{F}}$) for evoFT and from 24.7 % to 88.7 % for evoSR-type simulations. In general evoSR simulations resulted in larger areas that were temperate at the base. For the evoFT setup with the largest TIVF of 0.98 % ($T_{\text{s}}^{\text{JC}o}$, a_{s}^{Ar} , $q_{\text{geo}}^{\text{F}}$), the maximum thickness of the basal temperate ice layer was 374 m with a mean value of 20 m. The mean value was computed from all grid nodes with a temperate ice layer and not from all grid nodes. A larger maximum in TIVF of 1.13 % was found for the evoSR setup ($T_{\text{s}}^{\text{Fa}O}$, a_{s}^{VB} , $q_{\text{geo}}^{\text{F}}$). Here the basal temperate ice layer thickness reached 308 m with a mean of 26 m. Individual runs showed grid nodes with significant thicker basal temperate ice (e.g. 761 m in setup $T_{\text{s}}^{\text{Fa}O}$, a_{s}^{VB} , $q_{\text{geo}}^{\text{F}}$, evoFT) but these runs did not result in the maximum TIVF as the area with temperate ice above was smaller. In general, thicker temperate ice was found in evoFT-type simulations.

To investigate the differences between evoSR and evoFT simulations, we present in Figure 4.3 temperature–depth profiles at two deep drill locations (European Project for Ice Coring in Antarctica (EPICA) Dome C (EDC) and EPICA Dronning Maud Land (EDML)) where observational data exists and two selected locations RL1 and RL2 in the Recovery Lake area (see Figure 4.1). At

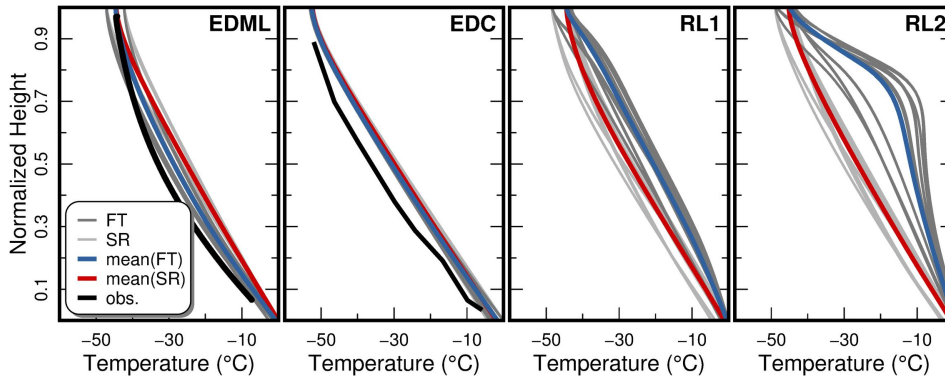


Figure 4.3: Comparison of simulated temperatures at selected locations. Observed borehole temperatures at EDML (Weikusat et al., 2017) and EDC (Zirizzotti et al., 2010) are shown in black. Thin light grey lines represent the different combinations of evoSR (SR) runs, thick dark grey lines the evoFT (FT) run. The mean of the presented evoSR runs is given by the red line and the mean of evoFT in blue. The sites RL1 and RL2 (see Figure 4.1) in the Recovery Lake area are located only 50 km apart. Note, the vertical axis is given as the height above the base normalized by the local ice thickness (base = 0, surface = 1).

EDC and EDML the simulated temperature profiles were in reasonable agreement with the borehole temperatures near surface and base, while they are systematically warmer elsewhere. The evoFT-type simulations match the observations at EDML better than evoSR-type ones, whereas at EDC the difference between both types of simulations is negligible. At this site the different surface forcing (temperature (T_{s}) and surface mass balance (SMB)) datasets match each other very well.

While the observations show parabolic profiles, indicating downward advection, the evoSR simulations result in more linear (vertical diffusion dominated) profiles. The evoFT-type simulations result in implausible temperature profiles at RL1 and RL2, from which general conclusions can be drawn. The examples shown in Figure 4.3 for sites RL1 and RL2, located in the vicinity

of LA reveal slight and strong convex shapes. This indicates upward advection especially at RL2. This is an obvious result of the flux correction applied to the SMB to match the fixed geometry, which is an interpolated quantity still based on sparse data. Thus, we focus on the evoSR-type simulations for further analysis of the model output.

In Figure 4.4 we show the occurrence of temperate ice at the base, given in percentage of the number of evoSR-type runs. In the main trunk of Recovery Glacier approximately all runs lead

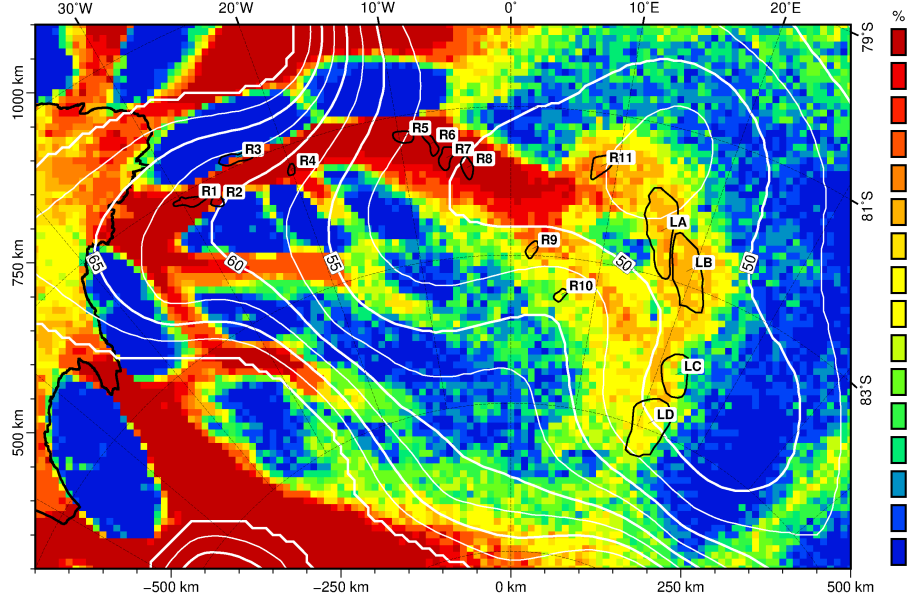


Figure 4.4: The occurrence of temperate ice at the base given in % based on the 15 runs with a free evolving geometry (evoSR). Lake outlines and the observed present day grounding line position are shown in black and grey, respectively. The mean geothermal flux is shown as white contours with $2.5 \times 10^{-3} \text{ W m}^{-2}$ interval. The thick black line denotes the present-day grounding line position.

to a temperate base, while in the area of LA and LB only approximately 10 out of 15 runs are that warm and the number of grid nodes at pressure melting point is further reduced at LC and LD. The distribution in Figure 4.4 for this lake area is strongly influenced by the very low heat fluxes from $q_{\text{geo}}^{\text{P}}$, that are below $35 \times 10^{-3} \text{ W m}^{-2}$. The subset of simulations with $q_{\text{geo}}^{\text{P}}$ (Figure S2 in the supporting information) reveals, that only very few grid nodes are temperate in just one out of five simulations. These grid nodes are located at LA and in between LA and LB. Further, we find that a temperate base is more likely downstream of LC, than in the vicinity of LC.

The ensemble mean and standard deviation (STD) of the local attenuation rates (two-way, see Equation 4.5) are shown in Figure 4.5 for the subset of evoSR-type simulations. These quantities have been derived from the modelled temperatures and the pure ice attenuation model given in Equation 4.7. In the area of LA–LD, the attenuation rates are about 20 to 25 dB km^{-1} with STD ranging from 2.5 to 5 dB km^{-1} . The attenuation rates increase downstream to $\sim 30 \text{ dB km}^{-1}$ with decreasing standard deviations ($< 2.5 \text{ dB km}^{-1}$) in the area of R5–R8. Attenuation rates up to about 40 dB km^{-1} are found between 15° W and 25° W. Largest STD appear near the

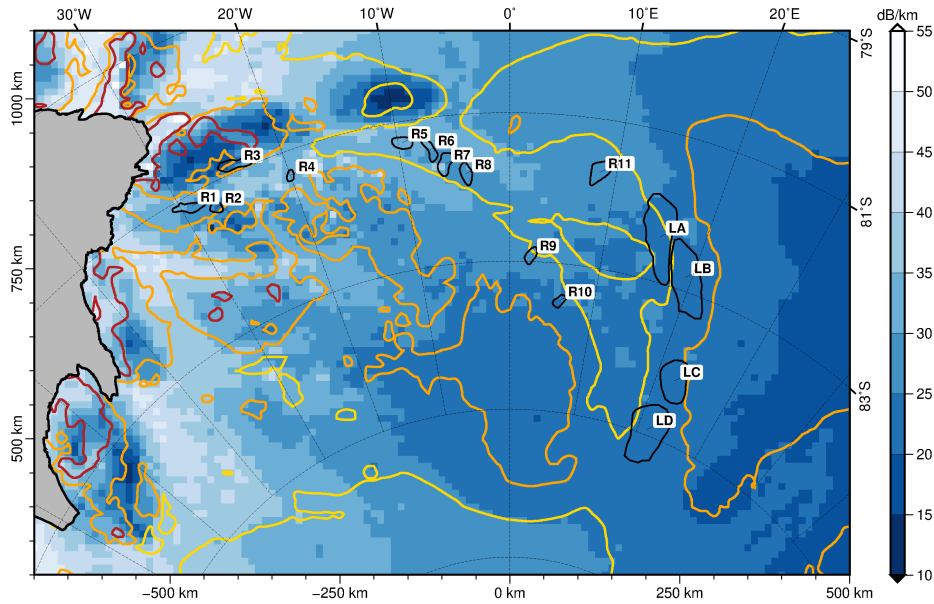


Figure 4.5: Depth-averaged attenuation rates (two-way) derived from the simulated ice temperature fields based on the evoSR model ensemble for the pure ice attenuation model. Selected contour lines at 2.5, 5.0 and 7.5 dB km^{-1} of the corresponding ensemble standard deviation are given in yellow, orange and red, respectively. The data is clipped at the present-day grounding line (thick black line).

present day grounding line, as individual model runs result in different grounding-line positions. Considerable larger attenuation rates can be found in the vicinity of the grounding line for Slessor Glacier and Support Force, the two large ice streams next to Recovery Glacier.

For a broader picture the ensemble means and standard deviations of the attenuation rates are also given for the entire Antarctic ice sheet in Figure S3 in the supporting information. On the continental scale it becomes even clearer, that the simulated attenuation rates in Recovery Glacier are lower than along the grounding line of most other ice streams and outlet glaciers.

4.3.3 SUBGLACIAL WATER FLUX AND HYDRAULIC POTENTIAL

The modelled subglacial water flux and locations where sinks in the hydraulic potential have been filled are shown in Figure 4.6. Note that our subglacial topography in Figure 4.6 specifically records the ice bed (upper lake surface - we have no information from the RES of the possible lake depths). While we did the routing with all available basal melt rates from PISM (evoSR $q_{\text{geo}}^{\text{S}}$, $q_{\text{geo}}^{\text{P}}$, $q_{\text{geo}}^{\text{F}}$), we only show the result for catchment wide melting at 0.006 m a^{-1} . The results using the PISM melt rates show the same flow pattern as the catchment wide melt variant, albeit with much reduced water flux and can be found in the supporting information Figure S4. A large portion of the water in the catchment drains along the main trunk of Recovery Glacier, reaching the sea at the grounding line. The modelled subglacial water flux varies in width and strength along the main trunk. Three medium sized sinks are present within the segment between the junction of Blackwall and Ramp glaciers with the Recovery. Close to S 81°S W 010° there is another sink

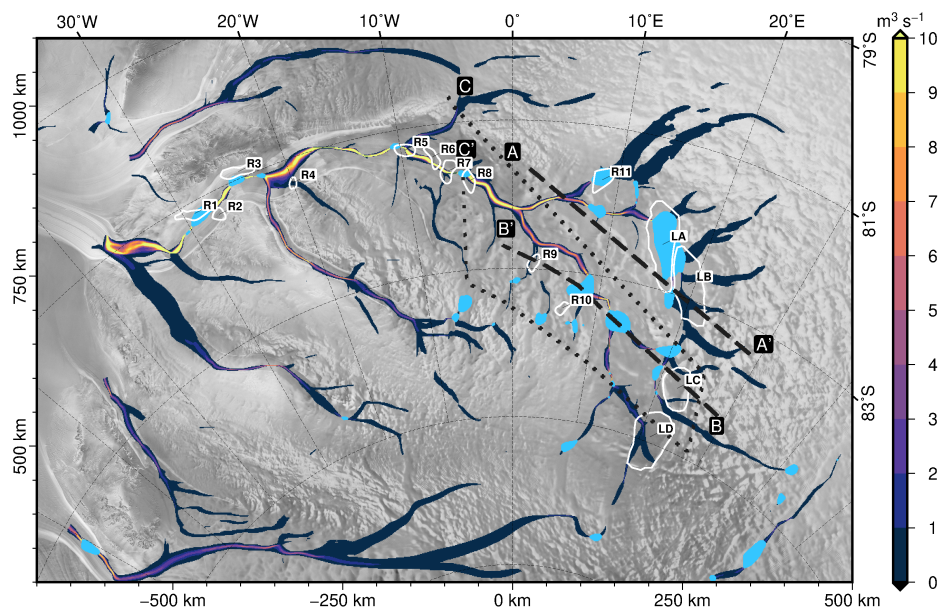


Figure 4.6: Magnitude of the subglacial water flux in $\text{m}^3 \text{s}^{-1}$ using catchment wide melting of 0.006 m a^{-1} (clipped below $0.1 \text{ m}^3 \text{ s}^{-1}$). Sinks in the hydraulic potential are shown in blue. Black dashed and dotted lines show the location of RES profiles shown in Figures 4.9–4.11.

which matches the position of the known R5 lake (see Figure 4.1), but has only about a quarter of its size. The same applies at R8 upstream.

Further upstream, in between point A and point B' the subglacial flow branches. The northern branch drains several lakes: R9, which coincides with a sink in our model, LA where we also observe as sinks in the potential (A4) and two smaller ones (A2 and A3). LB does not appear in our model as sink, however, a nearby small sink is found.

The southern branch reaches far upstream and drains pathways even upstream LC and LD. There is not a bit of these two lakes in the potential, but we find a number of smaller lakes in the vicinity. R9 and R10 do not appear in the hydraulic potential as well, though we find sinks slightly offset westwards. The RES section B–B', shown in Figure 4.10, runs across two larger sinks located between LC and R9. Panels (a) and (b) of Figure 4.10 show the water flux distribution and hydraulic potential between the lakes. We find moderate flux along Blackwall Glacier and a small sink far upstream. Also Ramp Glacier is underlain by a water stream, however, no sinks are found. At the upstream end of Ramp Glacier one medium and one small sized sink is located.

Flux computed with the melt rates from the evoSR PISM simulation using $q_{\text{geo}}^{\text{S}}$ (representing a moderate geothermal flux) is –as expected– much less and large areas have flux below $0.1 \text{ m}^3 \text{ s}^{-1}$ and are therefore clipped (see Figure S4b in the supporting information). However, the main drainage path is still active and also contributions from the Blackwall and Ramp glaciers are present. Almost all identified sinks are still connected to the drainage path with an exception upstream Ramp Glacier. Also, at the previously known lakes R9 and R10 almost no flux is visible. Using $q_{\text{geo}}^{\text{F}}$, the distribution of flux and sinks are nearly similar to $q_{\text{geo}}^{\text{S}}$, but for $q_{\text{geo}}^{\text{P}}$ the water extent is strongly reduced (Figure S4 in the supporting information). To investigate the sensitivity of the

flow patterns to errors in the topography, we disturbed the ice surface with a random variation of 1 m and the ice base with a variation of 25 m. The general pattern is very stable and only individual segments of the flow network have reduced flux or vanish.

4.3.4 ACTIVE LAKES FROM ALTIMETRY

Figure 4.7 displays colour coded integrated negative elevation anomalies derived from ICESat laser altimetry (see Figure S5 in the supporting information for positive and total anomaly maps). The distribution clearly indicates areas with large elevation anomalies in the main trunk of Recovery Glacier at locations R1, R7 and R10. Those anomalies have been previously interpreted as lake drainage events with a subsequent refilling (Smith et al., 2009; Fricker et al., 2014). The inset shows a zoom in to lakes R5 to R8 which were described as a connected system of active subglacial lakes (Fricker et al., 2014). The figure also demonstrates the limit of this technique since erroneous anomalies are found in areas with steep topography, at grounding lines and over crevassed areas as discussed in (Smith et al., 2009). The outcome of the two lake classification criteria described in Section 4.3.5 are also displayed in Figure 4.7. While the match of one criterion is widely found at and around LA–LB and downstream, fewer locations where both criteria match are found. East of 0°E, the sinks found with our modelling are matching with at least one criterion for nine of the larger sinks, while only one larger one does not match any of the two criteria.

4.3.5 LAKE IDENTIFICATION

Results of the 1D and 2D lake identification schemes are given in Table 4.3 and for 2D in Figure 4.7. Both approaches show very different results. With the 1D method over twice as many lake candidates were identified (which was expected, since the 2D method is a stricter condition). In both cases the candidates are distributed across the whole area, representing localised hydraulic sinks. Marked discrepancies between the two approaches are found across LA and LB. Here, the relative power criterion is fulfilled for the 2D approach nearly across the whole lake. Whereas, lake candidates from the 1D approach do not match any criteria. This location is covered by five flight tracks. Furthermore, none of the criteria is matching across lakes R5 to R9 for both approaches, whereas R10 at least partly fulfills the basal reflectivity criterion in the 1D approach.

4.3.6 BASAL REFLECTION COEFFICIENT

As discussed above, we are limited with our capability to determine the magnitude of r with sufficient certainty. Nevertheless, we interpreted low values of r as an indicator of a dry base (grey, $r < 0.1$) and high values for a wet base, respectively (blueish). This assignment was decided from the range of r shown in the right panel of Figure 4.8. While the absolute values strongly depend on the estimated absorption, the general pattern of the distribution remains unaffected by that. According to this indicator, most of the base of the study area is dry, in particular all areas outside the main trunk of Recovery, Ramp and Blackwall glaciers. Downstream of the southern end of lakes A–D, the basal reflection strengths ($r > 1$) are indicative of a wet base underlying the main trunk of Recovery Glacier is more likely than not having a wet base and in the main trunk r reaches maximum values exceeding 1. Using 0.1 as a rather conservative threshold this distribution (Figure 4.8) suggests that there are two branches in the upstream Recovery Glacier: (i) R10, LA and

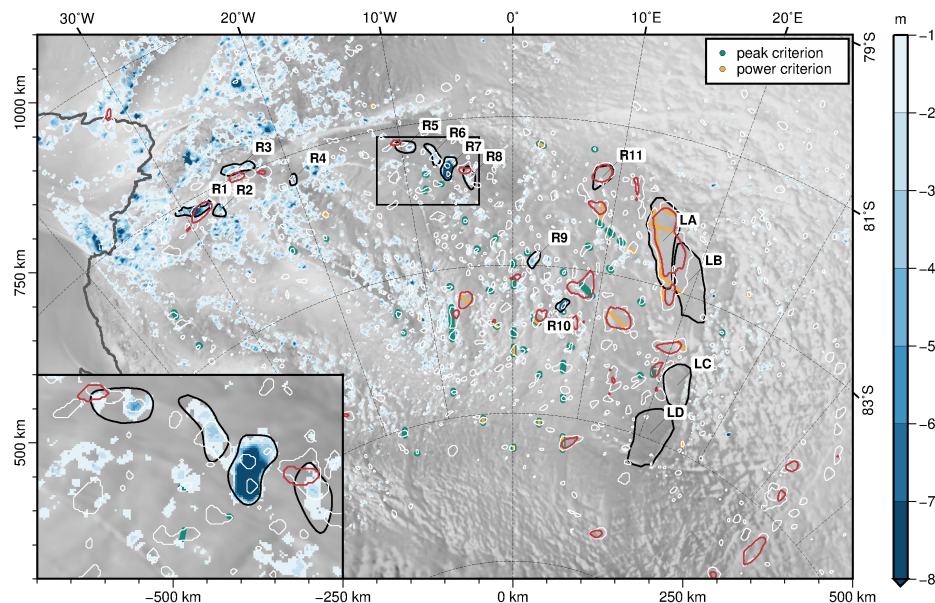


Figure 4.7: Elevation anomalies identified using ICESat. Shown are lake drainage events as integrated negative anomalies with a blue colour scale. Results of the lake classification scheme are shown as green dots along the flight profiles. Sink contours derived from the flux model are shown as closed polygons in light grey for the 2km and in red for the 10 km smoothing kernel.

LB and (ii) downstream LC/LD), which are separated by a dry bed. Blackwall Glacier is probably resting on a wet bed, while results for Ramp Glacier are ambiguous, as along and across flow profiles show different magnitude of r . The general pattern is similar to the distribution of the simulated temperate base and potentially driven by the effect of temperature on the absorption.

4.3.7 COMBINED ANALYSIS

We have selected three profiles for which we show a multitude of variables (water flux, hydraulic potential, temperate layer thickness (Hcts), basal homologous temperature, absorption, ice thickness (H), reflection coefficient, and peak-to-peak correlation) in Figures 4.9–4.11, with the aim of providing insight into the factors that influence the determination of r . This is the basis for the general discussion of the ability to determine r . For comparison with the studies of Langley et al. (2011) and Langley et al. (2014) we also calculated $P_r - C_1$ (geometrical corrected bed reflectivity), which corresponds to their $\delta[P_{bed}^c]_{dB}$. The profiles cross existing lake outlines as well as modelled potential lake sites.

A static correction has been applied to the presented radargrams in Figures 4.9–4.11 using the Bedmap2 surface topography (Fretwell et al., 2013) so the upper strong reflectors represents the ice surface. Below the surface, internal layers, dips, as well as crevasses are visible in addition to a multiple of the surface reflection. Further down, usually a single strong reflection stands out from the background noise. This is interpreted as the bed reflection and indicates a strong dielectric contrast.

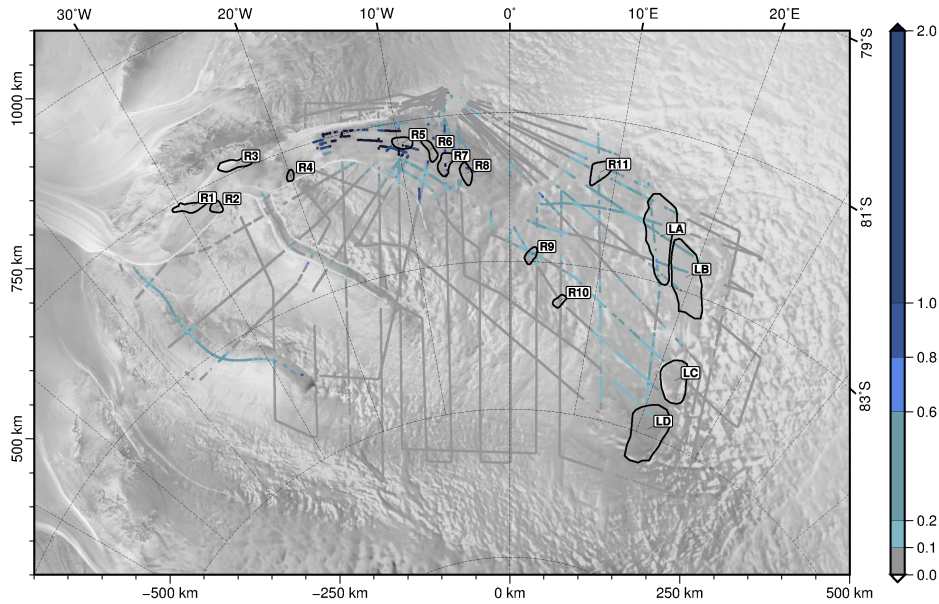


Figure 4.8: Basal reflection coefficient r . Colours denote likely dry regions (grey), and swampy to wet (turquoise to blue).

The radargram in Figure 4.9j) was recorded on a 430 km straight flight line (A–A' in Figure 4.6), at a constant flight level crossing the southern parts of LA and LB at km 247 to km 344. The ice thickness in this profile varies between 1700 m just west of LA and nearly 3700 m at the western edge of LB. The detected internal layering is less pronounced and slightly disturbed in the first third compared to the rest of the profile. This matches the onset of the ice stream, where we observe higher melt rates (see Figure 4.6) and high probability of temperate ice at the base (see Figure 4.4). Close to the middle of the profile, around km 237, the internal layering is disturbed by a band of increased noise, caused by surface clutter originating from (near) surface crevasses. The clutter is formed right at the edge of a nearly 2000 m high step in the topography of the ice base. Basal reflections were obtained for most parts of the profile, however, two larger breaks of about 20–30 km each and several shorter gaps occurred. The shorter gaps are most likely caused by steep bed topography. The internal layering above the first section without bed reflections (approximately km 43–69) indicates that the beginning of a steep depression might be located here, which would lead to off-nadir reflections. This is followed by an area where a substantial temperate layer at the base might form a region with gradually increased attenuation and thus reduces the dielectric contrast between ice and underlying bed. The flux routing show high water flux underneath parts of the modelled temperate ice layer, which partly compensates for the larger absorption, so that basal return power increases. The disappearance of basal return at the eastern part of LB is quite striking, even though the bed seems to rise more than the surface. The change in reflectivity coincides with decreasing basal water flux and an emerging layer of temperate ice. The internal layering points towards a rising bed followed by a steep peak before reflections show up again, revealing a range of about 40 km in length, about 350 m higher than its surroundings and several valleys about 100 m below the peaks of this range. Our data show that LA and LB are

separated by a step in the bed of about 200 m. Next to this step we find a sink in the hydraulic potential. The internal layering in this part of the profile inclines in profile direction towards south-east, while the bed rises, making the inclination of layers likely to be due to melting. The geometrically corrected basal amplitudes reveal large variations of about 10 dB along the section. These variations are least pronounced across LA and LB and extend further than the basal water flux would indicate. No model run shows a temperate layer from km 271 onward, while the base is always temperate (except for $q_{\text{geo}}^{\text{P}}$). The derived reflection coefficients indicate existence of a lake centered between LA and LB (around km 86 to 129).

The second profile B–B' (see Figure 4.6 for the location) is shown in Figure 4.10j. It is also about 430 km long and covers the area about 100 km south of the profile A–A'. It crosses LC (km 65–108) and turns north close to km 301 before crossing R9. At the onset of the profile, up to km 60, basal returns reveal an undulated bed overlain by approximately 2400 m thick ice. Across LC no clear basal reflections were obtained. Just west of the lake, starting at km 103 basal returns reappear and reveal a relatively smooth bed covered with 3000–3500 m thick ice. Two larger gaps in basal returns show up around km 232 and 275. Due to the quality criteria for the evaluation of the reflection coefficient, the picks between km 185 to 198 do not show up in panels (f), (h) and (i). From km 288 on, the bed is rising by about 1000 m until shot 348, followed by a 700 m deep depression with a width of about 50 km.

The profile crosses nine sinks in the hydraulic potential. Their width varies between 3 km and 37 km. None of it overlaps with LC, but one with lake R9, with maybe half the width of the lake. However, neither the extracted reflection coefficients nor the internal structure of the RES section show clear indications for subglacial lakes at these locations.

The internal layering above LC shows down-warping, but this is most likely caused by the depression and not by basal melting. Above the troughs, around km 280 and 376, the internal layering also follows the bed. Between km 198–215 the internal layers bend down while the bed dips down. This could be caused by basal melting. The section is located just above the western part of the largest sink in the hydraulic potential. The reflection coefficient r reaches values close to 0.5 above the large sink, indicating the presence of water at the base of the ice sheet. However, the spread for r , calculated using different geothermal heat flux assumptions, is relatively large compared to sections at the beginning and end of the profile. For reflections above lake R9 r reaches values between 0.1 and 0.3 which indicates the presence of a swampy bed.

The third radargram shown in Figure 4.11 (1285 km long, C–C' in Figure 4.6) covers the north-east of LC and crosses LD, as well as R8. The ice thickness along the profile varies between 1645 m (around km 1017) and 3685 m around km 516, revealing a highly undulated bed. Along the first 500 km the ice thickness is increasing from about 1800 m to 3000 m with multiple troughs in between. The deepest trough (km ~215) exhibits an elevation difference of about 1000 m with a slope exceeding 10%. The largest ice thickness is found north of LC, approximately 50 km before the turn of the profile towards south. The section east of LC reveals a plateau in the bed below 1800 m to 2800 m thick ice. Where the profile crosses LD (km 731–783), it exhibits a declining bed followed by a ~150 km wide depression. Between km 903 and 1075 another strongly undulated elevated bed under 1800–2800 m thick ice is found. Adjacent to this, in the North, two more troughs exist, followed by a rising bed towards the ice stream. At the southern edge of the ice stream the bed suddenly drops by more than 1000 m, from where on no returns were obtained from the centre of the Recovery Glacier and across lake R8.

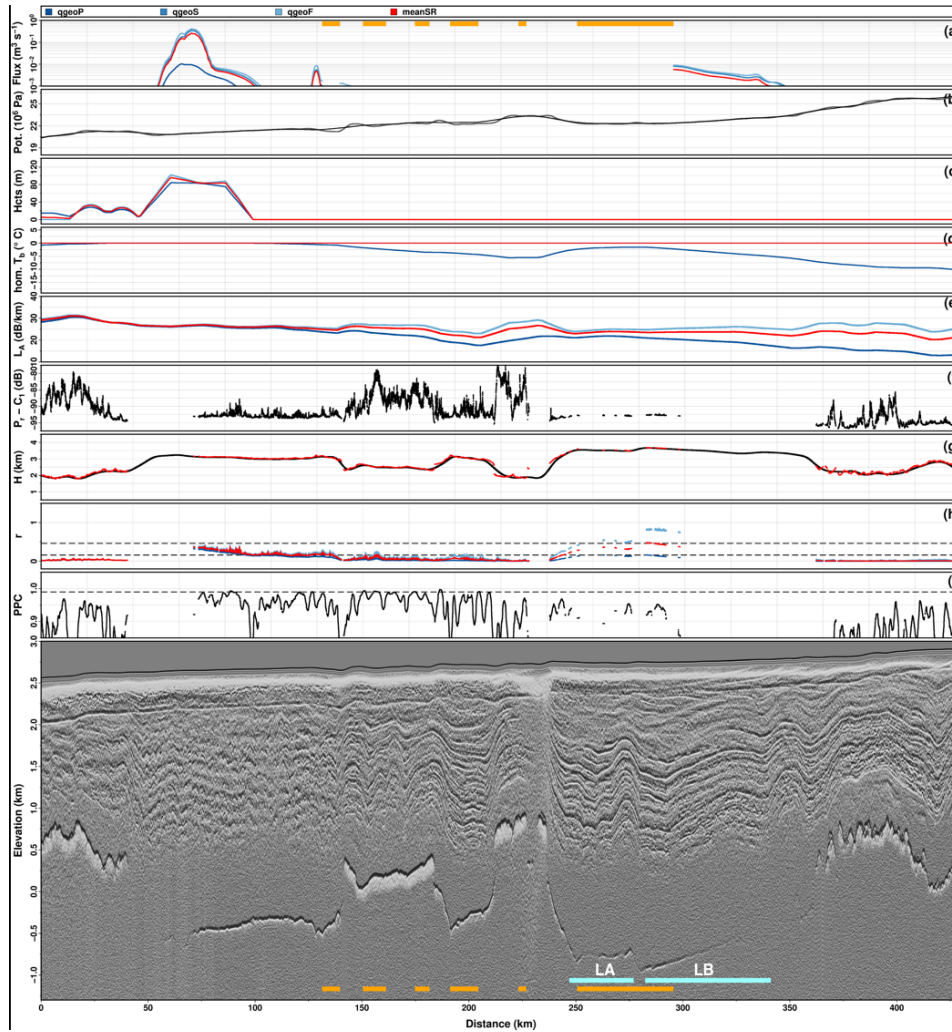


Figure 4.9: Section A–A', running from north-west towards south-east, covering southern part of LA and LB (see Figure 4.6). The panels show: (a) water flux (generated using the 10 km smoothed potential), (b) hydraulic potential, (c) thickness of the temperate layer, (d) basal homologous temperature, (e) radar attenuation —averaged over one kilometre—, (g) received signal power reduced by the factor C_1 for comparison with Langley et al. (2011) (f), ice thickness - semiautomatic picks (red) and new ice-thickness grid (black), (h) basal reflection coefficient, (i) peak to peak correlation and in (j) the processed radargram with static correction applied. Superimposed on (j) are the crossing of either formerly proposed lakes (light blue) or sinks in the two-dimensional hydraulic potential arising from this study (orange). Within the other panels, the blueish colours represent different geothermal heat flux distributions of the evoSR ensemble, while red represents their mean.

The 14 sinks we found in the hydraulic potential are 10–25 km in width and are distributed over the whole profile, starting at km 314. One sink overlaps with lake R9, but none matches LD. The section crossing the largest sink, centred around km 525, shows steep inclined internal layers

4 Missing evidence of widespread subglacial lakes at Recovery Glacier, Antarctica

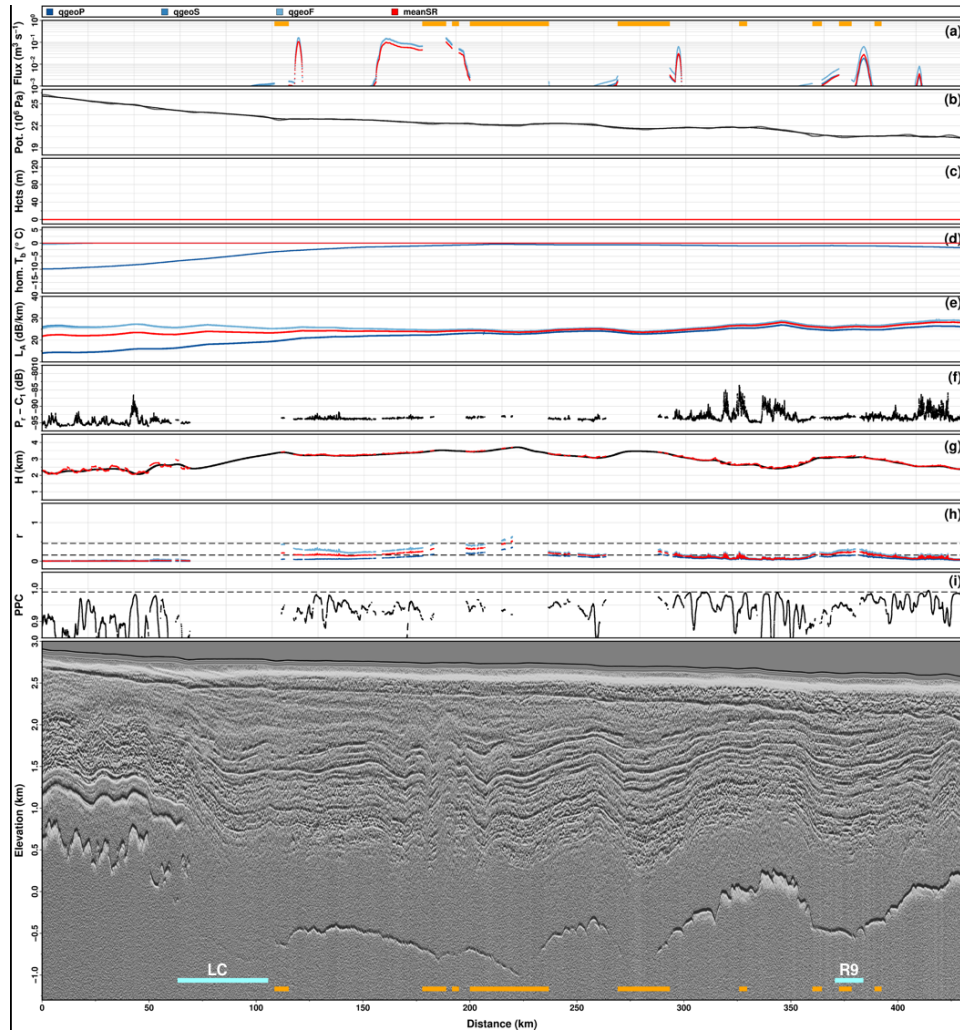


Figure 4.10: Section B–B', covering lake C and lake R9. See Figure 4.9 for description of the panels.

dipping into the trough. Since the slope of the layers does not decrease with increasing distance to the bed, this points towards a section with ongoing basal melting. The corresponding r for this segment of the RES profile indicates a swampy bed. There are three more sections with increased r : Before the deep trough, another depression at km 215–237 shows values of 0.5 and higher. Flux routing also shows a considerable amount of water passing this region and our modelling reveals a temperate layer which is up to 100 m thick. The second segment coincides with LD with values of r around 0.2 and at the southern edge of the ice, a short section reveals values of r around 0.5. Directly above LD no water flux was found, but downstream larger amounts of basal water are present according to our modelling. The edge of the ice stream is another region in which the basal water flux and an extensive layer of temperate ice with a predicted height of at least 120 m occurs. This is most likely the reason for the loss of basal returns in the ice stream. Between km

280 and 430 three shorter segments with increased r show up. Two of them, around km 409 and 430, exhibit a large PPC and noticeable basal water flux.

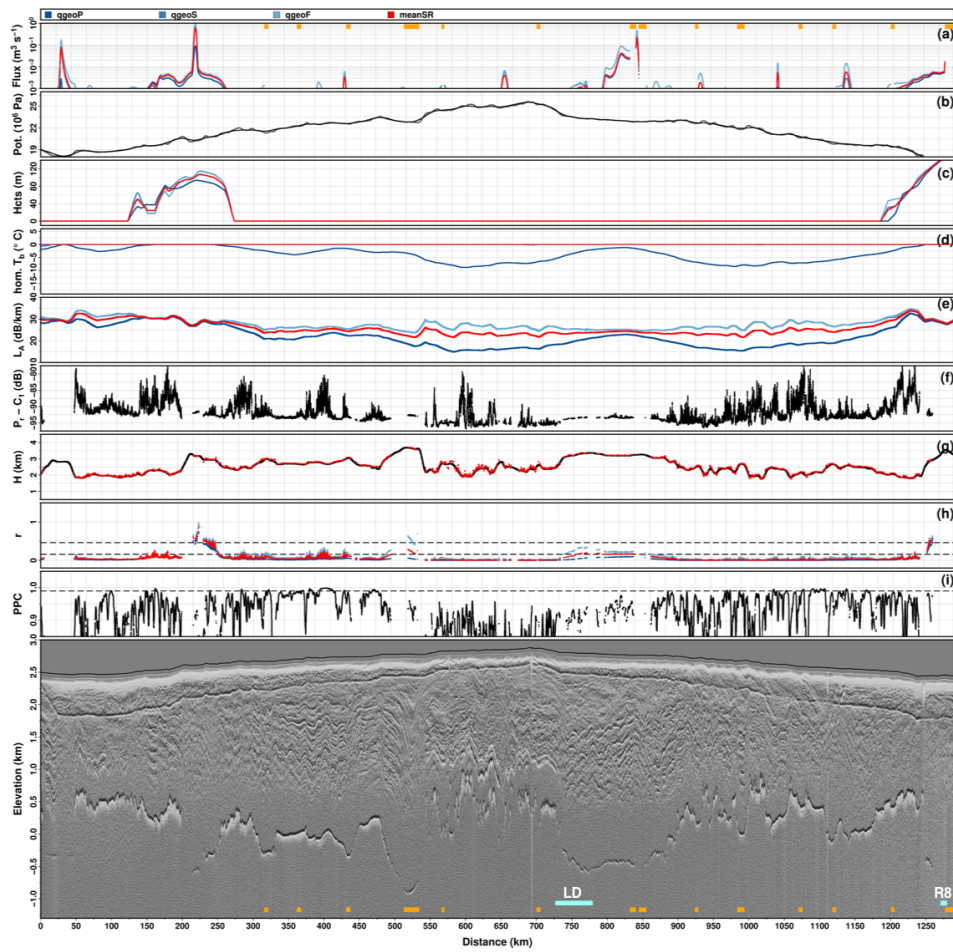


Figure 4.11: Section C–C', covering the north-east of LC, LD, as well as R8. See Figure 4.9 for description of the panels.

4.4 DISCUSSION

4.4.1 ORIGIN OF MISSING BASAL REFLECTIONS

The distribution of the ice-thickness picks show (see Figure 4.1), that we partially lose basal returns in the main trunk of Recovery Glacier. While the deployed RES system sounded ice of more than 3700 m thickness (detected maximum: 3759 m) in the surveyed area, no returns were received in regions where much thinner ice is expected. This could be caused either by a technical problem or by the fact that not enough energy is reflected back. The latter can be caused by large attenuation within the ice or a lack of dielectric contrast (permittivity, conductivity). With the current system settings of 1.6 kW transmitted power and an assumed loss of 20 dB km⁻¹ our RES system is able to penetrate up to 4000 m of ice (given the presence of a bright basal reflector).

There are no hints for technical problems such as a sudden increase in noise level or decreased TX power. Both were checked by examining the noise floor at the end of the registered shots, respectively the direct signal between the antennas.

In regions with horizontal layering signals are reflected back to the antennas, however, if ice flow disturbs the layering and creates crevasses, off-nadir-scattering occurs and no returns are detectable, because only a fraction of the energy is reflected back to the antenna. This is most likely the case for the glacier section west of 17°W. Furthermore, a lot of energy is reflected at the ice surface in regions with surface disturbance, such as surface crevasses. In that case, only a fraction of energy penetrates into the ice while the reflected energy is registered as noise. Steep bed topography also causes potentially non-normal incident reflections.

Since the attenuation of electromagnetic waves in ice is a function of temperature and frequency (Robin et al., 1969; Bogorodsky et al., 1985), the signal level can be reduced below the detection limit of the system. The two-way attenuation of ice at a 150 MHz varies exponentially between 1.2 dB km⁻¹ at -60°C and 49 dB km⁻¹ at -1°C (Robin et al., 1969). Thus, warm ice above wet beds might be the cause for vanishing basal reflections, also suggested by (Siegert et al., 2014). This is a potential explanation for the lack of reflections in the region of LA-LD and R5-R8 and upstream.

Another reason for the absence of reflection might be a gradual transition with a mixed layer with varying components of ice and sediments between the ice sheet and the bed. Dry sand, limestone, and other geological material have a permittivity only slightly larger than ice (Davis and Annan, 1989). Thus, a mixture might not produce a contrast large enough to cause a noticeable reflection. However, water filled sediments have a larger dielectric constant which would result in a power reflection coefficient of 0.18 at the base of the sheet for normal incident signal.

Finally, the presence of a temperate ice layer might suppress basal reflections. The microscopic water content within the ice changes the dielectric properties, according to a mixture theory, where a very small water content has a strong effect. As the water content within a temperate layer changes continuously and on small scales, a smooth transition of the dielectric constant from pure ice to water might prevent a strong reflection at the bed. In this case only the cold to temperate ice transition would cause a reflection. However, also the increase in absorption itself may cause the loss of the basal return if the transmitted power is not sufficiently large.

The above mentioned reasons in addition to findings of (Siegert and Bamber, 2000) indicating a lack of subglacial lake signals over relatively thick ice in East Antarctica, lead to the conclusion

that within the deep main trunk of recovery high attenuation rates and/or a temperate ice layer are likely to be expected. This is supported by our modelled ensemble of attenuation rates to be highest in the fast flowing regimes of Recovery, Ramp and Blackwall Glaciers (see Figure 4.5). A combination of large ice thickness and high attenuation rates as observed in the Recovery trunk will prevent enough energy reflected back to the radar, no matter of the bed conditions.

4.4.2 MISSING EVIDENCE IN LAKE IDENTIFICATION

Subglacial lakes were suggested to appear as bright, flat, mirror like reflections to be typical 10–20 dB stronger than reflections from lake surroundings (Siegert and Ridley, 1998). To provide such a clear strong contrast a thick body of water (>10 m) is required (Christianson et al., 2012; Siegert et al., 2014). Gorman and Siegert (1999) have shown, that RES systems are in some circumstances even capable to detect both interfaces of a water body: the ice-water and water-bed transition. The maximum detectable water thickness is limited by the high attenuation of electromagnetic waves in fresh water of 119 dB km^{-1} (Von Hippel, 1958) to about 20 m (Gorman and Siegert, 1999). Based on a simulation Christianson et al. (2012) found a minimum layer thickness to be discriminated must be thicker than 6 m. They state that thinner water layers produce a composite echo similar to single bed reflection. The minimum thickness depends for a burst RES system on its burst length, which is 600 ns for the AWI-RES system. Thus, the deployed AWI-RES system does not allow to detect the thickness of water bodies but should be able to detect water bodies.

In our analysis we followed (Oswald and Gogineni, 2008) and estimated the integrated reflectivity to minimize the high along track variability of the bed reflectivity (up to 10 dB) which has been shown to prevent clear lake identification in a series of RES studies (e.g. Wright et al., 2012; Siegert et al., 2014). Our results show a reduction of the variability (standard deviation across the Fresnel zone) by simply averaging along-track and a further reduction using the integrated power. However, with respect to the relative power analysis between lake and lake surroundings (Carter et al., 2007), one can observe that relative integrated power ratios are also minimized, which counteracts the positive effect of minimizing the Fresnel zone variability. Therefore, our results show that the use of the integrated power suggested by Oswald and Gogineni (2008) does not allow to reduce the uncertainty in the power criterion.

Our findings of high along track variability of the bed reflectivity are also in line with a detailed analysis of an active lake (Institute E2) using RES data (Siegert et al., 2014). They found that the RES was not able to clearly prove the existence of a deep (> 10 m) water body, although ICE-Sat analysis revealed a 6 m uplift 2 years before the airborne survey. However, they found areas with considerable higher (10 to 20 dB) basal reflectivity beside an high along track scatter in the vicinity of the lakes centre, suggesting but not proving the presence of water. Christianson et al. (2012) found a sudden 6 dB increase in a very detailed RES survey across the active subglacial Lake Whillans. The zone of higher reflectivity were found to be in the vicinity of the hydraulic low underneath a 15 m surface depression indicating wet basal conditions but no clear evidence of a thick (> 6 m) water body. Despite those known difficulties, but encouraged by the study of Carter et al. (2007), we applied their lake identification method to our data set. Our analysis was hampered by the absence of bed returns or their low signal/noise ratio in some but interesting areas within the Recovery Glacier and in the vicinity of the Bell lakes LA–LD as explained in section 4.4.1. In

consequence the 1D along-track lake classification is limited to areas with a clear continuous bed reflection with low small scale variability of the basal reflectivity. To overcome the limits of the 1D along track analysis we applied a 2D approach making use of the continuous spatial coverage of the newly derived ice-thickness grid (shown in Figure 4.2a) as input to determine the hydraulic sinks as lake indicators. Since a few automatic picks are available also in the mentioned problematic regions the means of the two criteria can be estimated and used for the lake identification in the 2D approach. Our findings show an inconsistency between both approaches. A clear indication that relative power or basal reflectivity can be used as reliable criterion over a large region supported by both approaches was not found, neither in areas with low nor with good coverage of bed returns. To our opinion the high spatial variability of the basal reflectivity, even across clear lake like reflections, make it difficult to be used as a reliable parameter to distinguish dry or wet beds, at least in our survey. Another study of Wright et al. (2012) applied the Carter scheme to the ICECAP survey across the Aurora basin in West Antarctica. To obtain basal reflectivity the received signal strength was corrected for geometric spreading and attenuation rates estimated using the GLIMMER model and Dome-C ice core chemistry. In addition the basal reflectivity was calibrated at the known Lakes Concordia and Aurora, which were crossed during the survey. The offset of 25 dB was simply added to the data set to bring the data in line with typical values for wet conditions (Peters et al., 2005). However, an offset of 25 dB suggests a higher attenuation rate as the modelled one, which in turn would change the distribution of the estimated basal reflectivity. Furthermore, Wright et al. (2012) showed a radargram across Lake Concordia in connection with the estimated basal reflectivity. Here a spread of 20 dB across the flat lake like reflection was found. In addition Wright et al. (2012) observed only a couple of lake-like reflectors which are classified as fuzzy or dim lakes. Their findings are similar to our newly presented ones, questioning the reliability to distinguish between wet and dry beds and/or to classify lakes based on basal reflectivity from RES especially for 'active' subglacial lakes. Siegert et al. (2016b) confirm this observation of a lack of evidence for deep pooled water in those active regions. Siegert et al. (2014) conclude, based on the incapability of RES to detect thin water bodies, that the level of stored water in Antarctica may be significantly underestimated. One may, however, also argue that if RES is not capable to give clear evidence of existence and extent of water bodies, one cannot draw any conclusions on over- or underestimation of the water volume at all.

4.4.3 TRUSTWORTHINESS OF BASAL REFLECTION COEFFICIENT

The estimation of the absorption rate based on ice modelling can be done in different ways, which each have their own assumptions and pitfalls. As we found the freely evolving ice thickness to result in more reasonable ice temperature profile, which brings us into the situation to deal with differences in modelled and observed ice thickness as a consequence. There are different ways that are conceivable and that we all tested. One can estimate (i) the absorption rate at each location and apply this to the ice thickness found in each shot (this is the basis for r in Figure 4.9–4.11) or (ii) to the ice-thickness grid or (iii) correct for the ice-thickness anomaly. With ice-thickness anomalies up to 300 m this could make up to 10 dB difference in the absorption at a particular location and is hence in the order of the variation of $P_r - C_1$. Even in case we would be able to obtain a better match between modelled and observed ice thickness, we would still be unable to specify the contribution of impurities on the absorption, because the nearest deep ice core is far

away from our study area. Thus our ability to estimate r is despite our intensive modelling effort low. Further complications arise from the fact the power of our system is too low and no phase information being recorded.

However, on the premise that our modelled temperature field gives a reasonable basis of the spatial variation of $L_A(T)$ assuming that neither impurities nor ice-thickness anomalies cause sudden changes in absorption, we can interpret the spatial distribution of r . This distribution is affected by the temperature in the way, that overestimation of L_A due to overestimated temperatures, leads to overestimation of r and thus low values of r are safe to interpret.

Thus we conclude: upstream of LA–LD we find no indication for subglacial water by means of radar and temperature modelling. There is no indication that ice in the main trunks of Recovery Glacier or Blackwall Glacier are resting on a dry base. The distribution of r (Figure 4.8) downstream of LA–LD suggests the presence of two branches separated by ice frozen to the base.

The spatial variability of r along the profiles (Figure 4.9–4.11) is rather low - dry areas extend over tenth to hundredth of kilometres. This also justifies the scale of the filter used for the flux routing. Larger values of r coincide with larger variability on short distance. Although, we do not have an absolute measure for r , we infer, that the variability in a wet basal system is high. We expect wet sediments, cavities and thin sheets alternating on spatial scales below ten kilometres.

Comparing our results with the findings of Langley et al. (2011) show similar variations in amplitude of the geometrically corrected P_r , but the geographical distribution has changed since their measurements during the Norwegian-US IPY traverse. While both data sets show relatively large corrected P_r values above LA and LB, and increasing values in their proxy for bed reflectivity is decreasing outside LA towards R11, while we find r to be on nearly the same level. This could be a hint for a change in the subglacial conditions in the vicinity of R11 between both campaigns.

R10 was originally proposed by Smith et al. (2009) based on elevation change and this has been confirmed by Fricker et al., 2014 using the same data basis of ICESat. We also found an elevation anomaly based on ICESat repeat track analysis. In contrast, r consistently indicates a dry base for all model ensemble members, with P_r being clearly above the noise level. Although we do find a hydraulic sink with the 2 km filtered hydraulic potential, it is not present with the 10 km filter, making its presence less likely. A further indication that the base is dry, is that the base is cold for all ensemble members of q_{geo}^P and only temperate for a few ensemble members of q_{geo}^S and q_{geo}^F . Last but not least, the radargram does not exhibit a lake-like reflection and no match with the lake classification parameters. The flight profile in flow direction across the lake shows a step in the basal topography with internal layers above that are dipping down. How can this be interpreted? Lowering of the ice surface would be consistent with a lake that drains to the extent that it would fell dry, however, it would be inconsistent with the hydraulic potential, that is based on reasonable data. Similar to the study of Wright et al. (2014) our findings enhance the critics of interpreting surface lowering as a definitive indicator of lake drainage.

Jacobel et al. (2010) found a high variability in relative basal reflectivity on local scale where only some are in line with a flat-lying bed reflection indicative for sub-glacial water. They used a constant one-way attenuation value of 8.6 dB for the entire 1700 km long US-ITASE traverse covering a large area from South Pole to Taylor Dome. They correlated surface velocity with relative basal reflectivity and found good correspondence between areas of high basal reflectivity and ice speed only in portions of the Byrd Glacier catchment, whereas 1/3 of the traverse showed high reflectivity in areas of low speed. Their results indicate a wide spread wet bed in East Antarctica.

Jacobel et al. (2010) analysis is based on Oswald and Gogineni (2008) by fitting a double Gaussian model to the whole reflectivity ensemble. This approach is based on the assumption of the existence of a statistically significant amount of water in the area of investigation and lacks a spatial varying attenuation rate which would significantly change the form of the histogram. Given our modelled absorption rates (see Figure S3) we developed a more critical view on the ability to distinguish between wet and dry basal conditions, which find also support by the study of Diez et al. (2018), who demonstrated the enormous effect of varying attenuation rates from 0 to 10 dB on the relative bed return power across Slessor Glacier. This nicely illustrates also our findings that the Carter scheme using differences between bed reflectivity across indicated lakes and its surroundings is strongly affected by the applied attenuation rate, which is hard to constrain with reasonable accuracy. Diez et al. (2018) showed that in one case a significant difference between the Recovery Slessor Gate and its surroundings is observed and in the other case using lower attenuation rates not. As we showed in Figure 4.5 our modelled attenuation rates in the Recovery area are spanning a wide range of 45 dB km^{-1} with uncertainties of up to 6 dB km^{-1} (see Figure 4.5). Diez et al. (2018) found $\sim 15 \text{ dB}$ decreased bed return power (only corrected for geometric spreading) for the Bailey Trough region compared to Slessor Glacier for depths of 2500 m. The authors interpret this difference to be caused by changes in basal properties and conclude a wet bed beneath Slessor Glacier and dry bed for the Bailey Trough. However, if we assume this change is simply driven by a spatial change in attenuation rate, this would yield to roughly 6 dB km^{-1} higher absorption in the Bailey Trough which is in line with our modelled rates showing a 5 dB km^{-1} higher rate. Based on that findings no change in bed properties could be concluded.

This example emphasise the importance to a better constrain attenuation rate and spatial variability respectively, which can vary over short distances easily by 5 dB km^{-1} as our modelling results emphasize (Figure S3). More importantly, attenuation rates are essential to estimate basal reflectivity from RES data and which in turn are widely used to characterise sub glacial conditions. If the reflectivity suggest a bed to be dry or wet has strong implications on the whole ice flow dynamics and is therefore a crucial parameter, which needs to be considered very carefully.

4.4.4 SYNTHESIS

Our analysis of P_r for estimation of the basal reflection coefficient was not successful and we were able to rule out technical problems of the radar system as the cause. This means, that the absorption of the ice is larger than expected from the ice thickness alone. This is consistent with the temperature distribution found in our modelling. Despite the large uncertainty due to the error in the geothermal heat flux, it becomes clear, that the ice stream consists of relatively warm ice. Although we cannot infer either a basal reflection coefficient nor any lake indicators, it is most likely that the main trunk of the ice stream consists of a wet base.

The modelling of the temperature field gave us the advantage to obtain a regional variable absorption of the ice. This enabled us to understand that we are equally limited by the absorption in the ice, as by the transmitted radar power. The spread within the model ensemble members clearly demonstrates, that ensembles are required, to obtain a basic measure for uncertainty.

The hydrology model provided additional hints on possible subglacial lake locations. Two of the lakes (LC and LD) do clearly not coincide with our sinks, two (LA and LB) appear as a single sink. Furthermore, various smaller sinks exist in the main area of the ice stream as well as in two

interconnected chains merging with the main trunk. The simulations using the modelled basal melt rates unveiled that water is only available in a limited area. While our hydrological model proposes a water sheet below those areas that have indeed higher velocities, the limited extent of the water sheet upstream R5–R11 does not allow to draw the conclusion that massive amounts of subglacial water are the driver for ice stream genesis at this glacier. Still, sliding is playing an essential role, as well as the deformation within an extensive temperate ice layer does, as shown by our ice model.

We have checked all our radargrams for the appearance and disappearance of internal layers with the purpose to use this as additional information about the streamishness of Recovery Glacier. We found that the upper most area down to 0°E/W, is showing a layered structure down to the lower third or quarter of the ice thickness. In this respect Recovery Glacier is similar to the North East Greenland Ice Stream (NEGIS) as shown in Vallenga et al. (2014). Layers within the ice are supposed to lower, once ice flows across a subglacial lake, as shown in Gudlaugsson et al. (2016) and Leysinger Vieli et al. (2007). There is no change in the layered structure upstream or across the large lakes (see Figure 4.11). At other locations, where there is remarkable down-welling of layers, a basal step is linked to the dipping of layers, like around km 516–538 in Figure 4.11.

Reversing the approach, we can check how flat the base of the ice stream is at locations where the large lakes are proposed. Our flight routes were chosen such, that we cross lakes also in along flow direction. Given the large extent of the LA–LD, the ice base would be expected to be considerably smoother when flowing across water than outside the proposed shore lines. None of those profiles show a flat base over the LA–LD, but all of the upstream margins of the proposed lake positions are in coincidence with steps in the basal topography. In some instances, our radar does not retrieve a basal signal in the vicinity of steps itself, but from the base retrieved we find remarkably large topographic steps over short distances. This does not support the hypothesis of lakes as major factors of genesis of this ice stream.

Still we lack ice-thickness data at a considerable area of the ice streams main trunk upstream of lakes R5–R8. In this area, the ice stream is, however, already streamish and thus we think that it does not limit our analysis of the cause of ice stream genesis. Fortunately, Forsberg et al. (2018) has increased the database in this area considerably, so that both datasets together are now giving a reasonable basis for modelling studies to come up.

4.5 CONCLUSION

Within this study we tested the hypothesis of large lakes to be present at the base of Recovery Glacier, as well as the possibility of these lakes to be dynamic and governing ice stream genesis.

We have to conclude that with the radar system used, we are unable to determine the basal reflection coefficient with sufficient accuracy to distinguish reliably between wet, dry and swampy areas. Beside the specific characteristics of our radar system, also a general limit for estimations of the basal reflection coefficient is present, foremost the estimation of the absorption within the ice. The uncertainty in estimating the temperature profile, as well as limited knowledge of impurities, are both factors that could become critical for this approach in general if the transmitted power is not sufficient to allow for the signal to be well above the noise level. The loss of radar returns we found is consistent with warm ice found in some areas of Recovery Glacier. This highlights

the importance of ice-sheet modelling and also the urgent need of improved geothermal heat flux estimates. While new radar systems, like CReSIS MCorRDS or AWI's new ultrawideband radar, will allow to improve the ability to retrieve basal returns, however, limitations of estimating the absorption of the radar wave within ice will remain as limitation for estimating the basal reflection coefficient at the ice base. Here, forward modelling may help to assess the limitations of different systems and to understand the effect of variability in thickness of water bodies over short distances on basal return power.

Our analysis strengthens the hypothesis that the features LA–LD are topographically controlled features, rather than lakes. A wet base downstream in the main trunk would be consistent with our findings in terms of reflection coefficient, ice and hydrology modelling. Two locations where prominent surface elevation change was found in altimetry in this and previous studies are covered well with radar data and basal returns. Also there the existence of a lake cannot be confirmed despite the existence of a solid database. This questions the surface elevation change approach for subglacial lake detection entirely. It also implies limits on the ability to observe subglacial lake drainage based on satellite altimetry and shines new light on the dynamics of subglacial lakes. Our study emphasises the grand challenges presented by Ashmore and Bingham (2014) that technological improvement are absolutely essential.

ACKNOWLEDGMENTS

We thank Neil Ross, Robert Bingham and an anonymous reviewer for their extremely useful and very supporting reviews. Their constructive comments helped a lot to improve the manuscript.

The RECISL campaign was conducted as an activity of AWI in the HGF Alliance Remote Sensing and Earth System Dynamics and was planned with the support of Dana Floriciou and Wael Abdeljaber (DLR), who estimated ice velocities based on TerraSAR-X imagery. Simulations of subglacial hydrology used a model which was developed during the GreenRISE project, a project funded by Leibniz-Gemeinschaft: WGL Pakt für Forschung SAW-2014-PIK-1. Development of PISM is supported by NASA grant NNX17AG65G and NSF grants PLR-1603799 and PLR-1644277. Furthermore we acknowledge the use of data products from CReSIS generated with support from the University of Kansas, NASA Operation IceBridge grant NNX16AH54G, and NSF grant ACI-1443054.

4.6 SUPPLEMENTAL INFORMATION

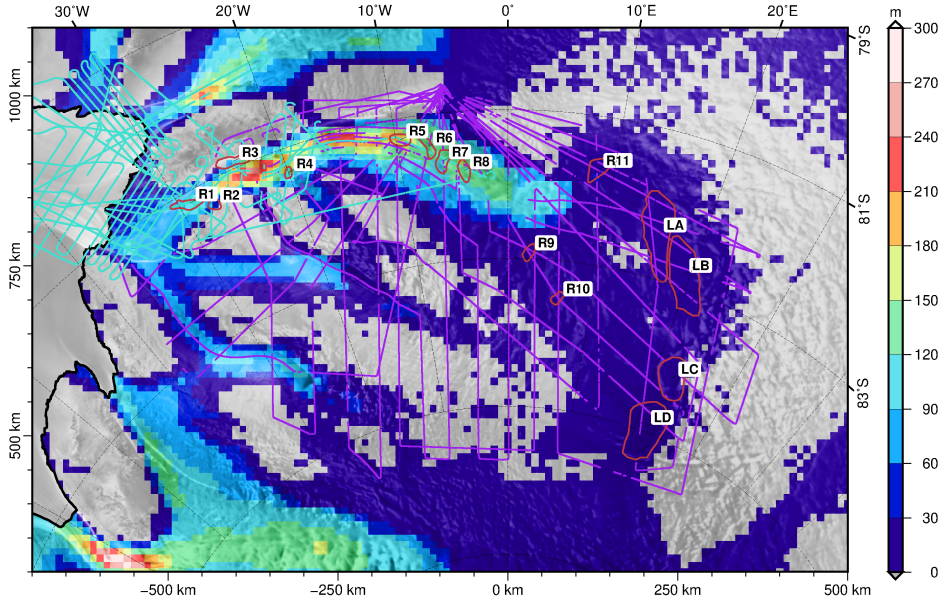


Figure 4.12: Ensemble mean (evoSR) basal temperature ice layer thickness in m. Lake outlines and the observed present day grounding line position are shown in red and black, respectively. Dots indicate basal returns of the radio echo signal from this study (purple) and from Operation IceBridge (Leuschen et al. (2010, updated 2017), turquoise).

Table 4.1: Summary of the data sets applied as boundary conditions for the different PISM simulations, where T_s is the ice surface temperature, a_s is the surface mass balance (SMB) and q_{geo} is the geothermal flux. Spatial means and standard deviations were evaluated on the initial 1 km grid for Recovery area only. The original data set of Fox Maule et al. (2005) was capped at a value of 0.07 W m^{-2} according to the recommendation for the SeaRISE-Antarctica set-up (Bindshadler et al., 2013).

	Reference	Value
T_s^{RA}	Wessem et al. (2014)	$(-42 \pm 7)^\circ \text{ C}$
T_s^{FaO}	Fortuin and Oerlemans (1990)	$(-39 \pm 9)^\circ \text{ C}$
T_s^{JCo}	Comiso (2000)	$(-36 \pm 9)^\circ \text{ C}$
a_s^{RA}	Wessem et al. (2014)	$(19 \pm 9) 10^{-7} \text{ kg m}^{-2} \text{ s}^{-1}$
a_s^{VB}	Berg et al. (2006)	$(19 \pm 7) 10^{-7} \text{ kg m}^{-2} \text{ s}^{-1}$
a_s^{Ar}	Arthern et al. (2006)	$(24 \pm 12) 10^{-7} \text{ kg m}^{-2} \text{ s}^{-1}$
$q_{\text{geo}}^{\text{P}}$	Purucker (2012b)	$(42 \pm 8) 10^{-3} \text{ W m}^{-2}$
$q_{\text{geo}}^{\text{S}}$	Shapiro and Ritzwoller (2004)	$(48 \pm 4) 10^{-3} \text{ W m}^{-2}$
$q_{\text{geo}}^{\text{F}}$	Fox Maule et al. (2005)	$(59 \pm 8) 10^{-3} \text{ W m}^{-2}$

Table 4.2: Thermal properties derived from the different PISM simulations, where the temperate ice area fraction (TIAF) and the temperate ice volume fraction (TIVF) are given in %. Bold numbers are high lighting minimum and maximum values of the evoFT and evoSR runs. All quantities are calculated for the grounded part of Recovery Glacier area on PISM's final 10 km resolution grid. References to the different forcing fields T_s , a_s and q_{geo} are given in Table 4.1.

Forcing		$q_{\text{geo}}^{\text{P}}$		$q_{\text{geo}}^{\text{S}}$		$q_{\text{geo}}^{\text{F}}$	
		TIAF	TIVF	TIAF	TIVF	TIAF	TIVF
evoFT	$T_s^{\text{RA}}, a_s^{\text{RA}}$	17.6	0.47	50.7	0.61	71.9	0.69
	$T_s^{\text{FaO}}, a_s^{\text{Ar}}$	19.6	0.55	46.5	0.70	75.1	0.80
	$T_s^{\text{FaO}}, a_s^{\text{VB}}$	19.3	0.55	45.4	0.70	74.9	0.78
	$T_s^{\text{JCo}}, a_s^{\text{Ar}}$	28.8	0.72	62.9	0.88	85.3	0.98
	$T_s^{\text{JCo}}, a_s^{\text{VB}}$	28.6	0.72	62.9	0.87	85.1	0.96
evoSR	$T_s^{\text{RA}}, a_s^{\text{RA}}$	24.7	0.71	60.6	0.77	83.0	0.84
	$T_s^{\text{FaO}}, a_s^{\text{Ar}}$	32.1	1.04	64.4	1.10	82.3	1.09
	$T_s^{\text{FaO}}, a_s^{\text{VB}}$	31.4	1.03	64.0	1.08	82.4	1.13
	$T_s^{\text{JCo}}, a_s^{\text{Ar}}$	33.8	0.92	73.6	1.00	88.7	1.00
	$T_s^{\text{JCo}}, a_s^{\text{VB}}$	31.4	0.88	72.4	0.95	87.4	0.95

Table 4.3: Indication of existence of lakes based on 1D and 2D lake candidates and a relative power and PPC criteria.

	1D approach	2D approach
number of lake candidates	483	192
rel. power criterion	55	24
PPC criterion	173	44
rel. power and PPC criterion	23	7

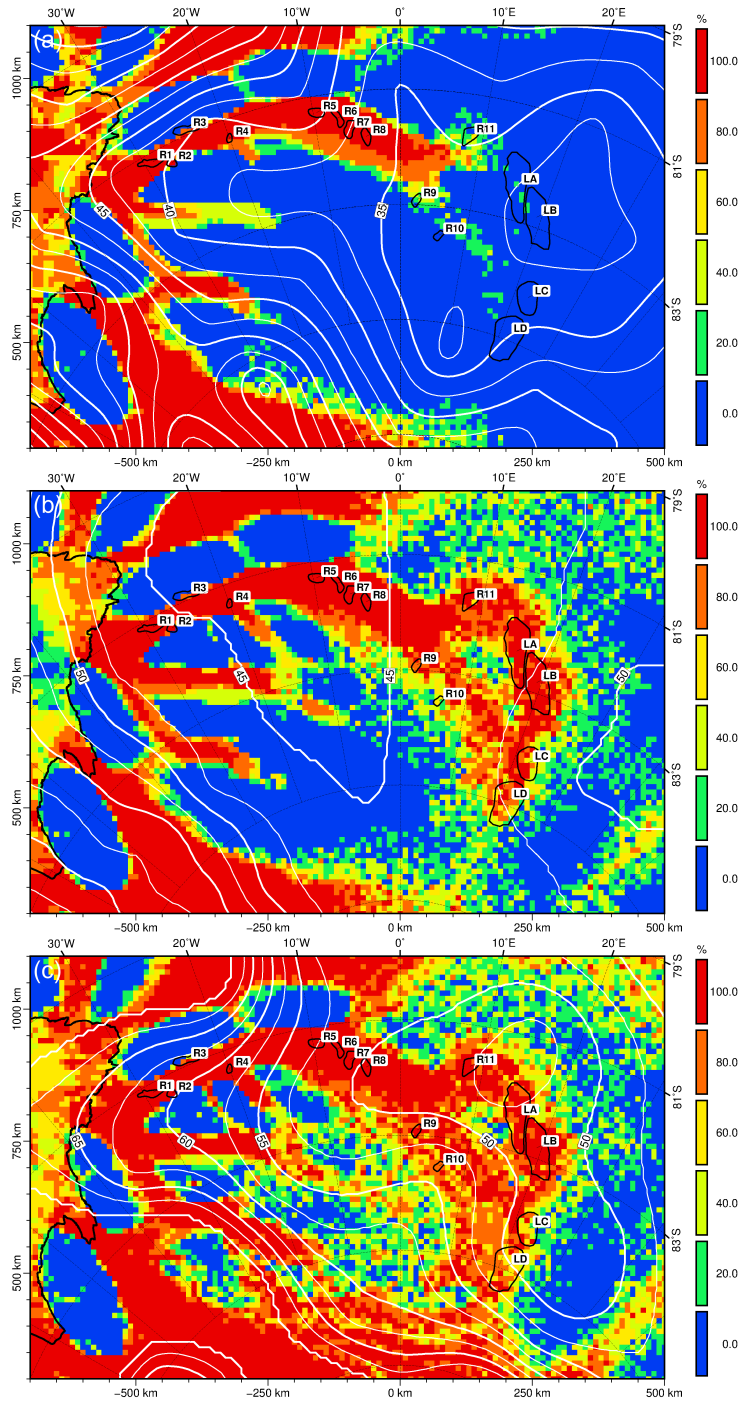


Figure 4.13: The occurrence of temperate ice at the base given in % based on the evoSR runs with a free evolving geometry deconvolved into three panels that show (a) ensemble results derived from $q_{\text{geo}}^{\text{P}}$ only; (b) $q_{\text{geo}}^{\text{S}}$ only; and (c) $q_{\text{geo}}^{\text{F}}$ only. Lake outlines and the observed present day grounding line position are shown in black. The geothermal flux is shown as white contours with $2.5 \times 10^{-3} \text{ W m}^{-2}$ contour interval.

4 Missing evidence of widespread subglacial lakes at Recovery Glacier, Antarctica

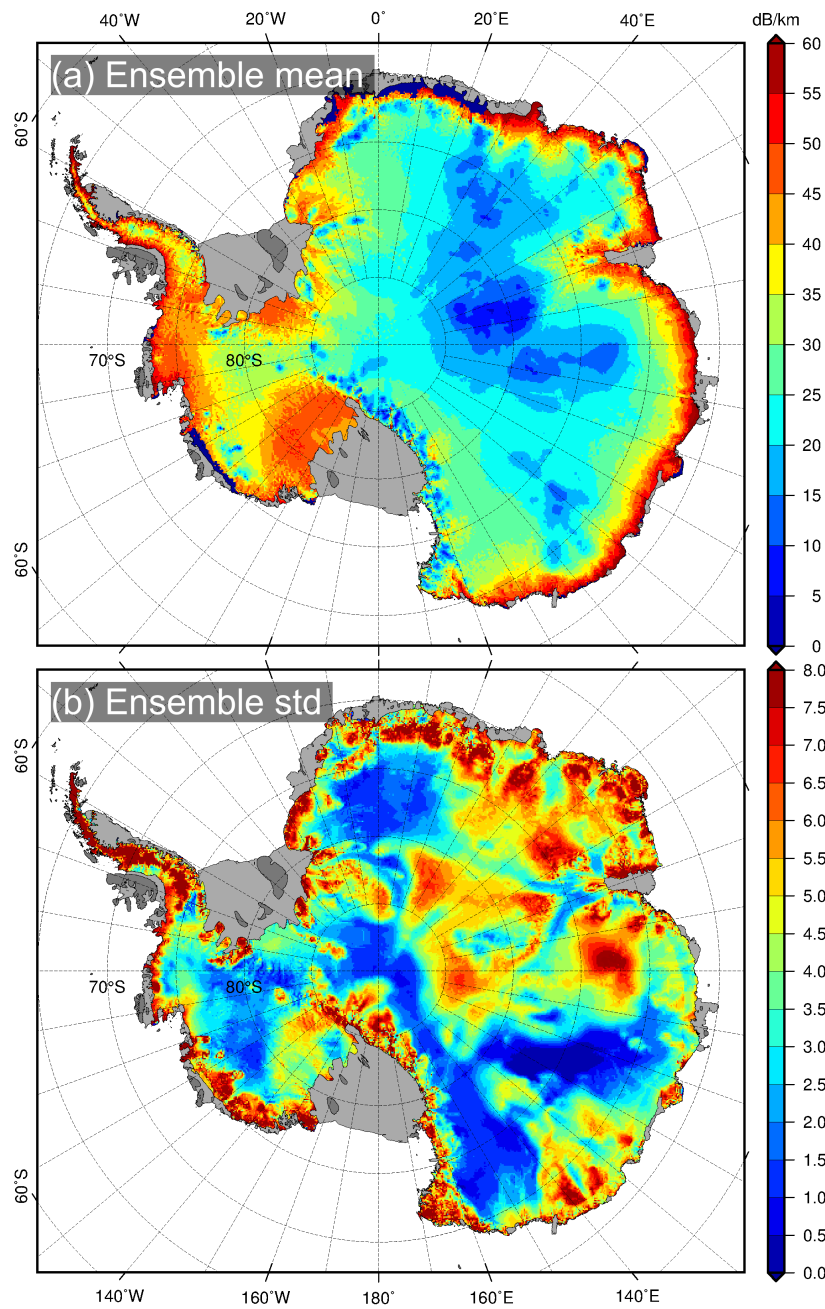


Figure 4.14: Depth-averaged attenuation rates (two-way) derived from the simulated ice temperature fields based on the evoSR model ensemble for the pure ice attenuation model (a). Uncertainty of the two-way attenuation based on the ensemble standard deviation (b). Note, the presented data is clipped at the present-day grounding line as the mean and standard deviation in the ice shelves is highly driven by the lateral extent of individual ensemble members in the model. Note, the colour scale is selected similar to Fig. 7 in Matsuoka et al. (2012).

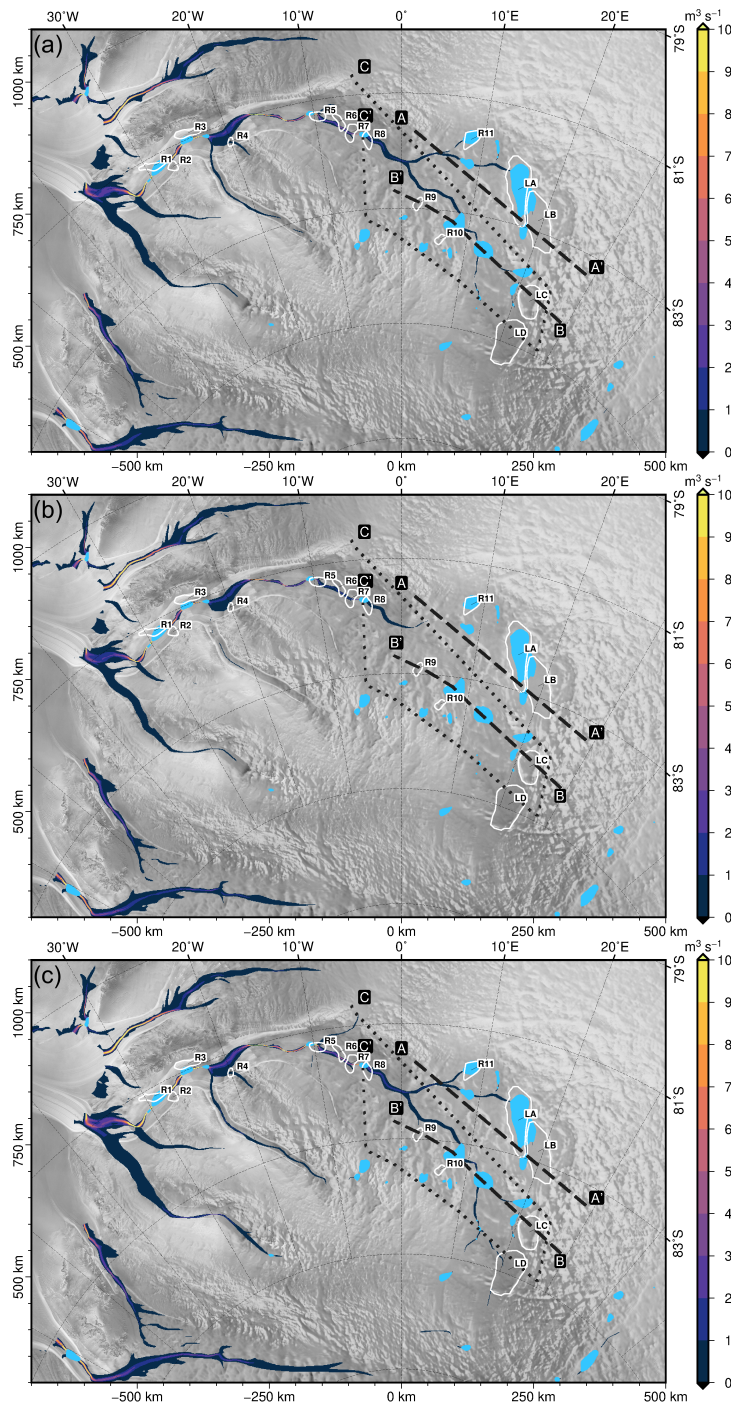


Figure 4.15: Basal water flux in $\text{m}^3 \text{s}^{-1}$ computed with different basal melt rates (clipped below $0.1 \text{ m}^3 \text{s}^{-1}$). Melt rates are from the the evoSR simulations $q_{\text{geo}}^{\text{S}}$, $q_{\text{geo}}^{\text{P}}$ and $q_{\text{geo}}^{\text{F}}$ in panels a to c respectively. Sinks in the hydraulic potential are shown in blue. Black dashed and dotted lines show the location of RES profiles.

4 Missing evidence of widespread subglacial lakes at Recovery Glacier, Antarctica

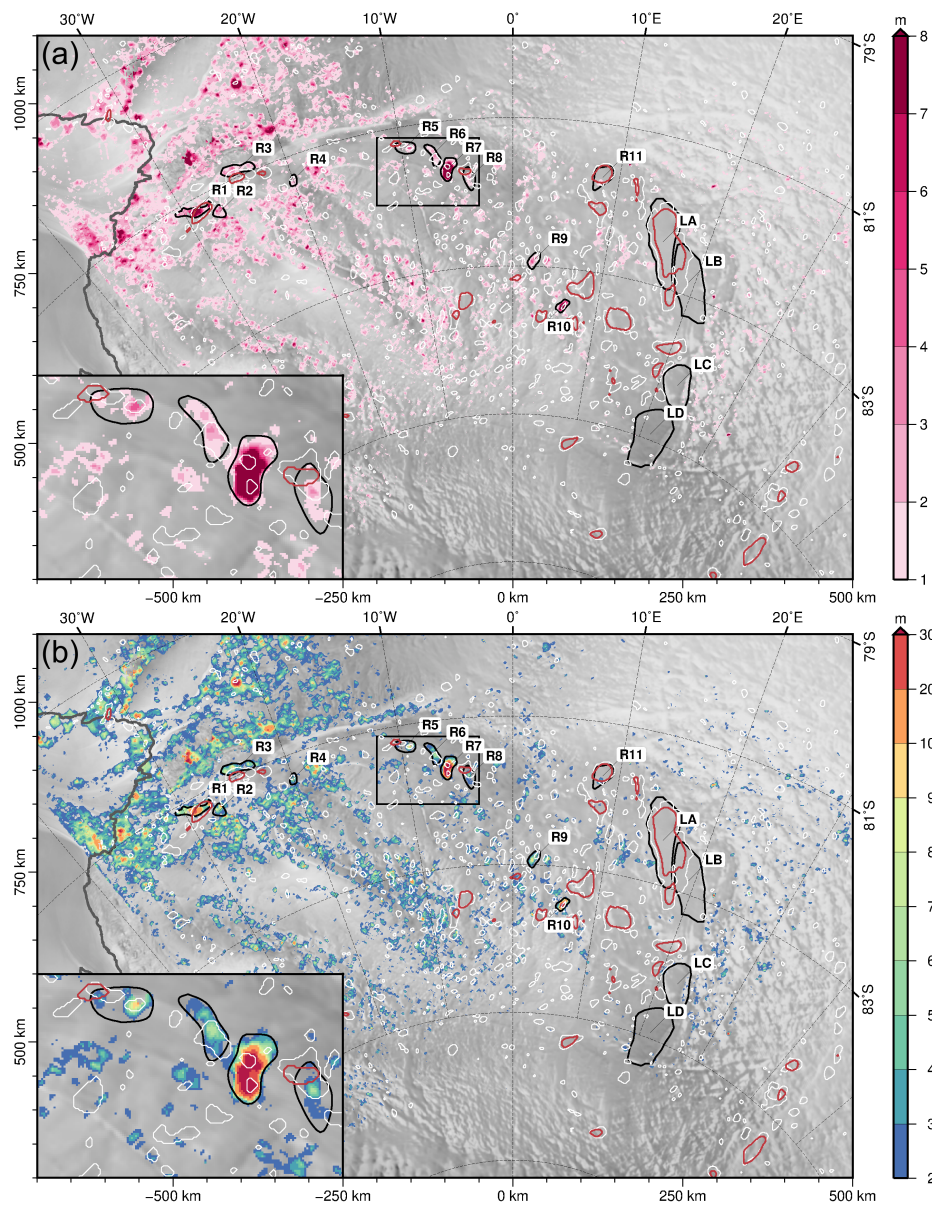


Figure 4.16: Elevation anomalies identified using ICESat. Shown are lake filling events as positive anomaly (a) and the total anomaly accounting for drainage and filling (b) Sink contours derived from the flux model are shown as closed polygons in light grey for the 2 km and in red for the 10 km smoothing kernel.

5 EURASIAN ICE-SHEET DYNAMICS AND SENSITIVITY TO SUBGLACIAL HYDROLOGY

CONTEXT

Subglacial hydrology controls sliding of ice sheets to a large extent. Water lubricates the base and enhances basal sliding, leading to increased ice velocities. By coupling a simple balance flux model for hydrology to an ice sheet model, this paper examines the effect of water flow on the past evolution of the Eurasian ice sheet. The addition of the hydrology leads to generally faster ice flow and more realistic model results. Using a hydrology model in the context of a paleo reconstruction of a former ice sheet, running the model for 280k years requires a very efficient implementation.

The paper aims to improve the modelling of the past Eurasian ice sheet by coupling a thin-film model of subglacial hydrology to the ice sheet model SICOPOLIS. Previous modelling studies of the ice sheet had generally too thick ice in the eastern part, which was improved by adding gradients in the temperature or precipitation forcings (Forsström and Greve, 2004). Incorporating subglacial hydrology has the potential to increase ice velocities, draining more ice and therefore improving the results. There is geological evidence from which Svendsen (2004) reconstructed the extent of the ice sheet to which the model is compared. Another focus of the paper is on the subglacial lakes which have existed below the ice over the modelling period, as they were able to store a significant amount of water.

The coupling of the basal hydrology component to the ice dynamics model is done by converting the balance flux into a water layer thickness and then defining sliding enhancement due to water as a function of the latter, as described in Section 3.2.3. However, with the maximum possible increase as a variable S_w , where values of [1, 3, 6] have been tested (1 meaning no effect of the water layer and 6 meaning a maximal six fold increase) The model was run at a horizontal resolution of 40 km and through a spin up period of 250 ka with a time step of 10 years. For the period of 40k to 10k years before present a time slice was analyzed for subglacial lakes every 250 years. For each slice the outputs of the ice model were interpolated onto a 1 km grid and combined with present day topography data. Then, sinks in the hydraulic potential were identified as possible lake locations and the total lake volume recorded as storage capacity (see Section 5.2.5).

This large scale application of a hydrology of subglacial hydrology on the Eurasian ice sheet at a coarse resolution and with a large time step gives insight into the effects of a coupled model, revealing important feedback and long-time evolution of the system.

CONTRIBUTION

For this publication I contributed the balance flux model and its implementation in Fortran, which the first author, E. Gudlaugsson used to set up the study and experiments. E. Gudlaugsson also wrote the publication text and designed the figures with contribution from all co-authors.

AUTHORS AND AFFILIATIONS

Eythor Gudlaugsson,¹ Angelika Humbert,^{2,3} Karin Andreassen,¹ Caroline C. Clason,⁴ Thomas Kleiner,² Sebastian Beyer²

¹*Centre for Arctic Gas Hydrate, Environment and Climate (CAGE), Department of Geology, UiT – The Arctic University of Norway, Tromsø, Norway*

²*Section of Glaciology, Alfred Wegener Institute Helmholtz Center for Polar and Marine Research, Bremerhaven, Germany*

³*Department of Geosciences, University of Bremen, Bremen, Germany*

⁴*School of Geography, Earth and Environmental Sciences, Plymouth University, Plymouth, UK*

ABSTRACT

Ice stream dynamics are strongly controlled by processes taking place at the ice-bed interface where subglacial water both lubricates the base and saturates any existing, underlying sediment. Large parts of the former Eurasian ice sheet were underlain by thick sequences of soft, marine sediments and many areas are imprinted with geomorphological features indicative of fast flow and wet basal conditions. Here, we study the effect of subglacial water on past Eurasian ice sheet dynamics by incorporating a thin-film model of basal water flow into the ice sheet model SICOPOLIS and use it to better represent flow in temperate areas. The adjunction of subglacial hydrology results in a smaller ice sheet building up over time and generally faster ice velocities, which consequently reduces the total area fraction of temperate basal ice and ice streaming areas. Minima in the hydraulic pressure potential, governing water flow, are used as indicators for potential locations of past subglacial lakes and a probability distribution of lake existence is presented based on estimated lake depth and longevity.

5.1 INTRODUCTION

During the Weichselian glacial period, large parts of the Arctic were ice covered. At its maximum the Eurasian ice sheet, consisting of both the Barents Sea Ice Sheet (BSIS) and the Fennoscandian Ice Sheet (FSIS), merged with the Celtic ice sheet in the south-west and extended all the way up the north continental shelf (Fig. 5.1), covering both the Barents and the Baltic Seas (Svendsen et al., 2004). A close historical equivalent to the West Antarctic Ice Sheet (WAIS) is the former BSIS. At the Last Glacial Maximum (LGM) the two ice sheets were more or less equivalent in both size and volume but whereas the BSIS completely disappeared, the WAIS endured (Svendsen et al., 2004; Anderson et al., 2002; Evans et al., 2006). Both ice sheets were grounded largely below sea level and both had large, dynamic ice streams that drained them (Andreassen and Winsborrow, 2009). The BSIS thus constitutes a close geological analogue to WAIS and its history can provide important insights into the future evolution of the WAIS. Subglacial hydrology is thought to have played a crucial role in the relatively fast disintegration of the BSIS (Bjarnadóttir et al., 2014; Winsborrow et al., 2010).

Temperate ice and subglacial meltwater are typically found either underneath very thick ice due to the geothermal flux and the insulating properties of ice or in areas of high deformation and/or frictional resistance such as closer to the margin (Siegert et al., 1996). Any subglacial meltwater that forms will drain from areas of high pressure potential towards areas with lower potential. Components of the subglacial drainage network can in general be divided into two different categories or subsystems; (1) an efficient system consisting of fast flowing water in channels carved into ice, bedrock or sediment (Röthlisberger, 1972; Nye, 1973), exhibiting low water pressures compared to ice overburden or (2) an inefficient system, exhibiting high water pressure, such as sheet flow (thin film) (Weertman, 1966) or flow through connected cavities (Lliboutry, 1968) or porous sediment (Shoemaker, 1986). Real drainage networks comprise a combination of the two and tend to have both diurnal and seasonal cycles (Wal et al., 2008; Andrews et al., 2014).

Subglacial water lubricates the ice base by effectively separating it from the underlying bed and decreasing the area and force of contact between the two (Iken, 1981; Schoof, 2010a). Within the sediment column, increasing pore water pressures decrease its yield strength, mainly by separating sediment particles from one another, leading to easier and faster sediment deformation (Tulaczyk et al., 2000a). Rapidly moving corridors of ice, ice-streams, typically move mostly by either basal slip or by deformation of the underlying sediments, both of which are highly dependent on the availability of subglacial water. In modern-day ice sheets, up to 90% of mass is lost through these fast flowing corridors of ice (Bamber, 2000). Inclusion of these processes in numerical ice sheet models is therefore of vast importance for the estimation of future ice loss in polar regions and changes in global sea level. By studying the dynamics of extinct ice sheets and how models respond to perturbations in external forcing we can learn much about how modern ice sheets are likely to respond to a changing climate in the future.

5.1.1 PREVIOUS MODELLING STUDIES

The Eurasian ice sheet has previously been modelled with 3D thermomechanically coupled ice sheet models such as by Payne and Baldwin, 1999 who established a connection between past ice streaming and fan-like landform assemblages on a hard-rock area of the Baltic Shield. Although

neither accounting for the Barents Sea part of the ice sheet nor subglacial sliding in general, their model output matched reasonably well with available empirical data of the time. Geological and geophysical data from the former Eurasian Ice Sheet as a whole were later summarized and used for a geological reconstruction of the Quaternary ice sheet development (Svendsen, 2004; Svendsen et al., 2004). As part of the same program, the Quaternary Environment of the Eurasian North (QUEEN), Siegert, 2004 used an inverse modelling approach to simulate the Eurasian ice sheets growth and decay, during the late Weichselian, matching the geological evidence presented. They varied climatic inputs in order to optimize the fit between model evolution and empirical data. Another modelling approach was adopted by Forsström and Greve, 2004 who used the shallow ice approximation (SIA) numerical model, SICOPOLIS (Simulation COde for POLythermal Ice Sheets), as we do in this study. Their model, although fitting the western limits well, extensively overglaciated the eastern part of the ice sheet which prompted them to introduce LGM anomalies, or strong west-east gradients in temperature and precipitation forcings, in order to reduce the extent of glaciation in the east, over the Kara Sea and the Pechora lowlands. SICOPOLIS was again used by Clason et al., 2014 who improved upon previous models by incorporating a parametrization of surface meltwater enhanced sliding (SMES). They produced a model fitting well with empirical data and again confirmed the necessity of strong west-east gradients in both temperature and precipitation to reduce glaciation in the east.

Here, we further build upon the Clason model, introducing a simple representation of the subglacial hydrological system, focussing specifically on the influence of subglacial-water-enhanced sliding on ice dynamics and the temporal evolution of the Fennoscandian and the Barents Sea Ice sheets, without the inclusion of SMES. In addition, we use the hydrological model to deduce probable locations of past subglacial lakes, their temporal perseverance, size and probability of existence.

5.2 MODELLING APPROACH

5.2.1 ICE SHEET MODEL

We use the thermodynamically coupled ice sheet model SICOPOLIS (Greve, 1997) in order to simulate the Fennoscandian and the Barents Sea Ice sheets. SICOPOLIS is a 3D, polythermal, two-layer model (temperate and cold ice) that uses a simplified set of equations (SIA) to calculate ice velocities, thickness, age, temperature and water content. Ice is treated as an incompressible fluid where strain rates are related to deviatoric stresses via Glen's flow law (Glen, 1955). Ice viscosity depends on temperature, water content and effective strain-rate (Paterson and Budd, 1982; Duval, 1977; Duval and Lliboutry, 1985). The SIA is incapable of correctly reproducing ice streams as higher order stresses are neglected although one can mimic their effect through enhanced sliding in temperate regions. Large-scale behaviour of ice sheets is generally well represented however. The model was run, with a horizontal grid size (Δx) of 40 km and a time step (Δt) of 10 a, for 250 ka to allow for sufficient spin-up time and to minimize any errors arising from arbitrarily chosen initial conditions, although we only present results from the last 100 ka with a special focus on the final 30 ka of the Weichselian (40 ka - 10 ka) as this is the main study period.

Isostatic adjustment follows the local-lithosphere-relaxing-asthenosphere (LLRA) approach where an ice load causes a local displacement of the lithosphere, balanced by a buoyancy force of the vis-

cously deforming asthenosphere (Greve and Blatter, 2009). Compared to computationally more expensive lithosphere treatments where elasticity is accounted for, the local approach results in a slightly more spatially-concentrated and less smooth isostatic response as there is no lateral effect beyond the ice load of each computational cell (as there is with an elastic lithosphere approach) (Le Meur and Huybrechts, 1996). This effect is not too pronounced though and mostly significant in regions with large ice-thickness gradients, such as close to the ice margins (Greve and Blatter, 2009).

Ice shelves are not treated explicitly, but instead the model is allowed to glaciare the seafloor above a certain threshold depth (1000 m). When ice moves into deeper water, ice thickness is set to zero which can be considered as a crude form of calving. Sensitivity studies show little dependence on this threshold depth, with the main differences between this and the typically used lower threshold of 500 m being that a small area within the North Sea resists glaciation for the lower threshold (Clason et al., 2014).

5.2.2 CLIMATE FORCING

We employ the same climatic forcing as in Clason et al., 2014 where climatic conditions were linked to the NorthGRIP $\delta^{18}\text{O}$ ice core record and a synthetic Greenland ice core record based on Antarctic data and the thermal bipolar seesaw model (Wolff et al., 2010; Andersen et al., 2006; Barker et al., 2011). Temperatures and precipitation were scaled between present day and LGM conditions using a combination of CFSR (Climate Forecast System Reanalysis) data for present-day conditions (Uppala et al., 2005; Saha et al., 2010; Dee et al., 2011) and IPSL (Institut Pierre Simon Laplace) CM5A-LR for LGM conditions (Kageyama et al., 2013). In order to get a realistic ice-sheet extent, comparable to that compiled by Svendsen et al., 2004, a linear gradient, from the west to the east, on the LGM temperature data was imposed, reducing temperatures in the west and raising them in the east. For further details see Clason et al., 2014.

5.2.3 SUBGLACIAL HYDROLOGY

Following (Kleiner and Humbert, 2014) we use a subglacial water-flow model where water is assumed to flow in a thin film between the underlying substrate and the ice (Le Brocq et al., 2009; Johnson and Fastook, 2002). The time dependent water depth (d) is given by:

$$\frac{\partial d}{\partial t} = M - \nabla(\mathbf{u}_w d), \quad (5.1)$$

where M is the basal melt rate, computed at every time step, and \mathbf{u}_w is the depth-averaged water velocity. A second equation relating water depth and differences in water pressure to the water velocity can be obtained by assuming that the flow can be described as laminar flow between two parallel plates as (Weertman, 1972):

$$\mathbf{u}_w = \frac{d^2}{12\mu} \nabla \Phi, \quad (5.2)$$

where μ is the viscosity of the water and Φ the hydraulic potential. The latter can be written in terms of water pressure p_w and an elevation potential

$$\Phi = \rho_w g z_b + p_w, \quad (5.3)$$

where ρ_w is the density of water, g the gravitational acceleration and z_b is the height of the bedrock relative to some fixed datum (WGS84, Polar Stereographic projection).

Water pressure can in turn be described by the ice overburden pressure (H is ice thickness, ρ_i is ice density) minus the effective pressure N

$$p_w = \rho_i g H - N. \quad (5.4)$$

Here, we assume that the effective pressure is everywhere equal to zero (Shreve, 1972), which simplifies the pressure potential to a purely geometrical equation where the potential gradient is described as a function of the surface and the bedrock gradient

$$\nabla \Phi = \rho_i g \nabla z_s + (\rho_w - \rho_i) g \nabla z_b, \quad (5.5)$$

where z_s represents the elevation of the ice surface.

It is assumed that the timescales governing water flow are much shorter than those governing the flow of ice and that Eq. 5.1 thus reaches steady state ($\frac{\partial d}{\partial t} = 0$) within each timestep of the ice flow model. Water fluxes are calculated recursively, at each time step, starting from the top of the hydraulic potential surface, in the direction of the hydraulic gradient following Budd and Warner, 1996. For an overview of different, typically used flux routing numerical schemes see Le Brocq et al., 2006.

5.2.4 BASAL SLIDING

We employ a Weertman-type sliding law that relates the basal shear stress and velocity (Weertman, 1957)

$$\mathbf{u}_b = -C_b |\tau_b|^{p-1} \tau_n^{-q} \boldsymbol{\tau}_b, \quad (5.6)$$

where \mathbf{u}_b is the basal horizontal velocity, $\boldsymbol{\tau}_b$ the basal shear stress and τ_n basal normal pressure which is taken to be equal to the ice overburden pressure. The sliding law is extended in order to allow for sliding at sub-melt temperatures and the thickness of the water layer following Kleiner and Humbert, 2014 and Johnson and Fastook, 2002.

$$C_b = (1 + f_w) f_T C_b^0, \quad (5.7)$$

$$f_w = (S_w - 1) \left[1 - \exp\left(-\frac{d}{d_0}\right) \right], \quad (5.8)$$

where $f_T = \exp(\nu(T - T_{pm}))$, ν is the sub-melt sliding parameter, T temperature, $T_{pm} = T_0 - \beta p$ the pressure dependent melting point, C_b^0 is a basal sliding parameter that depends for example on bed material and roughness, (d_0) is a typical scale of water layer thickness (here equal to 1 mm or 10^{-3} m) and S_w is the maximum increase in sliding velocity due to subglacial water. Here, we test three different values for S_w , [1, 3, 6] representing a maximum of a six fold

Table 5.1: Model parameters discussed in the paper

Parameter	Numerical Value
μ , Viscosity of water	1.8 m Pa s ⁻¹
ρ_w , Density of water	1000 kg m ⁻³
ρ_i , Density of ice	910 kg m ⁻³
g , Gravitational acceleration	9.81 m s ⁻²
(p, q) , Sliding coefficients	(3, 2)
C_b^0 , Sliding parameter	[11.2, 33.6] m a ⁻¹ Pa ⁻¹
S_w , Sliding parameter	[1, 3, 6]
d_0 , Scaling factor	1 mm
ν , Sub-melt sliding parameter	1 K
T_0 , Melting point (p=0)	273.15 K
β , Clausius-Clapeyron constant	9.8×10^{-8} K Pa ⁻¹
Δt , Model time step	10 a
Δx , Model grid size	40 km

increase in sliding velocity due to the water layer. A two part mask is used for bed roughness (C_b^0), a background value of 11.2 m a⁻¹Pa⁻¹ and 33.6 m a⁻¹Pa⁻¹ where the bed is considered to consist of a thick deformable layer of soft sediment (Clason et al., 2014). Numerical values for all other parameters discussed are presented in Table 5.1.

5.2.5 SUBGLACIAL LAKES

Model output, such as basal melt rates, temperature, ice thickness and isostatic adjustment are interpolated onto high resolution grids in a post-processing step, for a selection of time slices every 250 years in the period 40 ka - 10 ka, and used along with modern day topographic maps of the study area (General Bathymetric Chart of the Oceans (GEBCO), Weatherall et al., 2015) for high resolution calculations of meltwater routing (1 km grid size). These can be used to infer possible locations of subglacial lakes and their temporal duration. Before routing is calculated, any local minima (sinks) in the hydraulic potential need to be filled to brink, allowing water to continue further downstream. These local minima represent areas where subglacial water would be likely to pond on its way down the hydraulic potential. By mapping these out we get an idea of potential locations where subglacial lakes might have existed in the past and by looking at a selection of time slices we get a sense of how long they were likely to have persisted throughout changes in the ice sheet state or configuration. The height to which the sinks need to be adjusted in order to eliminate them is used as a proxy to estimate the potential depth of each subglacial lake, assuming that the change in potential arises solely from a change in water depth (Eq. 5.3). By summing up the estimated volume of all lakes, we get a rough approximation of total water storage capacity in subglacial lakes for the whole domain. Such a value is unlikely to be of very high accuracy, but relative changes in lake storage capacity with time might be considered to be more reliable. Additionally, although a water-film model is incapable of reproducing channels in a physically meaningful manner, areas where flow of meltwater converges to form a thick water layer can be

considered to be likely locations where channels would have formed in the past (Livingstone et al., 2015).

5.3 MODEL RESULTS

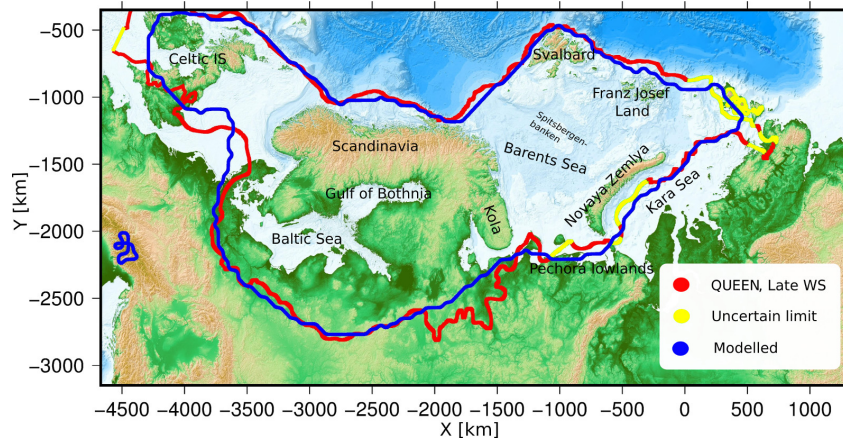


Figure 5.1: A map showing the study area as well as the modelled and reconstructed extent of the Eurasian ice sheet at the LGM. The reconstructed extent based on geological evidence from Svendsen et al., 2004 is shown in red with uncertain limits in green and modelled extent is shown in blue (for $S_w = 6$).

The model results show a two-peaked glacial maximum, with the latter peak occurring around 23.5 ka when both area and volume are at a maximum. We will refer to this peak as the LGM. The ice sheet extent at the LGM matches well with empirical data (Fig. 5.1) with relatively small differences in extent between model runs with or without water enhanced sliding (results for $S_w = 1$ are the same as for model run 1 in Clason et al., 2014). Maximum thickness of 4125 m is reached slightly later, or at 19 ka for simulations with hydrology-coupled (HC, $S_w > 1$) sliding. Maximum horizontal velocities are typically around 3000 m a^{-1} for $S_w = 6$ with peak values approaching 10 km a^{-1} over short time periods (Fig. 5.2c). A stronger coupling (higher S_w) between sliding and water layer thickness results in a lower overall ice volume building up with time (Fig. 5.2a) although the areal extent is not greatly affected (Fig. 5.2b,c). The ice sheet disintegrates rapidly shortly after 15 ka and by 10 ka has completely disappeared.

At the LGM, 20% of the ice sheet base is estimated to be temperate, mostly close to the margin in ice streaming areas. The coldest part of the ice sheet at the LGM, with basal temperatures well below the pressure melting point is roughly over Finland, in the center of the domain (Fig. 5.3). This is also the thinnest part of the ice sheet at that time and therefore the part where basal temperatures are most influenced by the cold surface temperatures above. Ice velocities there are close to zero during the LGM and only increase in that area during deglaciation when the ice sheet is smaller and the margin closer.

The model produces two major ice domes that merge around 34 ka with one ice dome centered over the Gulf of Bothnia (FSIS) and the other over the Barents Sea (BSIS, Fig. 5.3a). The

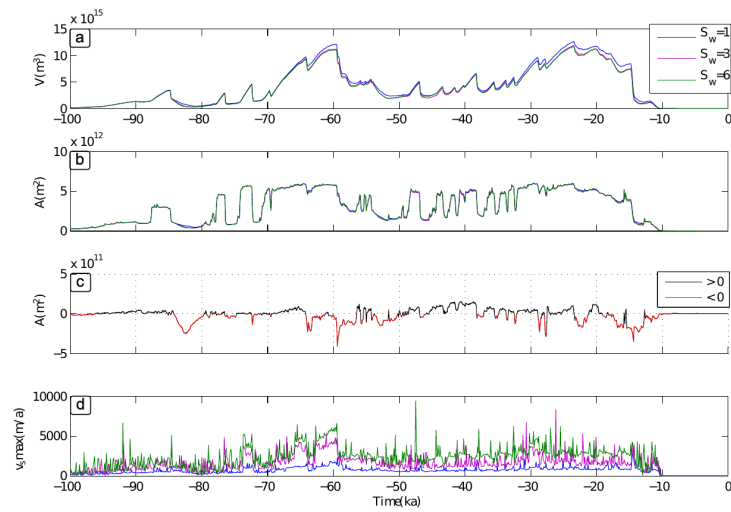


Figure 5.2: Comparison between simulations with different values of the sliding parameter S_w for the last 100 ka. Blue in subfigures (a,b,d) represents simulations without hydrology-coupled sliding ($S_w = 1$), purple $S_w = 3$ and green $S_w = 6$. (a) shows total ice volume in m^3 , (b) shows total area coverage of glacial ice in m^2 , (c) shows the difference in total area between simulations with ($S_w = 6$) and without ($S_w = 1$) a thin water film. Black denotes points in time when areal coverage is larger for simulations without HC sliding and red otherwise. (d) shows the maximum horizontal velocity of the whole domain at each point in time in m a^{-1} .

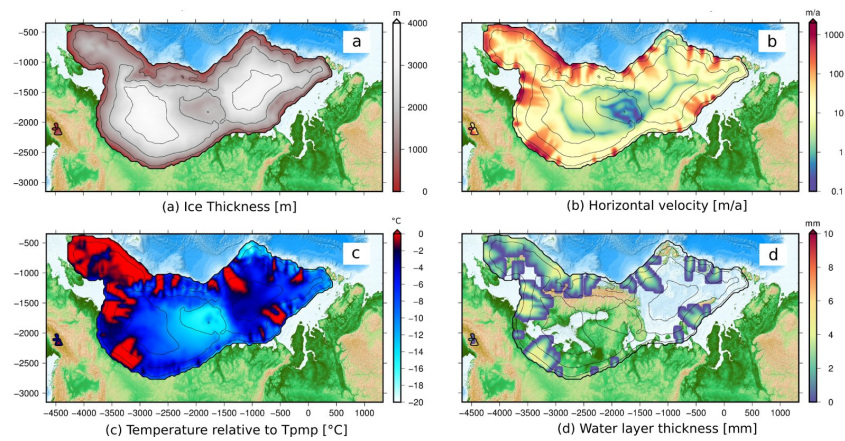


Figure 5.3: (a) Ice sheet thickness in m, (b) horizontal velocity in m a^{-1} , (c) basal temperature relative to pressure melting point in $^{\circ}\text{C}$ and (d) water layer thickness in mm for the $S_w = 6$ sliding scenario at 23.5 ka, the point of maximum ice extent and volume.

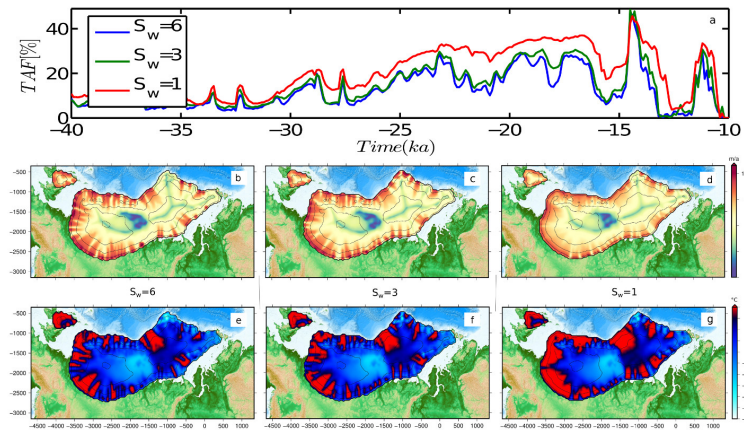


Figure 5.4: (a) Temperate area fraction (TAF) of the Eurasian Ice sheet between 40 ka and 10 ka. (b,c,d) a comparison of horizontal velocity in m a^{-1} and temperature (e,f,g) in $^{\circ}\text{C}$ relative to pressure melting point for the three sliding scenarios considered (at 20 ka). (b,e) are with $S_w = 6$, (c,f) with $S_w = 3$ and (d,g) without HC sliding ($S_w = 1$)

Fennoscandian dome then merges with the Celtic IS shortly before the LGM, or around 26.5 ka to produce one major ice sheet. The eastern extent of the ice sheet, in contrast to many previous modelling attempts, compares well with geological reconstructions (Fig. 5.1).

Incorporation of hydrology-coupled (HC) sliding improves the models ability to mimic ice streams and spatially confine their location. SIA generally produces broad areas of fast flow whereas the inclusion of hydrology-coupled sliding limits and confines fast-flowing areas to temperate areas with a thick water layer (Fig. 5.4) and thus better mimics real velocity patterns. Faster sliding leads to a reduction in the temperate area fraction (TAF) of basal ice, however, the width of ice streaming areas is probably still somewhat overestimated because of the limited grid resolution of the numerical model and simplified model physics.

Water is routed along the direction of the largest gradient according to Eq. 5.5 (Budd and Warner, 1996) and is limited to temperate areas of the ice sheet. The calculated thickness of the water layer used in the model rarely exceeds 6 mm (Fig. 5.3d), consistent with the thin-film assumption. No extra bedrock smoothing is applied before melt water is routed along the base to the margin as the 40 km grid resolution already represents considerable averaging simply because of the large grid size.

An example of water layer thickness at 23.5 ka, using interpolated model results and modified high resolution bathymetry (1 km grid size) is presented in Figure 5.5. Semicircular areas in red depict sinks in the hydraulic potential where water would likely pond on its way towards the margin and routing of subglacial water is limited to areas of the ice sheet with a temperate base.

Several subglacial lakes are predicted to have existed during the last glacial cycle (Fig. 5.6). Particularly in the Norwegian fjords and valleys as well as on the western side of Novaya Zemlya although the bathymetry data on either side of Novaya Zemlya is not of high quality. The island itself represents a significant hydrological barrier to subglacial flow of water with ice flowing generally from the west to the east, over the island, and large parts of the area having a temperate base

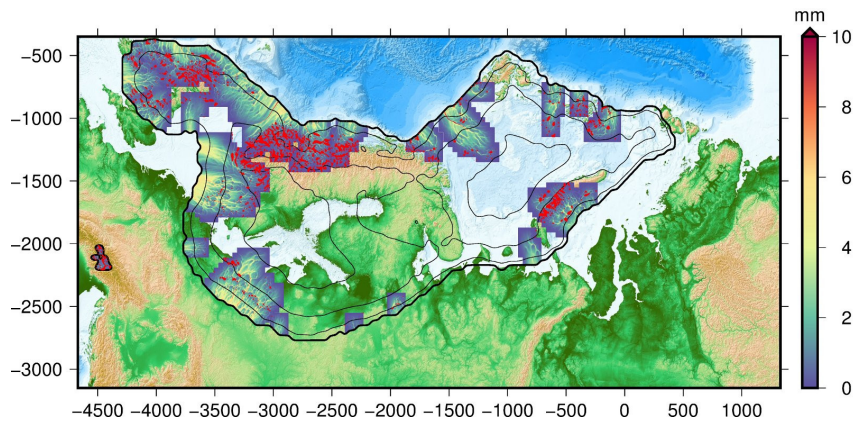


Figure 5.5: Map of water layer thickness at 23.5 ka calculated with a 1 km resolution bathymetric grid. Sinks in the hydraulic potential (potential subglacial lakes) are marked with red ($S_w = 6$).

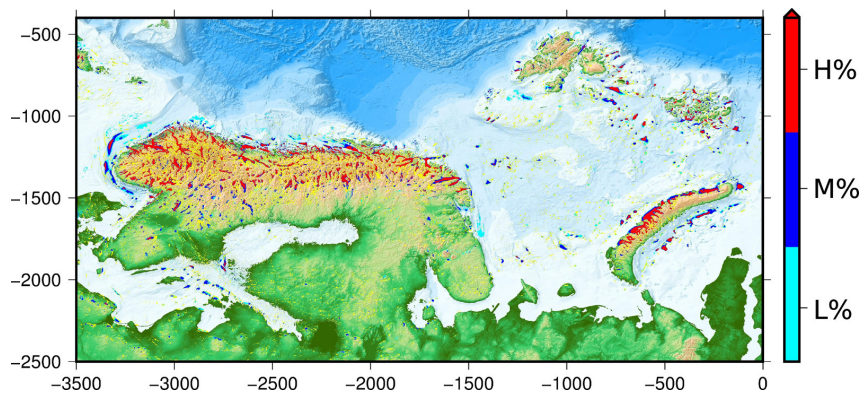


Figure 5.6: Map showing all predicted lake locations during the period 40 ka - 10 ka, color-coded based on perceived probability of existence. A deep, temporally persistent lake is deemed as having a higher probability of having existed than a shallow, shortlived one. Calculated with $S_w = 6$.

during much of the glaciation (Fig. 5.5). Few lakes probably existed in the Barents Sea area and on Svalbard compared to the Scandinavian mainland.

A criterion for the likelihood of a subglacial lake having existed is taken as the product of the estimated lake depth for each time slice and the time each cell persists as part of a subglacial lake. This is done with a grid resolution of 1km both with and without smoothing (5 km) of the underlying bathymetry. Smoothing eliminates mostly small, shallow sinks of the hydrological potential that would otherwise show up as potential lakes. For completeness and in order to separate these small shallow areas from the deeper and larger potential lake locations, the routing is calculated without smoothing as well. These shallow areas are represented by a yellow color in Fig. 5.6. All grid cells are then ranked with the above criteria, normalized and given a score (H)igh, (M)edium or (L)ow based on the probability of each cell having been part of a subglacial lake, with H representing lakes that are both deep and temporally stable and can thus be considered to be more likely candidates. Each category contains one third of all cells marked as having pertained to a subglacial lake at some point.

Figure 5.7 shows the temporal evolution of total lake storage capacity (LSC) as a function of time for the time period 40 ka to 10 ka. Changes in ice sheet geometry, switches in the thermal regime or deflections of the lithosphere all affect the storage capacity of subglacial water. Here we have opted for the more conservative estimate of lake storage, assuming that any change necessary in the hydraulic potential needed to fill local minima would come from a change in water level alone, leaving ice thickness untouched. This leads to a total amount of stored water of the same order of magnitude as estimated for Antarctica (Pattyn, 2008). The LSC generally follows the ice sheet evolution with sharp drops in volume and peaks in freshwater production associated with drops in LSC as well. The rate of loss in storage capacity of subglacial water can equal or surpass the amount of basal water produced during the same time, indicating that a considerable amount of subglacial water is poured out during deglacial periods. A larger more extensive ice sheet tends to support a greater storage of subglacial water underneath the ice sheet.

5.4 DISCUSSION

Overall, the modelled LGM extent of the FSIS and the BSIS matches well with the geological reconstructions of the former ice sheets (Svendsen, 2004; Svendsen et al., 2004), with the inclusion of subglacial hydrology representing a slight improvement both in extent and volume in the Barents Sea region. We have used the same climate forcings as Clason et al., 2014 which along with older work of Siegert, 2004 and Forsström and Greve, 2004 confirmed the need for strong west-east gradients in both temperature and precipitation patterns.

5.4.1 HYDROLOGY

The meltwater-enhanced sliding has a strong effect on the evolution of the ice sheets. Sliding velocities are coupled to the evolution of the thin water film and increase with increasing film thickness. This leads to considerably lower ice thickness and volume building up over time. During the early stages of inception little to no differences are seen in either volume or extent as the ice sheet is mostly cold-based. As soon as a part of the margin reaches pressure melting point and sliding picks up, it draws down ice from the surrounding area, deflecting flow directions towards

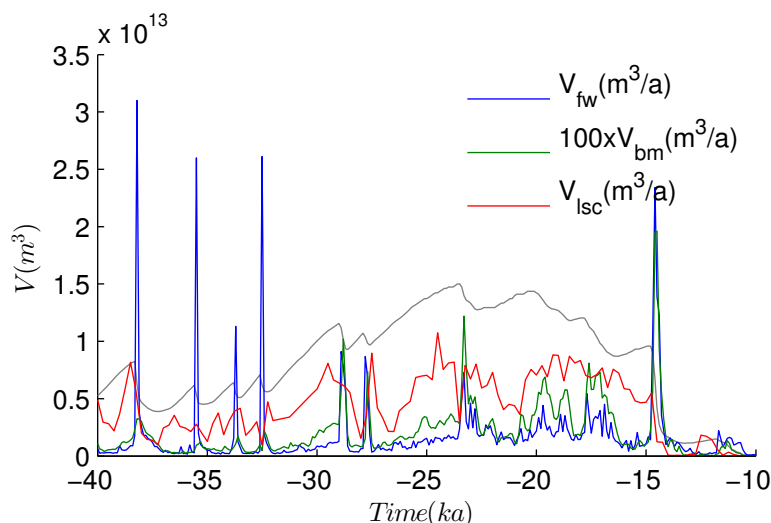


Figure 5.7: Total freshwater production (V_{fw}), basal melt volume ($100 \times V_{bm}$) and lake storage capacity (V_{lsc}) in $\text{m}^3 \text{a}^{-1}$ from 40 ka to 10 ka ($S_w = 6$). Ice volume is shown in gray in the background for comparison (not to scale).

the lowered surface. The total ice sheet extent is not greatly affected by hydrology-coupled (HC) sliding. Most notable are the differences during or following a warm period and a sharp decrease in volume where the lower thickness of the hydrology coupled ice sheet means that it is more vulnerable to the higher temperatures at lower altitudes and thus experiences more surface melt and a faster decline. During ice sheet growth and at peaks in volume the areal extent is generally slightly larger.

The effect of HC sliding on the basal temperatures, and most notably the percentage of the bed that is actually at pressure melting is greater. As can be seen from Fig. 5.4, a much larger part of the bed is at pressure melting for simulations without hydrology-coupled ice dynamics. When the movement of ice changes from flow by internal deformation to flow by rapid basal sliding, this affects the heat balance of the ice. When basal sliding ensues, heat generated by internal deformation within the ice column decreases but gets somewhat compensated for by frictional heating between the sliding ice and the underlying substrate. This however does not explain why models disregarding subglacial hydrology and its effect on sliding would overestimate temperate areas of the ice sheet. The explanation lies in the fact that for the HC sliding scenario, faster sliding leads to increased advection of cold ice from above in the transition zone, in addition to less deformational energy being available due to the lower ice thickness. Models neglecting subglacial hydrology are thus likely to overestimate temperate areas of the base as well as total ice volume compared to models that include subglacial hydrology and any associated enhancement in sliding. In simple models, such as the SIA, all stresses except vertical shearing are neglected whereas in reality, in ice streaming areas, deformation of ice is mostly due to longitudinal and lateral stresses and the internal deformational energy therefore incorrectly estimated. The SIA is technically invalid in such areas and along ice sheet margins and ice divides in general (Baral et al., 2001). As the ratio between movement by sliding versus movement by internal deformation increases, the less accu-

rate the SIA becomes (Gudmundsson, 2003). Including HC sliding in such models, although physically still lacking, is nevertheless worthwhile as it entails a better representation of reality and delineation of ice-streaming areas.

5.4.2 SUBGLACIAL LAKES

Many subglacial lakes are predicted to have existed during the last glacial cycle (Fig. 5.6) and several of them seem to have persisted over thousands of years and reached considerable depths. Not many lakes seem to form in the Barents Sea itself, an area of active palaeo-hydrology research, as the bathymetry there is generally quite flat and smooth. The most likely locations for formation of subglacial lakes in the BS seem to be around Spitsbergenbanken and Central Barents Sea (Fig. 5.1). Many lakes forming there would likely have been 'active' lakes with low water depths, short residence times and fast circulation of water much like lakes in similar settings in West Antarctica (Gray, 2005; Fricker et al., 2007). Drainage could be frequent and possibly complete on decadal timescales or slower, in which case the lake roof would come in and out of contact with the underlying sediments, thus complicating the possibility of identifying them today from geological remains. These predictions however, should be taken with precaution as several of the locations could be related to geomorphological features on the seafloor, features related to the deglaciation of the area which would not have been present in its modern-day form during the time when a subglacial lake is predicted to have formed there.

Subglacial lakes represent areas of the ice sheet base, fixed at the pressure melting point and incapable of exerting any shear stress on the overlying ice. The ice therefore slides freely above it, being held back only by longitudinal and lateral stresses. As all stress components are generally important around subglacial lakes, the SIA approximation is unable to account for them in a satisfactory way. Ice generally moves more like an ice shelf over large lakes, with uniform velocity. Deformational and frictional heating thus largely disappear in the ice above them (Gudlaugsson et al., 2016). As the ice speeds up it gets drawn down by vertical flow at the edges and the ice surface tends to level above it. This effect that subglacial lakes have on the ice surface also affects the hydrological potential and it has been hypothesized that this surface levelling has a stabilizing effect on their presence through deglaciation cycles or changes in ice configuration (Livingstone et al., 2012). They are thus likely to persist once formed, and lakes can be found in places, after re-organisation of the ice sheet geometry, where no corresponding sink in the hydrological potential, based on coarse geometry data alone, can be estimated.

5.4.3 WATER STORAGE

Subglacial lakes accumulate and store considerable amounts of meltwater and some estimates put the amount of stored subglacial water in Antarctica at around 12000 – 24000 km³, equivalent to about 0.5 – 1 m thick water layer if spread out evenly underneath the entire Antarctic Ice Sheet (Pattyn, 2008). Typical basal melt rates are on the order of a few millimetres per year and the time it takes for the ice sheet to produce the amount of stored water is thus on the order of a few hundred to a thousand years. During the last 100 ka years of its existence, the Eurasian IS went through several phases of deglaciation followed by repeated regrowth until its final demise around 10 ka ago. Deglaciation typically occurs rapidly in comparison to growth and as we see in

its final stages, the ice sheet almost completely disappeared over a period of roughly a thousand years from 13 ka to 12 ka (Fig. 5.2). Such drastic changes in ice sheet geometry and state have profound influences on the subglacial hydrological system. Not only do basal melt rates peak during deglaciation phases, but there are also profound changes in the storage of subglacial water due to the reconfiguration of the ice sheet geometry and isostatic uplift. The amount of water draining from subglacial lakes can therefore drastically increase the output of subglacial water reaching the margin during deglaciation. The effect that this will have on ice sheet dynamics in general will depend on how the water is transported downstream, either in a channelized system or via a distributed system. Its effects would range from little to a potentially significant increase in average ice velocities as witnessed at Byrd Glacier in East Antarctica a decade ago (Stearns et al., 2008) with faster deglaciation pursuing.

5.5 CONCLUSIONS

Water enhanced sliding leads to both a drop in ice volume and thickness and due to increased advection of cold ice from above and less available deformational energy, the fraction of the bed at pressure melting is reduced. Several subglacial lakes are predicted to have existed underneath the Fennoscandian and the Barents Sea Ice sheets, some of which coincide with large surface lakes in Scandinavia at present. A considerable amount of water will have been stored in these lakes during glacial times and flushed out during deglaciation phases, potentially multiplying the amount of available subglacial water in motion. A simple thin-film water model is unable to capture the true nature of such an increase, as channel formation is excluded and all added water leads to faster sliding. The question remains, what effect such dynamic water storage in both lakes and sediment would have on ice dynamics in general and future modelling efforts will have to focus on not only more realistic models of ice and water flow but also on including dynamic storage of subglacial water.

ACKNOWLEDGEMENTS

Funding for this work came from the Research School in Arctic Marine Geology and Geophysics (AMGG) at the University of Tromsø and from the Research Council of Norway (RCN), Statoil, Det Norske ASA and BG group Norway (grant 200672) to the PetroMaks project “Glaciations in the Barents Sea area (GlaciBar)”, This is also a contribution to the Centre of Excellence: Arctic Gas Hydrate, Environment and Climate (CAGE) funded by RCN (grant 223259). We would like to thank two anonymous reviewers and the scientific editors for reviews and comments that helped improve the article.

6 SIMULATION OF THE FUTURE SEA LEVEL CONTRIBUTION OF GREENLAND WITH A NEW GLACIAL SYSTEM MODEL

CONTEXT

This paper introduces the new coupled model of the Greenland glacial system IGLOO (Ice sheet model for Greenland including Ocean and Outlet glaciers) and uses it to study the contribution of Greenland to sea level rise for future climate change scenarios. A subglacial hydrology model that always assumes that water flows in a thin film and that the effective pressure is zeros is used, despite the fact that the drainage system in Greenland is known to evolve into channels over the melt season. Though, for the long term ice velocities over multiple years this does not play a huge role, because the drainage system is adapting to the available water supply (Sole et al., 2013; Moon et al., 2014) and this study is interested in decadal time scales.

The aim of this study is to determine and better understand the processes that control the mass loss in Greenland. Therefore, the ice sheet model SICOPOLIS is coupled to the basal hydrology model HYDRO and to a plume model for submarine melt of outlet glaciers (Beckmann et al., 2018). The bi-directional coupling between SICOPOLIS and HYDRO is done similarly to the description in Section 3.2.3, but with a slightly different way of prescribing the maximum factor that increases basal sliding due to the water layer thickness. Here, it is formulated as a weighting factor c_w that ranges between 0 (no influence on sliding) and 0.9 (maximum influence, up to ten-fold increase). The regional atmosphere model MAR supplied the ice sheet model with the SMB and determined the surface runoff for the plume model.

Apart from the ice dynamics for which the hydrology model is used here, it also is required for supplying the total subglacial discharge for the plume model which determines submarine melt of exemplary selected outlet glaciers. Due to the lack of a supraglacial water model, the simple approximation is made that the surface runoff is directly transported to the ice base. Water that exits the ice sheet is allocated to the closest known outlet glacier (see Section 3.2.4 and 6.2.4).

CONTRIBUTION

In collaboration with Ralf Greve, I added the balance flux method in form of the module HYDRO to the polythermal ice sheet model SICOPOLIS. The main experiment design has been done by R. Calov, as well as the realization of the coupled ice model runs. Together with R. Calov, I determined the optimal sliding parameters. For the partitioning of the surface runoff and subglacial discharge, I used CIDRE and supplied J. Beckmann with monthly discharge values for her plume model. R. Calov prepared the manuscript with input of all co-authors.

AUTHORS AND AFFILIATIONS

Reinhard Calov¹, Sebastian Beyer^{1,2,3}, Ralf Greve⁴, Johanna Beckmann¹, Matteo Willeit¹, Thomas Kleiner², Martin Rückamp², Angelika Humbert^{2,3}, and Andrey Ganopolski¹

¹*Potsdam Institute for Climate Impact Research, Earth System Analysis, Potsdam, Germany*

²*Alfred Wegener Institute, Helmholtz Centre for Polar and Marine Research, Bremerhaven, Germany*

³*University of Bremen, Bremen, Germany*

⁴*Institute of Low Temperature Science, Hokkaido University, Sapporo, Japan*

ABSTRACT

We introduce the coupled model of the Greenland glacial system IGLOO 1.0, including the polythermal ice sheet model SICOPOLIS (version 3.3) with hybrid dynamics, the model of basal hydrology HYDRO and a parameterization of submarine melt for marine-terminated outlet glaciers. Aim of this glacial system model is to gain a better understanding of the processes important for the future contribution of the Greenland ice sheet to sea level rise under future climate change scenarios. The ice sheet is initialized via a relaxation towards observed surface elevation, imposing the palaeo-surface temperature over the last glacial cycle. As a present-day reference, we use the 1961-1990 standard climatology derived from simulations of the regional atmosphere model MAR with ERA reanalysis boundary conditions. For the palaeo-part of the spin-up, we add the temperature anomaly derived from the GRIP ice core to the years 1961-1990 average surface temperature field. For our projections, we apply surface temperature and surface mass balance anomalies derived from RCP 4.5 and RCP 8.5 scenarios created by MAR with boundary conditions from simulations with three CMIP5 models. The hybrid ice sheet model is fully coupled with the model of basal hydrology. With this model and the MAR scenarios, we perform simulations to estimate the contribution of the Greenland ice sheet to future sea level rise until the end of the 21st and 23rd centuries. Further on, the impact of elevation–surface mass balance feedback, introduced via the MAR data, on future sea level rise is inspected. In our projections, we found the Greenland ice sheet to contribute to global sea level rise between 1.9 and 13.0 cm until the year 2100 and between 3.5 and 76.4 cm until the year 2300, including our simulated additional sea level rise due to elevation–surface mass balance feedback. Translated into additional sea level rise, the strength of this feedback in the year 2100 varies from 0.4 to 1.7 cm, and in the year 2300 it ranges from 1.7 to 21.8 cm. Additionally, taking Helheim and Store Glaciers as examples, we investigate the role of ocean warming and surface runoff change for the melting of outlet glaciers. It shows that ocean temperature and subglacial discharge are about equally important for the melting of the examined outlet glaciers.

6.1 INTRODUCTION

Since the last decade of the 20th century, the Greenland ice sheet (GrIS) loses mass with accelerating speed (e. g. Helm et al., 2014; Talpe et al., 2017), shaping one of the most important contributors to sea level rise (Shepherd et al., 2012; Rietbroek et al., 2016; Forsberg et al., 2017). This mass loss is not only driven by decreasing surface mass balance but also by increasing ice discharge via outlet glaciers. The partition between these two contributions to GrIS mass loss is about equal (Rignot et al., 2011a; Box and Colgan, 2013; Enderlin et al., 2014; Broeke et al., 2016). Understanding the processes determining the GrIS ice loss is vital for estimates of its contribution to future sea level rise.

Nowadays, the scientific community recognizes the large Greenland island as a complex system mainly composed of the ice sheet and numerous outlet glaciers (Joughin et al., 2010; Rignot and Mouginot, 2012), in subtle interaction with the surrounding ocean via fjord circulation (Straneo et al., 2012; Murray et al., 2010), and uprising meltwater plumes in an interplay with the calving outlet glaciers (O’Leary and Christoffersen, 2013). In our paper, we introduce the model IGLOO (Ice sheet model for Greenland including Ocean and Outlet glaciers, Fig. 6.1) intended to represent the major processes important for the future mass changes of the GrIS on timescales of some centuries. The idea of this model is to capture the complexity of the system by its involved model components and, at the same time, to treat the description of all single components as detailed as necessary (Claussen et al., 2002). We aim to have a tool with sufficient computational efficiency to enable large ensemble simulations on timescales important for future climate change. Knowl-

Table 6.1: Abbreviations in Fig. 6.1.

Abbreviations	Physical meaning
z_0	Observed present-day elevation of GrIS
z	Simulated elevation of ice sheet
ΔT_{GRIP}	Reconstruction of temperature anomaly from GRIP ice core
ΔT_s	Anomaly of surface temperature simulated by MAR
ΔM	Anomaly of surface mass balance simulated by MAR
ΔR	Anomaly of runoff simulated by MAR
T_s	Surface temperature
M	Surface mass balance
R	Surface runoff
Q	Subglacial discharge into the given fjord
B	Bottom melt simulated by SICOPOLIS
W	Thickness of basal water layer
T	Ocean temperature (function of depth)
S	Ocean salinity (function of depth)
d	Submerged part of the outlet glaciers
M_s	Submarine melt of the outlet glaciers

edge of the present-day state of the GrIS has been improving considerably. Not only that there are reliable data from numerous observations (e. g. Velicogna and Wahr, 2005; Bales et al., 2009;

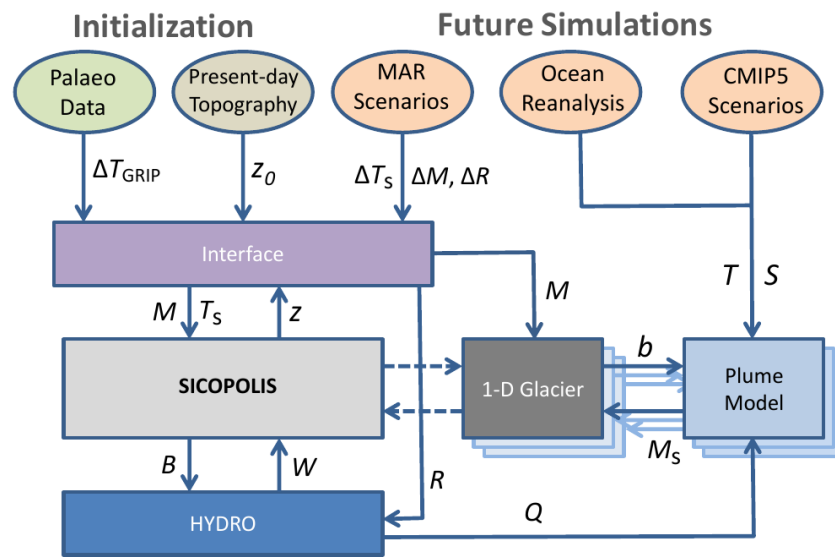


Figure 6.1: Flow diagram of the model IGLOO and the interaction between its components. The 1-D outlet glacier and plume models are generic models, i.e. they can be applied to each outlet glacier of the Greenland ice sheet. Coupling between the ice sheet model and the generic outlet glacier models is not implemented yet, denoted by dashed arrows. In this paper, coupling between HYDRO and the plume model is off-line. Simulations with the coupled generic outlet glacier models and plume models as well as details on the coupling between them are described in Beckmann et al. (2018). The exchange variables are explained in Table 6.1.

Morlighem et al., 2014), but also several modelling studies exist. Present-day GrIS velocities are resolved by ice sheet models in horizontal resolutions as high as 600 m, including flow patterns of outlet glaciers (Aschwanden et al., 2016). Robinson et al. (2012) explicitly demonstrated the multistable-hysteresis behaviour of the GrIS with a threshold of 1.6 °C above present-day global temperature for the decay of the GrIS; although such a decay will last at least about 1000 years. The past climate is an important element for GrIS ice sheet modelling as well, as it serves as constraint for parameters particularly capturing the present-day GrIS (Robinson et al., 2011; Stone et al., 2013) and as it provides the history of the temperature field inside the present-day GrIS (Goelzer et al., 2013), which is important for the initialization of the GrIS in future warming simulations. However, palaeo-simulations with free surface have the drawback that their resulting present-day ice thickness can differ considerably from observations (e. g. Calov et al., 2015). Such a simulated ice thickness is an unfavourable initial condition for projections because, in this case, the future simulation would start with ice which resides at the wrong locations or is absent at positions where it should reside according to observations. This leads to an erroneous drift in projected ice volume evolution. Therefore, we opt for a fixed domain approach (Calov and Hutner, 1996) in our palaeo-spin-ups or, more precisely, for a scheme that relaxes the simulated surface elevation towards the observed one (Aschwanden et al., 2013). This approach has the advantage that it provides a good approximation of present-day temperature-velocity field for initialization and at the same time prevents a spurious response in volume during future simulations of several hundred years. Different initialization methods are discussed by Saito et al. (2016).

There are several approaches to project future ice mass change of the GrIS, often with a special focus on a certain component of the Greenland glacial system. Classical surface mass balance approaches assume a passive ice sheet, but resolve the atmosphere with general circulation models of the atmosphere (e. g. Gregory and Huybrechts, 2006) or additionally with a regional model (Angelen et al., 2012; Rae et al., 2012; Fettweis et al., 2013). Several pioneering studies used three-dimensional dynamic ice sheet models in the shallow ice approximation (SIA) for projections of GrIS sea level contribution (e. g. Huybrechts and Wolde, 1999; Greve, 2000). Later, higher-order (Fürst et al., 2013) or even full-Stokes (Gillet-Chaulet et al., 2012; Seddik et al., 2012) ice dynamics was included for GrIS future projections. In a higher-order ice sheet model, Fürst et al. (2015) parameterizes ice sliding via ocean-temperature rise due to future climate change to investigate the impact of ocean warming on future projections of GrIS sea level contribution. Studies with an atmosphere-ocean general circulation model coupled to a SIA ice sheet model via surface-energy fluxes were undertaken by Vizcaino et al. (2015). Inspections of GrIS sea level contribution with a special focus on outlet glaciers were accomplished with a 3-D ice sheet model by Peano et al. (2017) or with a 1-D shallow shelf model (Nick et al., 2013).

Here, we opt for the new version of SICOPOLIS v3.3 (Bernales et al., 2017). This version includes hybrid dynamics, which incorporates via the shelfy stream approximation (SSStA; MacAyeal, 1989) longitudinal and lateral stresses, which are important for nearer-margin fast flow areas, along with horizontal plane shear (Hindmarsh, 2004) via the shallow ice approximation (SIA), important for the slow-flow regions in the more central regions of the ice sheet. Hybrid models have been developed before by Pollard and DeConto (2007), Pollard and DeConto (2012), Bueller and Brown (2009), Hubbard et al. (2009), Winkelmann et al. (2011), Fürst et al. (2013), and Pattyn (2017). They are a compromise between the shallow ice approximation and the full-Stokes approach. Key of these hybrid models is that SIA and SSStA operate on a common domain, although

there are other approaches to treat longitudinal and lateral stresses (Ritz et al., 2001). Compared to the SIA, the hybrid dynamics is more promising in reproducing the velocity field of the GrIS in the catchment area of ice streams, where there is already fast flow (Rignot and Mouginot, 2012). Although SICOPOLIS v3.3 has such an option, we do not apply ice-shelf dynamics in the model setting of SICOPOLIS in this study, because dynamics of outlet glaciers, which can have a floating tongue, is part of the outlet glacier component of IGLOO. With the IGLOO model, we investigate the response of GrIS outlet glaciers to global warming including ocean warming in a separate paper (Beckmann et al., 2018).

Models assuming a basal water layer for treatment of subglacial hydrology (Shreve, 1972) were often applied to the Antarctic ice sheet (Le Brocq et al., 2009; Kleiner and Humbert, 2014). Here, we apply such a model to the GrIS, because it captures the major pathways of basal water toward the outlet glaciers (Livingstone et al., 2013), i. e. the model resolves in a good approximation the partition of basal water for the main GrIS outlet glaciers. This is important for reproducing the subglacial discharge of outlet glaciers, which is fed into our model of meltwater plumes. Further on, our model for basal hydrology simulates a thickening of the basal water layer toward the major GrIS outlet glaciers, regions over which the ice velocity becomes higher (Rignot and Mouginot, 2012). Therefore, we couple the ice velocities to the basal water layer, while the basal melt rate of the ice sheet model provides the input to the model of basal hydrology. We expect this approach to be suitable for large-scale modeling of ice sheets on decadal timescales.

Simulating submarine melt rates at tidewater glaciers has been accomplished with different models that all share the core of the buoyant-plume theory (Sciascia et al., 2013; Xu et al., 2013; Slater et al., 2015; Carroll et al., 2015; Cowton et al., 2015; Slater et al., 2017). Recent studies (Jackson et al., 2017; Beckmann et al., 2018) show that the line plume model by Jenkins (2011) is an adequate tool to determine submarine melt rates for tidewater glaciers. In our paper, we apply a recently developed line plume model (Beckmann et al., 2018) after the equations of Jenkins, 2011 to two outlet glaciers, Store and Helheim Glaciers (Fig. 6.2), of the Greenland ice sheet. We have chosen Helheim and Store Glaciers for investigating the impact of future warming on glacier melt and for testing our methods because they are well examined glaciers. Numerous studies on these glaciers and their connecting fjord systems to the open ocean exist (Straneo et al., 2011; Sutherland and Straneo, 2012; Rignot et al., 2015; Jackson et al., 2014; Chauché et al., 2014). Some provide data on temperature- and salinity profiles inside the fjord from conductivity-temperature-depth (CTD) measurements or moorings.

We start with a description of the elements of the glacial system model IGLOO 1.0, including the future and past forcings utilized in our paper (Section 6.2). In Section 6.3, we describe our initialization method, while Section 6.4 compares the simulated present-day surface elevation and velocity with observations. Further on, modelled basal properties are compared with findings of other works. In Section 6.5, we present projections of GrIS sea level contribution, of GrIS total basal and surface runoff and of the submarine melt rates for two GrIS outlet glaciers (Store and Helheim Glaciers). The paper closes with a discussion (Section 6.6) and the conclusions (Section 6.7).

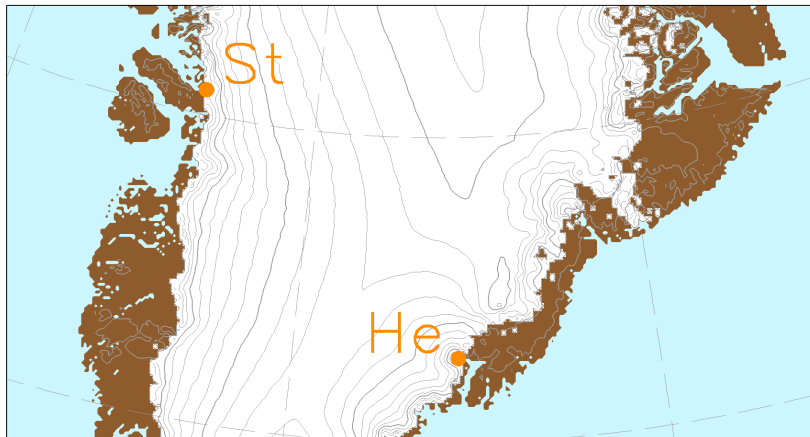


Figure 6.2: Geographical position of the outlet glaciers mentioned in the main text. “St” indicates location of Store Glaciers, while “He” marks position Helheim glacier.

6.2 ICE SHEET MODEL FOR GREENLAND INCLUDING OCEAN AND OUTLET GLACIERS (IGLOO), VERSION 1.0

6.2.1 ICE SHEET MODEL SICOPOLIS VERSION 3.3

SICOPOLIS (SIMulation COde for POLythermal Ice Sheets; www.sicopolis.net) is a dynamic/thermodynamic ice sheet model that was originally created by Greve (1995) and Greve (1997) in a version for the GrIS. Since then, SICOPOLIS has been developed continuously and applied to problems of past, present and future glaciation of Greenland (e.g., Robinson et al., 2011), Antarctica (e.g., Kusahara et al., 2015), the Eurasian ice sheet including subglacial water (Gudlaugsson et al., 2017), the entire Northern hemisphere (Ganopolski and Calov, 2011), the polar ice caps of the planet Mars and others (see www.sicopolis.net/publ for a comprehensive publication list). The description given here follows Greve et al. (2017) very closely.

The model simulates the large-scale dynamics and thermodynamics (ice extent, thickness, velocity, temperature, water content and age) of ice sheets three-dimensionally and as a function of time. It is based on the shallow ice approximation for grounded ice (Hutter, 1983; Morland, 1984) and the shallow shelf approximation for floating ice (Morland, 1987; MacAyeal, 1989). Recently, hybrid shallow-ice/shelfy-stream dynamics has been added as an option for ice streams (Bernales et al., 2017). The rheology is that of an incompressible, heat-conducting, power-law fluid (Glen’s flow law; e.g., Greve and Blatter, 2009).

A particular feature of SICOPOLIS is its very detailed treatment of ice thermodynamics. A variety of different thermodynamics solvers are available, namely the polythermal two-layer method, two versions of the one-layer enthalpy method, the cold-ice method and the isothermal method (Greve and Blatter, 2016). The polythermal and enthalpy methods account in a physically adequate way for the possible co-existence of cold ice (with a temperature below the pressure-melting point) and temperate ice (with a temperature at the pressure-melting point) in the ice body, a con-

dition that is referred to as “polythermal”. It is hereby assumed that cold ice makes up the largest part of the ice volume, while temperate ice exists as thin layers overlying a temperate base. In the temperate ice layers, the water content is computed, and its reducing effect on the ice viscosity is taken into account (Lliboutry and Duval, 1985).

SICOPOLIS is coded in Fortran and uses finite difference discretization techniques on a staggered Arakawa C grid, the velocity components being taken between grid points (Arakawa and Lamb, 1977). For solving the thickness evolution equation, we added a further option to the SICOPOLIS code (Appendix 6.8.1). The simulations of the GrIS discussed here are carried out in a stereographic plane (WGS 84 reference ellipsoid, standard parallel 71°N, central meridian 39°W), spanned by the Cartesian coordinates x and y . The coordinate z points upward.

6.2.2 SUBGLACIAL HYDROLOGY MODEL HYDRO

HYDRO is a diagnostic model that determines the subglacial water fluxes instantaneously via the hydrological potential Φ , which depends on the elevation potential and the water pressure p_w (Shreve, 1972):

$$\Phi = \rho_w g b + p_w, \quad (6.1)$$

with the ice base b , acceleration due to gravity g and density of water $\rho_w = 1000 \text{ kg m}^{-3}$. The water pressure depends on the ice overburden pressure and the effective pressure N (normal stress at the bed minus water pressure):

$$p_w = \rho_i g H - N, \quad (6.2)$$

wherein $\rho_i = 910 \text{ kg m}^{-3}$ is the density of ice and H is the ice thickness.

Following previous authors such as Le Brocq et al. (2009) and Livingstone et al. (2013), we assume the water moving in a thin (a few mm) and distributed water film. Under this premise, the water pressure and the ice overburden pressure are in equilibrium and therefore the effective pressure is zero. This enables us to reformulate Eq. (6.1) as

$$\Phi = \rho_w g b + \rho_i g H, \quad (6.3)$$

and then computing the water flux with a simple flux routing scheme as described by Le Brocq et al. (2006). This approach is only valid at large (km) scales and is not able to include local processes such as channels.

The flux routing method requires that every cell has a defined flow direction and that, by successively following these directions, the boundary of the study area is reached. Therefore, local sinks and flat areas must be removed prior to applying the routing scheme. We accomplish this by using a Priority-Flood algorithm as described in Barnes et al. (2014b), which fills depressions in a single pass and then add a small gradient to the resulting flats. Adding a gradient towards the outlet of the depression ensures that the hydraulic potential is altered in the smallest possible way. This procedure is a very efficient way to guarantee that all water is drained into the ocean.

The hydraulic potential is computed following Eq. 6.1, and we use the basal melt rates from SICOPOLIS as the water input for the routing scheme (see Section 6.2.4). The timescales of the water flow are much smaller than for the ice flow, thus, the steady-state water flux ψ_w can be obtained by integrating the basal melt rate along the hydraulic potential.

From the resulting water flux ψ_w , we can compute the water layer thickness W (Weertman, 1972; Weertman, 1966):

$$W = \left(\frac{12\mu_w\psi_w}{\text{grad } \Phi} \right)^{1/3}. \quad (6.4)$$

At locations where sinks in the hydraulic potential have been filled, we set W to a very high value (10 m) to account for the presence of a subglacial lake.

6.2.3 MELTWATER PLUME MODEL

A further element of IGLOO is the line plume model by Beckmann et al. (2018) (after Jenkins (2011)). It simulates the width-averaged submarine melt rate of a glacier and accounts for a uniformly distributed subglacial discharge along the grounding line. The plume model describes buoyancy-driven rise of subglacial meltwater until it reaches either neutral buoyancy or the water surface. Two counteracting processes control the maintenance or reduction of the plume buoyancy: submarine melting at the ice-ocean interface preserves the plume buoyancy, while simultaneously turbulent entrainment and mixing with the surrounding salty fjord water reduces it. The line plume equations are derived under the assumption that the plume is in equilibrium and are thus time-independent. The melt rate is determined by the plume velocity and temperature, which adapts to the boundary conditions along the glacier front or under the floating tongue. As input parameters, it requires the submerged part of the glacier front d and the subglacial discharge Q that leaves the glaciers grounding line over the whole glacier width, and a temperature-salinity depth (TSD) profile close to the glacier. The determination of the input parameters of the plume model is described in section 6.2.4.

6.2.4 COUPLING OF MODEL COMPONENTS

COUPLING OF SICOPOLIS WITH HYDRO

We use a slightly modified version of the Weertman-type sliding law proposed by Kleiner and Humbert (2014) to couple the basal hydrology model to the ice dynamics:

$$\mathbf{v}_b = -f_b C_b |\tau_b|^{p-1} \tau_n^{-q} \tau_b, \quad (6.5)$$

with the sliding velocity \mathbf{v}_b , basal sliding parameter C_b , basal shear stress τ_b , basal normal pressure τ_n (assumed as the ice overburden pressure) and the stress and pressure exponents $p = 3$ and $q = 2$. We introduce the dimensionless factor

$$f_b = f_T ((1 - c_w) + c_w f_w), \quad c_w \in [0, 0.9], \quad (6.6)$$

with

$$f_T = \exp\left(\frac{T - T_{\text{pmp}}}{\nu}\right) \quad \text{and} \quad f_w = \left(1 - \exp\left(-\frac{W}{W_0}\right)\right), \quad (6.7)$$

where f_T and f_w incorporate sub-melt sliding and basal hydrology respectively. Sub-melt sliding allows sliding below the pressure melting point T_{pmp} according to the decay parameter ν (Hind-

marsh and Le Meur, 2001), whereas the basal hydrology term depends on the water layer thickness W divided by a typical scale of the layer thickness W_0 .

The parameter c_w in Eq. 6.6 is a weighting factor between “background sliding” – determined by C_b – and enhanced sliding due to the basal water layer. Using $c_w = 0$ yields the standard model without any effect of basal hydrology, while $c_w = 0.9$ leads to the same expression as Kleiner and Humbert (2014). In our simulation with basal hydrology, we apply their parameter value, i. e. we set $c_w = 0.9$, while we specify the typical scale of the layer thickness by $W_0 = 0.005$ m. Further, our decay parameter is $\nu = 1^\circ\text{C}$.

The coupling is bi-directional. Basal melt B (including the water drainage from the temperate basal layer of the ice sheet) computed by SICOPOLIS is used to calculate the thickness of the basal water layer in HYDRO, which in turn affects the basal sliding (Eq. 6.7). Components and data exchange of the complete coupled model IGLOO are illustrated in Fig. 6.1.

OFF-LINE COUPLING OF SICOPOLIS AND HYDRO WITH THE PLUME MODEL

We establish a procedure of determining submarine melt rates with our line plume model (Section 6.2.3) for all Greenland outlet glaciers. This procedure applies only off-line yet, i. e., the input and output of the model components are exchanged manually via data files. To clarify, as this coupling is off-line, the sliding of ice (Section 6.2.4) is affected solely by basal melt, while the surface melt and basal melt can impact the meltwater plume.

For the subglacial discharge required by the plume model, we use HYDRO to route both the basal melt of SICOPOLIS and the surface runoff by MAR as basal water to the grounding lines of the outlet glaciers. We route on a monthly timescale to resolve seasonality. For the surface runoff, we assume that it penetrates directly down to the bedrock. Among others, Rignot and Mouginot (2012) provides data of the geographical position of many outlet glaciers. We use these data to allocate the water which leaves the ice sheet to individual outlet glaciers.

Although we simulate future scenarios, the grounding line position is considered to be fixed for this procedure. Of course, for glaciers close to another that share the same catchment area, a moving grounding line position might have severe effects. We will account for these dynamic glacier processes in the next version of IGLOO.

6.2.5 EVALUATING THE DATA FROM THE REGIONAL ATMOSPHERE MODEL MAR

The ice sheet model needs the mean annual surface temperature and surface mass balance (SMB) as climate forcings at the surface. In addition, the plume model requires monthly runoff. Here, we explain how we derive these forcing fields and their gradients from data of simulations by the MAR regional climate model (Fettweis et al., 2013). These fields and their gradients serve to define our climate forcing for the past (Section 6.2.6) and for the future (Section 6.2.7 and 6.2.8).

Historical MAR simulations using different climate reanalysis products to define the boundary conditions for the regional simulations are available. The boundary conditions for MAR future projections up to 2100 are provided by the output of several CMIP5 general circulation models for different RCP scenarios. Since the MAR simulations are performed for fixed surface elevation of the GrIS and we expect substantial changes in the ice elevation under future warming scenarios, we correct the regional model output for the change in surface elevation by applying the gradient method of Helsen et al. (2012). In their method, they derived a representative local elevation

gradient of the SMB in each grid point from a regression of simulated SMB and surface elevation within a given radius. Helsen et al. (2012) did this separately for accumulation and ablation regimes. Here, we extend their method by applying it also to surface temperature and runoff. The search radius is set to 100 km, but is extended until it includes at least 100 grid points, if necessary. For the surface mass balance, we apply the gradient method only to the ablation regime, because the regression is in many cases not well defined for the accumulation regime (Helsen et al., 2012). Therefore, we set the SMB elevation gradient for the accumulation regime to zero.

6.2.6 PAST CLIMATE FORCING AND IMPLIED SMB OF THE GRIS

Our past climate forcing consists of the surface temperature and the surface mass balance. By running the model over one glacial cycle, we determine an initial temperature-velocity field for our future warming scenarios. In particular, we yield the implied SMB for present day, which is used in our future simulations as the climatological present-day SMB.

The surface temperature for the past simulation is computed from the sum of the climatological field of the present-day surface temperature simulated by MAR, the temperature anomaly from the GRIP ice core and our temperature elevation correction obtained from the present-day MAR simulations:

$$T_s(x, y, t) = T_{s \text{ MAR(rea)}}^{\text{Clim 1961-1990}}(x, y) + \Delta T_{\text{GRIP}}(t) + \left(\frac{\partial T_s}{\partial z} \right)_{\text{MAR(rea)}}^{\text{Clim 1961-1990}} \Delta z(x, y, t). \quad (6.8)$$

The elevation correction in the last term of Eq. 6.8 is the surface temperature elevation gradient (Section 6.2.5) from the MAR reanalysis data times a surface elevation difference, which reads

$$\Delta z(x, y, t) = z(x, y, t) - z_0(x, y), \quad (6.9)$$

with the surface elevation z , simulated with the ice sheet model SICOPOLIS, and the observed surface elevation z_0 . For the observed surface elevation, we use the one by Bamber et al. (2013), which is the same as that utilized by Fettweis et al. (2013).

Here, the surface mass balance M is defined by relaxing the ice sheet's surface elevation towards the observed surface elevation as

$$M(x, y, t) = \frac{z_0(x, y) - z(x, y, t)}{\tau_{\text{relax}}}, \quad (6.10)$$

where τ_{relax} is a relaxation constant. With this relaxation method, we follow Aschwanden et al. (2013) and Aschwanden et al. (2016). Outside the ice sheet, we assign the high negative value of $M = -1000$ m ice/yr, which prevents the ice to flow outside its domain. With these forcings, we run the model over one glacial cycle. When the model reaches its present-day state ($t = 0$), we yield the implied SMB M_{impl} which is used in future simulations as

$$M_{\text{impl}}(x, y) := M(x, y, 0). \quad (6.11)$$

Through Eq. 6.10, the simulated surface elevation tends to approach the observed one, with a strength determined by $1/\tau_{\text{relax}}$. To make it clear, the implied SMB is the result of an iteration

and this SMB field corresponds approximately to the observed SMB but compensating for errors of the ice sheet model.

Just to note, if τ_{relax} equalled the scheme's time step for its ice sheet topography, the simulated surface elevation would fully match the observed one. This would correspond to a fixed domain, or more precisely, to a fixed surface simulation.

We made here the following simplifications: (1) We ignored changes in elevation and spatial extent of the GrIS during the past glacial cycle, (2) we assumed that the GRIP temperature record can be applied to the entire GrIS and (3) we assumed that the derived present-day elevation correction is valid for the entire glacial climate state.

Outputs of this procedure are the present-day implied SMB and a full nearly present-day topography set (surface and bedrock elevation) belonging to this implied SMB. Later on, the present-day implied SMB field is added to the anomaly forcing of future climate simulations (see Eq. (6.13)).

6.2.7 FUTURE CLIMATE FORCING OF THE GRIS

The surface temperature forcing is computed from the climatological temperature of MAR simulations for 1961–1990 forced by the ERA reanalysis boundary conditions, the anomalies from MAR simulations forced by CMIP5 model output and a temperature elevation correction as:

$$T_s(x, y, t) = T_s^{\text{Clim 1961–1990}}_{\text{MAR(rean)}}(x, y) + (T_s^{\text{MAR(CMIP5)}}(x, y, t) - T_s^{\text{Clim 1961–1990}}_{\text{MAR(CMIP5)}}(x, y)) + \left(\frac{\partial T_s}{\partial z} \right)_{\text{MAR(CMIP5)}}(x, y, t) \Delta z(x, y, t). \quad (6.12)$$

Here, the temperature elevation correction is determined via the product of the surface temperature elevation gradient (Section 6.2.5) of the MAR model with boundary condition from the CMIP5 models and the elevation anomalies simulated with the ice sheet model SICOPOLIS. As for the palaeoclimate, $\Delta z(x, y, t)$ are the simulated surface elevation anomalies (Eq. 6.9).

The SMB for future projections is computed as the sum of the implied SMB, simulated SMB anomalies relative to the reference period 1961–1990 and an elevation SMB correction as follows:

$$M(x, y, t) = M_{\text{impl}}(x, y) + (M_{\text{MAR(CMIP5)}}(x, y, t) - M_{\text{MAR(CMIP5)}}^{\text{Clim 1961–1990}}(x, y)) + \left(\frac{\partial M}{\partial z} \right)_{\text{MAR(CMIP5)}}(x, y, t) \Delta z(x, y, t). \quad (6.13)$$

Similar to temperature, the elevation SMB correction is calculated from the SMB elevation gradient of the MAR model with boundary condition from the CMIP5 models, multiplied by the simulated surface elevation anomalies.

Surface runoff is computed for each month from the climatological runoff of MAR simulations for 1961–1990 forced by the ERA reanalysis boundary conditions, the anomalies from MAR sim-

ulations forced by CMIP5 models output and a runoff elevation correction, which again is computed similarly to the temperature elevation correction:

$$R(x, y, t) = R_{\text{MAR}(\text{rean})}^{\text{Clim } 1961-1990}(x, y) + (R_{\text{MAR}(\text{CMIP5})}(x, y, t) - R_{\text{MAR}(\text{CMIP5})}^{\text{Clim } 1961-1990}(x, y)) + \left(\frac{\partial R}{\partial z} \right)_{\text{MAR}(\text{CMIP5})}(x, y, t) \Delta z(x, y, t). \quad (6.14)$$

Negative runoff values, which can result from this approach, are set to zero.

Figure 6.3 shows time series derived from the MAR data. During the 20th century, all curves show rather minor changes in average, besides a visible climate variability. This is in line with general knowledge (e.g. Box et al., 2009; Box and Colgan, 2013). The climate sensitivity is strongest for CanESM2, weakest for NorESM1, and MIROC5 lies in between. Of course, these 21st century warming trends correspond to IPCC AR5 (Collins et al., 2013) because the MAR forcing is from the CMIP5 models. The annual average temperature change over Greenland is stronger than the global one.

Over the years 1900-1949 MAR provides data only for MIROC5 and after the year 2100 MAR does not provide data for any of the GCMs used. However, since we need forcing for the years 1900-2300, we filled the gaps by means of an extrapolation procedure, which is described in detail in Appendix 6.8.2.

6.2.8 FUTURE CLIMATE FORCING OF THE PLUME MODEL

As future forcing of the plume model, we employ the subglacial discharge from HYDRO and SICOPOLIS (Section 6.2.4) under the RCP 8.5 scenario (Section 6.2.7) from MAR with MIROC5 only. Additionally, a scenario of the temperature and salinity profiles is needed to project future submarine melting. Even for the present day, measurements inside fjords are rare and do not cover all of Greenland's fjords. We use CTD profiles close to the glaciers obtained for the year 2016 for Store Glacier (data from NASA's OMG mission(<https://omg.jpl.nasa.gov/portal/>)) and the year 2012 for Helheim Glacier (Carroll et al., 2016). For the ocean warming scenario, we assume a linear temperature trend of 0.03 °C per year over the years 2000–2100 for the entire profiles.

The 3 °C ocean warming in 100 years lies in the upper range found by Yin et al. (2011) for SE and W Greenland. The determined temperature and salinity profiles, in combination with the HYDRO output, serve as the input parameters for the line plume model to determine present and future submarine melting for the Greenland outlet glaciers.

6.3 MODEL INITIALIZATION VIA PALAEO-RUNS

For the initialization of the ice sheet model, we use the forcings for the surface temperature and the surface mass balance as described in Section 6.2.6. Here, isostatic depression and rebound of the lithosphere due to changing ice load is modelled assuming a local lithosphere with relaxing asthenosphere with an isostatic time lag (LLRA approach, Le Meur and Huybrechts, 1996). For the geothermal heat, we use the spatial dependent data by Purucker (2012a). In order to cover one full glacial cycle, we run the model over 135 kyrs. Initial conditions of these runs are the present-day ice thickness and elevation by Bamber et al. (2013). The original data with 1 km × 1

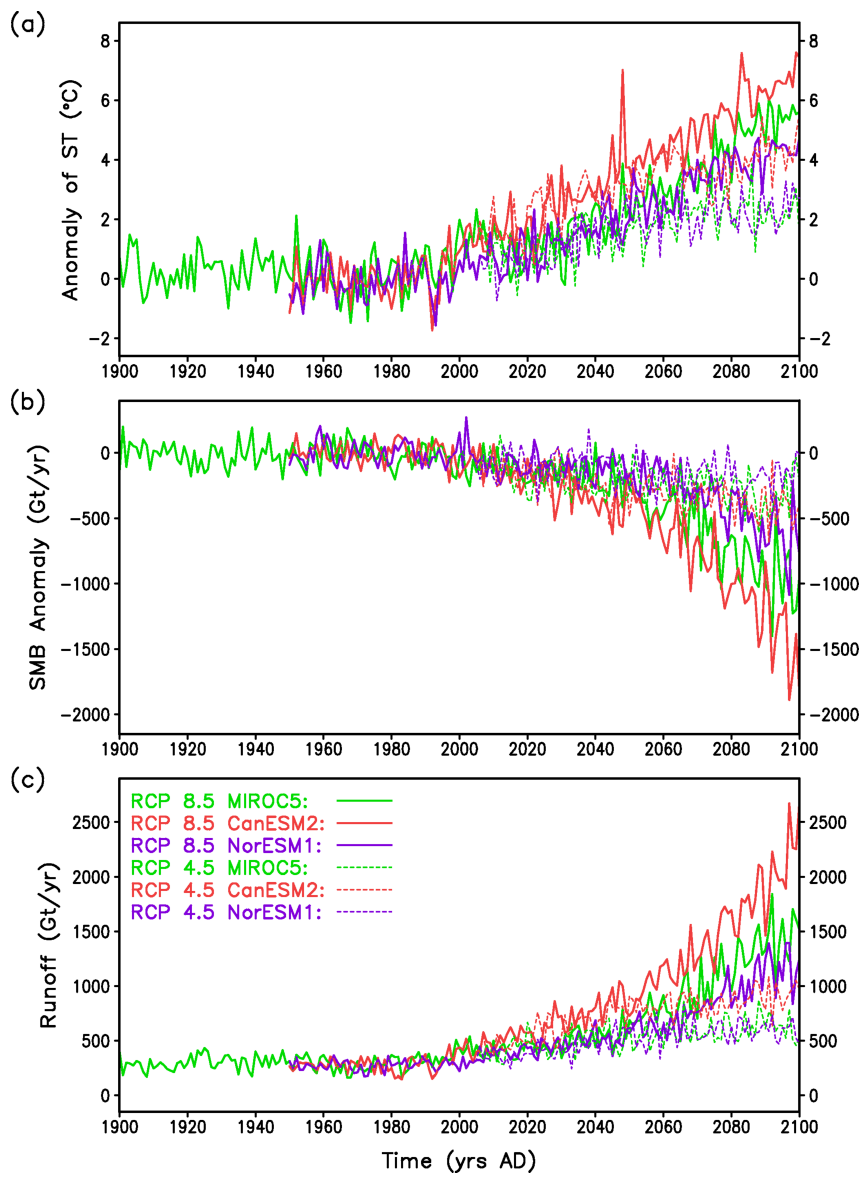


Figure 6.3: Forcings derived from the MAR regional model. (a) Anomaly of annual average surface temperature, (b) total annual surface mass balance anomaly, and (c) total annual runoff. Anomalies are taken with respect to the period 1961–1990 from the respective CMIP5 models. RCP 8.5 scenarios are indicated by the solid lines, while RCP 4.5 scenarios are shown by the dashed lines.

km horizontal resolution are downsampled to $5 \text{ km} \times 5 \text{ km}$ and $10 \text{ km} \times 10 \text{ km}$ grid spacings. To perform a simulation in $5 \text{ km} \times 5 \text{ km}$ horizontal resolution over the entire glacial cycle with the hybrid model is illusive, as it takes 1 day for 100 model years on one HLR2015 Lenovo NeXtScale nx360M5 processor. Therefore, we opt to perform the first 130 kyrs of the glacial cycle in $10 \text{ km} \times 10 \text{ km}$ horizontal resolution with the classical shallow ice approximation (SIA) employing the diffusivity method with an over-implicit ice-thickness solver. The last 5 kyr of the palaeo-run are performed in $5 \text{ km} \times 5 \text{ km}$ horizontal resolution. As we use different model hierarchies and settings, we devote some more explanation to these last 5 kyr.

During the last 5 kyrs of the run, we have three switches: one for refining the horizontal resolution, one for switching from SIA mode to hybrid mode, and a further one for switching from relaxing ice surface to free ice surface. The first switch at 5 kyr BP refines the horizontal resolution of the model from $10 \text{ km} \times 10 \text{ km}$ to $5 \text{ km} \times 5 \text{ km}$. The second switch at 500 years BP changes from SIA to hybrid mode and additionally applies the mass conservation scheme for the evolution equation of ice thickness (Eq. 6.15). The third switch, which releases the relaxing ice surface to free development, is imposed at 100 years BP (year 1900). We introduced this switch 100 years earlier than the start of our future sea level scenarios (Section 6.5.1) in order to avoid spurious trends in ice volume change in our scenarios, which can happen when the ice sheet is released to free surface evolution suddenly.

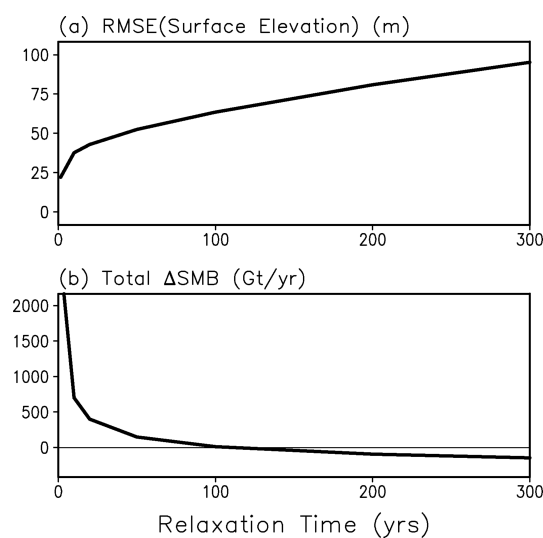


Figure 6.4: Total ice sheet quantities against relaxation constant. (a) Root mean square error (RMSE) of modelled to observed surface elevation. (b) Total difference between our simulated surface mass balance and the surface mass balance from the regional model MAR using ERA reanalysis 1961–1990 climatology.

The choice of the relaxation constant rests on numerous simulations in $10 \text{ km} \times 10 \text{ km}$ horizontal resolution in SIA mode, running the model over one glacial cycle until the present day. Figure 6.4 shows the root mean square error (RMSE) in surface elevation and the total difference in SMB (the total implied SMB over the GrIS minus the total SMB simulated by MAR). With increasing relaxation constant, the RMSE in surface elevation increases moderately, while the total

difference in SMB decreases strongly, i. e., there is a tradeoff between the RMSE in elevation and the total difference in SMB.

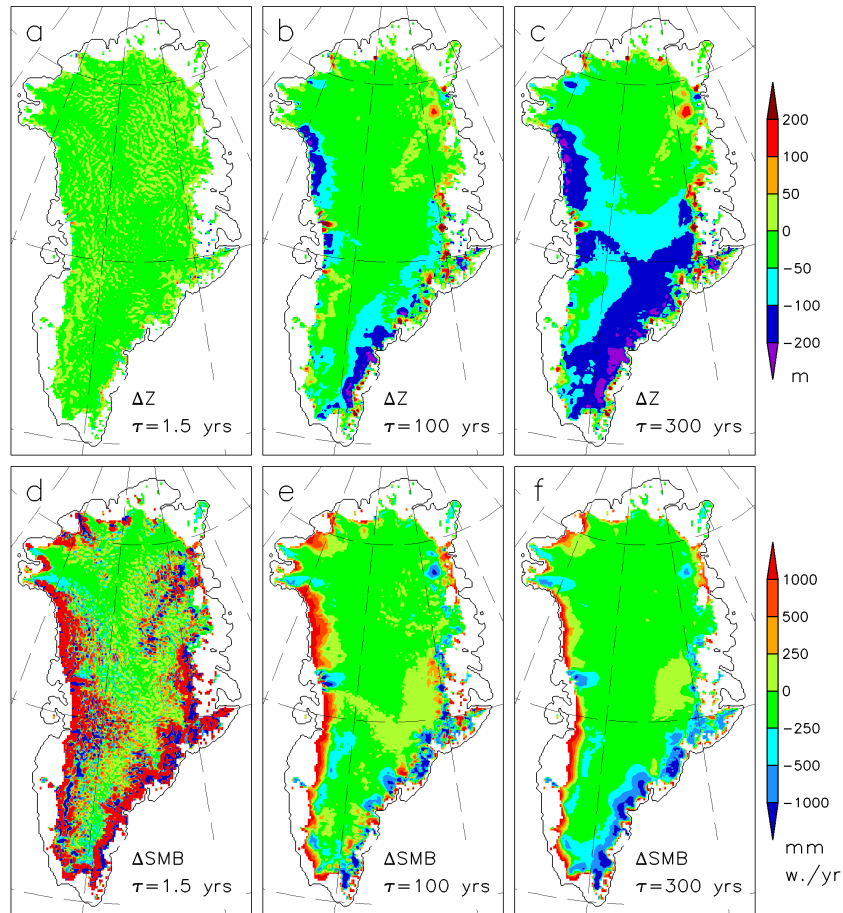


Figure 6.5: Differences between simulated and observed present-day 2-D fields for various relaxation constants, i. e., 1.5, 100 and 300 years. (a), (b) and (c): deviation of surface elevation from observed. (d), (e) and (f): deviation of our implied surface mass balance from the surface mass balance from the regional model MAR.

Figure 6.5 shows the spatial differences between the observed and modelled surface elevation and SMB for different relaxation constants. Again, the tradeoff for representing both surface elevation and SMB is visible. While the simulated elevation is very close to the observation for small relaxation constants, the SMB deviation is very high, even in the interior of the ice sheet, where the deviations reach the amount of magnitude of the accumulation rate. Therefore, too small relaxation constants should be excluded. For larger relaxation constants, both difference fields become smoother, but rather high deviations in surface elevation appear over vast areas of the GrIS. Therefore, too high relaxation constants should be excluded too.

6.4 PRESENT-DAY GREENLAND ICE SHEET

Here, we present our optimal simulation of the GrIS using the SICOPOLIS model version 3.3 with hybrid dynamics and the model for basal hydrology (HYDRO). Both models are fully coupled (see Section 6.2.4), and the horizontal resolution is always $5 \text{ km} \times 5 \text{ km}$ from now on. In the hybrid mode, a threshold of $r_{\text{thr}} = 0$ applies to the slip ratio (Eq. 8 in Bernales et al. (2017)), i. e., the SStA equations are solved over the entire ice sheet, and the ice velocities are the weighted sum from the SIA and SStA velocities with the slip ratio as weight. The boundary conditions and initialization method to yield the present-day GrIS are described in Sections 6.2.6 and 6.3, respectively. As relaxation constant for the surface elevation we use $\tau_{\text{relax}} = 100$ years. Optimal values for the sliding parameters are found by minimizing the error of simulated horizontal surface velocities for values $> 50 \text{ m/yr}$, using observations by Rignot and Mouginot (2012). For such velocities, we expect basal sliding and hybrid ice dynamics to be relevant. We found $C_b = 25 \text{ m}/(\text{Pa yr})$ to be optimal for the hybrid model with basal hydrology. By design of the initialization, the simulated surface elevation compares overall well with the observed one, see Fig. 6.6a,b. However, as our surface relaxation method leaves the ice sheet’s surface a certain degree of freedom (see also Fig. 6.5), the simulated ice surface over Summit and South Dome as well as on the ridge in between them is slightly lower. The simulated surface velocities (smaller than 2 m/yr) along the ridges are somewhat smaller compared to the observed ones (often larger than 2 m/yr). Such (small) mismatches also appear with other higher-order models, even in higher resolution (Aschwanden et al., 2016). Recall that we adjusted the sliding parameter C_b to match velocities higher than 50 m/yr with observations. The model resolves the major flow patterns of the GrIS, including the flow over the catchment area of the outlet glaciers and the fast flow of the major outlet glaciers and ice streams. Only the smaller-scale outlet glaciers, e. g. in north-west Greenland, are not fully resolved. Further, we cannot model outlet glaciers with floating tongues, such as Petermann, Nioghalvfjerdsbræ and Zachariæ Isstrøm. The Northeast Greenland Ice Stream (NEGIS) is the only larger scale feature which we cannot reproduce properly. This feature cannot be simulated without additional assumptions (see the Discussion section).

Figure 6.7 zooms in Jakobshavn Isbræ and the two major outlet glaciers Helheim and Kangerdlugssuaq. Here, the ability of the model to resolve the catchment areas of these outlet glaciers in a 50 to 500 m/yr range can be seen in more detail. However, the high-velocity patterns near the glacier termini do not fully match the simulations. In particular, the tributaries of Helheim and Kangerdlugssuaq glaciers and the tip of Jakobshavn Isbræ appear rather smooth compared to the observation. Fast flow mainly appears over regions with a temperate ice bed. The simulated basal temperature in Fig. 6.8a shows a pattern which agrees basically with the reconstruction by MacGregor et al. (2016). Regions where there is basal melt, mainly caused by basal friction, exhibit a 1 to 5 mm thick water layer (Fig. 6.8b). There is a pronounced thickening of the water layer with our Shreve-flow modelling toward major ice streams and outlet glaciers, which is most visible for NEGIS, Jakobshavn Isbræ and Helheim Glacier. Moreover, smaller outlet glaciers like Store Glacier and Daugaard-Jensen Glacier receive intensified basal water supply too.

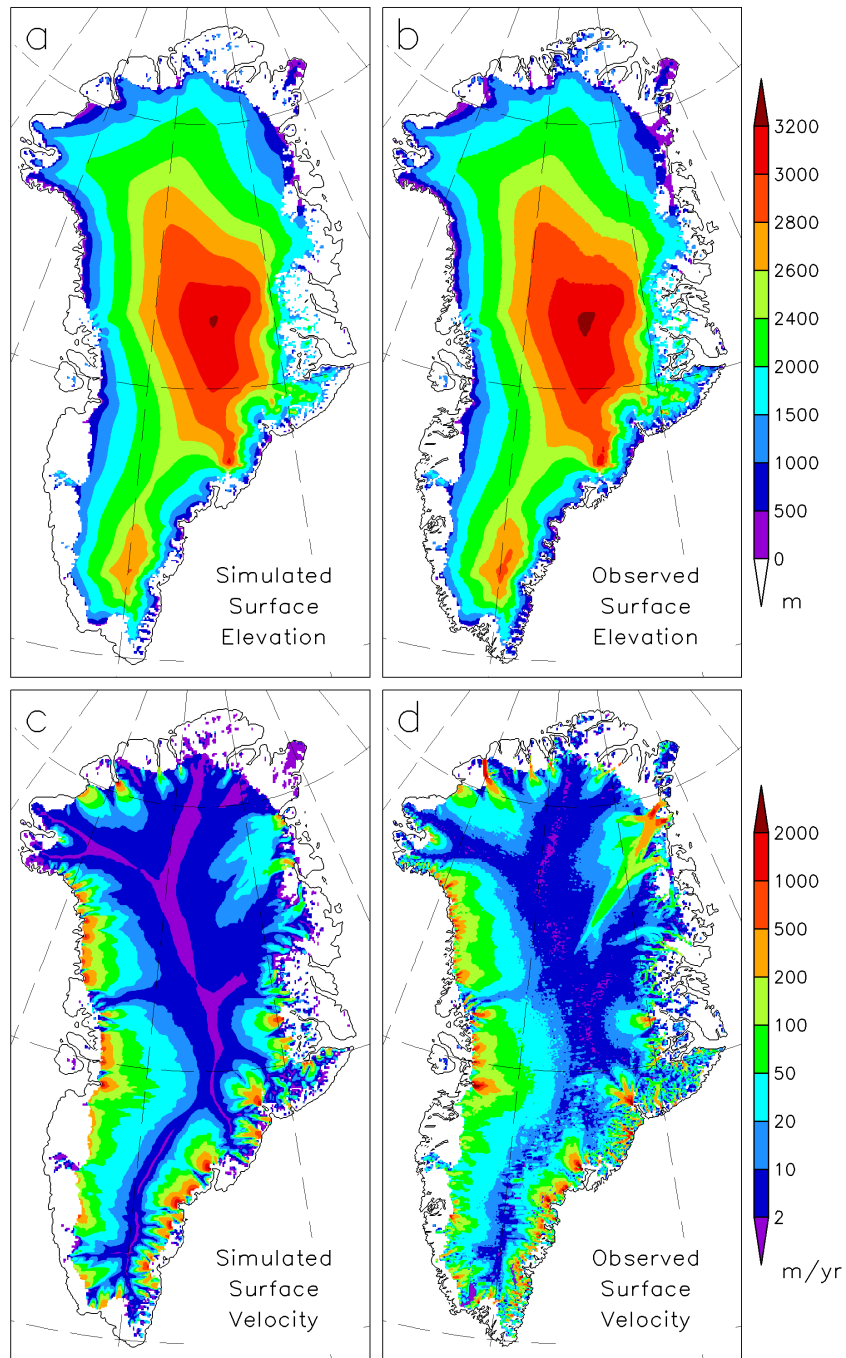


Figure 6.6: Comparison of our simulated with observed 2-D fields for present-day with 100 yrs relaxation constant. (a) Simulated surface elevation, (b) surface elevation by Bamber et al. (2013), (c) simulated horizontal surface velocity, and (d) horizontal surface velocity by Rignot and Mouginot (2012).

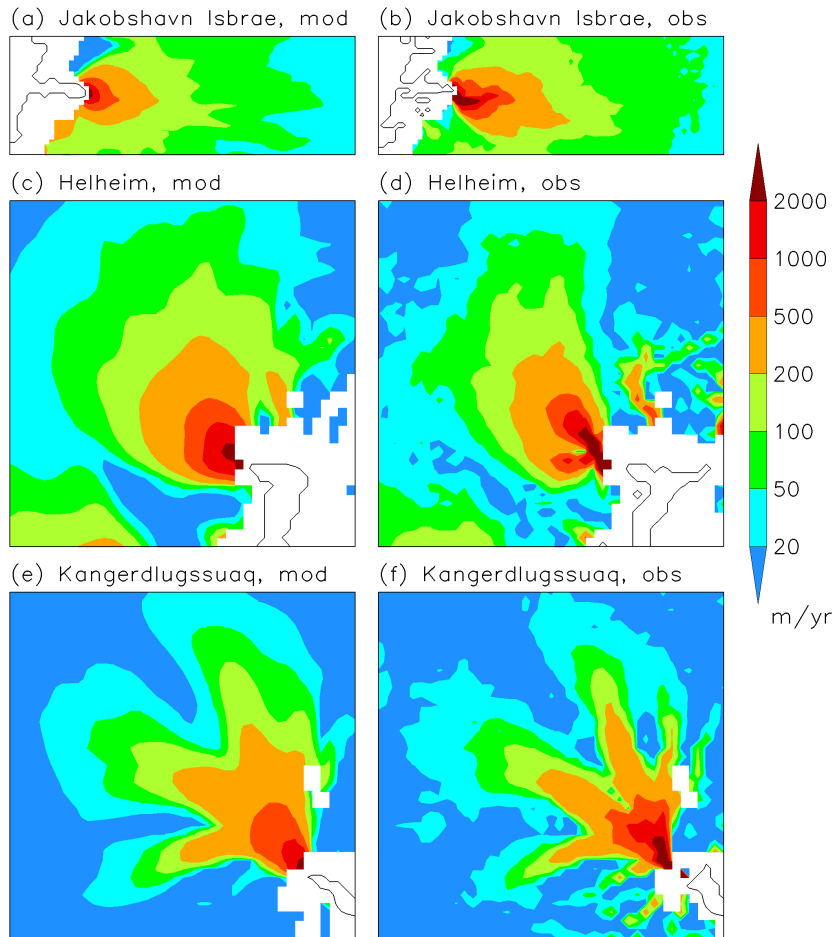


Figure 6.7: Comparison of observed and simulated velocity for major ice streams and outlet glaciers. Left side: modelled, right side: observed. (a, b) Jakobshavn Isbræ, (c, d) Helheim Glacier, and (e, f) Kangerdlugssuaq Glacier.

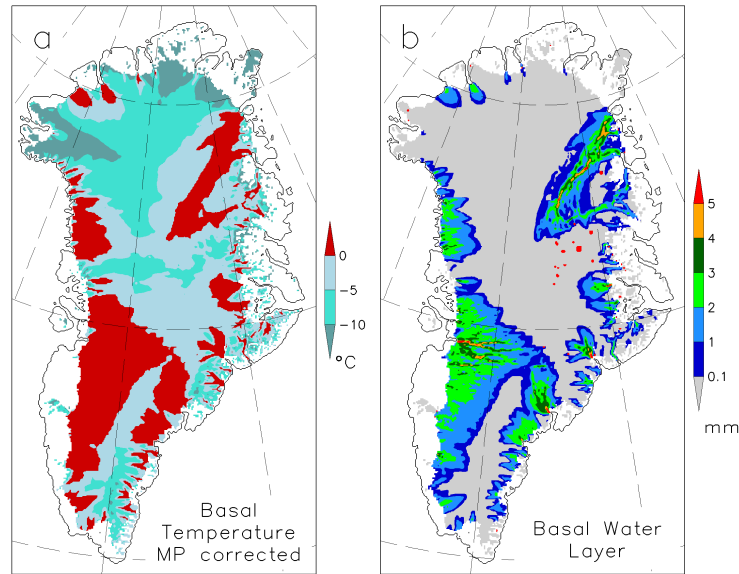


Figure 6.8: Simulated 2-D basal fields. (a) basal temperatures relative to pressure melting (in $^{\circ}\text{C}$), (b) thickness of basal water layer (in mm).

6.5 GREENLAND GLACIAL SYSTEM PROJECTIONS

6.5.1 PROJECTIONS OF THE GRIS'S SEA LEVEL CONTRIBUTION

For our projections of the contribution of the GrIS to global sea level rise, the GrIS is forced by SMB anomalies and surface temperatures derived from the MAR regional climate model (Section 6.2.7), making use of the initial ice sheet configurations explained in Section 6.3. As for the last 500 years of initialization, the fully coupled hybrid model including basal hydrology is utilized. Outside of the present-day GrIS area, similarly to the initialization, the prohibiting negative SMB is applied. In Fig. 6.9, we show the GrIS sea level contribution referenced to the year 2000. The control simulation forced solely with the implied SMB illustrates the characteristics of our initialization method. Indeed, with this forcing, there is almost no change in ice volume visible. Only after 300 years, a tiny ice volume change can be detected in Fig. 6.9b, due to the comparably small scale in the y -axis therein. This model drift amounts about 2 mm sea level contribution per 100 years. In spite of such a small change, we correct our simulated sea level contribution of the GrIS in the simulation with MAR forcing for the implied-SMB-only simulations.

Our projections of the GrIS sea level contribution for the year 2100 are close to simulations with a fixed present-day GrIS applying the cumulative SMB method (Church et al., 2013). This is in line with simulations with an active ice sheet model by Goelzer et al. (2013), who found that SMB is the major factor determining the GrIS sea level contribution over the 21st century. Our simulated GrIS sea level contribution for 2100 ranges from 1.9 cm (RCP 4.5, NorESM1) to 13.0 cm (RCP 8.5, CanESM2), see Table 6.2. Still, the ice dynamics (deformation and sliding velocities) plays a role in our simulations, indirectly via the SMB change. This can be seen when comparing the simulations with and without elevation SMB correction ($\partial M / \partial z$) Δz , Eq. 6.13. Ignoring the

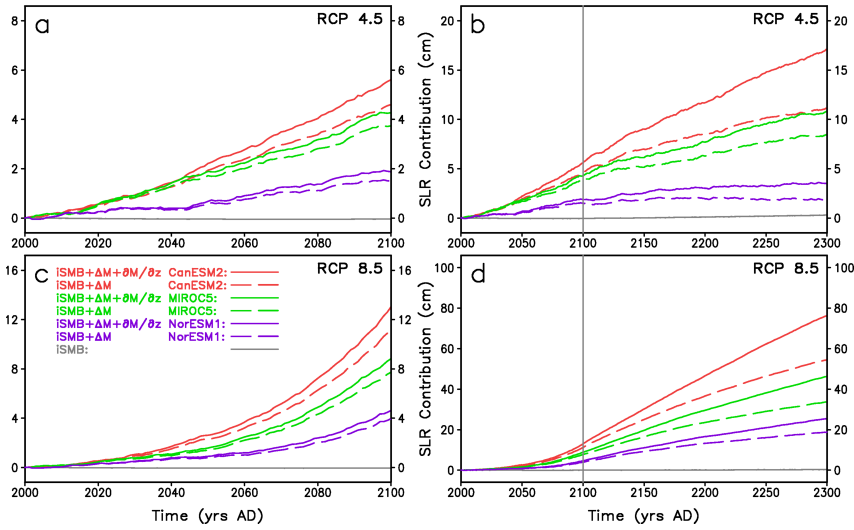


Figure 6.9: Contribution of the Greenland ice sheet to future sea level rise under MAR forcing for different scenarios. Sea level rise is referenced to the year 2000. Beyond 2100, the forcings of the projections are from prolongations of the original MAR data (see main text for details). This is indicated by the vertical grey line at the year 2100 in panels (b) and (d). RCP 4.5 projections: (a) years 2000–2100 and (b) years 2000–2300. RCP 8.5 projections: (c) years 2000–2100 and (d) years 2000–2300. The different CMIP5 general circulation models utilized by MAR are indicated by colours. Different line characteristics specify optimal simulations with (solid) and without (long dashed) elevation correction for the surface mass balance. The grey curves in panels (a) to (d) indicate a control simulation with solely the implied SMB (iSMB) as forcing. All simulations are with hybrid ice dynamics and HYDRO basal hydrology.

Table 6.2: Simulated GrIS contribution to sea level rise for the years 2100 and 2300 in cm. Columns specify the different GCMs used by MAR. Rows list the RCP scenarios used by the MAR GCMs and whether we excluded or included the elevation SMB feedback $\partial M/\partial z$ in our simulation.

MAR GCM	Year 2100 [cm]				Year 2300 [cm]			
	RCP 4.5		RCP 8.5		RCP 4.5		RCP 8.5	
$\partial M/\partial z$	off	on	off	on	off	on	off	on
NorESM1	1.5	1.9	4.0	4.6	1.8	3.5	18.8	25.5
MIROC5	3.7	4.3	7.7	8.8	8.5	10.8	33.7	46.3
CanESM2	4.6	5.6	11.3	13.0	11.2	17.1	54.6	76.4

elevation SMB correction diminishes simulated 21st-century GrIS sea level contribution between 0.4 and 1.7 cm. Of course, this effect is strongest for the extreme RCP 8.5 scenario together with CanESM2, the CMIP5 model exhibiting the most climate sensitivity.

At the end of the 23rd century the contribution of the GrIS to sea level rise ranges from 3.5 cm to 76.4 cm. The importance of the elevation SMB feedback clearly increases with the elapsed time of the projections, as the respective curves with $\partial M/\partial z$ on/off diverge more and more from each other. For RCP 8.5 with CanESM2, the relative increase of additional loss in ice volume due to elevation SMB correction nearly triples from 2100 to 2300, from 15% to 40%. Detailed numbers for the sea level contributions of the GrIS for the years 2100 and 2300 are listed in Table 6.2.

Overall, our simulations show a strong dependence of the GrIS sea level contribution both on the RCP scenarios and on the model used to force MAR.

6.5.2 PROJECTIONS OF THE GRIS'S TOTAL BASAL AND SURFACE RUNOFF

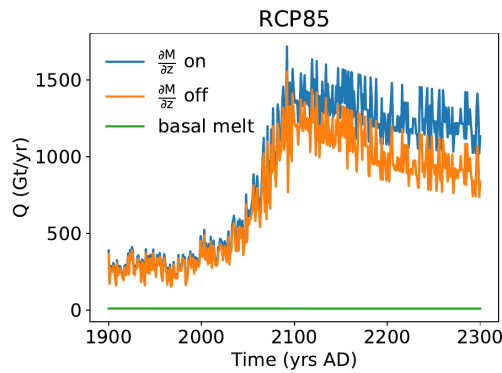


Figure 6.10: Time series of the components of subglacial discharge. The total basal melt (green) amounts to approximately 15 Gt yr^{-1} . Total surface runoff with surface elevation SMB feedback (blue) and without the feedback (orange).

For these projections, we use the basal melt from the two simulations by SICOPOLIS (Section 6.5.1) forced by the MAR data for which MAR used the MIROC5 GCM under the RCP 8.5 scenario. Surface and basal melt are routed over the ice base and distributed to the GrIS outlet glaciers. The details are explained in Section 6.2.4. Figure 6.10 depicts the total subglacial discharge split into surface runoff and basal melt. The total basal melt amounts to about 15 Gt per year, while the surface runoff increases up to 1700 Gt per year. Note that, after the year 2100, the surface runoff is decreasing due to the shrinking ice sheet area. Simultaneously, the effect of the elevation SMB feedback becomes more important after the year 2100, leading to much higher surface runoff than without the feedback (Eq. 6.14).

6.5.3 PROJECTIONS OF SUBMARINE MELT RATE FOR THE GRIS OUTLET GLACIERS HELHEIM AND STORE

Here, we inspect the impact of global warming under the RCP 8.5 scenario for two outlet glaciers: Helheim Glacier and Store Glacier. In detail, we analyse the impact of both subglacial discharge

and ocean warming – as single and combined effects – on the submarine melt rate of these outlet glaciers. While the subglacial discharge comes from simulations with SICOPOLIS and HYDRO under the RCP 8.5 scenario, the ocean warming originates from a scenario similar to RCP 8.5 (Section 6.2.8). For analysing the impact of the elevation SMB feedback on submarine melt, the plume model is forced by subglacial discharge computed with and without the surface elevation correction of surface runoff (Eq. 6.14). We calculate all submarine melt rates under the assumptions of both glaciers being tidewater glaciers (no floating tongues) and of their grounding-line depths and widths remaining constant in time. These depths and widths are acquired from present-day observations and amount to 500 m depth and 5 km width for Store Glacier (Chauché et al., 2014) and 650 m depth (Carroll et al., 2016) and 6 km width (Straneo et al., 2016) for Helheim Glacier. We chose the entrainment parameter to be $E_0 = 0.036$ as recommended by Beckmann et al., 2018.

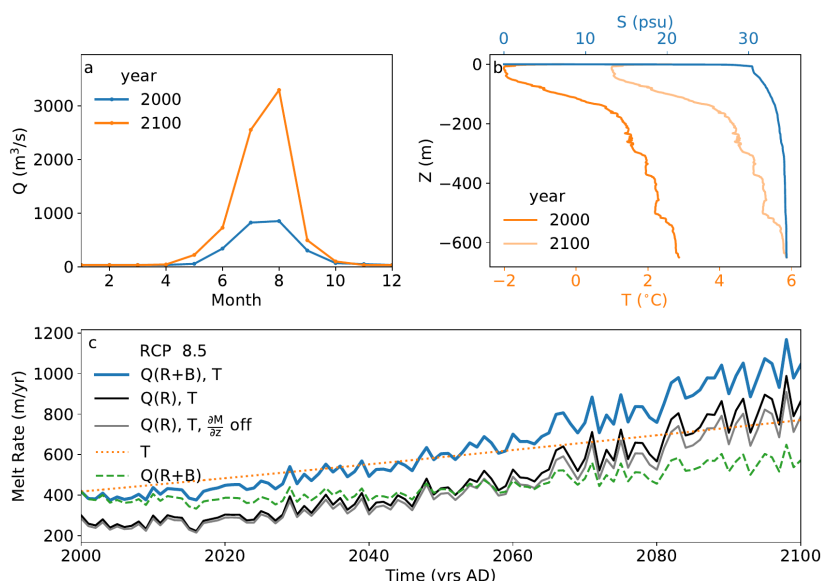


Figure 6.11: a) Monthly subglacial discharge derived from runoff and basal melt (R+B) for Helheim Glacier and the scenario RCP 8.5 in the years 2000 and 2100. b) Temperature-depth and salinity-depth profiles obtained from measurements for the years 2000 and 2100. The corresponding submarine melt rates are depicted in c). The effects of increased temperature and discharge only (orange dotted and green dashed lines respectively), as well as the combined effect (solid lines) are displayed until the year 2100. Melt rates with subglacial discharge or only surface runoff are depicted in black. Melt rates of subglacial discharge containing only surface runoff that was calculated without the surface elevation feedback are depicted in grey.

Figures 6.11 and 6.12 illustrate the monthly subglacial discharge and the temperature profiles for the years 2000 and 2100 and the resulting submarine melt rates for the RCP 8.5 scenario. For both glaciers, the increasing subglacial discharge and the increasing ocean temperature have an about equal effect on the rising submarine melt, with the ocean temperature becoming more important towards the end of the year 2100. However, the combined effect of increased subglacial discharge and temperature exceeds the single effects alone. As a result, submarine melt exhibits a 2.5-fold

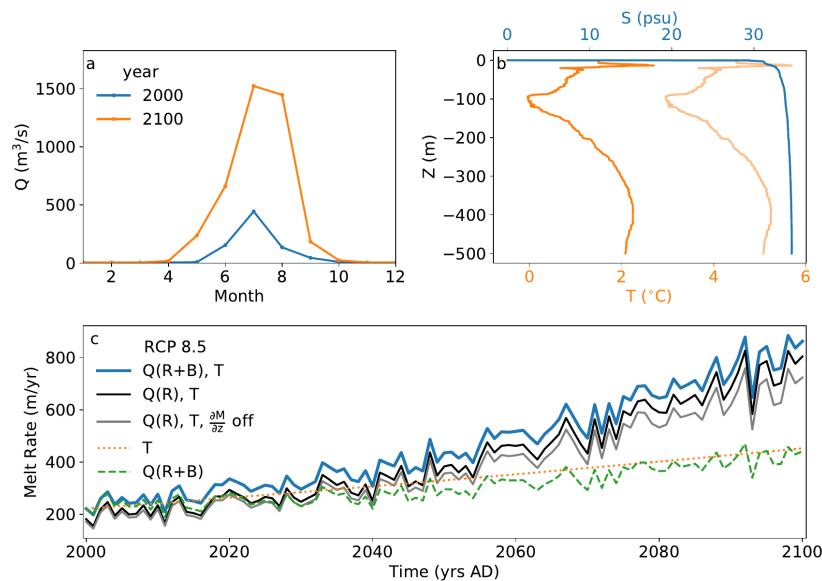


Figure 6.12: Similar to Figure 6.11, but for Store Glacier.

increase for Helheim Glacier and a 4-fold increase for Store Glacier in the year 2100 (Figs. 6.11c and 6.12c). Although for the year 2000 the amount of basal melt (38 m³/s for Helheim, 5 m³/s for Store) is small compared to summer subglacial discharge (818 m³/s for Helheim, 439 m³/s for Store), it has a significant effect on the annual submarine melt rate. Due to the basal melt in the winter months (including early spring and late autumn), the submarine melt rate enlarges in those months substantially as illustrated by Fig. 6.13 for Helheim Glacier. The slight increase in subglacial discharge for all months (Fig. 6.13a) shows clearly the biggest increase in submarine melt rate for the winter months (Fig. 6.13b) due to the cubic root dependence of submarine melt rate on subglacial discharge (Jenkins, 2011). On the annual average, this effect leads, for the year 2000, to an increase of submarine melt for Helheim Glacier by 40% and for Store Glacier by 20% compared to the case when basal melt was not accounted for (Figs. 6.11c and 6.12c). The missing effect of surface elevation correction does not show big impacts on submarine melt rate when turned off (Figs. 6.11c and 6.12c). However, as Fig. 6.10 suggests, this effect will become more important after the year 2100.

In these experiments, the future submarine melt rate was calculated assuming a constant glacier terminus position and geometry. These calculation have to be seen as a first approximation because we neglect several factors that may influence the submarine melt rate. For instance, if the glacier retreats, the resulting grounding line depth may change depending on the underlying bedrock. Another factor that might change the melt rate estimation considerably is the distribution of subglacial discharge within the year. Here, we assumed no time lag in between runoff and its emergence as subglacial discharge. Due to the cubic root dependence of submarine melting on subglacial discharge, we already see the possible strong effect of basal runoff from the ice sheet on the distribution of the submarine melt rate of an outlet glacier over the year (see Fig. 6.13). Thus, an inefficient drainage system that is delayed by, e. g., storage of water in subglacial lakes (Nienow

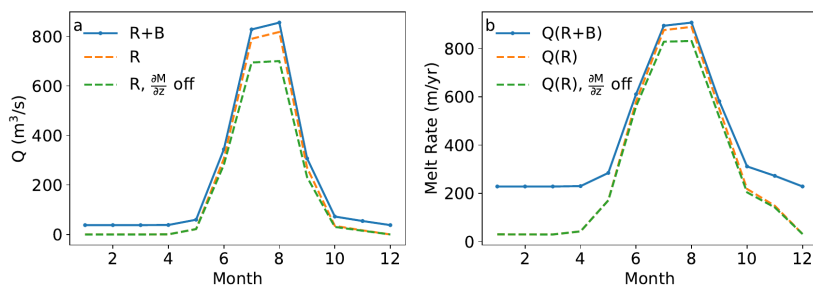


Figure 6.13: Subglacial discharge of Helheim Glacier a) for the year 2000 determined by runoff (R) only (dashed lines), with and without surface elevation feedback (orange, green) and runoff together with basal melt (R+B, blue solid line). The corresponding submarine melt rates b) with the same line colour and line style.

et al., 2017) might affect the seasonal distribution of subglacial discharge and thus the annual submarine melt rate substantially.

6.6 DISCUSSION

In Section 6.3, we investigated the role of the relaxation constant for initialization. For very small relaxation constants, i. e., an essentially fixed ice surface, the difference between implied and observed SMB at present day becomes very large (more than 2000 Gt/yr, compared to an insignificant amount for $\tau_{\text{relax}} = 100$ years). Note that the present-day magnitude of observed total SMB is only about 500 Gt/yr (e.g. Ettema et al., 2009). This means that computation with fully fixed surface should be treated with care, as the total artificial mass needed to keep the ice sheet close to observation is very high. A further advantage of the relaxation of the ice surface towards observed is that this smoothes the surface elevation, because the ice surface has a certain degree of freedom due to the relation constant while solving the evolution equation for ice thickness in the course of iteration of the ice sheet model. Such smoothing effect via running an ice sheet model with free surface over 100 yrs was already observed by Calov and Hutter (1996). Furthermore, they demonstrated that a smooth surface elevation avoids irregular variations in the velocity field.

In our simulations, we cannot reproduce the NEGIS ice stream correctly. Certainly, one reason is that we do not optimize the surface velocity by a spatially dependent basal sliding coefficient. With spatially dependent basal sliding coefficients, other studies such as Price et al. (2011) and more recently Peano et al. (2017) simulated the NEGIS in better agreement with observations. Nowadays, there are process-oriented approaches to capture effects important for basal sliding. For example, stronger basal melting at the onset of the NEGIS caused by increased geothermal heat due to a palaeo-hotspot (Rogozhina et al., 2016) could be one factor speeding up the simulated NEGIS velocity. A further factor can be a deepening of the basal topography in this region (Vallelonga et al., 2014).

For our 300-year sea level projections, which reach beyond the 21st century, we prolong the forcing data of the MAR model until the year 2300. Because we merely held the forcing constant between 2101 and 2300, the real RCP 8.5 forcing could be larger, i.e., we expect our simulations

with the RCP 8.5 scenario to be a lower estimate of sea level contribution of the GrIS, i.e., the estimate is a rather conservative one. Most certainly, even all our projections including RCP 4.5 are a conservative estimate, because a full coupling with ice–ocean interactions is missing in our model yet, and Fürst et al. (2015) found that ocean warming caused additional mass loss of the GrIS in his projections applying a parameterization of ocean warming.

Our additional sea level rise for the year 2100 due to elevation SMB feedback is somewhat higher than that by Le clec’h et al. (2017), who used the regional model MAR actively coupled to an ice sheet model for their simulations. In contrast, Edwards et al. (2014) found an even smaller impact of this feedback than Le clec’h et al. (2017), possibly due to an underestimation of its spatial dependence in Edward’s parameterization. As demonstrated to be important by Le clec’h et al. (2017) with fully interactive two-way coupling, this feedback deserves a detailed inspection in the future.

Our presented projections for the GrIS contribution to global sea level rise in the 21st century (1.9–13.0 cm) are consistent with previous publications. However, they do not account for the dynamic response of Greenland outlet glaciers to ocean warming and increase of subglacial discharge. This effect will be account for in a forthcoming paper. We also intend to couple the 3-D ice sheet model SICOPOLIS with the 1-D model for many outlet glaciers.

6.7 CONCLUSION

We introduced the coupled Greenland glacial system model IGLOO 1.0 designed to describe the most important parts of the Greenland glacial system: the ice sheet, the subglacial hydrological system, the outlet glaciers and the ice-ocean interaction in the Greenland fjords. Full coupling between the ice sheet model and the model of subglacial water HYDRO has been accomplished, while the coupling between HYDRO and the meltwater plume works only off-line yet.

The applicability of the hybrid mode of the ice sheet model SICOPOLIS 3.3 to the Greenland ice sheet was demonstrated. It showed that the model performs reasonably well, as the simulated velocity field compared well with observations, including the two major outlet glaciers Helheim Glacier and Kangerdlugssuaq Glacier and the Jakobshavn Isbræ ice stream. Further, for simulating optimal velocities, it is reasonable that the sliding coefficient for the model in hybrid mode is larger than that for the SIA model, as lateral strain partly compensates the effect of basal drag.

As initialization, we used a relaxation method similar to Aschwanden et al. (2013), but with a somewhat higher relaxation constant of 100 years. For this choice of the relaxation constant, we varied it systematically and investigated the resulting model behaviour by inspecting the RMS error in surface elevation as well as the difference between total simulated SMB and total SMB from the MAR regional climate model. It showed that, for a relaxation constant of 100 years, the deviation of our simulated total SMB from the MAR SMB is about zero, while —at the same time— the RMS of the simulated error in surface elevation stays reasonably small. Additionally, we showed that medium-value relaxation times lead to smooth 2-D fields of the implied SMB, while for too small relaxation times the fields become rather noisy, and for too large relaxation times regional deviations of the simulated elevation from the observed one become relatively large.

Furthermore, we performed projections of the contribution of the GrIS to sea level rise until the year 2300 with hybrid ice dynamics forced by SMB anomalies from the MAR regional model.

For the RCP 4.5 and 8.5 scenarios generated by MAR, three CMIP5 GCMs with different climate sensitivity were applied. Altogether, our projected GrIS sea level contribution for the year 2100 obtained with elevation SMB feedback ranges from 1.9 to 13.0 cm, and for the year 2300 from 3.5 to 76.4 cm. The elevation SMB feedback showed to be important. Generally, its impact increases in the long run with decreasing surface elevation (see Table 6.2).

Moreover, we demonstrated the importance of the different factors determining the increase of the melt rate of Greenland outlet glaciers under the extreme RCP 8.5 scenario, using Store and Helheim Glaciers as examples. It showed that the knowledge of near-terminus temperature and subglacial discharge in the fjord are both about equally important to determine the future melt of these two outlet glaciers. This underlines the importance of our approach with the Greenland system model IGLOO 1.0.

CODE AND DATA AVAILABILITY

SICOPOLIS is available at www.sicopolis.net. The HYDRO module is not included in the repository yet. MAR data used as basis for our forcing is available at <ftp://ftp.climato.be/fettweis/MARv3.5/Greenland/>.

6.8 APPENDIX

6.8.1 MASS CONSERVATING SCHEME FOR ICE THICKNESS EVOLUTION

We included a new numerical scheme into SICOPOLIS 3.3, which discretizes the advection term of the ice thickness equation by a strictly mass-conserving scheme in an upwind flux form:

$$A = \frac{(\bar{v}_x(i + 1/2, j)H_x^+ - \bar{v}_x(i - 1/2, j)H_x^-)\Delta y + (\bar{v}_y(i, j + 1/2)H_y^+ - \bar{v}_y(i, j - 1/2)H_y^-)\Delta x}{\Delta x \Delta y}, \quad (6.15)$$

where A is the advection term and \bar{v}_x, \bar{v}_y are the x - and y -components of the depth averaged velocity, respectively. Further, Δx and Δy are the horizontal spacings. The upwind coefficients read:

$$H_x^- = \begin{cases} H(i - 1, j), & \bar{v}_x(i - 1/2, j) \geq 0, \\ H(i, j), & \bar{v}_x(i - 1/2, j) < 0, \end{cases}$$

$$H_x^+ = \begin{cases} H(i, j), & \bar{v}_x(i + 1/2, j) \geq 0, \\ H(i + 1, j), & \bar{v}_x(i + 1/2, j) < 0, \end{cases}$$

$$H_y^- = \begin{cases} H(i, j - 1), & \bar{v}_y(i, j - 1/2) \geq 0, \\ H(i, j), & \bar{v}_y(i, j - 1/2) < 0, \end{cases}$$

$$H_y^+ = \begin{cases} H(i, j), & \bar{v}_y(i, j + 1/2) \geq 0, \\ H(i, j + 1), & \bar{v}_y(i, j + 1/2) < 0, \end{cases}$$

with the ice thickness H . The pairs (i, j) , $(i + 1/2, j)$ etc. indicate the indices of the staggered Arakawa C grid.

6.8.2 ADAPTING MAR DATA FOR THE FUTURE SIMULATIONS

One element of our initialization method (see Section 6.3) is the prevention of a model shock (Aschwanden et al., 2013) when we start the projections from the palaeo-spin-up and switch from fixed domain to free surface. Starting the free-surface simulations as early as possible is preferable in order to give the model the chance to recover from possible perturbations at the beginning. While the MIROC5 model provides data starting at the year 1900, the CanESM2 and NorESM1 models start later in time at 1950. For the latter two models, we randomly reshuffled the horizontal time slices (annual mean of surface temperature, SMB and monthly surface runoff) from the years 1950–1999 back in time to the years 1900–1949. This yields forcing data for the years 1900–2100 for all three CMIP5 models.

As ice sheets react on longer timescales, we needed longer scenarios and opted to prolong the scenario data until the year 2300. However, for the years 2101–2300, there are no direct scenario data available from MAR for any of the three used CMIP5 models. In particular, for RCP 8.5, we have the problem to choose a favourable sampling interval for the horizontal time slices. If we choose the sampling interval too short, there are not enough time slices to be assigned to the time beyond 2100, and there is almost no variability. If we choose the interval too long, there is an overestimation of variability during the artificially prolonged interval 2101–2300 due to the already present climate-warming trend in the MAR RCP 8.5 forcing for the years towards the year 2100. This problem is particularly prevalent for the anomaly in SMB. A sampling length of 10 years (years 2091–2100) is a good choice. Over this sampling interval, the horizontal time slices are repeatedly and randomly reshuffled forward in time to the years 2101–2300. We found that there still was an overestimation of variability in the prolonged data.

We circumvented this overestimation of variability for (and only for) the RCP 8.5 scenarios by computing over the sampling interval the temporal average, the maximum and the minimum of the anomaly of the total SMB, $\Delta M_{\text{tot}}^{\text{ave}}$, $\Delta M_{\text{tot}}^{\text{min}}$ and $\Delta M_{\text{tot}}^{\text{max}}$, respectively. Then, we apply the condition

$$\Delta M_{\text{tot}} > \Delta M_{\text{tot}}^{\text{ave}} + 0.3 \cdot (\Delta M_{\text{tot}}^{\text{max}} - \Delta M_{\text{tot}}^{\text{min}})/2 \quad (6.16)$$

in order to exclude time slices with too positive total SMB anomaly. In fact, we consider 2-D fields where ΔM totals are below its average, while we consider only about the first 1/3 where ΔM totals are above its average. Note that the totals of anomalies of surface mass balance are negative in these scenarios.

COMPETING INTERESTS

The authors declare no competing interests.

ACKNOWLEDGEMENTS

We are grateful to Fiamma Straneo and Dustin Carroll for providing us with temperature and salinity profiles of Helheim glacier. We are also grateful to Xavier Fettweis for hosting the website with the MAR data. Further, we would like to thank Ciarion Linstead for technical support with library installation. J. B., R. C. and S. B. were funded by the Leibniz Association grant SAW-2014-

PIK-1. M. R. was supported by the Helmholtz Alliance Climate Initiative (REKLIM). M. W. is supported by the Bundesministerium für Bildung und Forschung (BMBF) grants PalMod-2.1 and PalMod-2.2. R. C. is funded by the Bundesministerium für Bildung und Forschung (BMBF) grants PalMod-1.1 and PalMod-1.3. R. G. was supported by Japan Society for the Promotion of Science (JSPS) KAKENHI grant numbers 16H02224 and 17H06104, and by the Arctic Challenge for Sustainability (ArCS) project of the Japanese Ministry of Education, Culture, Sports, Science and Technology (MEXT).

7

MODELING THE RESPONSE OF GREENLAND OUTLET GLACIERS TO GLOBAL WARMING USING A COUPLED FLOWLINE-PLUME MODEL

CONTEXT

This research paper focuses on submarine melting at Greenlandic outlet glaciers. Mass loss of Greenland can partly be attributed to the retreat and acceleration of outlet glaciers, which is connected to increased submarine melting. The latter is caused by a warmer ocean and also larger subglacial discharge. A one-dimensional coupled line-plume glacier flowline model is used to investigate the response of twelve outlet glaciers to a warmer climate.

The paper's objective is to compute the contribution of individual glaciers to global sea level rise and estimate sources of uncertainty. It raises the question of which of the contributing factors (SMB, ocean temperature, subglacial discharge) has the largest impact on mass loss and how the marine-terminating outlet glaciers differ in their response. Therefore, the model is run to the year 2100 and the cumulative contribution to sea level rise is determined under the RCP 8.5 scenario.

Subglacial hydrology plays a role in that it determines the quantity of the discharge and where it enters the ocean. As in the previous chapter, the monthly averaged surface runoff and basal melt is routed along the hydraulic potential using `CIDRE` and is assigned to the closest glacier (within a maximum distance of 50 km) where it exits the ice sheet. Supraglacial processes are neglected, assuming that the runoff directly enters the subglacial system. The subglacial discharge turns out to have a comparable influence on future sea level rise to the effect warmer ocean water. This highlights the importance of including subglacial hydrology into large scale system models.

CONTRIBUTION

J.B designed the study together with A. G.. M.P. developed the glacier model. J.B. coupled the numerical plume model to the glacier model, and implemented the surface-correction method. Together with S.B, R.C and M.W, J.B. created the projected subglacial discharge and surface-mass balance data set for each glacier respectively. J.B. carried out the experiments, created figures and wrote the manuscript, supported by all co-authors.

AUTHORS AND AFFILIATIONS

Johanna Beckmann¹, Mahé Perrette¹, Sebastian Beyer^{1,2}, Reinhard Calov¹, Matteo Willeit¹, and Andrey Ganopolski¹

¹*Potsdam Institute for Climate Impact Research, Earth System Analysis, Potsdam, Germany*

²*Alfred Wegener Institute, Helmholtz Centre for Polar and Marine Research, Bremerhaven, Germany*

ABSTRACT

In recent decades, the Greenland Ice Sheet has experienced an accelerated mass loss, contributing to approximately 25 % of contemporary sea level rise. This mass loss is caused by increased surface melt over a large area of the ice sheet and by the thinning, retreat and acceleration of numerous Greenland outlet glaciers. The latter is likely connected to enhanced submarine melting that, in turn, can be explained by ocean warming and enhanced subglacial discharge. The mechanisms involved in submarine melting are not yet fully understood and are only crudely incorporated in some models of the Greenland Ice Sheet. Here, we investigate the response of twelve representative Greenland outlet glaciers to atmospheric and oceanic warming using a coupled 1D line-plume glacier-flowline model. The model parameters have been tuned for individual outlet glaciers using present-day observational constraints. We then run the model from present to the year 2100, forcing the model with changes in surface mass balance and surface runoff from simulations with a regional climate model for the RCP 8.5 scenario, and applying a linear ocean temperature warming with different rates of changes representing uncertainties in the CMIP 5 model experiments for the same climate change scenario. We also used different initial temperature-salinity profiles obtained from direct measurements and from ocean reanalysis data. Using different combinations of submarine melting and calving parameters that reproduce the present-day state of the glaciers, we estimated uncertainties in the contribution to global sea level rise for individual glaciers. We also performed a factor analysis, which shows that the role of different forcing (change in surface mass balance, ocean temperature and subglacial discharge) are diverse for individual glaciers. We found that changes in, ocean temperature and subglacial discharge are of comparable importance for the cumulative contribution of all twelve glaciers to global sea level rise in the 21st century. The median range of the cumulative contribution to the global sea level rise for all twelve glaciers is about 14 mm from which roughly 85 % are associated with the response to increased submarine melting and the remaining part to surface mass loss. We also found a weak correlation (correlation coefficient 0.35) between present-day grounding line discharge and their future contribution to sea level rise in 2100. If the contribution of the twelve glaciers is scaled up to the total present-day discharge of Greenland, we estimate the contribution of all Greenland glaciers to 21st-century sea level rise to be approximately 50 mm. This result confirms earlier studies that the response of the outlet glaciers to global warming has to be taken into account to correctly assess the total contribution of Greenland to sea level change.

7.1 INTRODUCTION

Sea level rise (SLR) is one of the major threats to humanity under global warming, and approximately one-fourth of the recent SLR can be attributed to the Greenland Ice Sheet (GrIS) (Chen et al., 2017). In the future projections of SLR, the GrIS is not only one of the major potential contributors but also a significant source of uncertainty. Two processes are largely responsible for the GrIS contribution to SLR: (1) increased surface melt induced by global warming and (2) dynamic mass loss due to retreat and acceleration of outlet glaciers (Khan et al., 2014). The latter, which is most pronounced for marine-terminating outlet glaciers (Moon et al., 2012), is potentially caused by an increase in submarine melting, which can in turn be attributed to a warming of the ocean and increased subglacial discharge (Straneo and Heimbach, 2013). Regarding the first mechanism, the maximum contribution due to increased surface melt is estimated to range between 0 to 130 mm by the year 2100 (Fettweis et al., 2013). Due to the possibility of applying relatively high-resolution regional climate models, confidence in this estimate has increased in the recent years (Broeke et al., 2017). The contribution of the second process remains highly uncertain because processes related to the response of marine-terminated Greenland glaciers are still not properly represented in the contemporary GrIS models (Straneo and Heimbach, 2013).

The principal objective of this paper is to quantify the response of marine-terminating outlet glaciers to future submarine melting and to analyze whether the impacts of ice-ocean interaction on SLR are comparable to long-term changes in surface mass balance (SMB). In order to assess Greenland's contribution to future sea level rise, several different model strategies have been proposed. The most common method is to use three-dimensional ice sheet models, tuned to present-day conditions, and apply future climate change projections based on global or regional climate models. However, such models still have relatively coarse spatial resolution and cannot properly resolve most of the outlet glaciers that terminate in Greenland's fjords. They also do not describe the interaction between glaciers and the ocean explicitly, but in some cases, for instance in Fürst et al. (2015), ocean melting is parameterized indirectly by increasing the basal sliding factor as ocean temperature increases. For the RCP scenario 8.5, they calculated a SLR between 155 and 166 mm at the year 2100 for the entire ice sheet atmospheric and oceanic forcing. Another method, followed by Nick et al. (2013), is to simulate single outlet glaciers individually using a 1-dimensional (1D) flowline model. Nick et al. (2013) performed simulations for four outlet glaciers that collectively drain about 22 % of the total solid ice discharge of the Greenland Ice Sheet. Assuming proportionality between the future contribution to SLR and present-day ice discharge, Nick et al. (2013) scaled up results obtained from four glaciers to the total estimate of all Greenland outlet glaciers, which resulted in a range between 65 and 183 mm by the year 2100. Taking this one step further, Goelzer et al. (2013) used the results from Nick et al. (2013) in a 3D coarse-resolution ice sheet model. They applied the 1D glacier thinning and grounding-line retreat scenarios as an external, pre-calculated forcing in the grid cells at the ice sheet boundary. Since only four glaciers had been simulated in the 1D model, they mapped the forcing from the original glaciers onto all other Greenland's marine-terminating outlet glaciers with a nearest neighbour approach. The incorporation added only 8 to 18 mm SLR on top of the stand-alone 3D ice sheet model simulation. Goelzer et al. (2013) argued that, that the smaller contribution results from smaller marine-terminating glacier that fully retreat in the 3D ice simulations, leaving no more ice-ocean, which is still included by the upscaling from Nick et al. (2013). Since we are especially interested in the

impacts of ice-ocean interactions on glacier dynamics, we followed an approach similar to Nick et al. (2013) but with several notable improvements. Firstly, for calculations of the vertically distributed submarine melt, we used a turbulent plume parameterization following Jenkins (2011). According to this parameterization, the submarine melt rate depends not only on ambient water temperature in fjords but also on seasonally varying subglacial discharge. The first idealized simulations of a coupled flowline-plume model were carried out by Amundson and Carroll (2018) by using the maximum melt rate as a frontal ablation factor to account for undercutting plus calving of tidewater glaciers, demonstrating the potential impact of the subglacial discharge on glacier dynamics. For the evolution of the surface mass balance, we used anomalies computed by the regional climate model MAR and corrected them for elevation change. Finally, we performed simulations for 12 representative Greenland glaciers (compared to four in Nick et al. (2013)). This enabled us to test the assumption used in Nick et al. (2013) that the contribution of individual Greenland outlet glaciers to SLR is proportional to their present-day discharge and therefore the total contribution of Greenland outlet glaciers can be obtained by scaling up contribution of individual glaciers proportionally to the entire present-day discharge of all outlet glaciers. We also estimated the uncertainties in the contribution of Greenland glaciers to SLR resulting from uncertainties in calving and ocean melt parameters and climate change scenarios.

The paper is structured as follows. First, we describe the coupled flowline-plume model, then how the input data were preprocessed together with the experimental setting and climate change scenarios. Finally, we present the results of our model simulations for present day and future scenarios.

7.2 THE COUPLED FLOWLINE-PLUME MODEL

Most of Greenland's outlet glaciers terminate in fjords that are connected to the ocean. Inside these fjords, observations of upwelling plumes along the edges of glaciers have drawn attention to the importance of submarine melting. Consequently, considerable efforts in modeling of submarine melt rate have been undertaken by using high-resolution 3D and 2D ocean general circulation models that are tuned to or parameterized after the buoyant-plume theory (Sciascia et al., 2013; Xu et al., 2013; Slater et al., 2015; Cowton et al., 2015; Carroll et al., 2015; Slater et al., 2017). However, such models are too computationally expensive and therefore impractical for simulating the response of the entire GrIS to climate change on centennial timescales. At the same time, recent studies demonstrate that the simple line plume model by Jenkins (2011) is an adequate tool to simulate plume behavior (Jackson et al., 2017) and to determine submarine melt rates for marine-terminated glaciers (Beckmann et al., 2018). Since the plume model is significantly less computationally expensive than 3D ocean models, it represents an alternative approach to introduce ice-ocean interaction into the GrIS model and still maintain the model's ability to perform a large set of centennial-scale experiments. Simulating the glacier dynamics with 3D ice sheet model requires very high spatial resolution ($\ll 1$ km) resulting in high computational cost (e. g. Aschwanden et al., 2016) and so far they cannot be used for centennial timescales. To reduce the computational cost we used instead a 1D depth- and width- integrated one-dimensional ice flow model (Enderlin and Howat, 2013; Nick et al., 2013) coupled to a line plume model (Beckmann et al., 2018).

7.2.1 GLACIER MODEL

The governing equations of the 1D model include mass conservation:

$$\frac{\partial H}{\partial t} = -\frac{1}{W} \frac{\partial(UHW)}{\partial x} + B \quad (7.1)$$

where H is ice thickness, t is time, U is the vertically averaged horizontal ice velocity, W is the width and x is the distance from the ice divide along the central flowline. B is the sum of SMB and submarine melting.

The conservation of momentum involves a balance between longitudinal stress, basal shear stress and lateral stress on the one hand, and driving stress on the other:

$$2 \frac{\partial}{\partial x} \left(H \nu \frac{\partial U}{\partial x} \right) - A_s \left[\left(H - \frac{\rho_w}{\rho_i} D \right) U \right]^q - \frac{2H}{W} \left(\frac{5U}{EAWW_s} \right)^{\frac{1}{3}} = \rho_i g H \frac{\partial h_s}{\partial x}, \quad (7.2)$$

where h_s denotes the ice surface height, D the depth of glacier below sea-level, ρ_i and ρ_w the ice and sea water density, respectively. Basal stress is parameterized with the basal sliding coefficient A_s and velocity exponent q and lateral stress involves a nondimensional width-scaling parameter W_s . Finally, the rate factor A and the enhancement factor E determine the viscosity ν

$$\nu = (EA)^{\frac{1}{3}} \left| \frac{\partial U}{\partial x} \right|^{-\frac{2}{3}}. \quad (7.3)$$

Calving occurs when surface crevasses propagate until the water level (Nick et al., 2013). Crevasses depth d_s is calculated from the resistive stress $R_{xx} = 2 \left(\frac{1}{A} \frac{\partial U}{\partial x} \right)^{1/3}$, as ice stretches, and can be enhanced by melt water depth d_w :

$$d_s = \frac{R_{xx}}{\rho_i g} + d_w \frac{\rho_0}{\rho_i} \quad (7.4)$$

where ρ_0 is the freshwater density.

Initial boundary condition is $U(x=0) = 0$, while at the calving front, we use

$$\frac{dU}{dx} = EA \left[\frac{\rho_i g H}{4} \left(1 - \frac{\rho_i}{\rho_w} \right) \right]^3 \quad (7.5)$$

The model employs a stretched horizontal grid with a horizontal resolution of 100 meters, where velocity is calculated at mid-points. At each time step of 3.65 days, the grid is stretched to keep track of the grounding line position, which is determined by the flotation criterion

$$H_{\text{float}} \leq |z_b| \frac{\rho_w}{\rho_i}, \quad (7.6)$$

where z_b is the bedrock depth. Glacier thickness H and bedrock depth z_b of each cell interface are determined by linear interpolation between the cell centered values.

The code is written in fortran, following the numerical procedure of Enderlin et al. (2013). The main differences compared to their original matlab code¹ is that we include a subgrid-scale treatment of the calving front boundary, and an improved treatment of the submarine melting.

7.2.2 PLUME MODEL

The plume model equations are described in Beckmann et al. (2018). We set the entrainment parameter E to 0.036, as suggested by Beckmann et al. (2018). Since the plume model in some cases underestimates and in others overestimates submarine melt rates (Beckmann et al., 2018), we also scale the simulated melt rate profile by a factor β , which we treat as a tuning parameter within the range 0.3 – 3 (see section 7.4.1). The plume model employs a finer spatial resolution of < 1 m.

7.2.3 COUPLING BETWEEN GLACIER AND PLUME MODEL

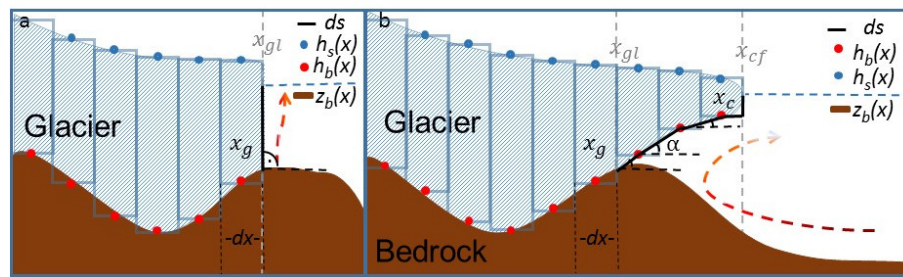


Figure 7.1: Visualization of 1D glacier model with the staggered grid for a) a tidewater glacier and b) a glacier with floating tongue. Red dots indicate where the values of glacier bottom h_b are defined and blue dots where surface elevation h_s of the glacier is defined. They are calculated at $dx/2$ - the half width of each grid cell. Last grounded cell has the coordinate x_g and last floating cell has the coordinate x_c . The grounding line gl_x is determined at the border of the last grounded cell, where the flotation criterion is not yet achieved. After the grounding line, the calculation of submarine melt along the distance ds (thick, black line) is performed with the line plume model. For a floating tongue (b) every grid cell may have a different angle for ds while for a tidewater glacier (a) the angle is set to 90 degrees. The bedrock elevation z_b (brown, thick line) is equal to h_b for the grounded part and is deeper for the floating part of the glacier.

Unlike Amundson and Carroll (2018), who used the maximum melt rate as a frontal ablation factor for tidewater glaciers, we take into account the entire vertical melt rate profile calculated with the plume model. Submarine melting volume flux is calculated for each cell and is applied as a vertical thinning rate on the floating tongue ($x_{g+1} \dots x_c$), or on the last grounded cell (x_g) in the case of tidewater glaciers (no floating tongue). The melt rate m is integrated from the grounding line (position x_{gl}) along the bottom face of the floating tongue (if any), and along the calving face (position x_{cf}) up to sea level (Fig. 7.1), or to the top height of the risen plume (which can stop before sea level). The cumulative melt rate is given by

¹available at <https://sites.google.com/site/ellynderlin/research>

$$M = \int m(s) ds = \int_{x_{gl}}^{x_{cf}} m(h_b(x)) \cdot (\cos \alpha)^{-1} dx + \int_{h_b(x_{cf})}^0 m(z) dz \quad (7.7)$$

where s is the distance coordinate along the tongue bottom and the vertical calving face, h_b denotes bottom ice elevation, and $\cos \alpha$ is the variable tongue slope (calculated from the relation $\tan \alpha = \frac{\partial h_b}{\partial x}$). The integral is distributed over various cells (or only one cell (x_g) in the case of a tidewater glacier, where the first integral term is also zero since $x_{gl} = x_{cf}$), and the volume flux is added to the vertical mass balance term B , along with surface mass balance. Since the plume model does not allow for negative values of α , its minimum value is set to 10^{-6} . If the plume already ceases before reaching the calving front x_{cf} , we calculate a 2nd plume that starts at $h_b(x_{cf})$ with the initial minimum default discharge value of $10^{-6} m^3 s^{-1}$ to assure a background frontal melting.

Subglacial discharge Q was computed off-line using the ice sheet model with explicit treatment of basal hydrology (Section 7.3.3), then applied to the line plume in distributed form $q = Q(W)^{-1}$. It is assumed that plume properties (velocity, temperature, salinity, and thickness) in the coupled model adapt instantaneously to changes in the glacier's shape, subglacial discharge, temperature and salinity profiles of ambient water. The glacier and plume model exchange information at every time step of the glacier model.

7.3 MODEL INPUT

7.3.1 THE CHOICE OF GLACIERS

In this study, we modeled twelve, well-studied Greenland outlet glaciers of different sizes and located in different regions of Greenland (Fig. 7.2). One criterion of this selection is that the glaciers should represent different types of ice flows and different environmental conditions. Also, did we include small marine-terminating glaciers to assure a more realistic upscaling as Goelzer et al. (2013) indicates. Besides that, for most of the chosen glaciers, Enderlin and Howat (2013) estimated melting to calving ratio which we use as an additional constraint on the choice of modeling parameters.

7.3.2 GLACIER GEOMETRY

For each individual glacier, bedrock elevation and width were determined by analyzing cross-sections taken at regular intervals along the glacier flow, generally covering a large portion of the glacier catchment area (Perrette et al., in prep). In each cross-section, the procedure comes down to calculating a flux-weighted average for bedrock elevation, ice velocity U and thickness H , and choose the glacier width W such that the flux F through the cross-section is conserved, i.e. $W = F/(UH)$ (Perrette et al., in prep). We use the BedmACHInev2 data for bedrock topography (Morlighem et al., 2014). Fjord bathymetry was extended manually by considering available data (Mortensen et al., 2013; Schaffer et al., 2016; Dowdeswell et al., 2010; Syvitski et al., 1996; Rignot et al., 2016). For ice velocity we use data from Rignot and Mouginot (2012). The resulting glacier profiles are depicted in Fig. 7.3.

7 Modeling the response of Greenland outlet glaciers to global warming using a coupled flowline-plume model

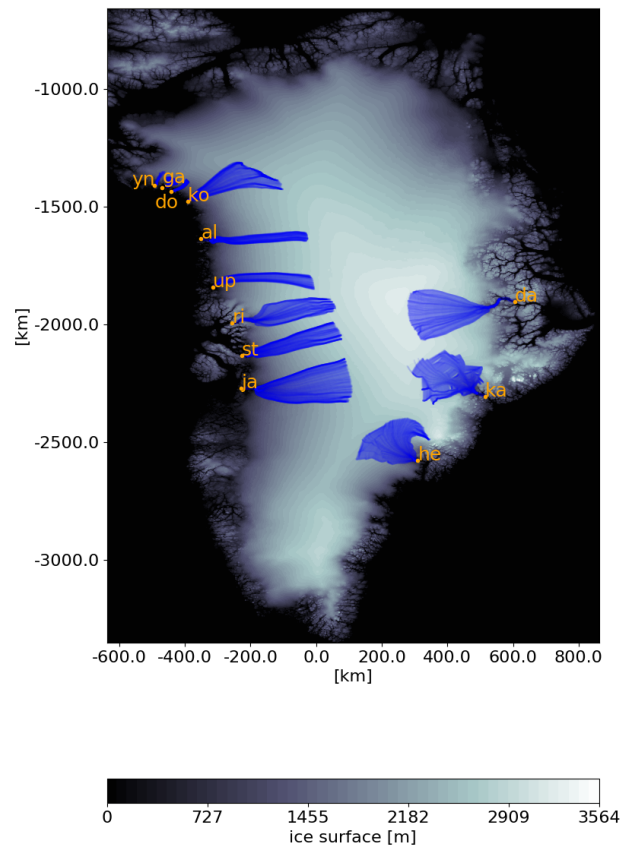


Figure 7.2: Terminus location (orange dot) with the catchment area (blue) of the twelve investigated glaciers: Alison Glacier (al), Daugaard-Jensen Glacier (da), Docker-Smith Glacier (do), Gade (ga) Helheim Glacier (he), Jakobshavn-Isbrae (ja), Kangerlussuaq Glacier (ka), Kong-Oscar Glacier (ko), Rink-Isbrae (ri), Store Glacier (st), Upernavik North Glacier (up), Yngvar-Nielsen Glacier (yn)

7.3.3 SUBGLACIAL DISCHARGE AND GLACIER SURFACE MASS BALANCE

To force the plume model, we use monthly averaged subglacial discharge. Subglacial discharge represents the sum of basal melt, water drainage from the temperate layer and surface runoff. The former two sources are computed directly in the ice sheet model (Calov et al. 2018). In reality surface runoff can travel along the ice surface until it either reaches an existing connection to the bedrock (e.g. crack) or it accumulates in a supraglacial lake that eventually drains, making a new connection. However, these processes are too complex and still poorly understood. This is why in our relatively coarse (5 km) resolution ice sheet model (Calov et al., 2018), we neglect these short scale processes and assume that runoff penetrates directly down to the bedrock. The surface runoff and SMB anomalies for present day and future scenarios are taken from experiments with the regional climate model MAR (Fettweis et al., 2013) and corrected for the future surface elevation

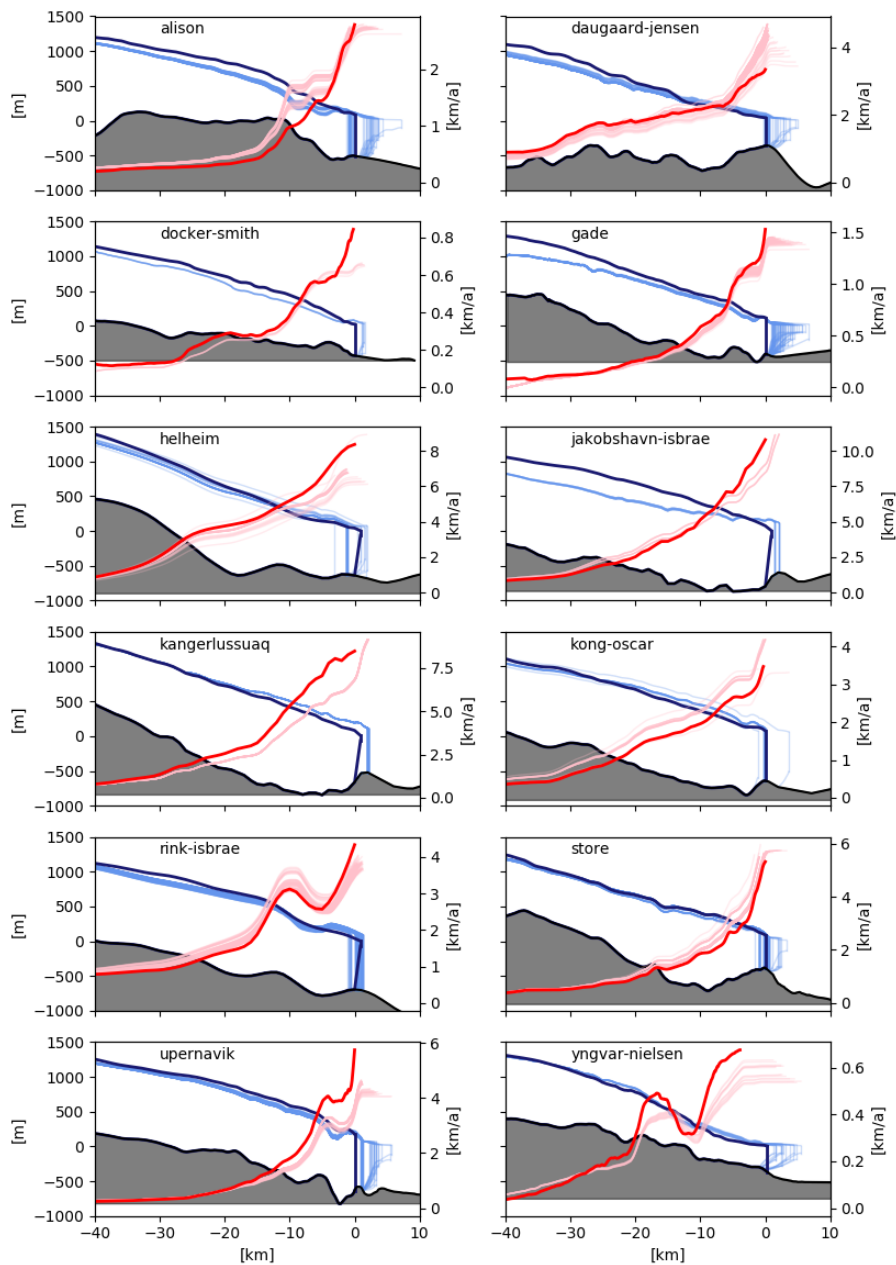


Figure 7.3: Glacier thickness (thick, blue) and velocity profile (thick, red) for the last 40 km to the grounding line from the derived geometry of the dataset published by Morlighem et al. (2014) and Rignot and Mouginot (2012). The resulting profiles of all stable states simulated by the line-plume glacier-flowline model are depicted in transparent lines.

change (Calov et al., 2018). The entire water (runoff, basal melt, and water from the temperate layer) is routed by the hydraulic potential using a multi-flow direction flux routing algorithm, as

described in (Calov et al., 2018). All water transfer is assumed to be instantaneous. Water that passes the grounding line (defined by the ice mask from SICOPOLIS) is assigned to the closest glacier within a maximum distance of 50 km.

In our future scenarios when simulating subglacial discharge we account for changes in surface runoff, basal melt, and ice sheet elevation but neglect the effect of grounding line retreat. This means that we route the subglacial discharge always to the present-day position of the grounding line.

In this study, we use a single scenario for future surface runoff and SMB change, namely, a simulation with the regional model MAR nested in the global GCM MIROC5 model forced by the RCP 8.5 scenario. Among the CMIP5 models, MIROC5 simulate climate change which leads to a medium contribution of GrIS to future SLR (Calov et al., 2018). To correct for possible model biases in the future scenarios for surface runoff and SMB, we added the simulated MIROC5 anomalies to the reference climatology simulated for the same period with the MAR model forced by ERA reanalysis data. We also corrected model surface runoff and SMB for changes in surface elevation by applying the gradient method of Helsen et al. (2012) as described in Calov et al. (2018). The surface runoff R over the ice sheet (SICOPOLIS) is determined as

$$R(x, y, t) = R_{\text{MAR(REAN)}}^{\text{Clim 1961-1990}}(x, y) + (R_{\text{MAR(MIROC)}}(x, y, t) - R_{\text{MAR(MIROC)}}^{\text{Clim 1961-1990}}(x, y)) + \left(\frac{\partial R}{\partial z} \right)_{\text{MAR(MIROC)}}(x, y, t) \Delta h_s(x, y, t), \quad (7.8)$$

where the runoff $R(x, y, t)$ on every grid cell (x, y) at any time t is calculated by the climatological mean from 1961–1990 of MAR (forced by reanalysis data) $R_{\text{MAR(rean)}}^{\text{Clim 1961-1990}}(x, y)$ plus the anomaly of the runoff relative to the climatological mean for the same period of time obtained by MAR forced with MIROC5 ($R_{\text{MAR(CMIP5)}}(x, y, t) - R_{\text{MAR(CMIP5)}}^{\text{Clim 1961-1990}}(x, y)$). For ice surface evolving in time $\Delta h_s(x, y, t) = h_s^{\text{obs}}(x, y) - h_s(x, y, t)$, the vertical gradient $\left(\frac{\partial R}{\partial z} \right)_{\text{MAR(MIROC)}}(x, y, t)$ determined for every time step, is additionally applied to accounting for the increase in surface runoff. The observed surface elevation h_s^{obs} of the ice sheet is taken from Bamber et al. (2013). Negative runoff values are set to zero. The correction of runoff for elevation change can be important in some case since as it was shown in Amundson and Carroll (2018), for tidewater glaciers, large and rapid changes in glacier volume can lead to a high increase in runoff due to surface lowering.

For the present-day condition, SMB is calculated from relaxation to observed surface elevation h_s^{obs} , with a different relaxation time scale τ for each glacier (see section 7.4.1):

$$\text{SMB} = \frac{h_s^{\text{obs}} - h_s}{\tau} \text{ in m/yr.} \quad (7.9)$$

We refer to this flux as implied SMB, calculated during the spinup experiment. For future scenarios, we added the anomaly of the SMB (relative to the year 2000) to the implied SMB. The anomaly for each grid cell of the glacier was computed from interpolation of the MAR anomaly of the centerline of the individual glacier and additionally corrected for the glacier elevation change similarly to the surface runoff (Eq. 7.8), but for the SMB-calculation, Δh_s is the glacier elevation change compared to present-day, assuming that the derived glacier shape from the present-day

dataset is for the year 2000. The time series of cumulative SMB (without surface correction) and the annual subglacial discharge for each glacier are shown in the supporting information (Fig. S1 and Fig. S2)

7.3.4 FJORD TEMPERATURE AND SALINITY PROFILES: CTD MEASUREMENT AND OCEAN REANALYSIS DATA

Determining vertical temperature and salinity profiles, which are the input for the plume model, is a challenging task. Measurements inside Greenland fjords are rare and do not cover all of them. For some fjords, several conductivity-temperature-depth (CTD) measurements exist, but they are mostly infrequent and often not performed close enough to the calving front. Hence, the question arises on how to treat fjords, where no CTD measurements are available. A possible solution is to use ocean reanalysis data. Here we use the TOPAZ Arctic Ocean Reanalysis data² (Xie et al., 2017) and compare them with existing CTD measurements as well as analyze potential impact of the differences between reanalysis and CTD profiles on the glacier response to climate change. The TOPAZ dataset was produced with the ocean model HYCOM using in situ measurements and satellite data sets. It covers the time span from 1991–2013 with a spatial resolution of 12.5 km. Below 200 m depth an error $> 1^{\circ}\text{C}$ and > 0.1 psu can occur. The dataset does not resolve the Greenland fjords and covers only the open ocean and continental shelf. It is known that the vertical T-S profile inside the fjords can resemble the profile in the open sea (Straneo et al., 2012; Straneo and Heimbach, 2013; Inall et al., 2014). However, often a grid cell in the ocean reanalysis data can be located hundreds of km from the fjord mouth, where other ocean conditions might prevail.

Figure 7.4 illustrates this problem for the Kangerlussuaq glacier: much colder temperatures are measured by CTDs at depths below 400 m inside of the fjord compare to the measurements at the same depths but far outside of the fjord. A calculation with the line plume shows that the melt rate with the mid-fjord CTD (white dot, and dashed line at ~ 210 km distance in panel b) would increase by 80 % when melt rate is calculated using the outermost CTD (white dot, at ≈ 400 km distance) for a typical subglacial summer discharge. Furthermore, the presence of sill (s) in the fjord and fjord circulation can affect significantly the T-S profile in the vicinity of the glacier front.

It is also important to note that T-S profiles obtained from CTD measurements have to be treated with caution because they represent only a ‘time shot’ of fjord properties which vary in time significantly (Jackson et al., 2014). Due to all these uncertainties, here we test how sensitive the model response is to the chosen present-day T-S profile when carrying out future climate change simulations (Section 7.5). To this aim, we first compared temperature-salinity profiles of the reanalysis data to available CTD measurements inside the fjords made as close as possible to the glacier fronts. We constructed the T-S profiles from the reanalysis dataset by detecting the closest grid-cell to the fjord mouth. For comparison, we used the reanalysis data at depth 200, 400 and 700 meters, since they represent typical depths of Greenland fjords and glacier grounding lines.

Figure 7.5 and 7.6 compare the temperature at these depths from reanalysis data with available CTD profiles measured over past several decades. Since Greenland is surrounded by the conti-

²http://marine.copernicus.eu/services-portfolio/access-to-products/\setbox0=\hbox{0}\hboxto\wd0\option=com_csw&view=details&product_id=ARCTIC_REANALYSIS_PHYS_002_003

7 Modeling the response of Greenland outlet glaciers to global warming using a coupled flowline-plume model

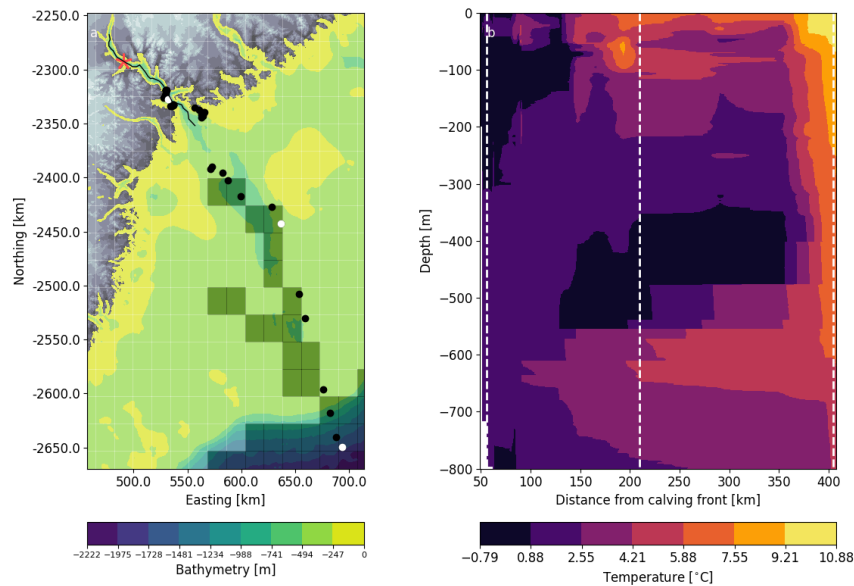


Figure 7.4: a) Bathymetry around Kangerlussuaq glacier (red star indicates glacier terminus). Black dots indicate the location of the CTD measurements in made September 2004. White dots show the location of CTD profiles used for the melt rate calculations. Grid indicates the resolution of the reanalysis data and grey shaded squares show which reanalysis data points have a minimum depth of 400m. b) Vertical temperature distribution as a function of the distance from the glacier terminus, obtained by interpolation of the CTD profiles. White dashed lines correspond to the position of the white-marked CTD positions in panel a.

nenal shelf with typical depths of 200-400 meters, most of the 700-meter depth points in reanalysis data are located outside the fjords in the deeper ocean, far away from the glacier mouth as shown in Fig. 7.7 for Store Glacier. For the Store Glacier, the temperature at 700m depth inside the fjord measured by CTD is much warmer than the temperature in reanalysis data at the same depth, which can potentially be explained by the shallow continental shelf. As Schaffer et al. (2017) showed, for the Nioghalvfjærdsfjorden Glacier, the continental shelf works similarly to a sill that blocks waters of greater depths and favors water masses above the shelf to pass into the fjord. For all of the investigated glaciers, we found better matching profiles of reanalysis to CTD profiles if we neglected the reanalysis temperature of 700m-depth locations (mostly outside continental shelf) and used instead the 400m-depth temperature (mainly on the continental shelf) for all depths below 400 m. If the grounding line depth was larger than 400 m, temperatures below that depth were assumed to be equal to the temperature at 400m- depth in the reanalysis data. The corresponding salinity profile at the same 400m-depth data point was equally modulated as the temperature profile. The location of the reanalysis data point is listed in Table 1 of the supporting information.

To produce a “present-day” T-S profile that resembles inside-fjord conditions, we averaged temperature and salinity from reanalysis data over period 1990–2010 in the grid cell closest to corresponding fjord mouth and with a depth of at least 400 m. If the fjord does not have ‘blocking’

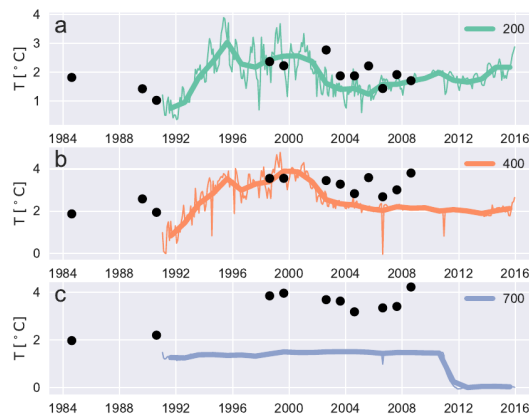


Figure 7.5: Monthly (thin lines) and annual mean (thick lines) of ocean temperature from reanalysis data of the closest point to fjord of Jakobshavn-Isbrae that has a minimum depth of a) 200m b) 400m and c) 700m depth. Location of these points differ due to the different area coverages for the corresponding depths (700m is mostly outside of continental shelf). Black dots show CTD measurements at the same depth but inside or close to the fjord.

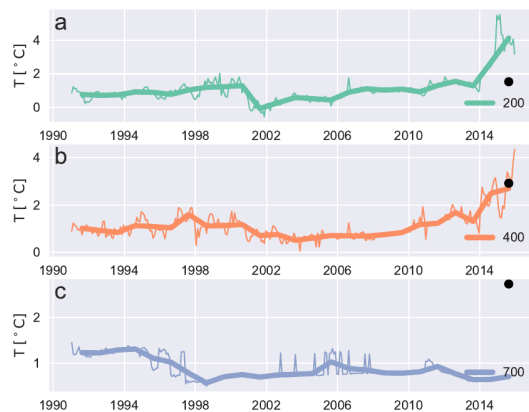


Figure 7.6: Same as in Fig. 7.5 but for Store Glacier.

sills, we extrapolate the water properties at 400m depth down to depths of the grounding lines as described above. For these investigated glaciers, we found no sills shallower than the 400m depth in the data set.

These T-S profiles constructed from the reanalysis data, as well as those from the CTD measurements, were used as the boundary conditions in the plume model. Figure 7.8 shows that the vertically averaged temperatures derived from reanalysis data are colder than those from CTD measurements for most of the selected glaciers. This bias also remains when choosing reanalysis

7 Modeling the response of Greenland outlet glaciers to global warming using a coupled flowline-plume model

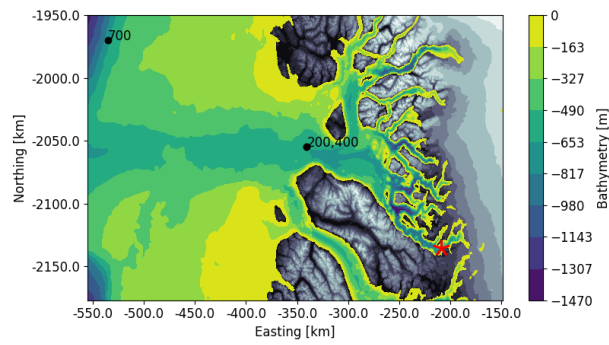


Figure 7.7: Bathymetry and bedrock data close to the terminus of Store Glacier (red star). The labels 200, 400 and 700 indicate where the reanalysis data closest to the glacier with the depth of 200 m, 400 m and 700 m were located.

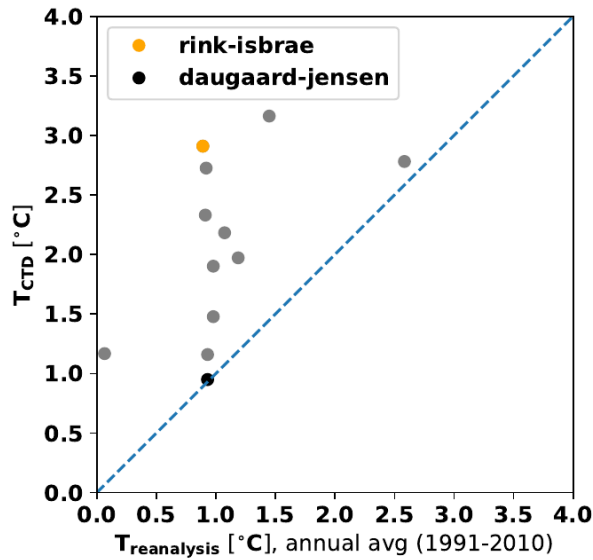


Figure 7.8: Depth-averaged temperature of CTD measurements closest to glacier front, inside the fjords (y-axis) and Reanalysis data of extrapolated 400m-depth points, averaged from 1991 -2010 (x-axis) for all 12 glaciers.

temperature for the same periods when the CTD measurements were taken (not shown). In the following section, we investigate how these biases may affect glacier response to future climate change.

For the simulations of the future, we prescribed simple scenarios for the ocean temperature anomalies based on temperature trends simulated by several CMIP5 models (GFDL-ESM2G, MPI-ESM-LR, and HadGEM2-CC). We use again the closest 400m-depth-point neighbor of each CMIP5 model dataset to the fjord mouth. From this model cell, the temperature trend is derived

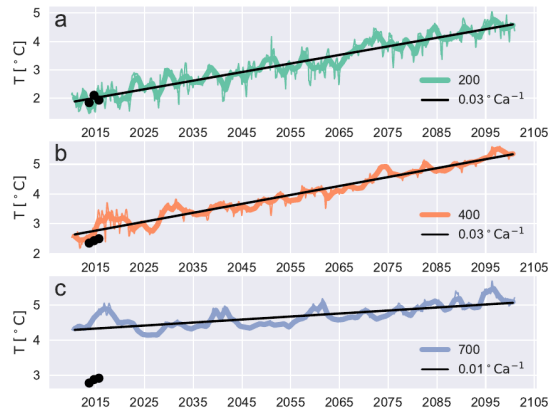


Figure 7.9: Monthly ocean temperature and centennial trend from the CMIP5 model MPI-ESM-LR in the closest points to the fjord of Rink Isbrae that have a model depth of at least a) 200m b) 400m and c) 700m depth. Black dots show CTD measurements at the same depth but inside the fjord.

with linear regression as illustrated in Fig. 7.9. The trend and cell location for each glacier and CMIP5 model are listed in Table S1 of the supporting information, while the resulting minimal and maximal temperature trend for each glacier is listed in Table 7.1.

Table 7.1: Minimal and maximal ocean temperature trend derived by three CMIP5 Models close to each glacier fjord at 400m depth. Detailed information are listed in table S1.

glacier name	$\Delta T_{\min} (^{\circ}\text{C}/100\text{a})$	$\Delta T_{\max} (^{\circ}\text{C}/100\text{a})$
Daugaard-Jensen	3	5
Helheim Glacier	2	3
Jakobshavn Isbae	2	4
Kangerlussuaq Glacier	3	4
Rink Isbrae	1	3
Store Glacier	1	3
Kong Oscar Glacier	1	3
Alison Glacier	1	3
Upernavik Isstrom	1	3
Yngvar Nielsen	1	3
Docker Smith Glacier	1	3
Gade Glacier	1	3

7.4 EXPERIMENTAL SETUP

7.4.1 SELECTION OF MODEL PARAMETERS AND MODEL SPIN UP

First, the stand alone glacier model (without the plume parameterization) was pre-calibrated to reproduce observed surface elevation, grounding-line position and velocity profile assuming a constant prescribed submarine melt rate. Dynamic parameters E , W_s , A_s and q were varied for this purpose (affecting basal shear stress, lateral stress, and calving front boundary condition), along with the freshwater depth in crevasses d_w and the constant melt rate m , for each glacier separately. For most glaciers we use 20 or 30 years for the surface relaxation time scale τ for SMB (Eq. 7.9), but for some glaciers (e.g. Daugaard-Jensen) τ was set to 100 years.

Once the four dynamic parameters and the relaxation time scale are set, we switch to the coupled glacier-plume model. For the spinup experiments, we used monthly subglacial discharge for the year 2000. Vertical temperature and salinity profiles in these experiments were taken from recent CTD data or reanalysis data, averaged over the time interval 1990–2010, and held constant. Thus, the only factors affecting submarine melt profile in spin-up experiments are the depth of grounding line and the shape of the floating tongue (if present).

We generate an ensemble by varying freshwater depth in crevasses d_w and the plume scaling parameter β (in a range from 0.3 to 3), which control calving and submarine melting, respectively. We run the coupled model for each combination over 100 years, so that the glacier is close to an equilibrium state and we exclude model versions whose grounding line is further than 2 km from the observed grounding line, as diagnosed from the 1D profile, or which displays a low-frequency oscillatory behaviour with advancing glacier front over the last 20 years. For the glaciers for which partition between calving and submarine melting was available from Enderlin and Howat (2013), we used this partition as an additional constraint for the model parameter combinations.

7.4.2 FUTURE CLIMATE SCENARIOS

For all future simulations, we used valid combinations of model parameters and corresponding initial conditions obtained at the end of 100-yrs spin-up runs. The anomalies of SMB were derived from the regional climate model MAR simulations as described in Section 7.3.3 (Fig. S1). To compute the submarine melt rate, we use the minimal and maximal ocean temperature trends for each glacier 7.3.4 listed in Table 7.1 (Section 7.3.4). The subglacial discharge was prescribed on a monthly time step with the derived subglacial discharge data from SICOPOLIS (Calov et al., 2018) for each glacier individually 7.3.3 (yearly values depicted in Fig. S2).

All forcing scenarios were applied for the years 2000–2100. In addition, we run the model for 100 years with zero anomalies of temperature, SMB, and subglacial discharge to determine unforced model drift.

To express ice volume loss in sea level rise equivalent we used the multiplication factor t under the assumption of oceans occupying $A_{\text{ocean}} = 360 \cdot 10^6 \text{ km}^2$:

$$t = \frac{\rho_{\text{ice}}}{\rho_{\text{fw}} A_{\text{ocean}}} \quad (7.10)$$

leads to a SLR of $2.55 \cdot 10^{-3} \text{ mm}$ for 1 km^3 of ice volume V_{SLR} .

The contributing ice volume V_{SLR} is calculated with the total glacier volume V_{glacier} subtracted by the floating ice volume V_{fl} , ice volume under sea level V_{uSL} and the additional 12

$$V_{\text{SLR}} = V_{\text{glacier}} - V_{\text{fl}} - V_{\text{uSL}} \frac{\rho_{\text{sw}}}{\rho_{\text{ice}}}, \quad (7.11)$$

with the density of ice $\rho_{\text{ice}} = 917 \text{ kg m}^{-3}$, sea water $\rho_{\text{sw}} = 1028 \text{ kg m}^{-3}$ and fresh water $\rho_{\text{fw}} = 1000 \text{ kg m}^{-3}$.

7.5 RESULTS

7.5.1 PRESENT-DAY STATE

The simulated glacier thickness and velocity profiles for the different submarine melting and calving ratios are depicted in Fig. 7.3. We found that for some glaciers the grounding line demonstrates a high sensitivity to the melting/calving ratio, while others are primarily controlled by their bedrock topography and have relatively small changes in their grounding line position over the whole melting/calving- range. The Gade and Upernavik North glaciers are, for example, representative of the latter case (Fig. S3). The simulated velocity profiles (Fig. 7.3) for Gade Glacier and Jakobshavn-Isbrae required a slightly thinner glacier than derived by the geometry of the dataset. We were only able to achieve stable states for Jakobshavn-Isbrae with the reanalysis dataset, since CTD measurements showed significantly warmer temperatures, and the resulting higher submarine melt rate in our simulations would lead to the retreat of the glacier on the retrograde bedrock.

Table 7.2: Each investigated glacier with the mean grounding line discharge from observation $\text{Flx}_{\text{gl}}^{\text{*E}}$ (Enderlin and Howat, 2013) and from the stable state simulations Flx_{gl} . The melt flux range for floating termini from all present-day simulations MeltFlx and from the observational data $\text{MeltFlx}^{\text{*E}}$ is calculated with the error ranges in Enderlin and Howat (2013) but with the condition $0 < \text{MeltFlx}^{\text{*E}} < \text{Flx}_{\text{gl}}^{\text{*E}}$. The respective ratio of melt flux /grounding line discharge in % is listed in the last to columns. Glaciers with * indicate were the melt rate partition of the simulation does not overlap with the error range of Enderlin and Howat (2013). Melt fluxes of are for floating tongue and thus $\text{MeltFlx} = 0$ indicates tidewater glaciers. Store Glacier is not examined in Enderlin and Howat (2013).

glacier	$\text{Flx}_{\text{gl}}^{\text{*E}}$ $10^9 \text{ m}^3/\text{a}$	Flx_{gl} $10^9 \text{ m}^3/\text{a}$	$\text{MeltFlx}^{\text{*E}}$ $10^9 \text{ m}^3/\text{a}$	MeltFlx $10^9 \text{ m}^3/\text{a}$	$\text{MeltFlx}^{\text{*E}}/\text{Flx}_{\text{gl}}^{\text{*E}}$ %	$\text{MeltFlx}/\text{Flx}_{\text{gl}}$ %
Alison	6.83	6.25 – 6.55	0.82 – 6.41	0.00 – 4.77	12 – 94	0 – 76
Daugaard-Jensen	9.34	7.36 – 8.45	4.12 – 9.34	0.00 – 5.26	44 – 100	0 – 69
Docker-Smith	1.06	1.05 – 1.07	0.00 – 0.87	0.22 – 0.66	0 – 82	20 – 62
Gade	4.85	2.63 – 2.81	0.00 – 4.85	0.16 – 2.14	0 – 100	6 – 77
Helheim	29.16	20.94 – 25.94	0.19 – 6.90	0.00 – 8.39	1 – 24	0 – 36
Jakobshavn Isbrae*	43.03	36.81 – 37.14	21.11 – 32.91	0.00 – 0.00	49 – 76	0 – 0
Kangerlussuaq	38.80	24.51 – 24.58	0.00 – 6.83	0.00 – 0.00	0 – 18	0 – 0
Kong-Oscar	11.86	10.34 – 12.86	3.06 – 6.28	0.00 – 2.64	26 – 53	0 – 26
Rink-Isbrae	10.95	11.20 – 12.25	0.00 – 6.85	0.00 – 0.00	0 – 63	0 – 0
Store	-	10.54 – 11.31	-	0.00 – 8.38	-	0 – 77
Upernavik North	17.12	7.48 – 7.87	5.81 – 11.20	0.03 – 5.92	34 – 65	0 – 78
Yngvar Nielsen	0.69	0.53 – 0.57	0.00 – 0.69	0.08 – 0.42	0 – 100	15 – 76

Table 7.2 provides a comparison to observational data derived by Enderlin and Howat (2013). Only the glaciers Kong-Oscar and Docker-Smith showed a grounding line flux Flx_{gl} matching the observational data. All other glaciers have smaller grounding line fluxes than in Enderlin and Howat (2013). However, it should be noted that many glaciers accelerated since 2000, so it is not clear whether the fluxes reported by Enderlin and Howat (2013) are true equilibrium fluxes. Additionally, Enderlin and Howat (2013) derived submarine melt rates for the floating termini of the glaciers. Note that Enderlin and Howat (2013) could not account for vertical glacier fronts due to their methodological approach. For a direct comparison to Enderlin and Howat (2013), we calculate MeltFlx of the simulated glaciers by only considering the mass loss from the floating tongue induced by submarine melting. The ratios of submarine melting to grounding line discharge of our simulations lie within the uncertainty ranges determined by Enderlin and Howat (2013). However, these uncertainties are quite large and thus allow broad parameter combinations for some glaciers. For Jakobshavn, a high calving flux was needed in order for the coupled glacier-plume model to obtain similar velocities as the present-day velocity profile (Fig. 7.3) derived from the dataset. This resulted in calibrated glacier profiles without any floating terminus (and a numerical $\text{MeltFlx} = 0$), which was not observed by Enderlin and Howat (2013). Thereafter, this simulated glacier does not match the ratio of submarine melting to grounding line discharge ratio determined by Enderlin and Howat (2013) ($\text{MeltFlx}^{\text{E}}/\text{Flx}_{\text{gl}}^{\text{E}}$ Table 7.2). The high calving flux required in order to obtain the precise grounding line position might result from inconsistency with bedrock data or an information loss received by the flux-weighted averaging.

7.5.2 FUTURE SIMULATIONS

After obtaining the present-day state, we then ran all valid model versions for 100 simulation years, applying MAR SMB anomalies, monthly subglacial discharge and two scenarios for ocean temperature change (minimum and maximum) as forcing. All results shown here have the model drift subtracted from the calculated values. The glaciers' response to climate change strongly depends on the combination of model parameters and scenarios, resulting in high uncertainty ranges. The simulations that led to a median-range³ SLR for each glacier is depicted in Figure 7.10. After 100 years, some glaciers retreat entirely and become land-terminated (Alison, Daugaard-Jensen, Kangerlussuaq, Store), while others barely show a change in the position of the grounding line (Helheim). The individual contribution of each glacier to SLR for the median-range³ SLR experiments is shown in Fig. 7.11 a. Jakobshavn-Isbrae shows the most significant contribution to SLR, due to the big catchment area and large retreat, followed by Kangerlussuaq Glacier due to its full retreat.

These median-range SLR experiments were forced by changes in SMB with the surface elevation feedback, ocean warming T and increased subglacial discharge Q . Together, all 12 glaciers add up to almost 14 mm SLR at the year 2100. To quantify the individual role of the forcing factors, the same model-experiments of the mid-range simulations were run excluding the different forcing factors. We found that from the 14 mm over 80 % of SLR is caused by increased submarine melting due to the additional ocean warming T and increased subglacial discharge Q (Fig. 7.11 b). Thereby both factors, (T and Q), contributed an equally high amount in SLR. The remaining 15 % of the 14mm SLR are attributed to the glacier's response to changes in SMB (Fig. 7.11 b, orange

³median for an odd number of simulations, the first value of higher half for an even number of simulation

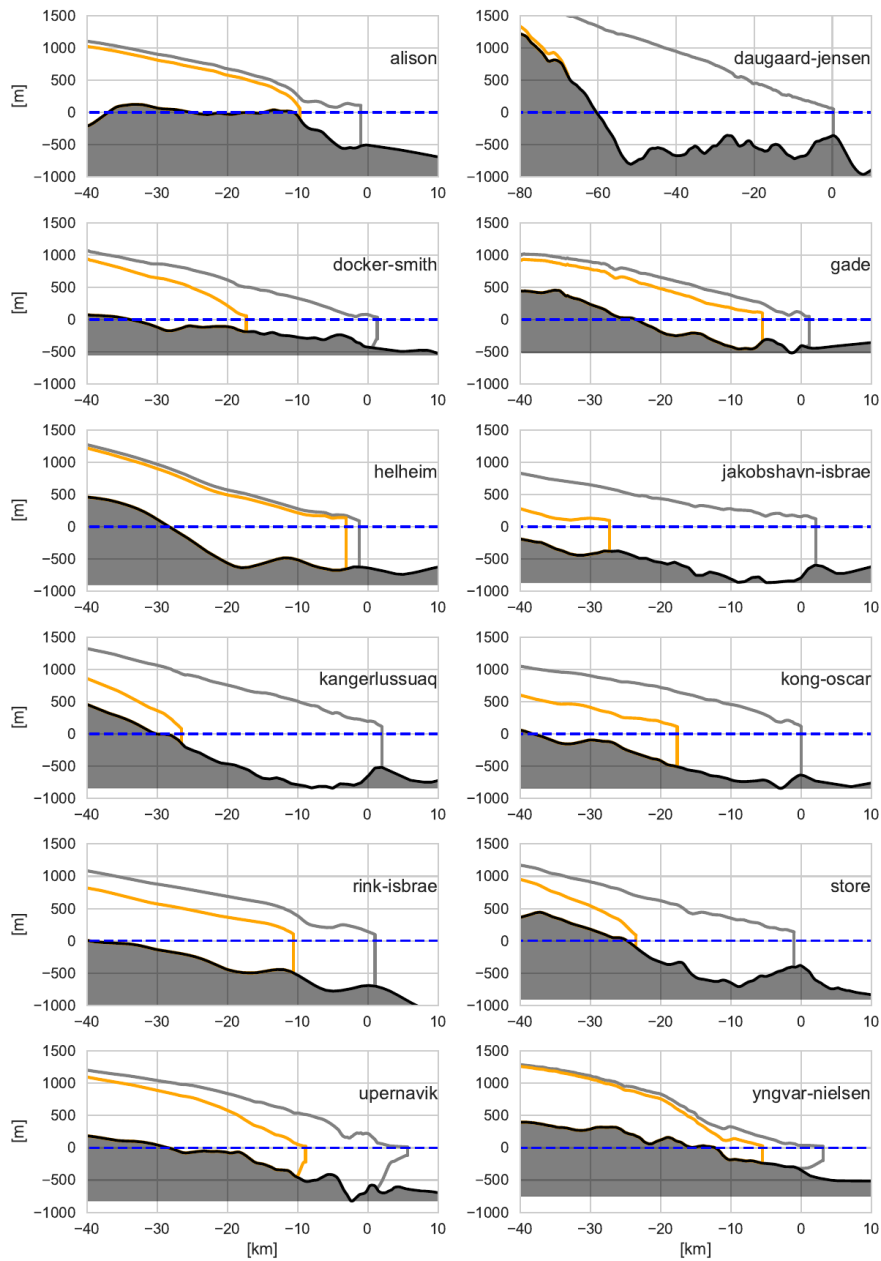


Figure 7.10: Retreat of median-range³ SLR scenario for RCP 8.5 forcing scenarios (SMB and ocean temperature and subglacial discharge) for all 12 glaciers at 2100 (orange). Corresponding initial states are depicted in grey. Daugaard-Jensen, showed full retreat with over 80 km.

curve). This is quite substantially, considering the fact that the SMB-forcing alone derived from MAR (without the glacier's response) has an almost negligible effect on SLR (Fig. 7.11 b, brown curve). For some glaciers, the cumulative SMB (SLR ignoring glacier response) is even increas-

7 Modeling the response of Greenland outlet glaciers to global warming using a coupled flowline-plume model

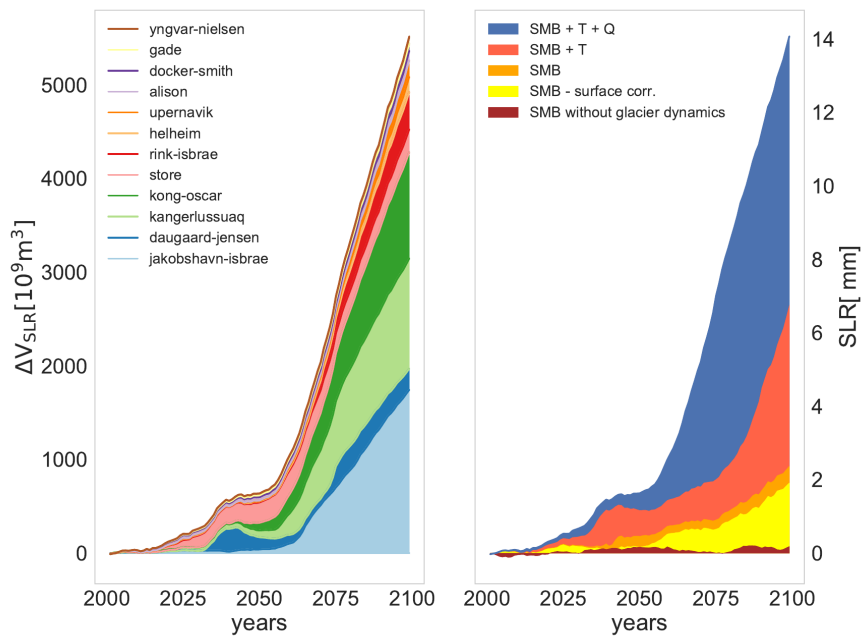


Figure 7.11: Cumulative sea level rise of median-range³ SLR scenario from Fig. 7.10 for all 12 glaciers. The glaciers' response to complete future forcing scenario (smb, subglacial discharge Q and ocean temperature T in blue), without subglacial discharge forcing (SMB + T ; pink), with SMB forcing only (orange) and excluding the surface elevation feedback (SMB, no dz; yellow). The SMB forcing vom MAR is calculated over the whole present-day catchment area of all glaciers (brown).

ing towards the end of this century (Fig S1). The increased mass loss by glacier dynamics origins if surface mass loss is concentrated at the glacier terminus, resulting in thinning and potentially triggering glacier retreat. Whether this, anyhow minor SMB forcing (brown curve) is corrected for surface elevation feedback (see Section 7.3.3) or not, is of no significance in respect to SLR (Fig. 7.11 b, orange and yellow curve).

These estimates of the role of separate factors (changes in SMB, ocean temperature and subglacial discharge) are, however, the result of the cumulative SLR of all glaciers. Each individual glacier may respond differently to the single forcing factor. For instance, the Kong-Oscar Glacier (Fig. 7.12) is slightly gaining mass with the SMB forcing and shows a retreat by 10 km and contribution 1 mm to SLR only due to ocean warming. When the increase in subglacial discharge is considered additionally to the same ocean warming, the glacier retreats another 10 km and contributes to approximately 3 mm of SLR.

At the same time, the Yngvar-Nielson Glacier (Fig. 7.12) is already retreating significantly in the experiment with the SMB forcing alone. Ocean warming and increased subglacial discharge also contribute to SLR, but for Yngvar-Nielson the largest SLR contributor is the SMB change. Above we discussed only median-range scenarios, but the uncertainty ranges are crucial when predicting SLR. Therefore, Fig. 7.14 shows the first and third quartile together with the median

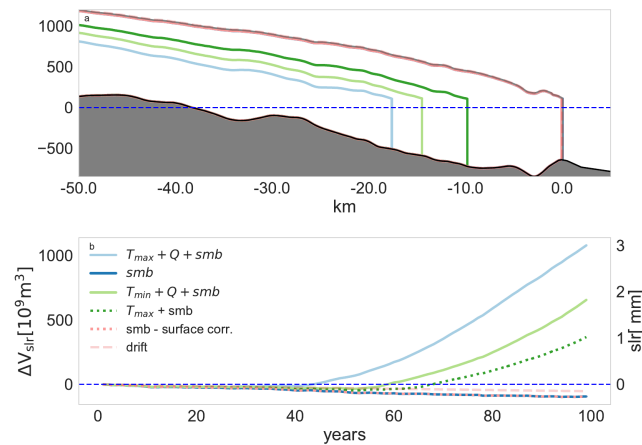


Figure 7.12: a) Kong-Oscar Glacier with a representative medium-slr retreat scenario applying forcing factors as subglacial discharge Q , ocean temperature T , surface mass balance smb with and without accounting for surface elevation correction ($smb - surface\ corr.$) for the medium SLR scenario. The corresponding SLR of each experiment is displayed in panel b).

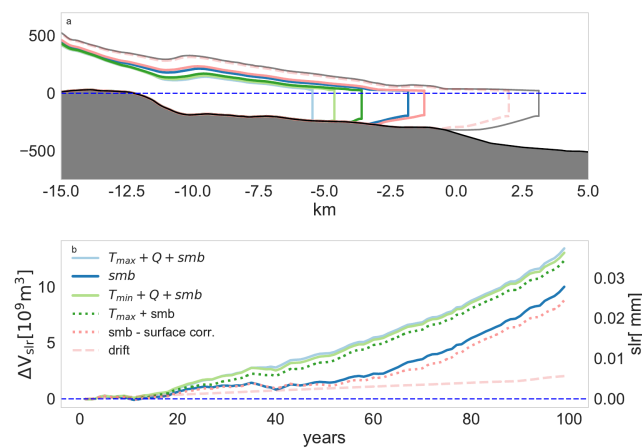


Figure 7.13: Same as 7.12 for the medium SLR scenario but for Yngvar Nielsen Glacier.

values of the individual glacier's contributions to SLR for all sets of valid model realizations and full forcing ($SMB + T$ (max/min) + Q) against the simulated present-day discharge. Their potential SLR and grounding line retreat are listed in Table 7.3 and 7.4. Figure 7.14 shows a correlation between present-day grounding line discharge and the contribution to future SLR. Jakobshaven and Kong-Oscar show the largest uncertainties. We investigate whether the uncertainty range results from the range of temperature forcing (T_{min}/T_{max}) or model parameters by distinguishing for experiments with (T_{min}/T_{max}) in Fig. 7.15. Figure 7.15 a shows that future SLR and its uncertainty related to SMB forcing alone are rather small (except for Jakobshaven-Isbrae). For glaciers like Daugaard-Jensen and Kong-Oscar, the negative SLR originates from the increase in SMB in

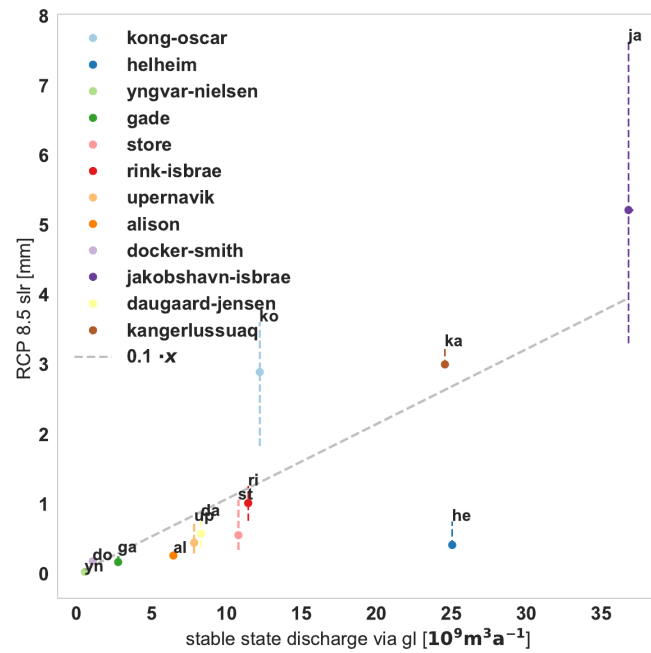


Figure 7.14: First to third quartile (median indicated with a dot) of contribution to SLR under RCP 8.5 for each glacier from Table 7.3 as a function of the present-day grounding line discharge. The future simulations were forced by changes in SMB, subglacial discharge and minimal and maximal ocean temperature trend 7.1. Grey dashed line, indicates a linear function of the present-day grounding line discharge in future SLR for 2100 obtained with an ordinary least square model from the median values. Slope and p-value are $0.1 \text{ mm km}^{-3} \text{ a}$ and 0.27, respectively. The correlation is weak with a correlation coefficient with 0.35.

this region under the RCP 8.5 scenario. Including the forcing factors of submarine melt, T and Q , leads to a relatively high SLR contribution and a high SLR uncertainty range for the Kong-Oscar, Kangerlussuaq, Rink, and Dugaard-Jensen glaciers, Fig. 7.15 shown by the blue columns. Since these high uncertainties arise also with the same forcing (only T_{\min} or T_{\max}), we attribute the major source of uncertainty to the different combinations of the model parameters d_w and β . For each experiment, we also investigated whether the choice of using CTD measurements or reanalysis data for the initial ocean temperature profile had an impact on the potential SLR. For the difference in SLR, we could only detect a slight increase when using reanalysis data instead of CTD data for a few glaciers (Fig. S4)

In spite of these uncertainties, we use the median scenarios from Fig. 7.14 to estimate the relationship between present-day glacial discharge and contribution to SLR for the year 2100 by fitting a linear function determined with the least square method. The derived slope ($0.1 \text{ mm km}^{-3} \text{ a}$) has weak correlation (correlation coefficient 0.35). With this slope and the total flux of all outlet glaciers ($\sim 450 \text{ Gt/a}$ (Enderlin et al., 2014; Rignot et al., 2008a)), the simple linear relationship would imply a total SLR contribution of roughly 5 cm from all Greenland outlet glaciers.

Table 7.3: Median, first and third quartile of SLR contribution from each glacier under RCP 8.5 (smb, subglacial discharge and ocean temperature (min and max)). Values are corrected from drift. Negative values in SLR indicate smb gain.

glacier	SLR mm		
	median	first quartile	third quartile
Alison	0.26	0.26	0.30
Daugaard-Jensen	0.58	0.38	0.83
Docker-Smith	0.18	0.15	0.19
Gade	0.17	0.14	0.30
Helheim	0.41	0.38	0.85
Kangerlussuaq	3.00	2.96	3.26
Kong-Oscar	2.89	1.83	3.61
Rink Isbrae	1.01	0.76	1.26
Store	0.62	0.38	1.10
Upernavik	0.45	0.30	0.76
Yngvar-Nielsen	0.03	0.03	0.03
Jakobshavn Isbrae	5.22	3.30	7.65
sum	14.83	10.88	20.14

Table 7.4: Median, first and third quartile of grounding line retreat from each glacier under RCP 8.5 (smb, subglacial discharge and ocean temperature (min and max)). Values are corrected from drift.

glacier	grounding line retreat km		
	median	first quartile	third quartile
alison	9.17	8.69	10.77
daugaard-jensen	39.26	30.88	39.78
docker-smith	15.13	14.23	16.49
gade	5.85	4.62	15.17
helheim	1.52	1.10	9.63
kangerlussuaq	28.52	28.44	28.53
kong-oscar	17.65	14.61	18.63
rink-isbrae	11.00	10.63	11.15
store	10.02	1.97	22.77
upernavik	6.91	2.68	16.32
yngvar-nielsen	4.69	4.28	5.22
jakobshavn-isbrae	38.57	19.85	40.53
sum	188.28	142.00	235.00

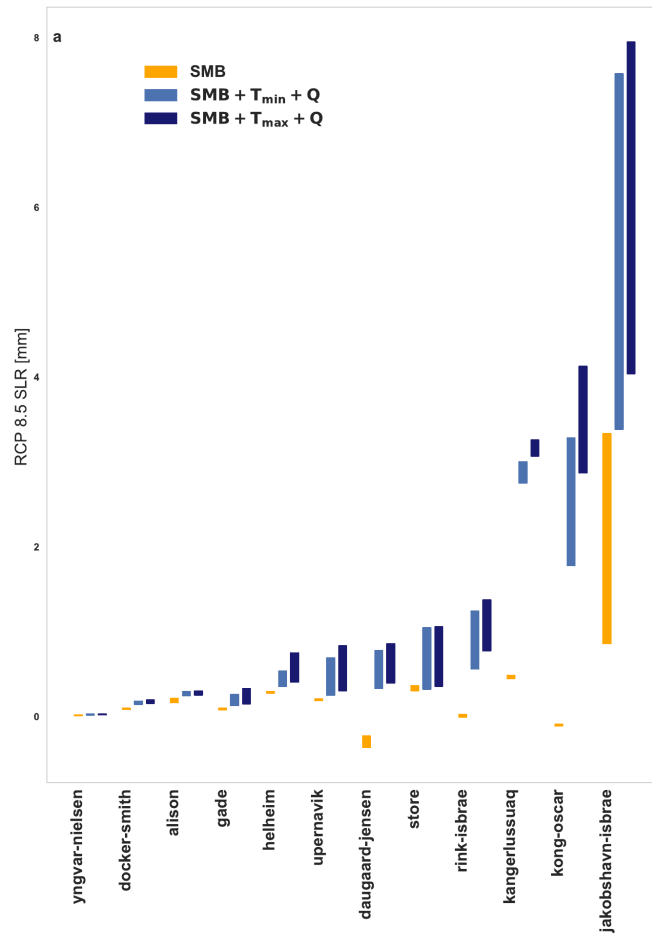


Figure 7.15: First to third quartile of contribution to SLR for each glacier. Future RCP 8.5 scenarios were either forced with SMB changes only (orange) or changes in SMB, ocean temperature (T_{min} and T_{max}) and subglacial discharge (blue).

7.6 DISCUSSION AND CONCLUSIONS

For 12 individual outlet glaciers of the GrIS, we investigated their potential contribution to SLR during the 21st century for the RCP 8.5 scenario. To study the role of future changes in SMB, ocean temperature and subglacial discharge, we used a 1D flowline model with a surface crevasse calving law coupled to a 1D line plume model Jenkins (2011). In our model, the calving flux can be altered by choosing a parameter for the melt water depth in crevasses, and the submarine melt rate can be changed by a scaling factor. We also used two different initial temperature-salinity profiles — one derived from reanalysis data and another from in-situ measurements inside the fjords. For the present-day simulations, we varied the submarine melting and the calving parameter to obtain a glacier profile similar to observations. For all outlet glaciers, we were able to achieve a reasonable agreement between the simulated and observed present-day profiles. However, for the Jakobshavn Isbrae glacier, the simulated submarine melt and grounding line discharge ratio does not agree

with that derived by Enderlin and Howat (2013), as this ice stream could not develop a floating terminus in our simulations.

In order to simulate the future glacial contribution to SLR under the RCP 8.5 scenario, we prescribed changes in SMB and subglacial discharge based on results of the regional climate model MAR. Anomalies of near-fjord ocean temperatures from CMIP5 global climate models served to generate minimum and maximum scenarios for the ocean temperature until year 2100. Simulated SLR contributions for the year 2100 compare well to values from Nick et al. (2013) for Jakobshavn Isbrae. The Kangerlussuaq Glacier exceeds the SLR estimation of Nick et al. (2013) by 2 mm, while for the Helheim Glacier our SLR estimations are below the estimations of Nick et al. (2013). The difference to Nick et al. (2013) can be explained by their different treatment of future calving fluxes (freshwater depth was linked to future runoff) or submarine melting (excluding subglacial discharge). Also, Nick et al. (2013) used the surface elevation and velocity profile from the center line and took the width as the whole catchment area, whereas at Jakobshavn Isbrae, the width was constrained to the width of the trough and the lateral flux was added. By contrast, we use a flux-weighted average of the whole glacier catchment area to represent each individual glacier.

We use a flux-weighted average of the whole glacier catchment area, whereas Nick et al. (2013) used for e.g. Jakobshavn Subarea a narrow channel and added lateral flow.

We also investigated how various forcing factors influence the simulated future SLR. For the ensemble of the 12 glaciers, SLR is sevenfold larger when the changes in subglacial discharge and ocean temperature were added to changes in SMB. This underlines the critical role of oceanic warming for future GrIS contribution to SLR. Moreover, we found significantly larger SLR when the subglacial discharge is allowed to increase in the scenarios. In fact, the amount of SLR attributed to subglacial discharge is similar to the SLR attributed to an increased ocean temperature. Thus, for future projections, both factors affecting submarine melt rate—subglacial discharge and ocean temperature—need to be taken into account. It should also be noted that our 1D flowline model is based on a crevasse depth calving law and thus does not account for undercut calving or buoyancy-driven calving (Benn et al., 2017), which in turn is strongly influenced by submarine melting. This mechanism might act as a further amplifier of glacial mass loss that is not reflected in our results.

Our experiments also reveal large uncertainty ranges, primarily attributed to the different combinations of the two model parameters that determine submarine melting and calving fluxes. Nonetheless, the simulated melt/calving ratios lie within the uncertainty range of observations, and reducing the uncertainties with more precise observational data would probably improve future simulations. On the other hand, our results were not significantly affected by the choice of CTD or reanalysis data when defining the initial ocean temperature and salinity profile. This suggests that accurate process-based models and observational constraints on submarine melt and calving are more important when making projections about future retreat of Greenland outlet glaciers. Additional uncertainty related to dynamic parameters and topography data (bedrock, width) are not included in this study.

Overall, we obtain a total Greenland glaciers SLR contribution of approximately 5 cm when assuming a linear relationship between the glacier's present-day grounding line discharge and future sea level rise. Our result is lower than the estimate in Nick et al. (2013) (6.5–18.3cm) due to the fact that we included smaller marine-terminating glaciers. As Goelzer et al. (2013) argues, these glaciers probably become land-terminating faster than glaciers with a large grounding line

discharge and have less mass influenced by ice-ocean interaction. Therefore we think that our upscaling method for this emissions scenario should not be used past the year 2100. Our simulations considered a constant catchment area for each glacier and did not account for potential lateral inflow from the ice sheet interior. Such increased mass inflow could result in a smaller grounding line retreat and thus decrease our SLR contribution estimate. However, an increased inflow would also result in a broadening of the catchment area, as Goelzer et al. (2013) indicate, which could increase mass loss further upstream. The full impact can only be assessed with experiments in which outlet glaciers and the parent ice sheet are fully coupled. For a first approximation, though, we treat the SLR of 5 cm as additional to that simulated with coarse resolution GrIS ice-sheet models, since the cumulative SMB forcing (without glacier response) over the glaciers' area is negligible. By adding the 5 cm contribution of outlet glaciers to the 8.8 cm simulated by Calov et al. (2018) for the year 2100 using the same climate scenario, we arrive at a total GrIS contribution 13.8 cm. This implies that the dynamical response of Greenland's outlet glaciers to global warming can increase GrIS contribution to SLR by over 50 %.

COMPETING INTERESTS

The authors declare no competing interests.

ACKNOWLEDGEMENTS

This work was funded by Leibniz-Gemeinschaft, WGL Pakt für Forschung SAW-2014-PIK-1. R. C. is funded by the Bundesministerium für Bildung und Forschung (BMBF) grants PalMod-1.1 and PalMod-1.3.

8

A CONFINED–UNCONFINED AQUIFER MODEL FOR SUBGLACIAL HYDROLOGY AND ITS APPLICATION TO THE NORTH EAST GREENLAND ICE STREAM

CONTEXT

This paper presents the newly developed model that is an implementation of the equivalent aquifer approach that is described in Section 3.4. There have been a number of recent models of subglacial hydrology that are able to represent the inefficient as well as the efficient water flow, as these two modes are important for the correct description of the seasonal evolution of the drainage system. Usually they do this by using a continuum approach for the distributed system and then require a secondary framework that describes channels in an explicit and discrete way. The nature of this description makes it necessary to locate potential channels in high-resolution grid, which increases computational cost, which is the main reason why these have so far only been used on small areas. The model by Fleurian et al. (2014) uses a different approach, incorporating two aquifer layers which are tuned in a way so that they resemble the properties of the two different drainage regimes. While this approach already simplifies the handling of subglacial channels and is a good candidate for continental scale modelling, it can generate unphysical negative water pressure. This is due to its assumption that the equivalent aquifer is always saturated.

The model that is presented in the following article drops that assumption and introduces the possibility for the aquifer to become unsaturated as a solution. This is done by including unconfined aquifer flow, as shown in Ehlig and Halepaska (1976) and gives the model its name: Confined–Unconfined Aquifer System (CUAS). The model is similar to the one by Schoof (2010b) in that it uses a uniform representation of channels and cavities. The equations for channel opening and closure (see Section 3.3) are adapted to the geometry following Fleurian et al. (2016) and are used to evolve the transmissivity of the equivalent layer.

The paper presents the model equations and numeric implementation. An artificial geometry is used to test the model and study the sensitivity of model parameters determining the evolution of the system and steady state results as well as the seasonal evolution of the drainage system is shown. It is then applied to the North East Greenland Ice Stream (NEGIS), using the geometry and basal melt from Aschwanden et al. (2016). With the computed effective pressure N the Ice Sheet System Model (ISSM) is used to compute surface velocities as a first application and test if CUAS could be an option for coupled hydrology–ice dynamics computations.

CONTRIBUTION

I developed the model and implemented the code with steady advise from A. Humbert and T. Kleiner. T. Kleiner and V. Aizinger advised me on the numeric implementation. M. Rückamp computed the ice flow velocities for the NEGIS experiment and prepared the velocity comparison figure. I prepared the manuscript with input from all co-authors.

AUTHORS AND AFFILIATIONS

Sebastian Beyer^{1,2}, Thomas Kleiner², Vadym Aizinger^{2,3}, Martin Rückamp², and Angelika Humbert^{2,4}

¹ *Potsdam Institute for Climate Impact Research, Earth System Analysis, Potsdam, Germany*

² *Alfred Wegener Institute, Helmholtz Centre for Polar and Marine Research, Bremerhaven, Germany*

³ *Friedrich–Alexander University Erlangen–Nürnberg, Erlangen, Germany*

⁴ *University of Bremen, Bremen, Germany*

ABSTRACT

Subglacial hydrology plays an important role in the ice sheet dynamics as it determines the sliding velocity of ice sheets. It also drives freshwater into the ocean, leading to undercutting of calving fronts by plumes. Modeling subglacial water has been a challenge for decades, and only recently new approaches have been developed such as representing subglacial channels and thin water sheets by separate layers of variable hydraulic conductivity. We extend this concept by modeling a confined and unconfined aquifer system (CUAS) in a single layer. The advantage of this formulation is that it prevents unphysical values of pressure at reasonable computational cost. We also performed sensitivity tests to investigate the effect of different model parameters. The strongest influence of model parameters was detected in terms governing the opening and closure of channels. Furthermore, we applied the model to the North East Greenland Ice Stream, where an efficient system independent of seasonal input was identified about 500 km downstream from the ice divide. Using the effective pressure from the hydrology model in the Ice Sheet System Model (ISSM) showed considerable improvements of modeled velocities in the coastal region.

8.1 INTRODUCTION

Subglacial water has been identified as a key component in glacial processes, it is fundamental in driving large ice flow variations over short time periods. Recent studies show considerable progress in modeling these subglacial networks and coupling them to ice models. Water pressure strongly influences basal sliding and can therefore be considered a fundamental control on ice velocity and ice-sheet dynamics (Lliboutry, 1968; Röthlisberger, 1972; Gimbert et al., 2016).

Generally, two fundamentally different types of drainage are identified: discrete channel / conduit systems and distributed water sheets or thin films. Distributed flow mechanisms are, for example, linked cavities (Lliboutry, 1968), flows through sediment/till (Hubbard et al., 1995), or thin water sheets (Weertman, 1957); those are considered to be an inefficient and slow system to transport water. Channels (Röthlisberger, 1969; Shreve, 1972; Nye, 1976) are seen as discrete single features or arborescent networks; they usually develop over the summer season when a lot of melt water is available. It is assumed that these channelized or efficient drainage systems able to drain large amounts of water in short time spans are predominant in alpine glaciers and on the margins of Greenland, where substantial amounts of surface melt water are capable of reaching the bed (Broeke et al., 2017). In the interior of Greenland and also in most parts of Antarctica, the water supply is limited to melt due to the geothermal and frictional heating within the ice (Aschwanden et al., 2016) – a circumstance favoring distributed systems.

Seasonal variations of ice velocity have been observed and attributed to the evolution of the drainage system switching between an efficient and inefficient state in summer and winter (Bartholomew et al., 2010). For this reason, a new generation of subglacial drainage models has been developed recently that is capable of coupling the two regimes of drainage and reproducing the transition between them (Schoof, 2010b; Hewitt et al., 2012; Hewitt, 2013; Werder et al., 2013; Fleurian et al., 2014; Hoffman and Price, 2014). While these models demonstrate immense progress for modeling spontaneously evolving channel networks, it is still a challenge to apply them on a continental scale. A comprehensive overview of the various operational and newly emerging glaciological hydrology models is given in Flowers (2015).

Distributed or sheet structures can naturally be well represented using a continuum approach, while channels usually require a secondary framework, where each feature is described explicitly. Water transport in channels is a complex mechanism that depends on the balance of melt and ice creep (Nye, 1976; Röthlisberger, 1969), channel geometry, and network topology. Additionally, the network evolves over time which further complicates modeling of this process. When simulating channel networks, particular care must be also taken to prevent the emergence of instabilities due to runaway merging of channels (see the discussion in Schoof et al. (2012)). This leads to increased modeling complexity and high computational costs. An exception to this is the work of Fleurian et al. (2014), where both systems are represented by Darcy flow through separate porous media layers. The layer representing the channels has its parameters (namely hydraulic conductivity and storage) adjusted to exhibit the behavior of an effective system.

We take this idea even further and only use a single layer of Darcy flow with locally adjusted transmissivity of the layer at locations where channels form. This means that we approximate the channel flow as a fast diffusion process similarly to work in Fleurian et al. (2014); however, a single Darcy flow layer with spatially varying parameters (effective hydraulic transmissivity) accounts for both drainage mechanisms. Similar approaches are known to have been applied to

modeling of fracture networks in rock Sیدن and Clinton (2002). This reduced complexity model does not capture channels individually but represents their effect by changing specific local properties. Since our model aims to simultaneously represent the main properties of both drainage mechanisms (efficient and inefficient), special care must be exercised when choosing the model parameters and relating them to the physical properties of a specific scenario. In particular, the geometrical and physical parameters used in this model are not directly comparable to observed quantities, but instead describe an idealized representation that gives the best fit to the available data. While this strategy may not help to advance the precise understanding of channel formation processes, it captures the overall behavior, is computationally efficient, and allows to examine the complex interactions on larger spatial and temporal scales.

In addition, we introduce a new Confined–Unconfined Aquifer Scheme (CUAS) that differentiates between confined and unconfined flow in the aquifer (Ehlig and Halepaska, 1976). While the assumption of always saturated – and therefore confined – aquifers may be true for glaciers with large water supply, it does not hold in areas with lower water input. Especially in locations far from the coast, the water supplies are often insufficient to completely fill the aquifer. Ignoring this leads to significant errors in the computed hydraulic potential and unphysical, i.a. negative, water pressure. This problem has been analyzed in detail by Schoof et al., 2012, but here we study the effect in the context of equivalent aquifer models using unconfined flow as a possible solution.

Large scale ice flow models often compute the basal velocity using a Weertman-type sliding law, where the inverse of the effective pressure (difference between ice overburden pressure and water pressure) determines the velocity at the base. Low effective pressure leads to high basal velocity. Without subglacial hydrology models, the ice models simply take the ice overburden pressure as effective pressure completely neglecting water pressure. This is a major reason why these models struggle to represent fast flowing areas such as ice streams. The effective pressure computed by our model can be easily coupled to an ice sheet model and improve results for fast flowing areas.

Our work is structured as follows. In the next section, we present the one-layer model of subglacial aquifer. In Sect. 8.3 the model is applied to artificial scenarios, and the sensitivity to model parameters and stability are investigated. In addition, results for seasonal forcing are presented there, and we show how the model evolves over time. Section 8.4 demonstrates the first application of the proposed methodology to the North East Greenland Ice Stream (NEGIS), which is the only interior ice stream in Greenland. It penetrates far into the Greenland mainland with its onset close to the ice divide, so sliding apparently plays a major role in its dynamics. A short conclusions and outlook section wraps up the present study.

8.2 METHODS

8.2.1 CONFINED–UNCONFINED AQUIFER SCHEME

The vertically integrated continuity equation in combination with Darcy’s law leads to the general *groundwater flow equation* (see e.g. Kolditz et al. (2015)):

$$S \frac{\partial h}{\partial t} = \nabla \cdot (T \nabla h) + Q \quad (8.1)$$

with h the hydraulic head (water pressure in terms of water surface elevation above an arbitrary datum also known as the piezometric head), S the storage coefficient (change in the volume of stored water per unit change of the hydraulic head over a unit area), T transmissivity of the aquifer, and Q the source term. For a confined aquifer, $T = Kb$, where K is the hydraulic conductivity, and b is the aquifer thickness. $S = S_s b$ with specific storage S_s given by

$$S_s = \rho_w \omega g \left(\beta_w + \frac{\alpha}{\omega} \right) \quad (8.2)$$

with material parameters for the porous medium (porosity ω , compressibility α) and water (density ρ_w , compressibility β_w).

In order to consider the general form covering both cases (confined and unconfined), we follow Ehlig and Halepaska (1976) and write the general form for the confined–unconfined problem:

$$S_e(h) \frac{\partial h}{\partial t} = \nabla \cdot (T_e(h) \nabla h) + Q. \quad (8.3)$$

Now the transmissivity and the storage coefficient depend on the head and are defined as

$$T_e(h) = \begin{cases} T, & h \geq b & \text{confined} \\ K\Psi, & 0 \leq h < b & \text{unconfined} \end{cases} \quad (8.4)$$

where $\Psi = h - z_b$ is the local height of the head over bedrock z_b and effective storage coefficient S_e is given by

$$S_e(h) = S_s b + S'(h) \quad (8.5)$$

with

$$S'(h) = \begin{cases} 0, & b \leq \Psi & \text{confined,} \\ (S_y/d)(b - \Psi), & b - d \leq \Psi < b & \text{transition,} \\ S_y, & 0 \leq \Psi < b - d & \text{unconfined.} \end{cases} \quad (8.6)$$

This means that as soon as the head sinks below the aquifer height, the system becomes unconfined, and therefore only the saturated section contributes to the transmissivity calculation. This also prevents the head from falling below the bedrock as detailed in Section 8.3.2. Additionally, the mechanism for water storage changes from elastic relaxation of the aquifer (confined) to dewatering under the forces of gravity (unconfined). The amount of water released from dewatering is described by the specific yield S_y . Since this amount is usually orders of magnitudes larger than the release from confined aquifer ($S_y \gg S_s b$), it is useful to introduce a gradual transition as in Eq. (8.6) controlled by a user defined transition parameter d .

Note that the transmissivity is not homogeneous making Eq. (8.3) nonlinear. This fits with our approach to describe the effective system (channels) by locally increasing the transmissivity. The benefit of this approach is discussed in Sect. 8.3.2.

Water pressure P_w and effective pressure N are related to hydraulic head as

$$P_w = \Psi \rho_w g \quad (8.7)$$

and

$$N = P_i - P_w \quad (8.8)$$

with g acceleration due to gravity, $P_i = \rho_i g H$ the cryostatic ice overburden pressure exerted by ice with thickness H and density ρ_i .

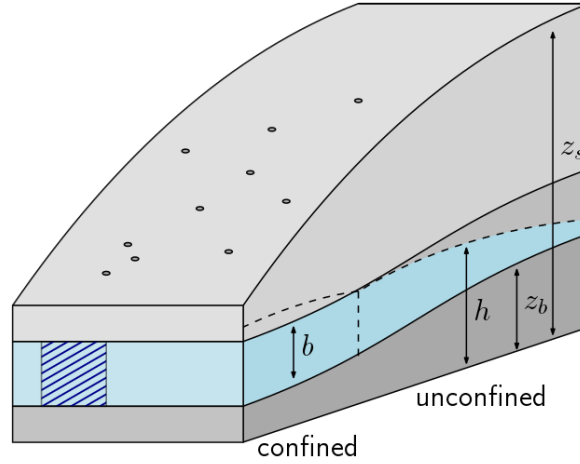


Figure 8.1: Schematics of the confined–unconfined aquifer scheme and artificial geometry for experiments. The hatched zone represents an area where the system is efficient. Dots on top indicate moulins.

8.2.2 OPENING AND CLOSURE

Opening and closure of channels is governed by melt at the walls due to the dissipation of heat and the pressure difference between the inside and outside of the channel leading to creep deformation. We follow Fleurian et al. (2016) in using the classical channel equations from Nye (1976) and Röthlisberger (1972) to scale our transmissivity in order to reproduce this behavior. However, the transmissivity T is evolved directly in our formulation instead of the aquifer thickness b in Fleurian et al. (2016), even though both models are fully equivalent in the way they represent the melt rate.

$$\frac{\partial T}{\partial t} = a_{\text{melt}} + a_{\text{cavity}} - a_{\text{creep}}, \quad (8.9)$$

in which

$$a_{\text{melt}} = \frac{g\rho_w K T}{\rho_i L} (\nabla h)^2, \quad (8.10)$$

$$a_{\text{cavity}} = \beta |\mathbf{v}_b| K \quad (8.11)$$

and

$$a_{\text{creep}} = 2An^{-n} |N|^{n-1} NT \quad (8.12)$$

with L the latent heat, β a factor governing opening via sliding over bedrock protrusions, \mathbf{v}_b basal velocity of the ice, A the creep rate factor depending on temperature, and n the creep exponent, which we choose as $n = 3$. Depending on the sign of N , creep closure as well as creep opening

can occur. Negative effective pressure over prolonged time is usually considered unphysical, and the correct solution to this would be to allow the ice to separate from the bed (see e.g. Schoof et al. (2012) for a possible solution). However, in the context of our equivalent layer model, Eq. (8.12) is still applicable because this is how a channel would behave for $N < 0$. In Sect. 8.3.1, we test the sensitivity of T and N to the magnitudes of K , β and A .

8.3 EXPERIMENTS WITH ARTIFICIAL GEOMETRIES

Testing out equivalent layer model and finding parameters for it is not straightforward, because there are no directly comparable physical properties. Moreover, observations and measurements of subglacial processes are in general difficult and sparse. We address this by testing the model with some of the benchmark experiments of the Subglacial Hydrology Model Inter-comparison Project (Fleurian et al., 2018b, in prep.).

The proposed artificial geometry mimics a land-terminating ice sheet margin measured 100 km in the x -direction and 20 km in the y -direction. The bedrock is flat ($z_b(x, y) = 0$ m) with the terminus located at $x = 0$, while the surface z_s is defined by a square root function $z_s(x, y) = 6\left((x + 5e3)^{1/2} - (5e3)^{1/2}\right) + 1$. Here, we use the SHMIP/B2 setup, which includes 10 moulins with constant in time supply. Boundary conditions are set to zero influx at the interior boundaries ($y = 0, y = 20, x = 100$) and zero effective pressure at the terminus. All experiments start with initial conditions that imply zero effective pressure and are run for 50 years to ensure that they reach a steady state.

8.3.1 PARAMETER ESTIMATION AND SENSITIVITY

SHMIP is primarily intended as a qualitative comparison between different subglacial hydrology models, where results from the GlaDS model (Werder et al., 2013) serve as a “common ground”. Here, we use it as a basis for an initial tuning and a study of the sensitivity of our model with regard to parameters. The upcoming results from the SHMIP are also the reason why we do not show a comparison to other models in this study but refer to the manuscript in preparation instead.

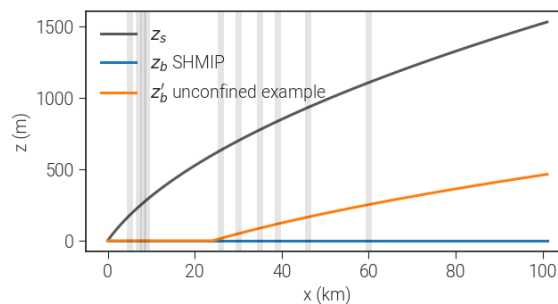


Figure 8.2: Experiments with artificial geometries. Vertical lines denote moulin positions for SHMIP/B2. The orange line shows the modified bedrock used to illustrate the impact of the confined/unconfined scheme as discussed in Sect. 8.3.2

Table 8.1: Physical constants used in the model. We distinguish between well known (upper half) and estimated / uncertain (lower half) parameters.

Name	Definition	Value	Units
L	latent heat of fusion	334	kJ kg^{-1}
ρ_w	density of water	1000	kg m^{-3}
ρ_i	density of ice	910	kg m^{-3}
n	flow law exponent	3	-
g	gravitational acceleration	9.81	m s^{-2}
β_w	compressibility of water ^a	5.04×10^{-10}	Pa^{-1}
α	compressibility of porous medium ^a	10^{-8}	Pa^{-1}
ω	porosity ^a	0.4	-
S_s	specific storage (Eq. (8.5))	$\approx 1 \times 10^{-3}$	m^{-1}
S_y	specific yield	0.4	

^aValues from Fleurian et al. (2014)

Table 8.2: Model parameters (upper) and variables computed in the model (lower)

Name	Definition	Units
T_{\min}	min. transmissivity	$\text{m}^2 \text{s}^{-1}$
T_{\max}	max. transmissivity	$\text{m}^2 \text{s}^{-1}$
b	aquifer thickness	m
d	confined / unconfined transition (Eq. (8.6))	m
Q	water supply	m s^{-1}
A	creep rate factor	$\text{Pa}^{-3} \text{s}^{-1}$
K	hydraulic transmissivity	m s^{-1}
\mathbf{v}_b	basal ice velocity	m s^{-1}
β	cavity opening parameter	
h	hydraulic head	m
S	storage	-
S_e	effective storage	-
T	transmissivity	$\text{m}^2 \text{s}^{-1}$
a_{melt}	opening by melt	$\text{m}^2 \text{s}^{-2}$
a_{cavity}	opening by sliding over bedrock	$\text{m}^2 \text{s}^{-2}$
a_{creep}	opening/closure by creep	$\text{m}^2 \text{s}^{-2}$
P_w	Water pressure	Pa
P_i	Ice pressure	Pa
N	effective pressure	Pa

In Table 8.1, we show the physical constants used in all setups and runs. The values in the lower half are properties of the porous medium and are only estimated. Since they are utilized in the context of the equivalent layer model this is not an issue. Table 8.2 contains the model parameters in the upper part and the variables computed by the model in the lower part.

We divide the sensitivity analysis into a general block investigating the sensitivity to the amount of water input into moulins, the layer thickness b , the confined / unconfined transition parameter d , grid resolution dx (Fig. 8.3) and a block that examines the parameters directly affecting channel evolution such as creep rate factor A , conductivity K , and the bounds for the allowed transmissivity T_{\min} and T_{\max} (Fig. 8.4). In Table 8.3, we list values that lead to the best agreement with the SHMIP benchmark experiments and thus are used in the following as the baseline for our sensitivity tests.

Table 8.3: Selected baseline parameters for all experiments unless otherwise noted. These parameters best match the SHMIP targets.

Name	Value	Units
T_{\min}	1×10^{-7}	$\text{m}^2 \text{s}^{-1}$
T_{\max}	100	$\text{m}^2 \text{s}^{-1}$
b	0.1	m
d	0	m
dx	1000	m
A	5×10^{-25}	$\text{Pa}^{-3} \text{s}^{-1}$
K	10	m s^{-1}
β	5×10^{-4}	
$Q_{\text{per moulin}}$	9	$\text{m}^3 \text{s}^{-1}$

In Figs. 8.3a and b, the model’s reaction to different amounts of water input through the moulins is shown. With deactivated transmissivity evolution ($T = \text{const.}$, dashed lines), larger water inputs lead to higher water pressure, hence lower effective pressure N . In this case, a moulin input of $18 \text{ m}^3 \text{ s}^{-1}$ leads to negative values of N . With activated evolution of T , the transmissivity adapts to the water input: as more water enters the system through moulins, the transmissivity rises. Vertical gray bars show the location of moulins along the x-axis, and the most significant increase in T occurs directly downstream of a moulin. This happens because the water is transported in this direction leading to increased melt. At the glacier snout ($x = 0$), the ice thickness is at its lowest so almost no creep closure takes place; hence, the transmissivity grows large for all tested parameter combinations. Significant development of effective drainage is visible for inputs above $0.07 \text{ m}^3 \text{ s}^{-1}$ (yellow line). The resulting effective pressure decreases with rising water input as the system becomes more efficient at removing water. Up to ca. 35 km distance from the snout this results in similar values of N for all forcings above $0.28 \text{ m}^3 \text{ s}^{-1}$. The system adapts so that it can remove all of the additional water efficiently. In Figs. 8.3i and j, the two-dimensional distributions of N and T are shown for the baseline parameters.

“Channels” (indicated by regions of high transmissivity) form downstream from moulins and continue straight towards the ocean. The effective pressure drops around water inputs and along the “channels”.

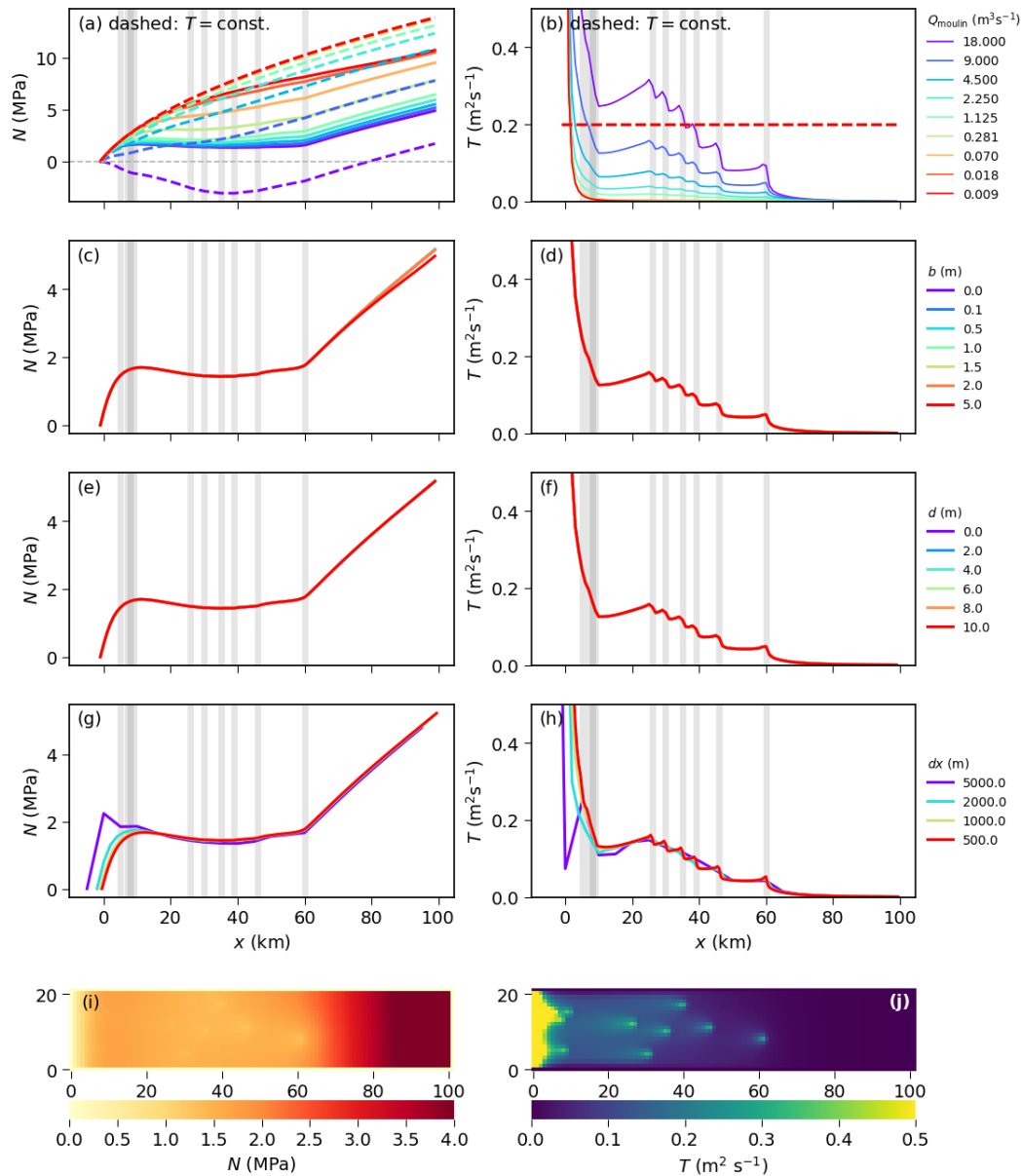


Figure 8.3: Results from the general sensitivity experiments showing the dependence of N (left) and T (right) on: (a)–(b) Water supply from moulins Q_{moulin} (results for deactivated transmissivity evolution are shown using dashed lines), (c)–(d) aquifer layer thickness b , (e)–(f) confined/unconfined transition parameter d , (g)–(h) grid resolution dx . Shown values are averaged along the y -axis to represent cross-sections at flow lines. Transmissivity plots are cut off at $0.5 \text{ m}^2 \text{ s}^{-1}$ to improve visibility of the relevant range. (i) and (j) show the two-dimensional distributions (map view) of the results using the best-fit baseline parameters.

We observe no sensitivity of our result to the layer thickness b (Figs. 8.3c and d). Because we use transmissivity, b does not influence the flow of water directly, but is important to decide when the system becomes unconfined, as well as determining the Storage (see Eq. 8.5). However, in this experiment the system has sufficient water input so that all cells are confined in the steady state and also the storage has not influence on the long time solution (The storage determines how fast a pressure change travels through the system, but is irrelevant for the steady state).

The large availability of water also explains why the confined–unconfined transition parameter d does not show noticeable effects on the results (Figs. 8.3e and f) – the system is always confined.

Grid resolution dx has low influence on the pressure distribution and a minor effect on the transmissivity downstream (Figs. 8.3g and h). However, coarse resolutions are unable to resolve the steps that appear at the moulins.

In Figs. 8.4a and b, we show the results for different values of T_{\min} . These act as a numerical limit to avoid infinite growths for ill-posed conditions and do generally not show influence on the results. If T_{\min} is chosen very large ($0.1 \text{ m}^2 \text{ s}^{-1}$ or larger), this dominates the balance between opening and closure and leads to high water flux, increasing the effective pressure.

T_{\max} (Fig. 8.4b and c) has no visible impact on the resulting pressure distribution.

The creep rate factor A determines the “softness” of the ice and therefore effects the creep term in Eq. (8.9). Larger values of A imply warmer ice; hence, more creep closure (see Figs. 8.4e and f). Note, that this also effects creep opening if $N < 0$.

The conductivity K describes the flux of water through the system and therefore determines the melt term (see Eq. 8.10). Larger values of K lead to higher transmissivity and more water transport resulting in lower P_w and higher N .

In order to explore the dependence on the cavity opening term, we assume the basal ice velocity $\mathbf{v}_b = 1 \times 10^{-6}$ (as in SHMIP) and vary the β term. β parametrizes the bedrock geometry and incorporates the height and distance of protrusion. As expected, larger values of β lead to more opening and, therefore, a higher effective pressure. With values as high as 1×10^{-1} , the cavity opening completely dominates the transmissivity evolution, and the effect of moulins is not visible anymore.

8.3.2 THE BENEFIT FROM TREATING UNCONFINED AQUIFER

As described above, the confined–unconfined aquifer approach is advantageous for obtaining physically meaningful pressure distributions. In the example illustrated in Fig. 8.5, we use a slightly modified geometry, where the bedrock rises towards the upstream boundary forming a slab $z'_b(x, y) = \max(3((x + 5e3)^{1/2} - (5e3)^{1/2}) - 300, 0)$. The supply is constant in time and space, and we choose a low value of $7.93e-11 \text{ m/s}$ ($\approx 2.5 \text{ mm/a}$) to compare our improved scheme to the simple confined only case. Fig. 8.5 shows a comparison of the steady state solutions: For the confined-only case, the hydraulic head drops below the bedrock at the upstream region. This results in negative water pressure for these regions. Addressing this by simply limiting the water pressure to zero would result in inconsistencies between the pressure field and the water supply. Our new scheme limits the transmissivity when the head approaches the bedrock and by this means ensures $p_w \geq 0$ in a physically consistent way. Additionally, the confined-only solution completely depends on boundary conditions and supply terms, basal topography has no influence in this case (apart from governing dK/dt). The possibility of the aquifer to become unconfined captures

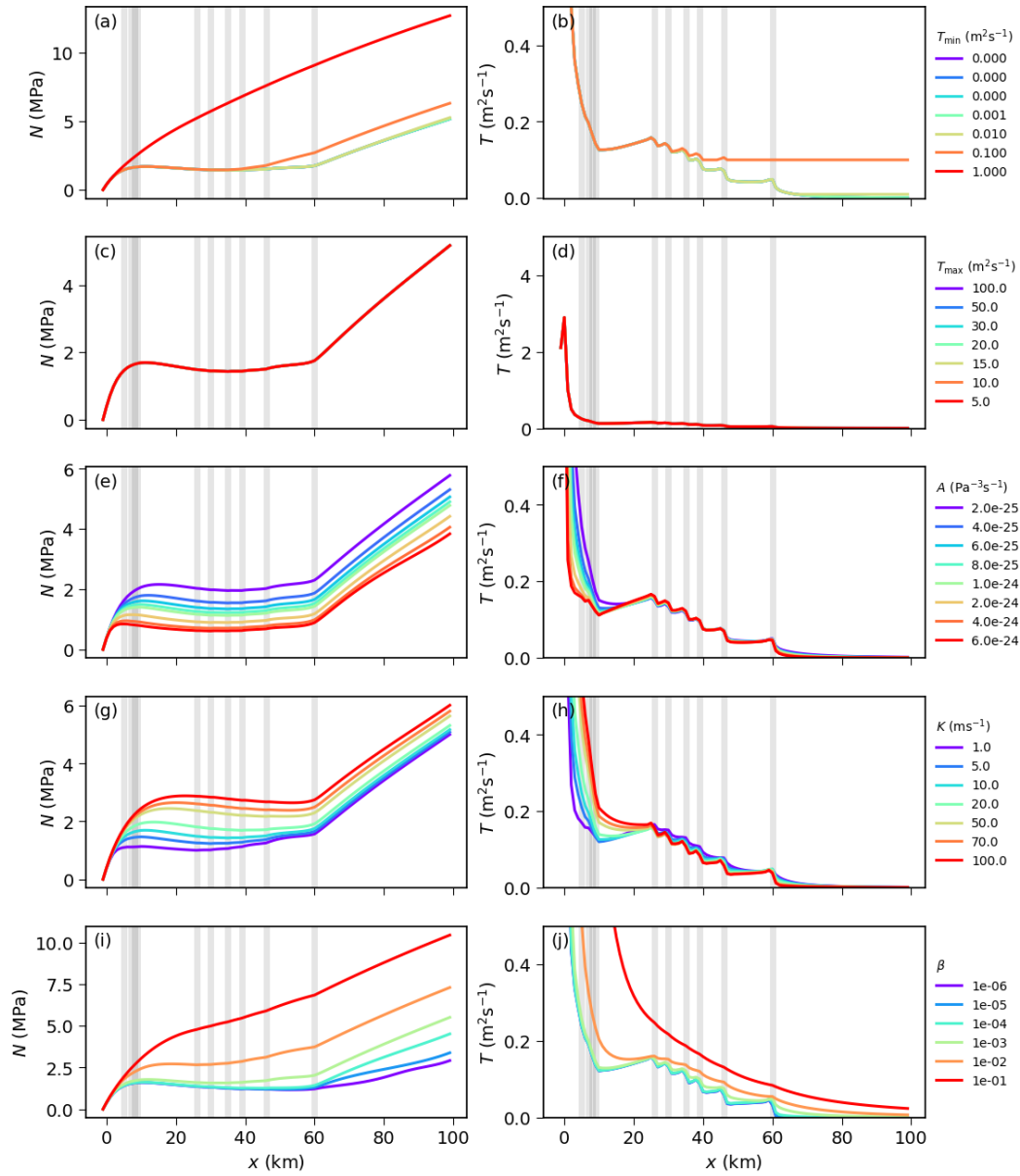


Figure 8.4: Results from parameters directly related to opening and closure: Limits on the transmissivity T_{\min} (panels a and b) and T_{\max} (panels c and d), creep rate factor A (panels e and f), conductivity K (panels g and h) and cavity opening parameter β (panels i and j). Shown values are averaged along the y-axis to represent cross-sections at flow lines. Transmissivity plots are cut off at $0.5 \text{ m}^2\text{s}^{-1}$ to improve visibility of the relevant range.

the expected behaviour much better: At high water levels, water pressure distribution dominates water transport, while at low levels the bed topography becomes relevant.

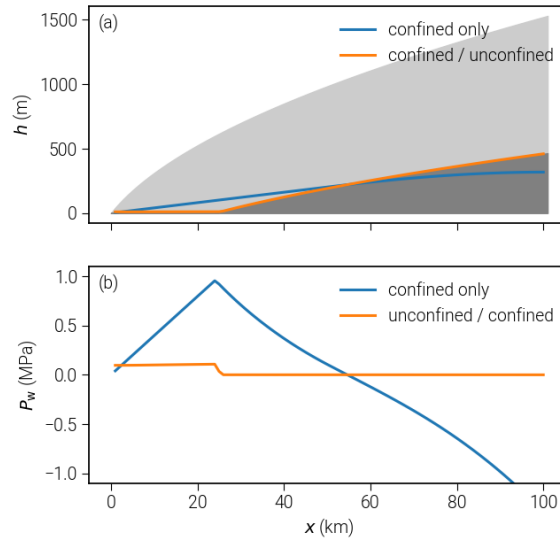


Figure 8.5: Advantages of using the confined/unconfined aquifer scheme (CUAS): Values of head and water pressure for geometries with non-flat bedrock. (a) Computed head for the confined and combined scheme with ice geometry in the background. In the confined only case, the head goes below bedrock. (b) Resulting water pressure, only for the combined scheme the pressure is always non-negative.

8.3.3 SEASONAL CHANNEL EVOLUTION AND PROPERTIES

In order to understand our model's ability to simulate the seasonal evolution of subglacial systems, we selected the setup SHMIP/D and ran it with different values of key model parameters. This experiment does not include any moulines but prescribes a non-uniform spatial distribution of supply instead that also varies seasonally. A simple degree day model with varying temperature parameter $d\Theta$ provides water input rising from the downstream end (lowest elevated) of the glacier towards the higher elevated areas over summer:

$$\Theta(t) = -16 \cos(2\pi/\text{yr } t) - 5 + d\Theta \quad (8.13)$$

$$Q_{\text{dist}}(z_s, t) = \max(0, (z_s \text{LR} + \Theta(t)) \text{DDF}) + Q_{\text{basal}}. \quad (8.14)$$

Here, $\text{yr} = 31\,536\,000$ s denotes the number of seconds per year, $\text{LR} = -0.0075 \text{ Km}^{-1}$ the lapse rate, $\text{DDF} = 0.01/86\,400 \text{ mK}^{-1}\text{s}^{-1}$ is the degree day factor, and $Q_{\text{basal}} = [7.93 \times 10^{-11} \text{ ms}^{-1}]$ is additional basal melt. The resulting seasonal evolution of the supply is shown in Fig.8.6a. The model is run for 10 years so that a periodic evolution of the hydraulic forcing is generated. Here, we present the result for one parameter set only since the model is not very sensitive in this setup.

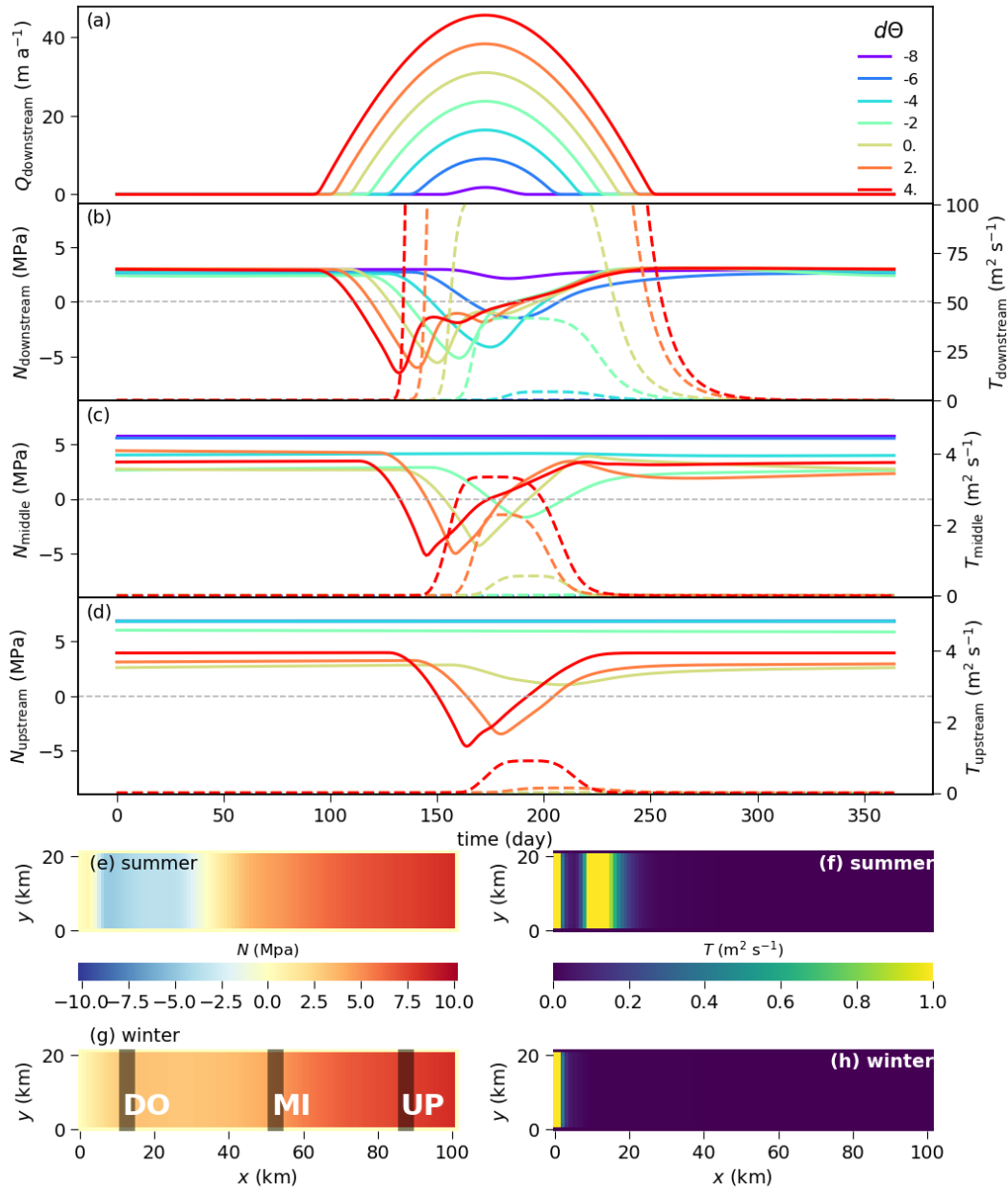


Figure 8.6: Results for one season of the SHMIP/D experiment. In panels (b)–(d), the left axis (effective pressure) corresponds to the solid lines, while the right axis (transmissivity) specifies the values for the dashed lines. The values at the given positions (upstream, middle, downstream) are averaged over the corresponding areas indicated in panel (g). Panels (e)–(h) show two-dimensional distribution maps of $d\Theta = -4$ run.

We chose three different locations to present N and T during the season: downstream of the glacier close to the snout, in the center, and at a far upstream location (Figs. 8.6b–d; the locations are marked in panel g). Shown time series are spatially averaged over these locations with solid lines representing the effective pressure and dashed lines the transmissivity. Water input increases during the summer months, while the corresponding effective pressure drops. With a time lag the transmissivity rises in response. Supply develops from downstream towards the upstream end of the glacier over the season so the decline in N at the downstream location (Fig. 8.6b) is instantaneous when the supply rises, while, at the further inland locations (Figs. 8.6c and d), N reacts later during the year. At the middle location, the drop in N is only visible for temperature parameters of -2 and higher. The rise in transmissivity occurs for the three highest temperatures. Finally, at the upstream position, only for $d\Theta = 4$ and $d\Theta = 2$ the effective pressure drops below zero, while for $d\Theta = 0$ the drop is smaller in magnitude and more prolonged. The transmissivity rise is only significant for $d\Theta = 4$ at this location. While the onset and minima of the decline in N strongly depend on the amount and timing of the water input for all values of $d\Theta$, the maximum of T and also the time when N returns to winter conditions is similar. For the downstream position, the maximum transmissivity is reached for day 210 (not visible in the figure), and N reaches its background value approximately 25 days later. At the center and upstream positions, this behavior is less pronounced but generally similar.

The observed behavior is expected and indicates that our model is able to represent the seasonal evolution of the subglacial water system. Increasing water supply over the year leads to rising water pressure and dropping effective pressure. When the transmissivity rises in response, the effective pressure goes up again despite the supply not yet falling again because the more efficient system is able to transport the water away. For the cases, where no visible change in T occurs such as $d\Theta = -6$ (blue line in Fig. 8.6b), the effective pressure follows the supply at the terminus with a small delay, while at the center position ($d\Theta = -2$, cyan line, Fig. 8.6c), the minimum is offset by the time needed for the supply to reach that location. The maximum in transmissivity T is reached later because, once the system becomes efficient, increased water transport stimulates melting that opens the system even more. This self-reinforcing process is only stopped when enough water is removed and the reduced water flux reduces the melt again. We assume that this leads to similar locations of the transmissivity maxima for different $d\Theta$ and the resulting similar reemerging of winter conditions in N .

In this experiment, N becomes negative during the seasonal evolution, which is not physically meaningful. We attribute such behavior to a lack of adjustment of water supply to the state of the system. In reality, the supply from runoff or supraglacial drainage would cease as soon as the pressure in the subglacial water system becomes too high; here we simply continue to pump water into the subglacial system without any feedback. This then leads to negative values of N . It is also consistent with the finding that N becomes negative earlier in the season in cases of higher supply. This deficiency will be addressed in future work.

8.4 SUBGLACIAL HYDROLOGY OF NEGIS, GREENLAND

The role of subglacial hydrology in the genesis of ice streams in general is not well understood yet. NEGIS is a very distinct feature of the ice sheet dynamics in Greenland; thus, the question

about the role of subglacial water in the genesis of NEGIS is critical. The characteristic increase in horizontal velocities becomes apparent about 100 km downstream from the ice divide (Vallelonga et al., 2014). Further downstream, the ice stream splits into three different branches: the 79° North Glacier (79NG), Zacharias Isbrae (ZI), and Storstrømmen. Thus far, large scale ice models have only been able to capture the distinct flow pattern of NEGIS when using data assimilation techniques such as inverting for the basal friction coefficient (see e.g. horizontal velocity fields in Goelzer et al., 2017). It is assumed that most of the surface velocity can be attributed to basal sliding amplified by basal water instead of ice deformation (Joughin et al., 2001). This means that the addition of a subglacial hydrology might have the potential to improve the results considerably. While many glaciers in Greenland have regularly draining supraglacial lakes and run-off driving a seasonality of the flow velocities, little is known about the effect at NEGIS (Hill et al., 2017). Because of this lack of data, to avoid an increased complexity, and to focus on the question if basal melt alone can account for the development of an efficient system, we do not include any seasonal forcing into our experiment.

Our setup includes the major parts of this system. The pressure-adjusted basal temperature Θ_{pmp} obtained from PISM (Aschwanden et al., 2016) is utilized to define the modeling region. We assume that for freezing conditions at the base ($T_{\text{pmp}} < 0.1$ K) basal water transport is inhibited and take this as the outline of our model domain. Fig. 8.7 shows the selected area and PISM basal melt rates used as forcing.

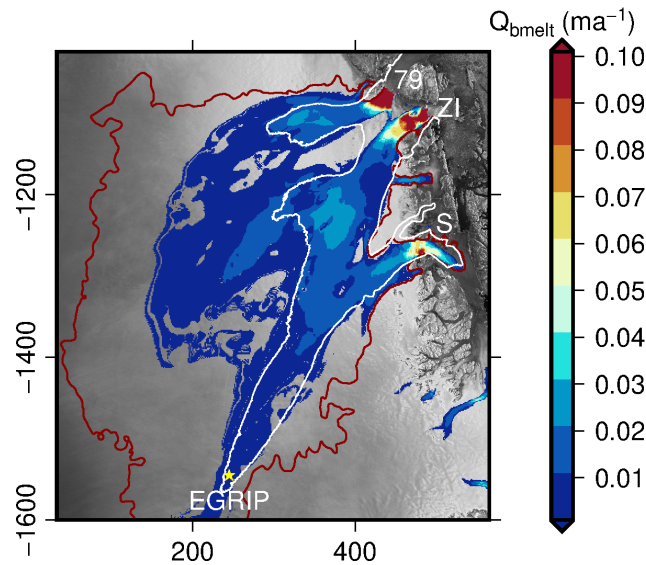


Figure 8.7: Boundary conditions and forcing for NEGIS experiment. Shown is the basal melt rate from PISM and contour line for $\Theta_{\text{pmp}} = -0.1$ K (red) used as model boundary. The white line indicates the 50 m a^{-1} velocity contour.

For the ice geometry, we use the bed model of Morlighem et al. (2014) interpolated on a 1.2 km grid. Boundary conditions at lateral margins are set to no flux, whereas the termini at grounding lines are defined as Dirichlet boundaries with a prescribed head that implies an effective pressure of zero. This means that the water pressure at the terminus is equal to the hydrostatic water pres-

sure of the ocean assuming floating condition for the ice at the grounding line. Parameters used for this experiment are the same as in our sensitivity study (Table 8.3). The simulation is run for 50 a to reach steady state. Despite a high resolution (444×481), computing time for this setup is still reasonable (3.5 hours on a single core of Intel Xeon Broadwell E5-2697). The resulting distributions of effective pressure and transmissivity are shown in Figs. 8.8a and b, respectively. As expected, effective pressure is highest at the ice divide and decreases towards the glacier termini. Transmissivity is low for the majority of the study area with the exception of the vicinity of grounding lines and two distinct areas that touch in between 79NG and ZI. The northern area (marked I in Fig. 8.8b) is located at the northern branch of 79NG and has no direct connection to the snout. The second area (marked II in Fig. 8.8b) emerges in the transition zone between the southern branch of 79NG and Zacharias Isbrae and covers an area approximately twice as large as area I with higher values of T . It reaches down to the snout of ZI.

Comparing the effective pressure distribution to the observed velocity (Rignot and Mouginot, 2012) – we chose the 50 ma^{-1} contour line as indicator of fast flow – we observe a high degree of overlap between the fast flowing regions and those with low effective pressure (below 1 MPa) over most of the downstream domain of our study area. Storstrømmen shows higher effective pressure downstream than 79NG and ZI, which is in accordance with lower observed horizontal velocities for that glacier (Joughin et al., 2010). At the location where the small sidearm branches north, we observe extremely low effective pressure and high transmissivity; however, we attribute this problem to an anomalously high basal water supply in our forcing data. At the onset of the NEGIS, the effective pressure is high, and no relationship to the flow velocity can be observed. To further examine the possible influence of our hydrology model to basal sliding, we investigate the impact on the sliding law. We chose to compare our computed N_{CUAS} to the reduced ice overburden pressure defined in Huybrechts (1990) as $N_{\text{HUY}} = P_i + \rho_{\text{sw}}g(z_b - z_{\text{sl}})$ for $z_b < z_{\text{sl}}$ and $N_{\text{HUY}} = P_i$ otherwise. The quotient of H_{HUY} to N_{CUAS} is shown in Fig. 8.8c to demonstrate where the application of our hydrology model would increase basal velocities.

In order to demonstrate the effect of the modeled subglacial hydrology system on the NEGIS ice flow, we setup a simple, one-way coupling to an ice flow model. Here, we use the Ice Sheet System Model (ISSM, Larour et al., 2012), an open source finite element flow model appropriate for continental scale and outlet glacier applications (e.g. Bondzio et al., 2017; Morlighem et al., 2016). The modeling domain covers the grounded part of the whole NEGIS drainage basin. The ice flow is modeled by the higher order approximation (HO, Blatter, 1995; Pattyn, 2003) in a 3D model, which accounts for transversal and longitudinal stress gradients. In the HO-model we do not perform a thermo-mechanical coupling, but prescribe a depth-averaged hardness factor in Glens flow law instead. Model calculations are performed on an unstructured finite element grid with a resolution of 1 km in fast flow regions and of 20 km in the interior. The basal drag τ_b is written in a Coulomb-like friction law:

$$\tau_b = -k^2 N \mathbf{v}_b, \quad (8.15)$$

where k^2 is a positive constant. We run two different scenarios, where (1) the effective pressure is parametrized as the reduced ice overburden pressure, $N = N_{\text{HUY}}$, and (2) the effective pressure distribution is taken from the hydrological model at steady state, $N = N_{\text{CUAS}}$. The value of k^2 is tuned in order to have ice velocities of approximately 1500 ma^{-1} at the grounding line at the

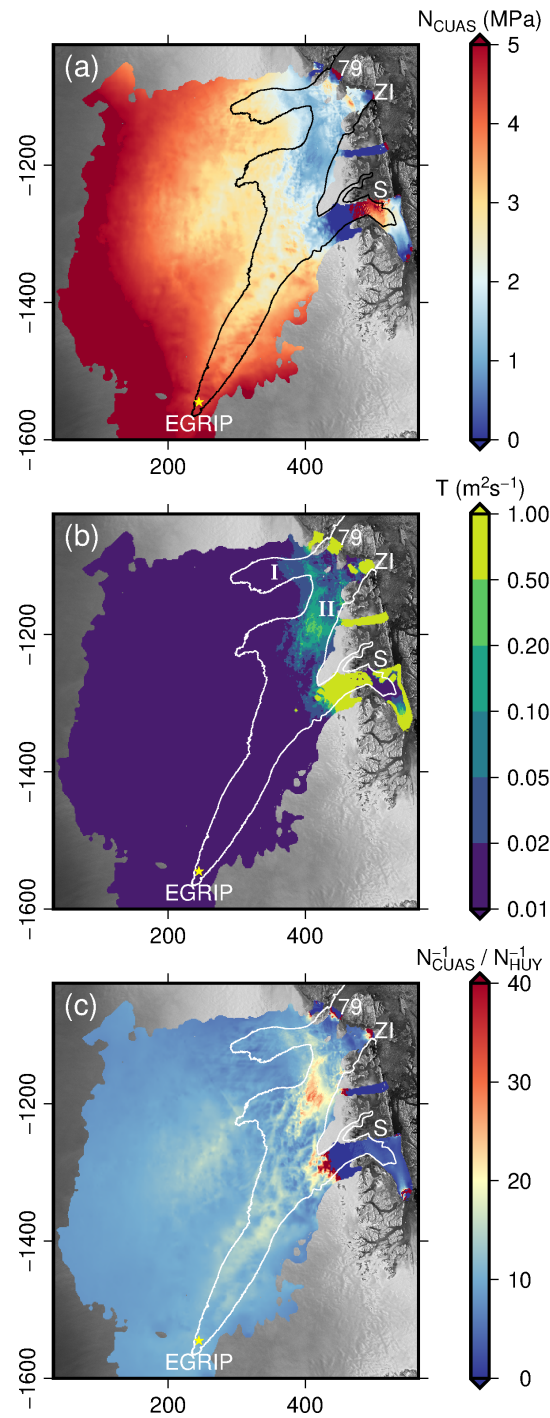


Figure 8.8: Results for NEGIS region with forcing due to basal melt (PISM) representing winter conditions. White lines indicate the 50 m a^{-1} velocity contour. Panel (a) shows effective pressure N_{CUAS} , (b) transmissivity T (logarithmic scale), and (c) shows the quotient of the ice overburden pressure above flotation and the effective pressure computed by CUAS.

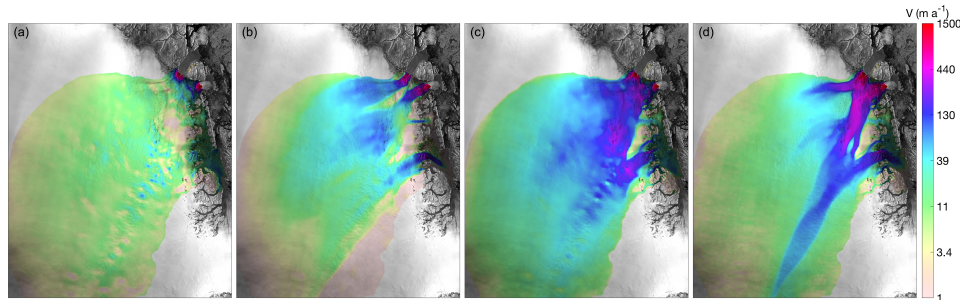


Figure 8.9: Horizontal surface velocity: ISSM with reduced ice overburden pressure N_{HUY} (a), PISM result from Aschwanden et al. (2016), interpolated to unstructured ISSM grid (b), ISSM with effective pressure from our hydrology model N_{CUAS} (c), and observed velocities (Rignot and Mouginot, 2012) (d).

79NG. For both scenarios, the value of k^2 is 0.067 sm^{-1} . The results for both scenarios are shown in Fig. 8.9a and c, respectively. Additionally, we show the observed velocities (Fig. 8.9d, Rignot and Mouginot, 2012) and the PISM surface velocities (Fig. 8.9b, Aschwanden et al., 2016). Note that the latter is a PISM model output on a regular grid interpolated to the unstructured ISSM grid.

Velocities computed with the reduced ice overburden pressure are generally too low and do not resemble the structure of the fast flowing branches at all. The result from PISM shows distinct branches for the different glaciers, which display a relatively sharp separation from the surrounding area. Note, that PISM also uses a basal hydrology model as described in Bueler and Pelt (2015). Velocities are slightly lower than observed velocities especially for Zacharias Isbrae and in the area, where ZI and 79NG are closest. In the upper part towards the ice divide, the ice stream structure is not visible in the velocities. The ISSM model using effective pressure computed by CUAS produces high velocities towards the ocean that closely resemble N . The observed sharp transition between the ice streams and the surrounding ice is poorly reproduced. While the stream structure is way too diffused, the different branches can be discerned and the velocity magnitude for the glaciers appears reasonable. The inland part is similar to observed velocities but – as in the PISM simulation – the upper part where NEGIS is initiated is not present. The onset of NEGIS is thought to be controlled by high local anomalies in the geothermal flux (Fahnestock et al., 2001), which PISM currently does not account for. Higher geothermal flux would lead to more basal melt, hence, water supply in the hydrology model. However, the consequences for the modeled effective pressure would require further experiments which are not in the scope of this paper.

In Tab. 8.4, we show the root mean square error (l_2 -norm), Pearson correlation coefficient r^1 , and Δv (l_1 -norm) between the modeled and observed velocities.

We find it impressive that even without extensive tuning, we can considerably improve the velocity field in ISSM by our simple one-way coupling to the hydrology model. However, the results in this section are to be understood not as a thorough study of the NEGIS but as a first application of the model to a real geometry. A complete study requires extended observations in order to determine the optimal model parameters. However, we are confident that our results represent the general aspects of the hydrological system at NEGIS. Based on our sensitivity and seasonal experiments (Sect. 8.3.1 and Sect. 8.3.3) we expect the high-transmissivity-areas to be a stable feature,

Table 8.4: Comparison of modeling results for horizontal ice velocity to observed values (Rignot and Mouginot, 2012). Herein RMS denotes the root mean square error or l_2 -norm, r^2 is the Pearson correlation coefficient, and ΔV is the l_1 -norm.

	RMS (ma^{-1})	r^2	Δv (ma^{-1})
ISSM with reduced ice overburden pressure	152.30	0.77	78.63
PISM (Aschwanden et al., 2016)	132.05	0.84	65.42
ISSM with N computed from CUAS	101.95	0.88	44.61

which would extend or retract depending on the chosen values of the melt and creep parametrizations but not change their location. Available supply plays a more important role here, and we assume that different basal melt distributions – or the addition of surface melt – might considerably change the position and the extent of the efficient system and, therefore, the effective pressure distribution as can be seen in Sect. 8.3.3.

The onset of NEGIS is not well reproduced in the PISM simulation as well as in our ISSM result. Since the ice is slow in the PISM results in that area, basal melt rates are low, and, since we use these as input in our hydrology model, it is expected that our model computes low water pressure here. In our opinion, this represents another point in favor of having a real two-way coupling between the ice model and the basal hydrology model in order to obtain good results. These results could then in turn be used to guide further optimization of the modeling parameters in our hydrology model in the future.

8.5 CONCLUSIONS

We present the first equivalent aquifer layer model for subglacial hydrology that includes the treatment of unconfined water flow. It uses only a single conductive layer with adaptive transmissivity. Since extensive observations of the subglacial system are rare, our approach to fit a simple parametrization of the effective Darcy model to the available data can be an advantage.

We find strong model sensitivity to grid spacing dx , the parametrization of melt a_{melt} , creep closure a_{creep} , and the cavity opening parameter, while the sensitivity to the limits of transmissivity and the confined–unconfined transition parameter d is low. Our model robustly reproduces the seasonal cycle with the development and decline of the effective system over the year.

In our NEGIS experiments, we find the presence of a partial efficient system for winter conditions. The distribution of effective pressure broadly agrees with observed velocities, while the upstream part is not represented correctly. When coupled to ISSM, our hydrology model notably improves computed velocities.

A number of aspects of the proposed model can be further developed; those include improved parametrizations of several physical mechanisms (e.g. adding feedback between pressure and water supplies), changing the hydraulic transmissivity coefficient to a tensor-valued one to better represent the anisotropy of channel networks, and, last but not least, transition to a mixed formulation of the Darcy equation discretized on an unstructured mesh in order to preserve mass conservation and to improve resolution in the areas of interest.

8.6 APPENDIX

8.6.1 PARAMETRIZATION OF EVOLUTION OF TRANSMISSIVITY

We use the same parametrization as Fleurian et al., 2016 detailed here using the notation in Cuffey and Paterson, 2010.

Opening and closure

The conduit expands when there is more melt than ice inflow due to creep, thus the mass change per unit length is given as:

$$\rho_i \frac{\partial A_c}{\partial t} = \dot{M}_{\text{melt}} - \dot{M}_{\text{creep}} \quad (8.16)$$

(Cuffey and Paterson, 2010, Eq. 6.42), in units of mass change per unit length ($\text{kg m}^{-1} \text{s}^{-1}$).

This is equivalent to

$$\rho_i \frac{\partial b}{\partial t} = \dot{m}_{\text{melt}} - \dot{m}_{\text{creep}}, \quad (8.17)$$

which describes the mass change per unit area ($\text{kg m}^{-2} \text{s}^{-1}$) or specific mass balance.

Creep term

Nye, 1976, found for the closure on channels due to creep that

$$\frac{1}{R_c} \frac{\partial R_c}{\partial t} = A \left[\frac{N}{n} \right]^n, \quad (8.18)$$

with R_c denoting the channel radius and A_c the channel area ($= \pi R_c^2$) (notation as in Cuffey and Paterson, 2010, Eq. 6.15). Multiplication by $2\pi\rho_i R_c^2 = 2\rho_i A_c$ on both sides, leads to

$$2\pi\rho_i R_c \frac{\partial R_c}{\partial t} = 2\rho_i A_c A \left[\frac{N}{n} \right]^n \quad (8.19)$$

Rewriting the left side to area, using the chain rule ($\frac{\partial A_c}{\partial t} = 2\pi R_c \frac{\partial R_c}{\partial t}$) yields

$$\rho_i \frac{\partial A_c}{\partial t} = 2\rho_i A_c A \left[\frac{N}{n} \right]^n, \quad (8.20)$$

thus,

$$\dot{M}_{\text{creep}} = 2\rho_i A_c A \left[\frac{N}{n} \right]^n, \quad (8.21)$$

or again as a change per unit area

$$\dot{m}_{\text{creep}} = 2\rho_i b A \left[\frac{N}{n} \right]^n. \quad (8.22)$$

Melt term

Heat produced over ds in unit time is $Q_w G$ and pressure melting point effects are $\rho_w Q_w c_w B \frac{dP_i}{ds}$, which leads to

$$\dot{M}_{\text{melt}} L_f = \underbrace{Q_w G}_{\text{heat produced}} - \underbrace{\rho_w Q_w c_w B \frac{dP_i}{ds}}_{\text{PMP effect}} \quad (8.23)$$

(Cuffey and Paterson, 2010, Eq. 6.16), where \dot{M}_{melt} represents the melt rate (mass per unit length of wall in unit time) and the magnitude of gradient of the hydraulic potential is given by

$$G = |\nabla \phi_h|, \quad \text{where} \quad \phi_h = \rho_w g h. \quad (8.24)$$

Neglecting the PMP effects we get

$$\dot{M}_{\text{melt}} = \frac{Q_w G}{L_f}. \quad (8.25)$$

As before, we can write that as a change per unit area instead:

$$\dot{m}_{\text{melt}} = \frac{Q'_w G}{L_f}, \quad (8.26)$$

where Q'_w is now the flux per unit length(). Using $Q'_w = qb$ (confined case, unconfined would be $Q'_w = q(h - z_b)$) and $q = K \nabla(h)$ (ommiting the minus, because we need the magnitude here) this is

$$\dot{m}_{\text{melt}} = \frac{K \nabla(h) b \nabla(\rho_w g h)}{L_f} \quad (8.27)$$

which can be rewritten to

$$\dot{m}_{\text{melt}} = \frac{\rho_w g K b (\nabla h)^2}{L_f}. \quad (8.28)$$

Evolution equation

Inserting \dot{m}_{creep} from Eq. 8.22 and \dot{m}_{melt} from Eq. 8.28 into Eq. 8.17 and dividing by ρ_i results in

$$\frac{\partial b}{\partial t} = \frac{\rho_w g K b (\nabla h)^2}{L_f \rho_i} - 2bA \left[\frac{N}{n} \right]^n, \quad (8.29)$$

which is equation (6) in Fleurian et al. (2016).

Formulation in transmissivity

By multiplying Eq. 8.29 with the constant hydraulic conductivity coefficient K we obtain our evolution equation for the transmissivity:

$$\frac{\partial T}{\partial t} = \frac{g \rho_w K T (\nabla h)^2}{L_f \rho_i} - 2AT \left[\frac{N}{n} \right]^n. \quad (8.30)$$

Our reasoning behind evolving T instead of b are twofold: first, our combination of confined/unconfined aquifer flows would be conceptually confusing when formulated in terms of b -evolution and may

cause unintended side effects on the storage term; second, the transmissivity formulation is more general, since it can also model situations when K is varying without any re-formulation.

To account for cavity opening by the ice sliding over bedrock protrusions, we add another term to the evolution equation (8.9).

8.6.2 DISCRETIZATION

We discretize the transient flow equation (Eq. (8.3)) on an equidistant rectangular grid using a Crank-Nicolson scheme. For sake of completeness, we give the equations for a non-equidistant grid here.

For the spatial discretization, we use a second-order central difference scheme (e.g., Ferziger and Perić, 2002) leading to the spatial discretization operator for the head \mathcal{L}_h :

$$\mathcal{L}_h = T_{i+\frac{1}{2},j} \frac{h_{i+1,j} - h_{i,j}}{(\Delta fx)_i (\Delta cx)_i} - T_{i-\frac{1}{2},j} \frac{h_{i,j} - h_{i-1,j}}{(\Delta bx)_i (\Delta cx)_i} + T_{i,j+\frac{1}{2}} \frac{h_{i,j+1} - h_{i,j}}{(\Delta fy)_j (\Delta cy)_j} - T_{i,j-\frac{1}{2}} \frac{h_{i,j} - h_{i,j-1}}{(\Delta b1)_j (\Delta cy)_j} + Q \quad (8.31)$$

where half-grid values of T denote harmonic rather than arithmetic averages computed using Eq. (8.4), where

$$(\Delta cx)_k = (x_{k+1} - x_{k-1})/2, \quad (8.32)$$

$$(\Delta fx)_k = x_{k+1} - x_k, \quad \text{and} \quad (8.33)$$

$$(\Delta bx)_k = x_k - x_{k-1} \quad (8.34)$$

denote central, forward, and backward differences, respectively. Re-writing this more compactly in compass notation

$$\mathcal{L}_h = d_S h_S + d_W h_W + d_P h_P + d_E h_E + d_N h_N + Q \quad (8.35)$$

with

$$d_W = \frac{T_{i-\frac{1}{2},j}}{(\Delta x)_i^2}, \quad d_E = \frac{T_{i+\frac{1}{2},j}}{(\Delta x)_i^2}, \quad d_S = \frac{T_{i,j-\frac{1}{2}}}{(\Delta x)_j^2}, \quad d_N = \frac{T_{i,j+\frac{1}{2}}}{(\Delta x)_j^2}, \quad (8.36)$$

and $d_P = -(d_W + d_E + d_S + d_N)$.

We use the Crank-Nicolson semi-implicit method for computing our hydraulic head

$$\frac{\Delta h}{\Delta t} = \Theta \mathcal{L}_h(h^{n+1}) + (1 - \Theta) * \mathcal{L}_h(h^n) \quad (8.37)$$

(with $\Theta = 0.5$ for Crank-Nicolson) and then update the transmissivity with an explicit Euler step:

$$T^{m+1} = T^m + \Delta t (a_{\text{melt}}^m + a_{\text{cavity}}^m - a_{\text{creep}}^m), \quad (8.38)$$

where we use a combined forward- backward-difference scheme for the discretization of $(\nabla h)^2$ in Eq. (8.10):

$$(\nabla h)^2 \approx \frac{1}{2} \left[\left(\frac{h_{i,j} - h_{i-1,j}}{(\Delta_b x)_i} \right)^2 + \left(\frac{h_{i+1,j} - h_{i,j}}{(\Delta_f x)_i} \right)^2 + \left(\frac{h_{i,j} - h_{i,j-1}}{(\Delta_b y)_j} \right)^2 + \left(\frac{h_{i,j+1} - h_{i,j}}{(\Delta_f y)_j} \right)^2 \right]. \quad (8.39)$$

Compared to central differences, this stencil is more robust at nodes with large heads caused by moulines.

The time step is chosen sufficiently small so that the discretization error is dominated by the spatial discretization. Additionally, we check that the time step is small enough for the unconfined component of the scheme to become active by restarting the time step with a decreased Δt if at any point $h < z_b$.

All variables are co-located on the same grid, but the transmissivity T is evaluated at the mid-points between two grid cells using the harmonic mean due to its better representation of transmissivity jumps (e.g. at no-flow boundaries).

A disadvantage of this discrete formulation is that it is not mass-conservative (see, e.g. Celia et al. (1990)). The solution to this is to use a mixed formulation for Darcy flow in which also the Darcy velocity is solved for. However, in our application, the resulting error is very small, and we plan to implement the mixed formulation approach in future work.

COMPETING INTERESTS

The authors declare that they have no conflict of interest.

8.7 ACKNOWLEDGEMENTS

This work is part of the GreenRISE project, a project funded by Leibniz-Gemeinschaft: WGL Pakt für Forschung SAW-2014-PIK-1. We kindly acknowledge the efforts of Basile de Fleurian und Mauro Werder who were designing and supporting the SHMIP project. We highly benefited from their well developed test geometries and fruitful discussions not only at splinter meetings.

Basile helped in the development of the method by suggesting unconfined aquifer flow as a solution for negative water pressure.

We acknowledge A. Aschwanden for providing basal melt rates, temperatures and velocities simulated by PISM. Development of PISM is supported by NASA grants NNX13AM16G, NNX16AQ40G, NNH16ZDA001N and by NSF grants PLR-1644277 and PLR-1603799.

9 SHMIP THE SUBGLACIAL HYDROLOGY MODEL INTERCOMPARISON PROJECT

CONTEXT

The difficulties to verify a subglacial hydrology model (due to the lack of observations) and the absence of a single unique theory of the subglacial drainage system, available models incorporate different physical processes, leading to diverse modelling concepts. This makes it difficult to compare them and the studies that have been conducted using these models.

The Subglacial Hydrology Model Intercomparison Project (SHMIP), which is presented in the following paper, aims to establish a set of synthetic experiments that can be used to assess different drainage models and compare them to one another. The 13 participating models reach from zero dimensional lumped element model to two dimensional models that incorporate channels as well as cavities. Since the models are so diverse in their design, effective pressure and discharge have been chosen as general and ‘observable’ quantities along which the models can be compared. Six different experiments have been designed to determine steady state and transient behaviour, as well as the influence of different topographies. Since the physics of the participating models are very different, it is not easy to generate comparable results. The chosen solution was to suggest to tune models to a reference run, done with a trusted model. The experiments are comprised of a steady state setup for uniform supply, localized input with prescribed moulin locations, diurnal cycle, seasonal cycle, bed overdeepening on a valley topography and a seasonal cycle on a valley topography.

In the context of the thesis, this benchmark provides an excellent opportunity to test the model that was presented in the previous chapter. Especially, because the equivalent aquifer approach requires a reference to work. Unfortunately, I was unable to complete the experiments on the valley topography due to numeric problems with the boundary condition and time constraint.

The supplemental information of this paper is not included in this thesis, because it consists of over a hundred pages of results for all models.

CONTRIBUTION

B.dF. and M.A.W. designed the experiments, ran their respective models, analysed the model results and wrote the paper. All the other co-authors ran their respective models and provided feedback both on the intercomparison design and paper writing. I set up the CUAS model, implemented the experimental setup, tuned it to the given reference, analyzed the results and wrote the model description part for CUAS. With B.dF, I discussed on how to compare the single drainage component of CUAS to the models that used two different components for the drainage system.

AUTHORS AND AFFILIATIONS

Basile de Fleurian¹, Mauro A. Werder², Sebastian Beyer^{3,4}, Douglas J. Brinkerhoff⁵, Ian Delaney², Christine F. Dow⁶, Jacob Downs⁷, Olivier Gagliardini⁸, Matthew J. Hoffman⁹, Roger LeB Hooke¹⁰, Julien Seguinot², Aleah N. Sommers¹¹

¹*Department of Earth Science, University of Bergen and Bjerknes Centre for Climate Research, Bergen, Norway*

²*VAW, ETH Zurich, Zurich, Switzerland*

³*Potsdam Institute for Climate Impact Research, Potsdam, Germany*

⁴*Alfred Wegener Institute, Helmholtz Centre for Polar and Marine Research, Bremerhaven, Germany*

⁵*Geophysical Institute, University of Alaska Fairbanks, Fairbanks, AK, USA*

⁶*Geography and Environmental Management, University of Waterloo, Waterloo, Canada*

⁷*Department of Mathematics, University of Montana, Missoula, MT, USA*

⁸*Univ. Grenoble Alpes, CNRS, IRD, IGE, F-38000 Grenoble, France*

⁹*Fluid Dynamics and Solid Mechanics Group, Los Alamos National Laboratory, Los Alamos, NM, USA*

¹⁰*School of Earth and Climate Sciences and Climate Change Institute, University of Maine, Orono, ME, USA*

¹¹*Civil, Environmental and Architectural Engineering, University of Colorado, Boulder, CO, USA*

ABSTRACT

Subglacial hydrology plays a key role in many glaciological processes, including ice dynamics via the modulation of basal sliding. However, there is no unique theory with which the subglacial drainage system should be modelled. Consequently many different physical processes form the basis of the available models. Given this context, the Subglacial Hydrology Model Intercomparison Project (SHMIP) provides a set of synthetic experiments to compare past, present, and future models. We present results of these experiments from the 13 participating models focusing our evaluation on the effective pressure and discharge. The results show that for many applications (e.g. steady states and annual variations, or low input scenarios) a simple model, such as an inefficient system-only model, a one or zero dimensional model, or a porous-layer model will provide results comparable to those of more complex models. However, when studying short term (e.g. diurnal) variations of the water pressure, the use of a two-dimensional model incorporating physical representation of both efficient and inefficient drainage systems will yield significantly different results compared to simpler models and should be preferentially applied. The results SHMIP also emphasised the importance of water storage in the response of water pressure to transient recharge. Finally, we find that the localisation of the recharge points has a limited impact except in regions of very sparse moulin density.

9.1 INTRODUCTION

Subglacial water flow has long been the subject of glaciological studies (see Clarke, 1987, for a historical overview). The early quantitative treatments of subglacial drainage were motivated by a diverse range of problems: Weertman, 1962 considered how a water layer at the glacier base impacts sliding, Röthlisberger, 1972 developed his theory of channelised flow (through R channels) in connection with hydro-power generation related work, and Nye, 1976 extended R channel theory with time-dependence to investigate glacier lake outburst floods. Recent development in subglacial drainage theory is driven largely by motivation to better understand and represent glacier sliding, along with other aspects such as outburst floods and subglacial sediment dynamics in models.

It is indeed this link to ice dynamics which spurred the most recent, ongoing burst of subglacial drainage model development. Currently, we do not fully understand the impact of increased surface melt in a warming climate on ice dynamics (e.g. IPCC, 2013). For glaciers and land-terminating portions of the ice sheets, an acceleration in ice flow may lead to increasingly negative mass balances by moving ice to lower, warmer, elevations (Ridley et al., 2010). For marine or lake terminating glaciers, ice dynamics plays a significant role in the volume of ice that will be calved at the front of the glaciers, but may be mostly driven by processes at the terminus (Veen, 2002). This dynamic component amounts to approximately half of the mass loss of Greenland (Enderlin et al., 2014) and most of the mass loss of Antarctica (IPCC, 2013). A large part of mean ice velocity is due to slip of the glacier over its bed (e.g. Morlighem et al., 2013; Cuffey and Paterson, 2010; Engelhardt and Kamb, 1998). Basal slip is a combination of both sliding of the glacier ice over its bed and deformation of a water saturated till layer underlying the ice (Cuffey and Paterson, 2010). Both components of slip are primarily driven by the presence of water at the base of the glacier, in particular by its pressure (e.g. Wal et al., 2008; Iken et al., 1993; Iken and Bindshadler, 1986). Thus to assess the impact of increased surface melt on ice dynamics, we need to determine the response of the subglacial system to enhanced water input; current theories and models suggest that water pressure, and thus ice flow speed, could either increase or decrease, depending on the situation (e.g. Tedstone et al., 2015; Doyle et al., 2014; Sole et al., 2013; Shannon et al., 2013).

The scarcity of data and complexity of the subglacial system makes it difficult to pinpoint the water-induced processes acting at the base of glaciers. Therefore, a large number of subglacial hydrology theories have been developed since the 1960s to reproduce the flow of water at the bed of the glaciers (e.g. Creyts and Schoof, 2009; Kamb, 1987; Walder, 1986; Nye, 1973; Röthlisberger, 1972; Weertman, 1962). Existing subglacial drainage models have been developed based on these theories according to specific needs, preferences, and practical considerations, leading to a plethora of models whose results can be difficult to set in context with each other. For example, over the last couple of decades, a number of subglacial hydrology models have been developed that compute basal water pressure directly from meltwater input (e.g. Fleurian et al., 2014; Werder et al., 2013; Flowers et al., 2004), with a comprehensive overview given in Flowers, 2015. Another approach is to use a pressure definition as a closing equation for the subglacial hydrology model (e.g. Kavanagh and Tarasov, 2017; Bueller and Pelt, 2015).

This intercomparison project sets out to alleviate the problem of multiple theoretical approaches to subglacial hydrology by establishing a set of synthetic simulation suites and comparing the results of the participating models running those suites. This study should therefore help potential

users of these models to make a more qualified decision as to which model to choose for their application. Likewise for model developers, this may help to assess where further model developments are needed and gives a reference to gauge the characteristics of their future models.

The aim of this intercomparison is different from some of the ice flow intercomparison projects (e.g. Payne et al., 2000). In the case of the latter, the physics is reasonably well established for ice flow, although boundary conditions remain less clear. For subglacial hydrology, however, a complete and “true” theory is lacking. In other cases, such as the ice-thickness estimation intercomparison ITMIX (Farinotti et al., 2017), a set of measurements is available to test the models against. Unfortunately, observations of subglacial drainage are sparse, difficult to interpret (e.g. borehole measurements, Rada and Schoof, 2018) and unlikely to fully constrain all the parameters of a subglacial drainage model (e.g. Brinkerhoff et al., 2016). Furthermore, to date, applications of subglacial drainage models to real topographies and forcings are few and often hampered by modelling difficulties. We therefore decided that for this first Subglacial Hydrology Model Intercomparison Project (SHMIP) a comparison to observational data was not suitable and instead opted for synthetic test cases. This allows for qualitative comparison of the participating models.

Note that this intercomparison in no way aims to assess the correctness of the participating models. In particular, this means that no attempt is made to verify or validate the results provided by these models. We feel that the former point is not the task of an intercomparison project, while the latter may form the basis of a future SHMIP exercise where comparisons against field measurements are conducted. All of the results of the SHMIP exercise are openly accessibly at Fleurian et al., 2018a for further studies.

We first give a brief overview of subglacial drainage modelling and describe the physics implemented by the participating models. We then describe the approach taken by SHMIP and the different suites of experiments, before presenting results from the 13 models. Finally, we provide a synthesis of model results, and discuss strengths and potential shortcomings based on the results of the intercomparison project.

9.2 THE WIDE VARIETY OF SUBGLACIAL HYDROLOGY MODELS

The design of this intercomparison exercise allowed any model that calculates effective pressure (defined as ice overburden pressure minus subglacial water pressure) to participate in the exercise. The project thus attracted a wide range of models: from a zero dimensional lumped element model to models simulating the entire two dimensional glacier bed; including models developed in the 1980s to models under current development; and ranging from models simulating one component of the system, for instance R channels, to models coupling several systems. Table 9.1 gives an overview of the participating models.

Often the components of the drainage system are classified into two types: inefficient (and slow) drainage, and efficient (and fast) drainage, with the former usually represented as a distributed system and the latter as a channelised system (e.g. Flowers, 2015). This difference is a consequence of how the steady-state of such a system transforms under an increase in discharge: in an inefficient system pressure increases, as steeper gradients are required to conduct the increased discharge; conversely, in an efficient system pressure decreases, as the system’s capacity increases enough to allow operation at lower gradients.

Table 9.1: Summary of the participating models. The model label is defined as the two initials of the experimenter; if the used model was published/written by someone else, then one initial of the first author is appended (e.g. *cdf*); models implemented by the experimenter from a published model are cited as “implementing: original publication”; two different models of the same experimenter are distinguished by a subscript number; two submissions of the same model using different parameters are distinguished by a prime. “Suites” lists the suites for which model results were submitted. “Dim.” gives the number of spatial dimensions of the model, which is used in the text to differentiate between them, i.e. 0D, 1D or 2D models. “Model Type” is a brief description of the type of model, which is used throughout the text; these are defined within the section “Subglacial hydrology modelling”.

Label	Experimenter	Citation	Suites	Dim.	Model type
<i>db</i>	D. Brinkerhoff	Brinkerhoff et al., 2016	A,D-F	0D	conduit
<i>id</i>	I. Delaney	implementing: Kessler and Anderson, 2004	A-C,E,F	1D	conduit
<i>rh</i>	R. LeB Hooke	implementing: Röthlisberger, 1972	A,E	1D	one-channel (steady state only)
<i>cdf</i>	C. Dow	Pimentel and Flowers, 2010	A	1D	macroporous-sheet/one-channel
<i>jd</i>	J. Downs	implementing: Hewitt, 2011	A-E	2D	cavity-sheet
<i>jsb</i>	J. Seguinot	Bueler and Pelt, 2015	A-F	2D	cavity-sheet
<i>as</i>	A. Sommers	Sommers et al., 2018	A-C,E,F	2D	cavity-sheet (with melt opening)
<i>sb</i>	S. Beyer	Beyer et al., 2017	A-D	2D	(one) porous-layer
<i>bf</i>	B. de Fleurian	Fleurian et al., 2016	A-F	2D	(dual) porous-layer
<i>mh₁</i>	M.J. Hoffman	Hoffman and Price, 2014	A,D	2D	cavity-sheet/one-channel
<i>mh₂</i>	M.J. Hoffman	Hoffman et al., 2018a	A-D	2D	cavity-sheet/channels
<i>og</i>	O. Gagliardini	Gagliardini and Werder, 2018	A-F	2D	cavity-sheet/channels
<i>og'</i>	O. Gagliardini		E,F	2D	as <i>og</i> (but with $c_t = 0$)
<i>mw</i>	M.A. Werder	Werder et al., 2013	A-F	2D	cavity-sheet/channels
<i>mw'</i>	M.A. Werder		C,D	2D	as <i>mw</i> (but with $e_v = 10^{-4}$)

Many of the participating models are based, at least partially, on a linked cavity drainage system to represent the inefficient component of the drainage system, either using discrete elements (Kessler and Anderson, 2004) or a 2D sheet (Hewitt, 2011). The efficient component, if it is included, is usually represented as Röthlisberger channels (R channels) following Röthlisberger, 1972. The *cdf* model uses a different type of water sheet/inefficient system based on Flowers et al., 2004. Two models (*bf* and *sb*) pursue a different strategy and model the drainage as a porous aquifer, which is used to approximate discharge both through the inefficient and through the channelised system. In the following section, the different types of drainage system are briefly described. For a more in-depth comparison of subglacial drainage models, refer to the excellent review paper by Flowers, 2015.

9.2.1 SUBGLACIAL HYDROLOGY MODELLING

Common to all participating models is the use of a conservation of water equation which takes the form

$$\frac{\partial h}{\partial t} + \nabla \cdot \mathbf{q} = m, \quad (9.1)$$

where h is the local size of the water body (height, area or volume, depending on the formulation), q is the water flux, and m is a source term (accounting for meltwater input from the surface via the englacial system as well as water produced by geothermal flux, frictional heat from sliding, and heat produced by dissipation in the subglacial flow). The second common ingredient is the use of

a “water flow law” relating q with hydraulic potential gradient $\nabla\phi$ using a linear (Darcy flow) or nonlinear relation (Darcy-Weisbach or Manning)

$$\mathbf{q} \propto \nabla\phi \quad \text{or} \quad \mathbf{q} \propto \sqrt{\nabla\phi}, \quad (9.2)$$

where the hydraulic potential $\phi = p_w + \rho_w g z$ is the sum of water pressure p_w and elevation potential (with water density ρ_w , acceleration due to gravity g and elevation z). The factor of proportionality may depend on other state variables, in particular h . Both these equations can be applied in 2D (a sheet), in 1D (a channel or width integrated water sheet), or in 0D (integrated on the whole domain).

However, these are two equations for three unknowns q , ϕ , and h and therefore a third equation is needed to close the mathematical description of a subglacial drainage system type. Typically, this equation describes the size of the drainage space. The different participating models implement this third equation in various ways, which will be discussed in the following subsections. Furthermore, some models couple two drainage types together.

9.2.2 SHEET DRAINAGE

Over the years several formulations of water draining through a distributed system, often called a sheet drainage system, have been proposed e.g. Creyts and Schoof, 2009; Kamb, 1987; Walder, 1986; Weertman, 1962. The participating models use two types of sheet-like drainage. The first, proposed by Flowers and Clarke, 2002, is an empirical relation between water sheet thickness h and water pressure p_w based on data from Trapridge Glacier (Canada)

$$p_w = p_i \left(\frac{h}{h_c} \right)^{\frac{7}{2}}, \quad (9.3)$$

where p_i is ice overburden pressure and h_c is a critical sheet thickness. A model implementing this type of sheet drainage system will be referred to as a *macroporous-sheet model* (Table 9.1).

The second formulation used by some of the participating models is based on a linked cavity drainage system (Kamb, 1987; Walder, 1986). In a 1D setting, this formulation was advanced by Kessler and Anderson, 2004 and Schoof, 2010b; Hewitt, 2011 then generalised it to 2D by using a cavity height averaged over a suitably large patch of the glacier bed. The formula takes the form of a rate equation for h (cavity cross sectional area in 0D and 1D or average sheet height in 1D and 2D) which, when saturation is assumed, reads:

$$\frac{\partial h}{\partial t} = v_o - v_c, \quad (9.4)$$

where v_o is an opening rate, typically dependent on the sliding rate and bed roughness, and v_c is a closure rate due to ice creep. One possible form is

$$v_o = h_r u_b \quad \text{and} \quad v_c = \frac{2A}{n^n} h N^n, \quad (9.5)$$

where h_r is the bed roughness height, u_b is the ice sliding speed, A is the ice rate factor, n is Glen's exponent, and $N = p_i - p_w$ is the effective pressure. A model implementing this type of sheet drainage system will be referred to as a *cavity-sheet model* (Table 9.1).

Note that in most models the opening term v_o does not contain any energy dissipation term (c.f. next section), which was in the original description (Kamb, 1987; Walder, 1986), as its implementation is not trivial (Dow et al., 2018) and it can lead to mathematical issues such as runaway drainage space growth (Schoof et al., 2012). As an exception, model *as* does include opening by melt from dissipation, in conjunction with a different approach to the momentum equation (eq. 9.2) (Sommers et al., 2018). For a more detailed overview of sheet-like drainage consult the excellent overview given in Bueller and Pelt, 2015.

9.2.3 CHANNELISED DRAINAGE

The classic theory of channelised subglacial drainage, through R channels, was developed by Röthlisberger, 1972 and Shreve, 1972. Further work extended the theory to include time dependence and water temperature as a free variable (Spring and Hutter, 1982; Nye, 1976), and to enable the use of broad low conduits, rather than semi-circular ones (Hooke et al., 1990). Whereas other theories of channelised drainage exist, such as canals (Walder and Fowler, 1994) (although these can also be considered as a type of distributed system), all of the participating models implementing channelised drainage use R channels. Furthermore, none of the participating models include water temperature as a state variable and instead assume that water temperature is always either at the pressure melting point or at 0°C. The equation describing the channel cross-sectional area S is similar to the cavity-sheet equation

$$\frac{\partial S}{\partial t} = V_o - V_c. \quad (9.6)$$

The closure V_c is again by ice creep and is identical to eq. (9.5) (replacing h by S). Conversely, channel opening is due to ice melt at the channel walls

$$V_o = \frac{-Q \phi' + c_t c_w \rho_w Q p_w'}{\rho_i L}, \quad (9.7)$$

where the prime $'$ is short for the spatial derivative $\frac{\partial}{\partial s}$ along the channel, c_t is the Clapeyron slope, c_w the heat capacity of water, ρ_i the density of ice, and L the latent heat of fusion. The first term in the numerator is the dissipated energy in the flow (i.e. mechanical energy converted to thermal energy by the flow). The second term takes into account the changes in sensible heat due to pressure melting point variations, with the Röthlisberger constant $c_t c_w \rho_w \approx 0.3$. This second term can be neglected if the water is assumed to be always at 0°C. A model implementing this type of R channel drainage will be referred to as a *one-channel model*, if implementing one channel, or a *channels model*, if implementing a network of channels (Table 9.1).

The equations of a single cavity (eq. (9.4)) and an R channel (eq. (9.6)) can be combined into one

$$\frac{\partial S}{\partial t} = v_o + V_o - V_c \quad (9.8)$$

(Kessler and Anderson, 2004), sometimes termed a conduit (Schoof, 2010b), thus giving a drainage element which opens both by sliding and by melting. When opening by sliding dominates, the system behaves like a cavity, and otherwise, like an R channel. A model implementing this type of drainage system will be referred to as a *conduit model* (Table 9.1).

The equations (9.1), (9.2), and (9.6) describe a single R channel. However, the subglacial system is thought to consist of a network of these channels. Relatively recent advances (Hewitt, 2013; Werder et al., 2013; Schoof, 2010b) made the simulation of such a network of R channels possible.

9.2.4 POROUS LAYER DRAINAGE

The approach to modelling a network of R channels described above has several drawbacks, such as having to resolve each channel with the mesh and having no obvious continuum limit. This, among other things, inspired the development of the porous layer drainage models. These do not try to model the drainage system as described by the theory presented above but instead use one or several porous layers as an equivalent for different types of subglacial drainage. Porous layers are usually considered an inefficient drainage system at the base of glaciers (Shoemaker, 1986), but with proper parameter choice these layers can be configured to be as transmissive as highly efficient systems (Teutsch and Sauter, 1991). These models also rely on mass-conservation (eq. (9.1)) and Darcy flow (eq.(9.2)). To close the model, either a fixed layer thickness h is assumed, or the layer evolves according to a function of the pressure.

Two main approaches are used to simulate systems with different efficiencies within this porous layer framework. Either several layers with different conductivities can be implemented or a single layer where the transmissivity (the constant of proportionality in eq. (9.2)) may evolve. The porous layer models included here assume a non-zero compressibility (β) adding a significant amount of storage S_s to these models:

$$S_s = \rho_w g \omega h \beta \quad (9.9)$$

where ω is the porosity of the layer. A model implementing this type of drainage system will be referred to as a *porous-layer model* (Table 9.1).

9.2.5 ADDITIONAL DRAINAGE ELEMENTS

There are additional drainage elements incorporated in some subglacial drainage models, such as drainage through till e.g. Flowers and Clarke, 2002. In the participating models, only the variation of water storage as a function of water pressure is included as an additional process to those described above. Storage is represented in the englacial system as being well connected to the subglacial system (i.e. the englacial water table height corresponds to the subglacial water head). This necessitates a modification of the conservation equation (eq. (9.1))

$$\frac{\partial h}{\partial t} + \frac{\partial h_e}{\partial t} + \nabla \cdot q = m, \quad (9.10)$$

to include the effective storage component thickness h_e , which is given in terms of the water pressure $h_e = e_v \frac{p_w}{\rho_w g}$ with e_v the englacial void fraction.

9.2.6 COUPLING OF COMPONENTS

Subglacial drainage is thought to occur through different types of drainage systems, co-evolving in space and time and exchanging water with each other (e.g. Iken and Truffer, 1997). To approximate this complex behaviour, many models couple multiple system components together. One example is the conduit mentioned above (eq. (9.8)), combining an R channel and a cavity. Table 9.1 gives an overview over the coupled systems of each model. The individual models will be described in more detail in the following section. A model implementing several types of drainage systems will be referred to with the combination of systems it implements e.g. *cavity-sheet/one-channel model* and *macroporous-sheet/one-channel model* (Table 9.1).

9.3 PARTICIPATING MODELS

In this section a brief description of the participating models is provided within the context of the hydrological systems described above. For more details, refer to the relevant publication or, if unpublished, to the supplementary material or the source code. Table 9.1 gives a summary and below additional information is provided.

db: conduit model (0D)

Name and citation LSHM: Brinkerhoff et al., 2016

Developer(s) D. Brinkerhoff

Availability Open source¹

Type A lumped model integrating the englacial storage and specific size of a conduit over the glacier.

Pressure dependence of the melting point No

Spatial discretisation Lumped

Parameters/tuning Parameters as given in Table 9.3, no tuning.

Programming language

id: conduit model (1D)

Name and citation A single conduit model; following Kessler and Anderson, 2004; unpublished

Developer(s) M.A. Werder

Availability Open source².

Type A flowline model consisting of a englacial reservoir linked to a single conduit by a linked-cavity network.

Pressure dependence of the melting point No

¹available on request

²<https://bitbucket.org/maurow/1dhydro>

9 SHMIP The Subglacial Hydrology Model Intercomparison Project

Spatial discretisation Finite element
Parameters/tuning As given in Table 9.3 except for $c_t = 0$; no tuning.
Programming language Matlab/Octave

rh: one-channel model (steady state only) (1D)

Name and citation ProfilQ, PFQ, and PFQA: Hooke et al., 1990; Hooke et al., 1989
Developer(s) R. Hooke
Availability Closed source.³
Type A flowline model solving for a single, steady-state R othlisberger channel.
Pressure dependence of the melting point No
Spatial discretisation Integration headward from the terminus.
Parameters/tuning Parameters as given in Table 9.3, no tuning.
Programming language Fortran

cdf: macroporous-sheet/one-channel (1D)

Name and citation Macroporous-sheet model; Pimentel and Flowers, 2010
Developer(s) G. Flowers, S. Pimentel, C. Dow
Availability Closed source⁴
Type A 1D flowband model where a single flow-following semi-circular R channel exists per specified width of the 1-D vertically-integrated macroporous sheet.
Pressure dependence of the melting point Yes
Spatial discretisation Finite difference
Parameters/tuning Tuning on N of A5.
Programming language

jd: cavity-sheet model (2D)

Name & citation Implementation of Schoof et al., 2012
Developer(s) J. Downs
Availability Open source⁵
Type a 2D linked cavity model
Pressure dependence of the melting point No

³available on request

⁴available on request

⁵<https://github.com/JacobDowns/SheetModel/tree/shmip>

Spatial discretisation Finite element

Parameters/tuning Tuning with k on N of A5. Tuned parameters were then used in A6, as well as suites B and C. Otherwise as in Table 9.3.

Programming language FEniCS and petsc4py packages in Python

jsb: cavity-sheet model (2D)

Name and citation PISM v0.7.3: Bueler and Pelt, 2015.

Developer(s) E. Bueler, W. van Pelt and C. Khroulev.

Availability Open source^{6,7}.

Type A 2D cavity-sheet model,

Pressure dependence of the melting point No

Spatial discretisation Finite difference

Parameters/tuning No tuning. As given in Table 3 except for the englacial void fraction of $e_v = 1 \times 10^{-3}$ in A–D and $e_v = 1 \times 10^{-2}$ in E–F.

Programming language C++ / Python

as: cavity-sheet model (with melt opening) (2D)

Name and citation SHaKTI: Subglacial Hydrology and Kinetic Transient Interactions v1.0; Sommers et al., 2018

Developer(s) A. Sommers, H. Rajaram, M. Morlighem

Availability Open source⁸

Type A 2D cavity-sheet model with a single set of equations to represent both sheet-like and channelised drainage

Pressure dependence of the melting point Yes

Spatial discretisation Finite element

Parameters/tuning Tuned to N of model run A3. Parameters are as given in Table 3, with the exception of $A=5e-25$ for suites A, B, C, and E. Storage used only in suite E.

Programming language C++ with Matlab interface

sb: (single) porous-layer model (2D)

Name and citation Confined-unconfined aquifer model, Beyer et al., 2017

Developer(s) S. Beyer, T. Kleiner, A. Humbert

⁶<http://www.pism-docs.org>

⁷<https://github.com/juseg/pism-shmip>

⁸<https://issm.jpl.nasa.gov/documentation/hydrologysakti/>

Availability Closed source⁹.

Type A 2D single porous layer model where the evolution of the drainage system is implemented through variations of the transmissivity.

Pressure dependence of the melting point No

Spatial discretisation Finite difference

Parameters/tuning Tuned on N of A3 and A5.

Programming language Fortran and Python.

bf: (dual) porous-layer model (2D)

Name and citation Double continuum approach: Fleurian et al., 2016; Fleurian et al., 2014

Developer(s) B. de Fleurian

Availability Open source¹⁰

Type A 2D double porous layers model where one layer simulates the inefficient drainage system and the other, with a higher conductivity, the efficient system.

Pressure dependence of the melting point No

Spatial discretisation Finite element

Parameters/tuning Tuned on N of runs A3 (for the inefficient layer) and A5 (for the efficient layer)

Programming language C++ with Matlab and Python interfaces for ISSM, Fortran for Elmer/Ice

mh₁: cavity-sheet/one-channel model (2D)

Name and citation Subglacial hydrology model implemented in Community Ice Sheet Model; Hoffman and Price, 2014; Hoffman et al., 2016

Developer(s) M.J. Hoffman

Availability Closed source¹¹

Type A 2D cavity-sheet coupled to a single R channel that runs between grid cells along the centerline of the domain.

Pressure dependence of the melting point No

Spatial discretisation Finite difference

Parameters/tuning As given in Table 9.3; no tuning.

⁹available on request

¹⁰<https://issm.jpl.nasa.gov/documentation/hydrologydc/>

¹¹available on request.

Programming language Fortran

mh₂: cavity-sheet/channels model (2D)

Name and citation Subglacial hydrology model implemented in Model for Prediction Across Scales-Land Ice (MPASLI); Hoffman et al., 2018a; following Bueler and Pelt, 2015 but extended to include channels and use an unstructured grid

Developer(s) M.J. Hoffman

Availability Closed source¹²

Type A 2D coupled sheet and R channel model.

Pressure dependence of the melting point Yes

Spatial discretisation Finite volume

Parameters/tuning As given in Table 9.3; no tuning.

Programming language Fortran

og: cavity-sheet/channels model (2D)

Name and citation Elmer/Ice 8.2 implementation of GlaDS model; Gagliardini and Werder, 2018

Developer(s) O. Gagliardini, M.A. Werder

Availability Open source¹³

Type Same mathematical model as *mw*.

Pressure dependence of the melting point Yes

Spatial discretisation Finite element

Parameters/tuning As given in Table 9.3; no tuning.

Programming language Elmer finite element library, in Fortran

og' (as *og*)

Name and citation This is the same model as above (*og*) with the pressure dependence of the melting point turned off.

Parameters/tuning As given in Table 9.3 except with $c_t = 0$ for Suites E and F; no tuning.

Pressure dependence of the melting point No

mw: cavity-sheet/channels model (2D)

Name and citation Glacier Drainage System (GlaDS) model; Werder et al., 2013

Developer(s) M.A. Werder, C. Schoof, I.J. Hewitt, C. Dow

¹²public release in spring 2018, open-development henceforth.

¹³<http://elmerice.elmerfem.org/wiki/doku.php\setbox0=\hbox{0}\hboxto\wd0{id=solvers:glaDS>

Availability	Closed source ¹⁴
Type	A 2D coupled sheet and R channel model.
Pressure dependence of the melting point	Yes
Spatial discretisation	Finite element
Parameters/tuning	As given in Table 9.3; provided the base-case for the tuning scenarios.
Programming language	Matlab/Octave

mw' (as *mw*)

Name and citation	This is the same model as above (<i>mw</i>) with a different value for the englacial void fraction.
Parameters/tuning	As given in Table 9.3 except with $e_v = 10^{-4}$ for suites A-D.

9.4 INTERCOMPARISON CALL AND SETUP

The idea of an intercomparison of subglacial hydrological models was born during the International Glaciological Society (IGS) symposium on “Observations, Modelling and Prediction of the Cryospheric Contribution to Sea Level Change” in 2014. From these discussions and further meetings, an initial setup of the intercomparison was designed. After further refinement with the help of early testers, the setup and detailed instructions were posted on a website¹⁵ (the website contents are included in the supplementary material) and a call for participation was announced on the CRYOLIST email list on 14 October 2016. The deadline for submissions was 23 June 2017 with submissions received from 13 models.

The present intercomparison project deviates from many previous ones of other components of the ice dynamic system as there is no agreed theory on subglacial drainage nor is there a sufficiently dense dataset to allow a relatively conclusive comparison to reality. With these limitations in mind, we designed the intercomparison around six synthetic suites of experiments (labelled from A to F) each consisting of a set of four to six numerical experiments, subsequently referred to as runs. The suites are designed to allow a wide variety of models to take part in the intercomparison and to test a large range of scenarios. The main requirement is that models should output the effective pressure, which is used as the main diagnostic variable throughout the intercomparison. This approach excludes models based on a routing-approach (e.g. Le Brocq et al., 2009) and the till-layer based models (e.g. Bougamont et al., 2014). These alternative models do not explicitly compute effective pressures but instead use a pressure field unrelated to the state of the drainage system.

9.4.1 TOPOGRAPHIES

The intercomparison uses two different synthetic glacier topographies (Fig.9.1, Table 9.2). The first one (Fig.9.1a), used for the suites A to D is a synthetic representation of a land-terminating,

¹⁴available on request

¹⁵<https://shmip.bitbucket.io/>

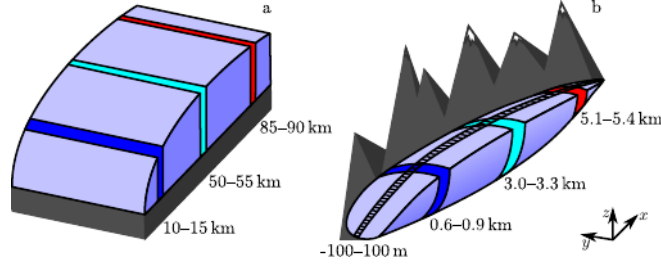


Figure 9.1: Sketches of the topographies used for the SHMIP, (a) 100 km long synthetic ice sheet margin with a maximum thickness of 1500 m, and (b) 6 km long synthetic valley glacier with a 600 m altitude difference between summit and terminus. The coloured and hatched bands are the regions used in the presentations of the results.

Table 9.2: List of symbols and fixed parameters used in the definition of the suites of experiments.

Name	Value and units	Symbol
Bed elevation	m	z_b
Surface elevation	m	z_s
Glacier outline	m	y_o
Time coordinate	s	t
Spatial coordinates	m	x, y
Lapse rate	-0.0075 Km^{-1}	$\frac{dT}{dz}$
Day	$24 \times 3600 \text{ s}$	s_d
Year	$365 \times s_d \text{ s}$	s_y
Degree day factor	$0.01/s_d \text{ mK}^{-1}\text{s}^{-1}$	DDF

ice sheet margin as seen, for instance, in Werder et al., 2013. This ice-sheet topography is 100 km long (in the x direction) and 20 km wide (in the y direction), with a flat bed, parabolic ice surface, and a maximum ice thickness of 1500 m:

$$\begin{aligned} z_s(x, y) &= 6 (\sqrt{x + 5000} - \sqrt{5000}) + 1, \\ z_b(x, y) &= 0, \end{aligned} \quad (9.11)$$

where z_s and z_b are the surface and bed elevation in metres, and x and y the horizontal spatial coordinates in metres. Note that to avoid numerical issues, the minimum ice thickness is 1 m.

The second topography (Fig. 9.1b), used for the suites E and F, is a synthetic, valley-glacier geometry. It is inspired by Bench Glacier, Alaska, USA (e.g. Fudge et al., 2008), is 6 km long, 1 km wide, and has 600 m of altitude difference. Its shape is given by the following two equations:

$$\begin{aligned} z_s(x, y) &= 100 \sqrt[4]{x + 200} + \frac{x}{60} - \sqrt[4]{2 \times 10^{10}} + 1, \\ z_b(x, y, \gamma) &= f(x, \gamma) + g(y) h(x, \gamma), \end{aligned} \quad (9.12)$$

in which γ is a parameter controlling the bed overdeepening, and f , g and h are helper functions defined as follows:

$$\begin{aligned} f(x, \gamma) &= \frac{z_s(6000, 0) - 6000\gamma}{6000^2} x^2 + \gamma x, \\ g(y) &= 0.5 \times 10^{-6} |y|^3, \\ h(x, \gamma) &= \frac{\left(-\frac{4.5x}{6000} + 5\right) (z_s(x, 0) - f(x, \gamma))}{z_s(x, 0) - f(x, \gamma_b) + 10^{-16}}, \end{aligned} \quad (9.13)$$

where $\gamma_b = 0.05$ is the parameter that is used as a reference γ and which gives the closest matching bed elevation to that of Bench Glacier. By design, the glacier boundary is the same for all γ and its half-width is given by

$$y_o(x) = g^{-1} \left(\frac{z_b(x, 0) - f(x, \gamma_b)}{h(x, \gamma_b) + 10^{-16}} \right). \quad (9.14)$$

9.4.2 BOUNDARY CONDITIONS

For the two geometries, the boundary conditions are prescribed to give a realistic distribution of the water pressure. The most important boundary is the margin of the ice sheet ($x = 0$ km) or terminus of the glacier ($x = y = 0$ km) where the water pressures are required to be null. The flux at this boundary is then free to evolve. All the other boundaries are treated as zero-flux boundaries.

9.4.3 PARAMETERS AND OPTIONAL TUNING

The two topographies are complemented by a set of physical parameters (see Table 9.3), which are used in the cavity-sheet/channels drainage formulations (eq. (9.1)–(9.10)). Models that implement this cavity-sheet/channels formulation (or a very similar one) were instructed to use the provided parameters in their model runs. Note that the englacial void fraction e_v is different for suites A–D and suites E–F.

However, a wider range of physics is incorporated in the participating subglacial hydrology models (and presumably future models that may use this intercomparison as a test setup), which require additional and/or different parameters. It is then not clear how to best produce results—which are comparable to each other—from running synthetic test cases with models that contain different physics. Our approach to this problem was to suggest tuning models whose parameters are not captured in Table 9.3 to the width-averaged effective pressure output of two reference runs of a model employing the cavity-sheet/channels formulation (GlaDS model, *mw*, tuning instructions¹⁶). Optionally, tuning could also use the width-averaged sheet and channel discharge. The chosen reference runs are two steady state runs with low and high recharge (runs 3 and 5 from suite A, Fig. 9.2m) which correspond to a sheet-only state and a channelised state of model *mw*. The models which used tuning are *cdf* (only A5), *jd* (only A5, for high discharge), *as* (only A3), *sb*, and *bf* (a white outline in Fig. 9.2 indicates a tuned model). All models tuned to effective pressure, and model *as* also roughly tuned to discharge. Note that the tuning was optional and

¹⁶<https://shmip.bitbucket.io/instructions.html/sec-1-2>

Table 9.3: Physical parameters appearing in the drainage model description with the values to be used, as applicable, for the simulations (eq. (9.1)– (9.10), upper part). Additional reference parameters from GlaDS-model (lower part).

Name	Value	Symbol
Water density	1000 kg m^{-3}	ρ_w
Glacier Density (ice+firn)	910 kg m^{-3}	ρ_i
Acceleration of gravity	9.8 m s^{-2}	g
Latent heat of fusion	334 kJ kg^{-1}	L
Specific heat capacity water	$4220 \text{ J kg}^{-1} \text{ K}^{-1}$	c_w
Clausius-Clapeyron constant	$7.5 \times 10^{-8} \text{ K Pa}^{-1}$	c_t
Glen's n	3	n
Ice flow constant ^a	$3.375 \times 10^{-24} \text{ Pa}^{-3} \text{ s}^{-1}$	A
Ice sliding speed	$1 \times 10^{-6} \text{ ms}^{-1}$	u_b
Bedrock bumps height	0.1 m	h_r
Englacial void fraction	0 (A–D) or 10^{-3} (E,F)	e_v
Bedrock bump wave-length	2 m	l_r
Turbulent flow exponent α	5/4	α
Turbulent flow exponent β	3/2	β
Sheet “conductivity”	$0.005 \text{ m}^{7/4} \text{ kg}^{-1/2}$	k_s
Sheet-width contributing to R channel melt	2 m	l_c
R channel “conductivity” ^b	$0.1 \text{ m}^{3/2} \text{ kg}^{-1/2}$	k_c

^aWhere the ice flow constant is for a closure relation as described in eq. (9.5)

^bequivalent Darcy-Weisbach $f = 0.195$ for semi-circular channel

that no tuning would not preclude participation. However, no participant used this option. Note that the prescribed tuning is unlikely to constrain all parameters of a subglacial drainage model, for instance any parameters reflecting transient behaviour will not be constrained. However, we feel that this tuning strategy presents a balance between making the model outputs comparable without requiring models employing other physics to over-fit and thus pushing them into a regime which is not representative for them. Last, note that results which are different from the reference run do not mean that the corresponding model is less correct, but merely different.

9.4.4 SUITE A: STEADY STATE

Table 9.4: Listing of the variable parameters for each suite of experiment runs. Suites A-D are using the synthetic ice-sheet margin topography, and suites E and F are using the synthetic valley glacier. See the description of each suite for more information on the varying parameter.

Suite	Varying parameter	Run: 1	2	3	4	5	6
A	water input m (m s^{-1})	7.93×10^{-11}	1.59×10^{-9}	5.79×10^{-9}	2.5×10^{-8}	4.5×10^{-8}	5.79×10^{-7}
B	number of moulins	1	10	20	50	100	n/a
C	relative amplitude R_a	1/4	1/2	1	2	n/a	n/a
D	temperature offset ΔT ($^{\circ}\text{C}$)	-4	-2	0	2	4	n/a
E	bed parameter γ	0.05	0	-0.1	-0.5	-0.7	n/a
F	temperature offset ΔT ($^{\circ}\text{C}$)	-6	-3	0	3	6	n/a

The six runs of suite A are based on the ice-sheet topography (eq. (9.11)) with a steady and spatially uniform water input. The primary objective of suite A (besides above discussed tuning) is to show the model results for a simple steady-state in terms of effective pressure and discharge. The input increases by four orders of magnitude from a low value corresponding to basal melt production (run A1, $m \approx 2.5 \text{ mm a}^{-1}$) to a high water input based on the peak water discharge driven by surface melt as observed in Greenland (run A6, $m \approx 50 \text{ mm d}^{-1}$ (Smith et al., 2017), see Table 9.4).

9.4.5 SUITE B: LOCALISED INPUT

The importance of input localisation is investigated in suite B. To test this, the spatially uniform input that was used in run A5 is instead fed into an increasing number of moulins (i.e. point inputs). The number of moulins increases from one (B1) to 100 (B5) between which the discharge is equally partitioned (see Table 9.4). The location of the moulins is randomly generated for each run and then used in all the different models. Experimenters running 1D models were instructed to collapse the moulin onto a single flowline. Additionally a distributed input, as in run A1, is included to represent basal melt.

9.4.6 SUITE C: DIURNAL CYCLE

The effects of the diurnal melt cycle on the response of the subglacial drainage system, i.e. short time scale dynamics, is targeted by suite C. The starting point for the runs of this suite is the steady

state achieved in run B5 (steady input into 100 moulin). The different runs are performed with diurnal melt cycles of increasing amplitude with recharge into each moulin given by

$$R(t, R_a) = \max\left(0, M_{in} \left[1 - R_a \sin\left(\frac{2\pi t}{s_d}\right)\right]\right), \quad (9.15)$$

where t is the time in seconds, s_d the number of seconds per day and $M_{in} = 0.9 \text{ m}^3\text{s}^{-1}$ the background moulin input from run B5 (see Table 9.2). The models are to be run until a periodic state is reached. The relative amplitude of the forcing R_a ranges from 0.25 for run C1 to 2 for run C4 (see Table 9.4). For run C4, the negative input values given by the high amplitude of the signal are cut off (see supporting Fig. S9) and therefore this run has an overall higher water input than C1 to C3 ($\simeq 20\%$ of volume increase). As in B5, a uniform and constant background input equal to the recharge of A1 is applied.

9.4.7 SUITE D: SEASONAL CYCLE

The seasonal evolution of the drainage system, i.e. the long time scale evolution, is investigated in suite D. It uses initial conditions from run A1, which represent the water input during winter. From this starting point, a seasonal cycle is applied to the water input and the model is run until a periodic yearly state is achieved. The forcing is computed from a simple degree day model driven by a temperature parameterisation. The temperature at 0 m elevation is given by

$$T(t) = -16 \cos\left(\frac{2\pi t}{s_y}\right) - 5 + \Delta T. \quad (9.16)$$

The runs of this suite are achieved by increasing the value of ΔT , i.e. increasing the mean annual temperature, from -4°C to 4°C (see Table 9.4).

The distributed recharge is then computed from the following degree day model formulation

$$R(z_s, t) = \max\left(0, DDF \left(T(t) + z_s \frac{dT}{dz}\right)\right), \quad (9.17)$$

where $\frac{dT}{dz} = -0.0075 \text{ Km}^{-1}$ is the lapse rate and $DDF = 0.01/86400 \text{ m K}^{-1}\text{s}^{-1}$ is the degree day factor (Table 9.2). As in suite B and C, a uniform and constant basal melt input equal to that of A1 is applied in all runs.

9.4.8 SUITE E: OVERDEEPENING OF VALLEY TOPOGRAPHY

Suite E is designed to investigate the effect of bed slope on the models. The common base for this suite is the synthetic valley topography (eq. (9.12)). The different runs of this suite are achieved by altering the shape of the bed topography to define a more or less pronounced overdeepening (see Table 9.4). The water input is constant and uniformly distributed at twice the rate of run A6 ($m \approx 100 \text{ mm d}^{-1}$). Note that reference parameters for the valley runs set a non-zero storage (Table 9.3).

9.4.9 SUITE F: SEASONAL CYCLE ON VALLEY TOPOGRAPHY

Suite F runs a seasonal water forcing—mirroring suite D—for the synthetic valley glacier using the baseline value of the topography parameter $\gamma = \gamma_b$. First the model is run to a steady state with water input as in A1, this steady state is then used as an initial condition for all the runs. Following this, a seasonal forcing as specified with eqs. (9.16) and (9.17) is applied using temperature offsets between -6°C and 6°C (see Table 9.4).

9.5 RESULTS

This study aims to illuminate the differences between various subglacial hydrology formulations and model implementations. Our evaluation focuses on effective pressure as that is the principal coupling to ice dynamics, which in turn is the primary motivation behind subglacial drainage studies. All of the submitted results are open source and can be accessed at Fleurian et al., 2018a for further investigation. We condense the results into three types of figures: steady-state with distributed recharge (suites A and E, Figs. 9.2 and 9.6), steady-state with moulin input (suite B, Fig. 9.3), and transient simulations (suites C, D and F, Figs. 9.4, 9.5 and 9.7). Figures 9.3, 9.4, 9.5 and 9.7 only present one or two runs in detail on which we focus the discussion. However, the figures for the other runs are provided in the supplementary material as well as numerous additional figures for each run and model.

Steady-state suites A and E are evaluated using the width-averaged effective pressure (N) (in suite A the full width and in E a band of 200 m width is used, indicated by the hatched band in Fig. 9.1b) and the percentage of flux in the efficient (channelised) system (Figs. 9.2 and 9.6). The latter is calculated, for most models, as the ratio of width-averaged channelised flux to total flux. This ratio is straightforward to compute for models that calculate the flux separately in the two systems, but for models relying on a single system to model both efficient and inefficient drainage another quantity is used as a proxy: for *sb*, the flux is considered to pass through the efficient drainage system when the conductivity is above its baseline level; for *as*, *db*, and *id* the ratio of melt opening rate to total opening rate is used; and for *jd*, *rh* and *jsb* no proxy-quantity was calculated as they are single system models. In our analysis, we classify the drainage system as efficient if more than 10% of the discharge is through the efficient/channelised system. We set this threshold at 10% because we find that at this stage the effective pressure is beginning to be characteristic of an efficient system with an increase in flux leading to an increase in effective pressure.

We evaluate Suite B, also at steady-state, by looking at the change between runs B1 and B4, which use localised moulin input, as compared to run A5, which uses the same total input but distributed uniformly (Fig. 9.3).

The results of suites C, D and F are transient states. Their width-averaged effective pressures are evaluated in three bands as displayed in Fig. 9.1, their width-integrated discharge is evaluated in either the lowermost band (C) or all three bands (D,F) (Figs. 9.4, 9.5 and 9.7). Additionally, the phase lag is calculated between the recharge forcing and effective pressure signal, as well as the effective pressure amplitude.

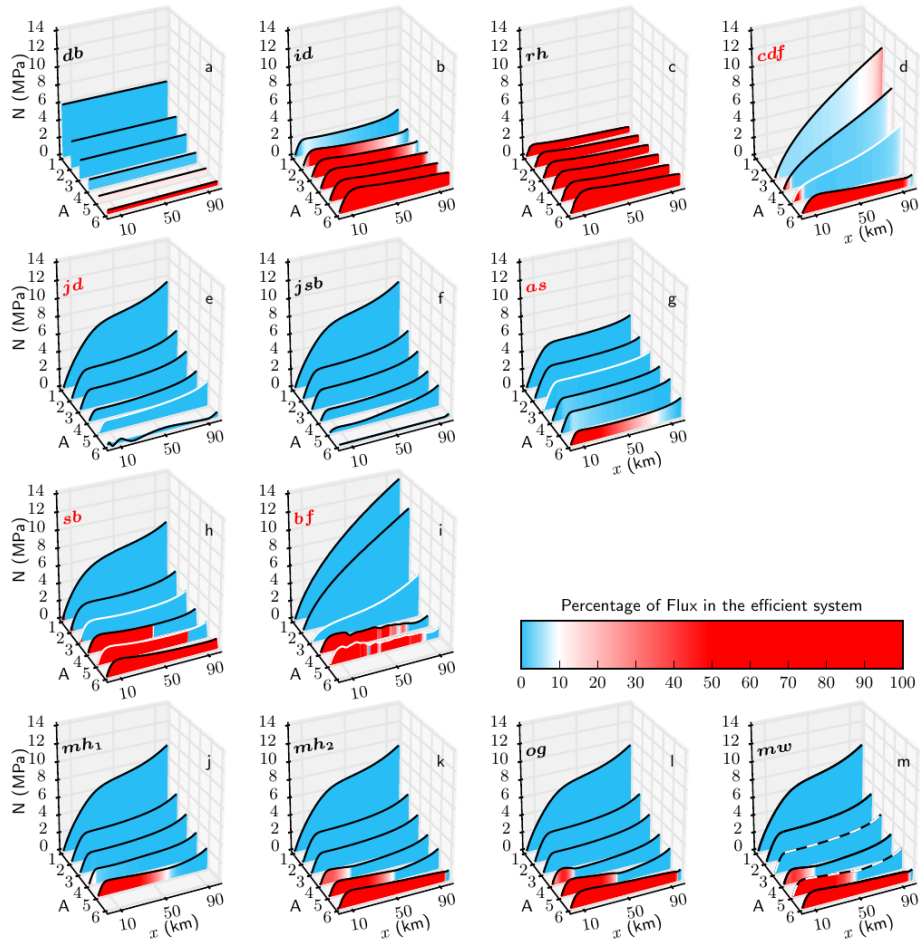


Figure 9.2: Suite A results: mean value of the effective pressure (N) versus distance from the terminus (x) for all runs (axis labelled A). Each submission is displayed in its own panel with the submission label printed. The results with the black and white dashed outline are the reference simulations used for tuning, models that were tuned to any of the reference simulations have their submission name in red and the fitted run is/are highlighted with a white outline. The colours represent the level of channelisation of the system we considered. Here a shift from inefficient to efficient drainage system occurs when 10% of the total flux is drained by the efficient drainage system.

9.5.1 SUITE A: STEADY STATE

All the results of this suite (Fig. 9.2) follow the widely acknowledged rule that, in a steady-state, a higher discharge in an inefficient drainage system (blue colours) will lead to decreasing effective pressure. This can be observed both as a decrease of N with decreasing distance to the terminus (x -coordinate) and with increased recharge forcing (runs A1 to A6). Conversely, an increase in discharge in an efficient drainage system (red colours) leads to an, albeit much smaller, increase in steady-state effective pressure.

The channel model rh shows increasing effective pressure for runs A1 to A6 as is expected. The A6 run produces higher N than the ones of the fully channelised cavity-sheet/channels models (mh_2 , og and mw), because all water is conducted through a single R channel, whereas the cavity-sheet/channels models have several in parallel (see supplement). The conduit model id shows similar results to rh except for the very lowest input where the single cavity of that model can accommodate all the flux. The 0D model db shows channelisation setting in at A5.

Moving upglacier from the terminus, all model runs—except the ones of 0D db and the ones staying near $N = 0$ throughout—show a steep increase of effective pressure in the first 10 km. This effect is driven by geometry and boundary conditions. The models using a cavity-sheet (jd , jsb , as , mw , mh_1 , mh_2 and og) then have a more levelled N in the centre part of the ice sheet and a final increase near the upper domain boundary. Of those models, the ones using exclusively a cavity-sheet drainage system (jd and jsb), show lower effective pressure starting from run A4 than the ones also incorporating an efficient system. The cavity-sheet of as produces effective pressure values positioned between those of the cavity-sheet and of the cavity-sheet/(one-)channel models, due to the way it allows for efficient drainage to develop by including opening by melt across the entire domain.

The models using tuning (cdf , jd , as , sb and bf) get a reasonable fit to their target input scenarios with a better fit for the higher input scenarios (when targeted). Using the tuned parameters, cdf and bf show effective pressures largely above the one of the reference simulation mw for runs A1 and A2 (A3 for cdf , for which A1 and A2 did not converge), and show no levelled region in the middle part of the domain. The porous-layer models sb and bf then predict more channelisation for A4; A6 of sb then closely follows mw , as does cdf (bf did not converge for this run). The different approaches to the porous approximation is particularly clear in this suite where the single layer model allowing variations in transmissivity (sb) closely follows the results of mw with slightly lower effective pressure. For the cavity-sheet model jd , the tuning to A5 does not yield significant improvement in the results of run A6 (where the tuned values are used).

9.5.2 SUITE B: STEADY STATE WITH MOULIN INPUT

Suite B tests the impact of localised recharge, i.e. through moulins, on the effective pressure distribution whilst keeping the total input constant. We show results for runs B1 and B4 (Fig. 9.3) where recharge is through 1 and 50 moulins, respectively. Figure 9.3 shows the difference in effective pressure between run B1 and A5 on the left column, the right column shows the difference between run B4 and A5.

The results show a clear demarcation between two different behaviours. For the higher moulin counts (greater than 20, run B3–B5), with B4 shown as representative example in Fig. 9.3j–r, the

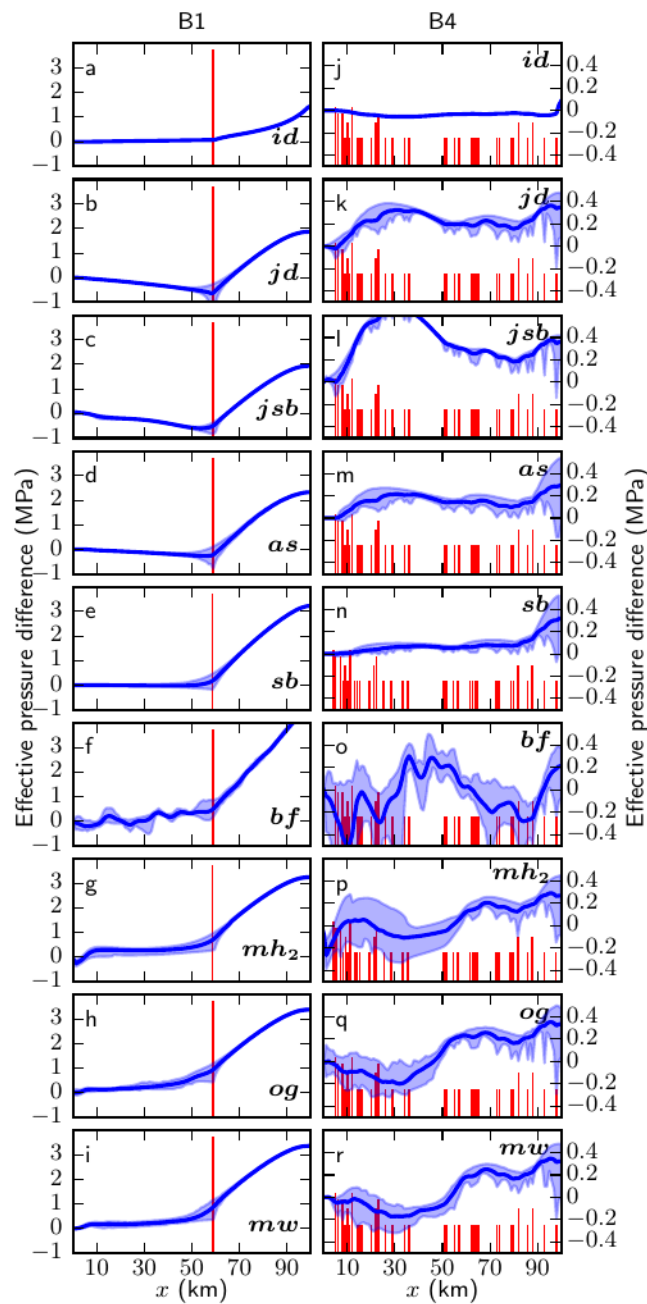


Figure 9.3: Suite B results: effective pressure difference between run B1 and reference run A5 (with same total recharge). The same plot is presented on the right column for run B4, note that higher effective pressure in B yields a positive value. The width-averaged difference is the solid blue line, and width-minimum and maximum difference are given by the light blue band. The red bars indicate the moulin locations, their height scaled with the logarithm of input; the higher bars for B4 (right) are due to multiple moulins located at the same x -coordinate.

impact of the localised input on effective pressure is relatively small (Note the difference in scale between left and right columns) and of similar magnitude over the whole domain. The results from *id* show an almost nonexistent variation of the effective pressure between simulations A5 and B4 along most of the domain. It is interesting to note that the effective pressure drops locally at moulin locations for all of the 2D models (Fig. 9.3b–i and k–r), which shows as little spikes along the lower bound of the pressure envelope (see also supplementary material).

The two runs B1 and B2 with lower moulin count (1 and 10, respectively), with B1 plotted in Fig. 9.3a–i, show the largest difference from A5 upstream of the highest moulin where effective pressure increases. This makes sense as the discharge upstream of the highest moulin is very small as it is due only to basal melt in the B runs. Downstream of the uppermost moulin the differences are much smaller, ranging from almost zero to mostly less than 0.5 MPa (roughly 10% of the ice overburden pressure). Generally, the models with only an inefficient system have lower effective pressure than A5 below the uppermost moulin (negative values) and the others have higher effective pressure.

9.5.3 SUITE C: DIURNAL CYCLE

Suite C probes the time evolution of effective pressure and discharge in response to a diurnal melt-water forcing using the moulins of B5 as input locations (Fig. 9.4). Our evaluation will focus on run C3 but figures of the other runs can be found in the supplementary material. All models produce a similar average effective pressure in the range 1 to 3 MPa; averaging the effective pressure over a day gives effective pressures almost identical to the one obtained for the steady-state run B5 for the models with higher storage values (*jsb*, *sb*, *bf*, *mh₂* and *mw'*) and *as*. The other models (*id*, *jd*, *og* and *mw*) show a lowering of the average effective pressure with the increase of the forcing amplitude (see supplementary figures).

The main difference between the models is the magnitude of the simulated diurnal effective pressure variation (Fig. 9.4b–k), which is chiefly dependent on the amount of available englacial and/or subglacial water storage. Participants running a model including a storage component were instructed to set it to zero. However, many models require some amount of storage for numerical reasons and thus retained non-zero storage for this suite. The model *mw* was also run with non-zero storage (model *mw'*) to investigate the effects of this variable, which is discussed below. Models that have low storage have large effective pressure amplitudes and little lag (1–2 h) between maximum recharge and minimum N (Fig. 9.4A–J). Conversely, models with ample storage have a very small effective pressure amplitude and the lag is about 6 h, corresponding to a quarter period. The pressure amplitudes increase with higher forcing amplitude, and are again much more pronounced for the models with little storage. This difference is nicely illustrated by the two submissions of the same model *mw* and *mw'*, the former using no storage, the latter using storage (Fig. 9.4j,k). Note that the models *jsb* and *mh₂* acquire their storage-like behaviour from solving a regularised pressure equation (Bueller and Pelt, 2015) without actually storing water.

The same variations, or lack thereof, also show up in the width-integrated discharge of the lower band (Fig. 9.4l–u). The cavity-sheet/channels models with little storage (*og* and *mw*) show a larger amplitude in the efficient system discharge, because the recharge via moulins directly feeds that system. The cavity-sheet/one-channel models show a partitioning of $\sim 50 \text{ m}^3 \text{ s}^{-1}$ in the efficient and $\sim 25 \text{ m}^3 \text{ s}^{-1}$ in the inefficient system. In model *as*, most of the flux is through

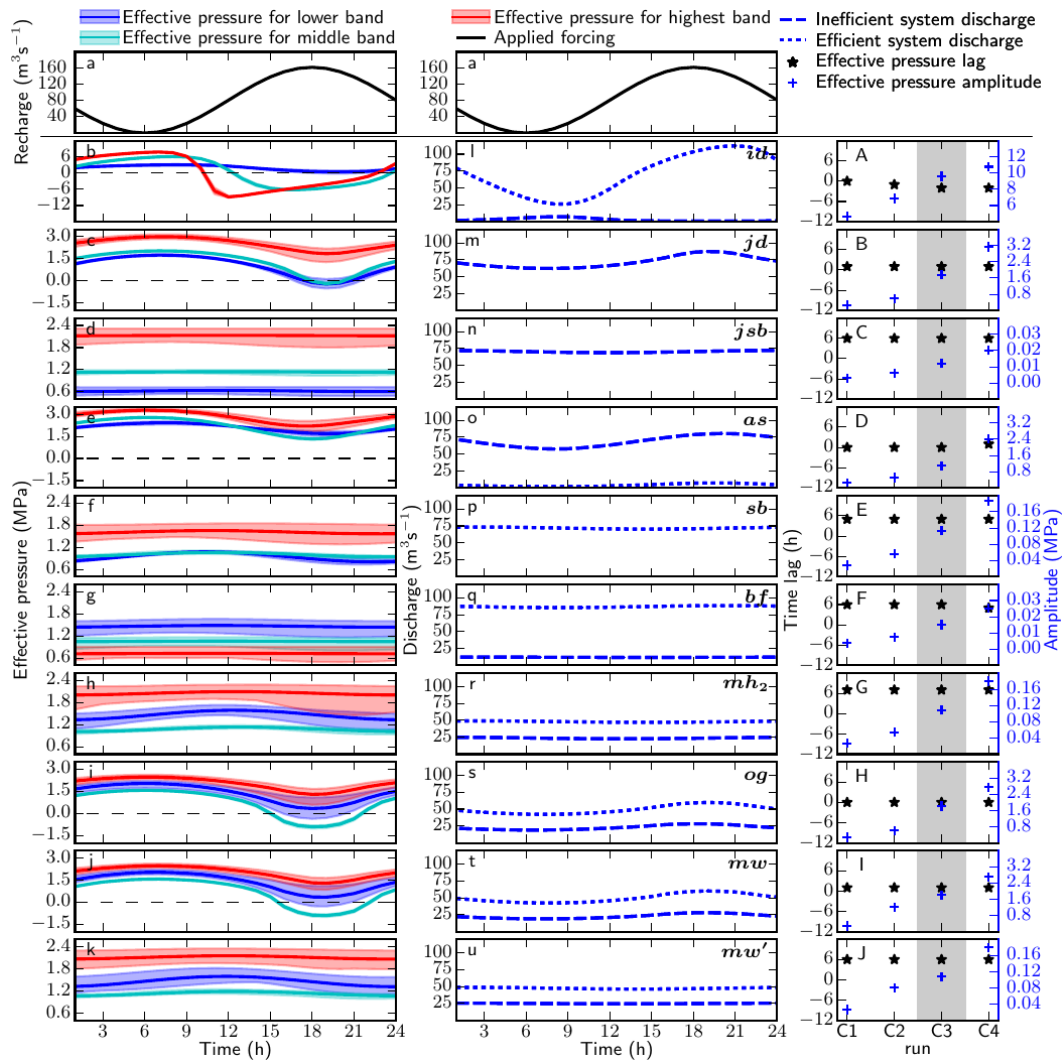


Figure 9.4: Suite C results: Left and centre columns show run C3 with a panel for each submission, right column shows all runs. The top row shows total recharge for the whole domain (a). Each other row shows the results of one model (model label in the middle column). The left column (b to k) shows evolution of the mean effective pressure in the three bands as defined in Fig. 9.1a, where the coloured line shows the mean value and the shading represents the spread within the band, the dotted black line marks zero effective pressure. The middle column (l to u) shows evolution of the discharge in the inefficient (dashed) and efficient (dotted) drainage system for the lower band. The right column (A to J) shows the time lag between maximum recharge and minimum effective pressure (black stars) and amplitude of the effective pressure variation (blue cross) averaged over the entire domain for runs C1 through C4. Note the scale for amplitude of effective pressure variations varies between models. The greyed region in the right column emphasises that run C3 is plotted in the left two columns.

the inefficient system with a slight increase of the efficient drainage when the recharge is at its maximum. Conversely, the two porous-layer models conduct most/all of the discharge in the efficient system.

9.5.4 SUITE D: SEASONAL CYCLE

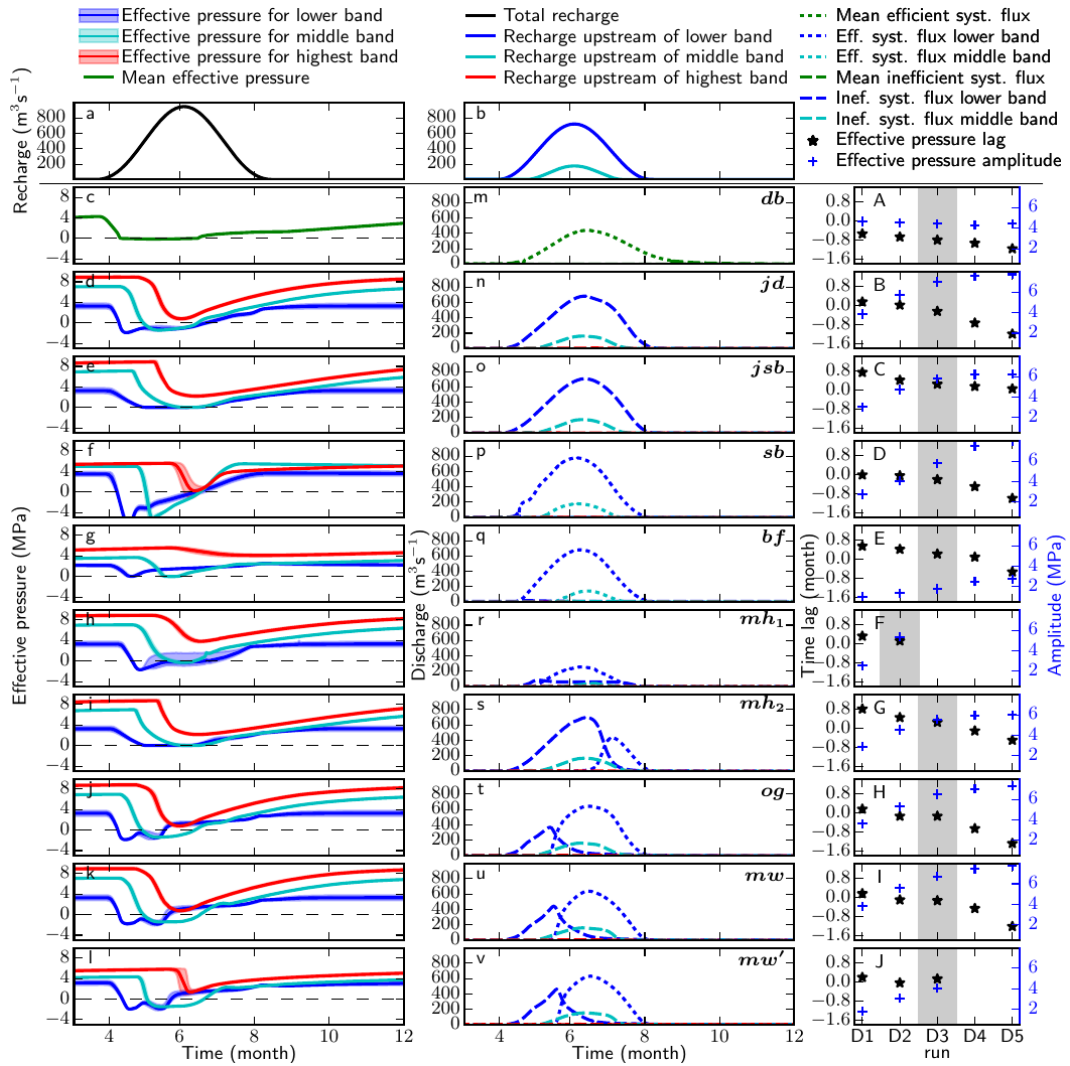


Figure 9.5: Suite D results presented as in Fig. 9.4 but with the following differences: Middle column plots discharge at all three bands defined in Fig. 9.1a. The greyed region in the last column emphasise which run is plotted in the two left columns: D3 for all models except for mh_1 where it is D2 (which has thus lower discharge).

The results of suite D, a seasonal cycle with distributed recharge, are presented in the same style as those of suite C. Our evaluation here will focus on run D3 (Fig. 9.5, see supplementary material for other runs).

During winter, the effective pressure of all of the models runs is high at around 3 to 8 MPa with the lower bands having lower N (first column of Fig. 9.5). This is in contrast to recorded winter pressures (e.g. Wal et al., 2015), which tend to show effective pressures close to zero. The comparison of the two mw models illuminates the impact of storage where a higher storage value (mw') leads to a lower effective pressure during winter.

A common trait of the effective pressure response to the recharge increase in spring is a drop in effective pressure, a spring event (Röthlisberger and Lang, 1987), which propagates upstream to the highest band by mid-summer. Those models that do not cap N at zero simulate negative effective pressures during this phase on some bands, persisting for several months in many instances. All the models, except the double porous-layer (bf), show a rather similar amplitude of the effective pressure variations, whereas the bf model shows a notably smaller amplitude on the highest band of the domain. The mw' model with more storage than mw shows a delayed drop in the effective pressure in highest band (red), which is also a characteristic observed in the porous-layer models for the same reasons.

The response of the different models tend to diverge after the initial effective pressure drop. A major difference between the models with two types of drainage systems is the evolution from inefficient to efficient system: The cavity-sheet/channels models first carry most of the discharge in the distributed system and then transition—but only in the lower band—to channelised drainage (middle column Fig. 9.5) with model mh_2 showing a markedly later transition than the other two. For the porous-layer models, this shift happens earlier in the season and also reaches the middle band. This is due to the instant activation of the efficient system once a threshold effective pressure is reached. The cavity-sheet models show an asymmetric discharge with an increase that is slower than the recharge increase and a steeper discharge decrease at the end of the melt season. The 0D model db shows the inverse behaviour with faster discharge increase and a longer duration for the decrease of the discharge.

The rightmost column of Fig. 9.5 shows the amplitude of the effective pressure variations and the time lag between the time of maximum recharge and the effective pressure minimum for all D runs. All models show similar trends for those two values: the effective pressure minimum occurs earlier as the water recharge increases (from D1 to D5). For most models, the effective pressure minimum follows peak recharge for lower recharge intensity, and precedes peak recharge with higher recharge intensity. The amplitude of the effective pressure variation also increases as discharge increases, except in the 0D model (db). This is due to the fact that in model db , the effective pressure is limited to positive values, which already limits the amplitude for D1.

9.5.5 SUITE E: OVERDEEPENING OF VALLEY TOPOGRAPHY

Suite E tests the influence of an overdeepening on the simulated steady-state drainage system (Fig. 9.6). This suite is performed with the synthetic valley glacier topography (Fig. 9.1b). The main impact of an overdeepening should come through the pressure dependence of the melt-opening term (second term of eq. (9.7)), which at the supercooling threshold (e.g. Werder, 2016) should lead to R channel shutdown.

This shutdown is indeed what is seen in the channel model rh : for run E3, which is below the supercooling threshold, it produces positive effective pressures throughout; however for E4, which is beyond the threshold, its channel shuts down at ~ 1 km and N reaches 0 (at which point

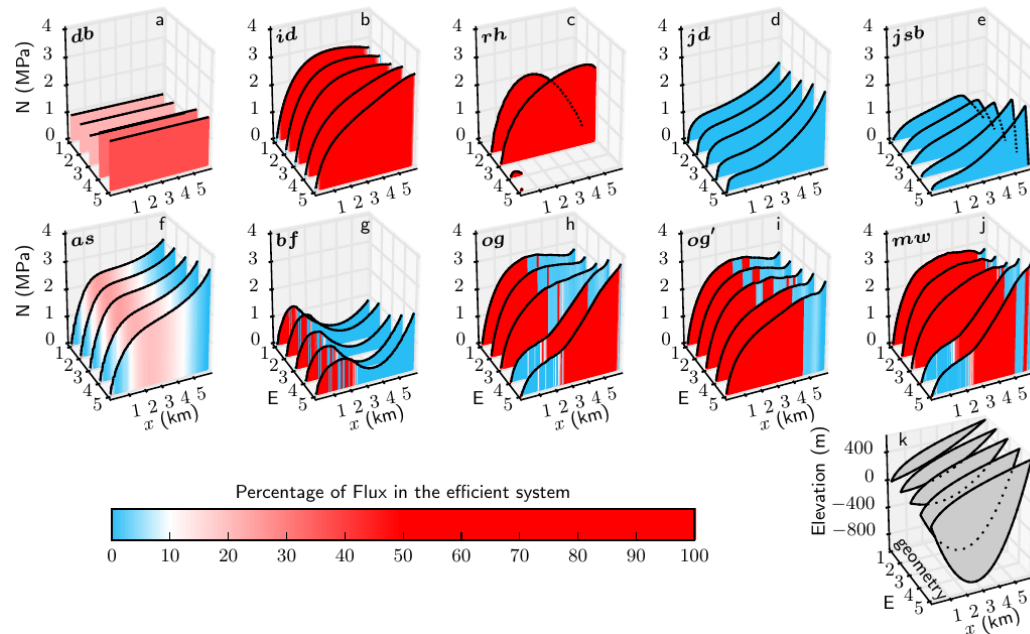


Figure 9.6: Suite E results presented as in Fig. 9.2, with the centre-line topography used for each run in panel k. For the 2D models, the effective pressure and the fraction of flux in the efficient system are calculated by averaging values in a band along the centre-line of width 200 m (hatched band in Fig. 9.1b).

the model fails). The *id* model has similar physics as *rh* but does not include the pressure-melt term in eq. (9.7). Consequently, the overdeepening has very little influence on the shape of the effective pressure curve as the (constant) surface slope is then the dominating influence.

Similarly, the cavity-sheet models *jd* and *jsb*, which have no pressure-melt dependence (eq. (9.5)), show little impact of the overdeepening, producing positive effective pressures throughout. The pronounced difference between *jd* and *jsb*, in particular towards the upper glacier, is due to the fact that the *jsb* model constrains water pressure to always be positive. This means that effective pressure has to go to zero at all boundaries (where ice thickness is zero), including the upper glacier margin. All other 1D and 2D models which submitted results for suite E (and F) have no such constraint and thus will in general produce negative water pressure in part of the valley glacier domain (see supplementary material). The *as* model, also a cavity-sheet model but including opening by melt everywhere and a pressure dependant term, shows small effects due to the overdeepening. The different discharge formulation used in this model allows for representation of laminar and turbulent flow regimes, as well as the wide transition between them, producing smooth transitions between inefficient and efficient systems. As the topography deepens, more of the bed is in a flow regime closer to laminar (i.e. lower Reynolds number, with linear dependence on potential gradient). This corresponds to the idea of the efficient system diminishing (or channel shutdown) with more dramatic overdeepening, and is apparent in the extension of the downstream blue region (inefficient system) from E1-E5 in Fig. 9.6f.

The cavity-sheet/channels models *og* and *mw* show no negative effective pressures, unlike *rh*, even though they do contain the pressure-melt term. However, N is reduced markedly for the two runs E4 and E5 (where the supercooling threshold is exceeded) and in the same region the drainage system transitions from efficient for $x > 2$ km back to inefficient for $0 < x < 2$ km. This means that the channel system does shut down and that the water is then carried in the cavity-sheet (and also in channels along the sides of the overdeepening, see supplementary material). The cavity-sheet/one-channel model *og'* is as *og* but with the pressure-melt term turned off, again this therefore shows very little impact of the overdeepening and the efficient system is operating throughout.

The porous-layer model *bf* shows a pronounced impact of the valley topography but only minor changes as the overdeepening is enlarged, therefore its bed topography has little impact. It produces an efficient system up to 2 km, then an inefficient one, which causes effective pressure to drop markedly to a minimum at 4 km.

For the 0D model (*db*), which has no pressure-melt term, the effective pressure is similar for the first three runs and then rises slightly for the last two. This is unlike the other models, which all show a decrease of the effective pressure (albeit only a small one when there is no pressure-melt term). This effect might be caused by the use of an averaged topography in this lumped model.

9.5.6 SUITE F: SEASONAL CYCLE ON VALLEY TOPOGRAPHY

Suite F has the same objective as suite D—to explore the seasonal drainage cycle—but using the valley-glacier topography of E1 (i.e. without overdeepening, Fig. 9.1). Its results are presented in the same style as suite C and D with the evaluation focusing on run F4 (Fig. 9.7 and supplementary material).

During winter, the effective pressure of all models is relatively high and markedly higher than during times of meltwater input (left column). The lowest is produced by the *jsb* model, in particular at the highest elevation. This is again due to this model constraining the water pressure to be positive, as mentioned in the previous section. This constraint is also the reason why its effective pressure has the largest spread of all models (light coloured bands in Fig. 9.7e), as it needs to go to zero at the lateral margins. All other models have very little lateral spread in effective pressure and compute negative water pressures towards the margins.

All models show a more or less pronounced decrease in effective pressure as melt sets in (approximating a spring event), some in the upper two bands only, some in all, except *jsb* which shows no impact in the highest band. A rapid drop of N is simulated by the cavity-sheet/channels models *og*, *og'* and *mw*, the porous-layer model *bf*, and the conduit model *id*. A more gradual drop is shown by the cavity-sheet models *as* and *jsb* and the 0D model *db*.

The conduit model *id* shows an instant response in effective pressure at all elevation bands followed by a rapid recovery to a steady summer value. The cavity-sheet/channels models show a pronounced drop over about one month with a slight recovery after channelisation sets in (see discharge plot in middle column). The porous-layer model *bf* shows a more gradual drop to almost zero effective pressure and then a rapid recovery as the efficient layer is activated, which is also clearly visible in the discharge plots. The two cavity-sheet models show a much more gradual response, in particular *jsb*, which is probably due to ample water storage. The *as* model shows

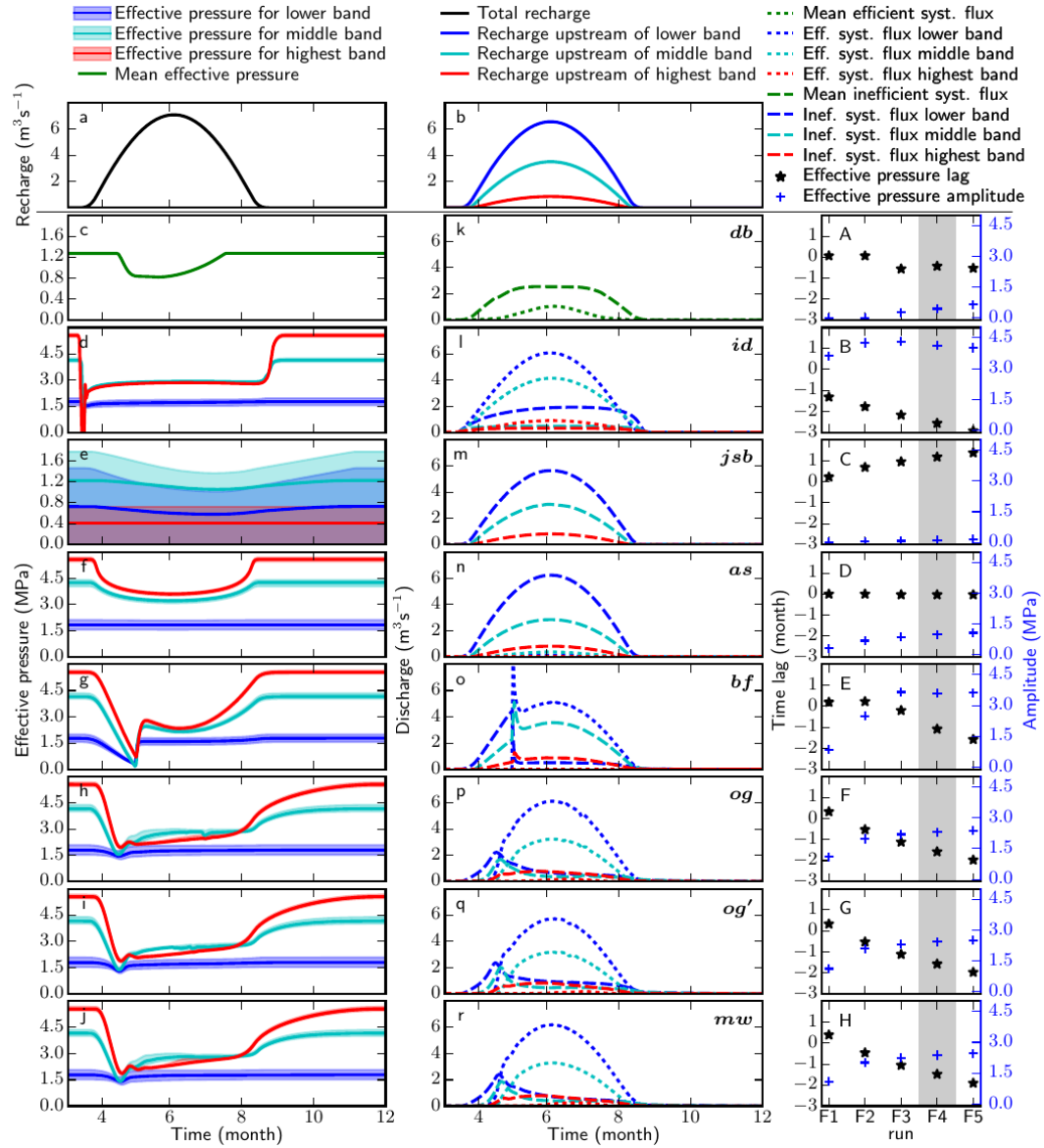


Figure 9.7: Suite F results presented as in Fig. 9.5. The left and middle columns display results of run F4. The three bands for which results are plotted are marked in Fig. 9.1b.

little opening due to melt in the peak summer season, which is represented in the middle column by the low discharge through the efficient system.

At the end of the summer, the return to the winter state happens at different rates. For the models *db*, *id*, *as* and *bf* the return happens simultaneously with recharge shutdown. The cavity-sheet/channels models and the cavity-sheet model *jsb* recover much more slowly over the course of a few months.

The dynamic response to the forcings of different magnitudes of runs F1 to F5 (right column) shows that in most models the time of minimum effective pressure (taken as an average over the whole domain) leads the time of maximum recharge by around one month, with this lead time increasing with increased recharge intensity. Similarly, the amplitude of the effective pressure increases with increased forcing. Exceptions to this are: *jsb*, for which effective pressure lags recharge and the amplitude stays very low; and *as*, which shows an increasing amplitude but zero lag, due to the fact that zero storage is used by this model in this suite.

9.6 DISCUSSION

The SHMIP exercise consists of six suites of four to six experiment runs, which are set up to enable a comparison of subglacial drainage system models. The experiments were developed such that a wide variety of models could participate with the only requirement being that effective pressure was computed. This excluded some models, notably the routing-type models which use a hydraulic potential (and thus effective pressure) independent of the state of the drainage system (e.g. Le Brocq et al., 2009); and the models which only consider local water balances, such as subglacial till models (e.g. Tulaczyk et al., 2000b; Bougamont et al., 2014). Nonetheless, our publicly available results could be re-interpreted in terms of discharge only and compared to the outputs of those types of models.

To allow the comparison of models with different physical approaches, two reference simulations are provided for the tuning of models that require it. The choice of the reference runs (ice sheet geometry, steady state and uniform input runs A3 and A5) is such that fitting to these results should not bias the rest of the intercomparison, which presents simulations with different characteristics. Likewise, the choice of a cavity-sheet/channels model for this reference simulation (*mw*) is motivated by the fact that this approach is the most widespread and so gives a set of parameters for the bulk of existing models. The tuning procedure (or need for tuning) was left to the discretion of the experimenter and was not a mandatory step of the intercomparison. Note that models that are tuned use similar parameter values as in other studies conducted with these same models.

The 13 participating models show a broad agreement between each other in all suites. In particular, they agree with one of the fundamental theoretical considerations of subglacial drainage: in an inefficient drainage system a discharge increase will lead to a decrease in steady-state effective pressure and, conversely in an efficient drainage system, a discharge increase will lead to an increase in steady-state effective pressure (Fig. 9.2). Conversely, none of the models are showing the low effective pressure that is usually observed during winter (e.g. Wright et al., 2016). The more specific responses of the models are generally similar across groups of models incorporating similar physics (see last column of Table 9.1). Considering the complexity in analysing and interpreting

the published subglacial hydrology records (e.g. Rada and Schoof, 2018), our discussion of the SHMIP results will focus on an intercomparison of the model results and reference observations where applicable. A direct comparison to observations is beyond the scope of this study and is left to a future SHMIP.

A large number of models use a cavity-sheet drainage system (*jd*, *jsb*, *as*, *mh₁*, *mh₂*, *og*, *mw*), which leads to consistent results for all of these in the low recharge scenarios (A1–A3, winter period of D and F). The 0D conduit model *db* also produces results consistent with the cavity-sheet models for those scenarios. The other models show different behaviours at low recharge: the two layered porous-layer models (*bf*) as well as macroporous-sheet model (*cdf*) produce much higher effective pressures than the cavity-sheet models. This is due to the fact that in these models the conductivity of the inefficient drainage system does not adapt to the discharge of the system. Conversely, the 1D channel or conduit models (*rh*, *id*), which are designed for higher recharge scenarios, show much lower effective pressure at low discharge, which follows R channel theory. The scaling of the transmissivity to a cavity opening formulation in the single layer porous model (*sb*) allows for a reduction in the layer conductivity at low discharge yielding effective pressure distributions closer to those of *mw*.

For higher recharge runs, the response of the models with and without an efficient drainage component diverge as can be seen in suite A (run A4 to A6) and E1 and E2 (which have no overdeepening). Notably, the representation of the efficient drainage system in the porous-layer models seems to well capture the dynamics observed in the cavity-sheet/channels models for suite A. However, whereas for the steady-state runs (suite A, B and E) the differences between cavity-sheet-only and cavity-sheet/channels models are large, for seasonal forcings (suites D and F) they are much smaller, for instance *jd* is very similar to *mw* in suite D except for the band closest to the margin (10–15 km, Fig. 9.5). The likely cause is that the transient “summer” state in suite D and F is far away from a steady-state channelised system. This means that in those runs the distributed system drains more of the subglacial discharge than it would in a steady-state corresponding to a high summer recharge magnitude. This interpretation can be supported by field measurements. Based on borehole observations in a land-terminating area of the Greenland Ice Sheet, Meierbach-tol et al., 2013 suggested that channels do not reach further inland than approximately 20 km. In the same region, tracer experiments indicate that the channelised system extended inland at least 41 km but not as far as 57 km (Chandler et al., 2013).

The impact of the topography on steady-states can be seen by comparing results of the high recharge runs of suite A (A5, A6) with the run E1 (or E2) of suite E where there is no overdeepening and recharge is similar. The channel models (*db*, *id*, *rh*, *og*, *mw*) produce about twice as high an effective pressure in E1 versus A6 (e.g. *id* in Fig. 9.2b vs. Fig. 9.6b), which is due to the steeper surface slopes and shorter glacier length. Similarly, the cavity-sheet-only models (*jd*, *jsb*, *as*) produce effective pressure around zero in A6, whereas in E1 it is around 1 MPa, again due to the influence of topography.

The moulin-recharge suite B showed that the impact of localised input on average effective pressure is relatively minor in all models, with variations usually below 10% of the ice overburden pressure. However, there is one exception: it matters where the upper moulin is located, as above that moulin the effective pressure is much higher than what a uniform input predicts. The farthest inland location where water reaches the glacier bed is indeed a topic of current studies (e.g. Hoffman et al., 2018b; Gagliardini and Werder, 2018; Poinar et al., 2015). Introducing lo-

calised inputs also modifies the local effective pressure (with lower effective pressure at the moulin locations) and the distribution of the efficient channelised drainage system (see supplementary figures). This decrease of effective pressure at moulin locations is consistent with observations that hydraulic head is higher in the vicinity of moulins (Andrews et al., 2014; Gulley et al., 2012).

The transient runs illustrate the importance of storage (in the sense of a direct functional relationship between pressure and storage as in eq. (9.10)) and also of storage-like effects that can arise from numerical regularisation. For the diurnal-variation suite C, storage impacts the pressure variation amplitude, with the results ranging from almost zero (high storage) to 13 MPa of amplitude (no storage) (Fig. 9.4). These amplitudes can be compared to the observations from Haut Glacier d’Arolla (Gordon et al., 1998), where amplitudes varying from 0 to 0.9 MPa were observed in a cluster of borholes. Note that the two models jsb and mh_2 do not implement actual storage but use a storage-like term to regularise the pressure equation (see Bueler and Pelt, 2015), which shows some of the same effects as actual storage. The discharge also has a muted diurnal variation compared to the recharge as storage increases. Therefore, observations of recharge and proglacial discharge could help further constrain the storage capacity of a glacier drainage system (e.g. Brinkerhoff et al., 2016; Bartholomew et al., 2012; Huss et al., 2007).

For the seasonal forcings (suite D and F), storage has a lesser impact as the drainage system has more time to react to the more gradually changing recharge. In the mw model, increasing storage (mw') leads to lower effective pressure during the winter and also to a delayed but sharper response in spring in the two higher elevation bands. The former is due to increased water flow (and thus lower N) during winter as more water can be released from storage. The latter is due to the dampening effect that increased storage has on the subglacial water pressure response.

The seasonal-forcing runs of all models show a high effective pressure during winter, higher than during the whole melt season (except for the porous-layer models in the highest elevation band in suite D, Fig. 9.5f,g). This is contrary to many borehole observations (e.g. Rada and Schoof, 2018; Dow et al., 2011; Fudge et al., 2005), which show a shutdown of the drainage system leading to effective pressures around zero. There has been some recent progress in modelling such a shutdown (Rada and Schoof, 2018; Dow et al., 2018; Downs et al., 2018; Hoffman et al., 2016) but none of the participating models include such processes. An alternative view is that the participating models, as well as many others, only ever simulate the well-connected system, which could potentially persist at high effective pressures throughout the winter, however with a footprint small enough that it is rarely observed.

All the models show pronounced “spring events” (Iken and Bindshadler, 1986) for both suite D and F, i.e. low effective pressure as the surface melt forcing sets in. Effective pressure then increases again as the drainage system adjusts to the higher flux. Of note is that this increase in effective pressure also occurs in models with only an inefficient system, such as jd (Fig. 9.5d). This is because an inefficient system will also (transiently) respond to an increase in recharge with an effective pressure drop and a subsequent drop as the drainage space and thus the efficiency increases (eq. (9.4)), as explained in Hoffman and Price, 2014. The duration of the effective pressure drop varies from less than a month to several months. These pressure drops can be compared to observed speed-up events ranging from one to several months depending on the location of the measurements (Wal et al., 2015; Hoffman et al., 2011; Bartholomew et al., 2010).

Most models reach negative effective pressures in suite D for extended periods of time in both the lower and middle band. The models that do not reach negative N either constrain it to be

positive (db , jsb , mh_2) or, in the case of bf , instantly activate the efficient drainage system when $N = 0$ is reached (this activation can be seen nicely in Fig. 9.7o). This is arguably the more realistic behaviour as month-long periods of negative effective pressures over the large areas predicted by the other models is not observed and would have a much more dramatic impact on ice dynamics than “spring events”. However, likely none of the models capture the drainage system dynamics as N approaches zero correctly, as then uplift of the ice should occur which includes non-local effects due to elastic and viscous behaviours (Walker et al., 2017; Tsai and Rice, 2010). Note that in the seasonal suite F, zero or negative effective pressures are only reached very briefly by bf and id , all others have $N > 0.7$ MPa; again this is due to the larger surface slopes and shorter length of the valley topography compared to the topography of suite D.

The simulated transition back to the winter state at the end of the melt season is of varying temporal length. The porous-layer models recover very quickly, in less than a month for suite D and even quicker for F, and afterwards the effective pressure only increases slightly. The cavity-sheet models in addition to the 0D-conduit model db react much more slowly and transition over three to four months to the winter state in suite D. The large-scale effective pressure considered in SHMIP (mean value over an altitudinal band rather than local effective pressure) is not necessarily suited for direct comparison to observations. However, the interpretation of Rada and Schoof, 2018 presenting different “stages” is particularly helpful. The transition of effective pressure back to its winter level can be compared to “stage 2”, which lasts around a month and is approximately represented in our seasonal suite F for the valley glacier topography. This result however depends on the interpretation of both the model results and the field observations and will be open for debate as long as more efficient ways to compare modelled and measured effective pressure are developed.

Of the participating models, the most physically complex models are the cavity-sheet/channels models. They largely reproduce the theoretically expected behaviours as explained above. This was the main reason we picked the output of such a model as a tuning benchmark (runs A3 and A5 of mw). The models that used this tuning were the ones which use implementations based on different draining components: the macroporous-sheet model (cdf), the porous-layer models (sb , bf), the cavity-sheet model including energy dissipation (as) and one cavity-sheet model (jd) (only for a subset of the experiments). No models participated that incorporated other physically based theories of drainage than cavity(-sheets) and R channels, such as canals (Walder and Fowler, 1994) or other distributed drainage types (e.g. Creyts and Schoof, 2009).

The models which implement only a cavity-sheet show shortcomings when applied to higher input scenarios with effective pressures that are too low. However, in the seasonal runs, which are probably the most realistic forcings in this intercomparison exercise, they show little difference to the cavity-sheet/channels models even though recharge is high in mid summer. This high input can, in the case of these models, be accommodated by the increase in efficiency of the cavity-sheet system. This shows that they are probably applicable to many situations. However, they lack the fast rebound of the effective pressure in their frontal region, which might be of high relevance for ice dynamics considerations (e.g. Wal et al., 2015). They benefit from less model complexity and from a clearer mathematical foundation, in the sense that they approximate a continuum solution (Bueler and Pelt, 2015). The as model gains wider applicability by introducing the pressure melting-opening term (e.g. run A6). The momentum equation used in this model facilitates the transition between flow regimes that allows for the process of self-organised channelisation to oc-

cur and be represented stably, while including the melt term everywhere (Sommers et al., 2018). Previous model formulations found the inclusion of a melt term to be problematic (Schoof et al., 2012) albeit possible (Dow et al., 2018).

The porous-layer models yield similar results to the cavity sheet/channels models for many of the suites. The *sb* model is able to generate quite complex effective pressure variations with a single layer model. The double layer approach of *bf* is applicable to the steeper valley glacier topography and produces a comparable response to the cavity sheet/channels models in suite F.

The results from the 0D, conduit model (*db*) illustrates that simplification can be pushed far. The overall behaviour of the model is qualitatively in line with the more complex cavity sheet/channels models. However, this model is biased toward lower effective pressure and compares better to the values on the lower region of the domain than to the overall mean value of the spatially distributed models. This could be due to the design of the model itself but also to the chosen parameterisation or chosen topography. Also notable is that the *db* model is one of the few subglacial drainage models which has been rigorously fit to observations using Bayesian methods (Brinkerhoff et al., 2016); most other models have only been hand-tuned (if at all) to fit observations (e.g. Koziol and Arnold, 2018; Fleurian et al., 2016).

The three 1D models (*rh*, *cdf*, *id*) show results consistent with the theories they implement. Their shortcomings are likely related more to approximations of the theory than to the fact they are implemented in only one dimension. This is certainly in part due to the fairly one-dimensional geometries of our test suites. The performance of these models suggests that 1D models are valuable in settings where geometry can be reduced to a flow line with insignificant lateral variation.

9.7 CONCLUSION

Thirteen models participated in this first subglacial hydrology model intercomparison project (SHMIP). They incorporate a wide range of different drainage system types, with a focus on inefficient drainage through linked-cavities, efficient drainage through R channels, and approximations of both of these systems by using drainage through porous-layers. All participating models were required to calculate effective pressure distributions. No models participated that incorporated other physically based theories of drainage such as canals (Walder and Fowler, 1994) or other distributed drainage types (e.g. Creyts and Schoof, 2009). It should also be noted that models not computing the effective pressure such as routing models were excluded due to its choice as a diagnostic variable.

The test suites of SHMIP cover a range of scenarios similar to those which subglacial drainage models are currently applied to. The suites use synthetic, idealized topographies of a land-terminating ice-sheet margin and a mountain glacier, with idealized recharge forcing ranging from steady input, to seasonal and diurnal variations. However, a few interesting and relevant scenarios are not included, such as the classic test case of jokulhlaups (e.g. Flowers et al., 2004; Clarke, 2003; Nye, 1976). A tide water glacier test-case is missing, which would be both interesting in a Greenland-like scenario, but also in an Antarctica-like scenario (e.g. Dow et al., 2016). Considering realistic modelling, some more complex forcings, such as a seasonal forcing with superimposed diurnal variations, and also real glacier topography would be of interest. These will be useful test targets to be included in a future iteration of SHMIP.

This intercomparison project provides a qualitative comparison of several state-of-the-art and legacy subglacial hydrology models. The use of a two-component model is strongly advised when considering high recharge scenarios, complex topographies, or observing short term variations in the subglacial hydrological system. For larger systems with low water fluxes, the use of a cavity-sheet only model should be considered as they achieve results comparable to more complex cavity-sheet/channels models. These cavity-sheet/channels models are needed when the dynamics of the efficient system is important, for instance in valley glaciers or when recharge is constant enough to let channels develop. Porous layer models are a viable approximation to the more physically realistic approaches in that they capture qualitatively the inefficient and efficient system dynamics, but a careful assessment of their parameters and flux formulations should be performed to ensure that they accurately represent the flow regime corresponding to the recharge applied to the model.

This intercomparison reveals that the effect of localised drainage is important on small scales but does not have significant impact on the overall distribution of water pressure. Special care, however, should be taken when specifying the location of the highest-altitude input point, as this altitude has a significant effect on the subglacial water pressure downstream.

Experiments introducing diurnal and seasonal variations have emphasized the impact of water storage on the results of the models and more particularly on the timing of their response in term of pressure. This could enable the parameterisation of storage from observations of the lag between water input and pressure response but also put a constraint on models which introduce the storage as part of their equations (as the porous layer models for example) or as a stabilisation mechanism (as in mh_1 for example).

Another well-known and important point, also highlighted by this exercise, is the need to use appropriate model parameters. However, these parameters are often largely unknown and future efforts need to focus on inferring them from observations (e.g. Brinkerhoff et al., 2016; Werder et al., 2010) or through other means, such as laboratory experiments. Once these techniques of parameter inversion of subglacial drainage models become more established and reliable, a SHMIP exercise using observational data will become viable.

ACKNOWLEDGEMENTS

B.dF. and M.A.W. want to thank everyone that took part in the discussions leading to SHMIP (Tim Creyts, Ian Hewitt, Christian Schoof, Gwenn Flowers, Jesse Johnson, Ed Bueler, Ugo Nanni, Angelika Humbert, Alison Banwell, Ian Willis, Stephen Price and others). B.dF. was supported by the European Research Council under the European Community 7th Framework Programme (FP7/2007–2013)/ERC under Grant Number 610055 (ICE2ICE) and computations were performed on resources provided by UNINETT Sigma2 - the National Infrastructure for High Performance Computing and Data Storage in Norway S.B. was supported by the GreenRISE project, a project funded by Leibniz-Gemeinschaft: WGL Pakt für Forschung SAW2014-PIK-1. I.D. was supported by the Swiss National Science Foundation (SNSF) National Research Programme (NRP) 70 “Energy Turnaround”, Project No.153927. C.D. was supported by the Canada Research Chairs Programme and the Natural Sciences and Engineering Research Council of Canada (Discovery - RGPIN-03761-2017) J.D. wants to thank Jesse Johnson for his help in implementing the model, he was funded for this work by NSF grant 1543533. O.G. was supported by the Agence Nationale

pour la Recherche (ANR) through the SUMER project (Blanc SIMI 6-2012). M.J.H. was supported by the Laboratory Directed Research and Development Early Career Research Program at Los Alamos National Laboratory (20160608ECR). J.S. was supported by the Swiss National Science Foundation (SNSF) grant no. 200021-153179/1 to M. Funk and the Swiss National Supercomputing Centre (CSCS) allocation no. s573 to J. Seguinot. A.S. was supported primarily by a NASA Earth and Space Science Fellowship (NNX14AL24H), and thanks Harihar Rajaram and Mathieu Morlighem for their invaluable contributions to model formulation and development.

10 CONCLUSIONS

10.1 ACHIEVEMENTS

The aim of this thesis is to study the feasibility of different numerical modelling approaches towards subglacial hydrology on a large scale and use evaluate their performance in different applications. In Chapter 2, I review the basic principles of subglacial hydrology. The current scientific understanding of the drainage system is assessed and it is reviewed how basal water flow is connected to the movement of large ice masses. Section 2.2 summarizes the different elements of the drainage system that need to be considered for formulating a comprehensive model. There is a wide variety of subglacial hydrology models that have been developed in the glaciological community. Owed to the difficulty to obtain and interpret integral observations of the drainage regime below the ice, there is no complete and established theory for subglacial hydrology and models employ a variance of different physical processes. Therefore, Chapter 3 explains the basic “recipe” that is the base for most models and reviews the different model approaches that have been made so far. While there were already some models that could be applied to continental scale modelling (e.g. Kleiner and Humbert, 2014), they were not in a state where they could easily be tested and coupled to the ice sheet model SICOPOLIS, which was used in the GreenRise project.

10.1.1 BALANCE FLUX MODELLING

The first objective was to implement a simple and efficient drainage model and couple it to SICOPOLIS. This was done by implementing the balance flux approach, as shown by Le Brocq et al. (2006) and Kleiner and Humbert (2014) and described in Section 3.2. An important addition was the addition of an efficient treatment of hollows and flats in the hydraulic potential, using the methods proposed in Barnes et al. (2014b) and Barnes et al. (2014a). This work resulted in the application of the model in context of the “*Missing Evidence of Widespread Subglacial Lakes at Recovery Glacier, Antarctica*” (Chapter 4), where the model could be tested. Despite the large uncertainties in the basal reflection coefficient, the spatial variability of the signal provides a possibility to assess the performance of the drainage model and showed good agreement with the additional indicators on where to expect water.

For the study of ice sheets over large time periods it is important to incorporate all the relevant physical mechanisms while still ensuring that the model can be run over the intended time period in a reasonable time. Processes at the margin of ice sheets play a major role in their evolution, where the often applied shallow ice approximation is not accurate (Gudmundsson, 2003). While the addition of a hydrology model can not account for the different physics, it is still worthwhile, because it results in a better representation of the flow (see Section 5.4.1). Coupling of the balance flux method to SICOPOLIS results in a model that can be used to investigate the role of subglacial hydrology over large time periods and resulted in the publication of “*Eurasian ice-sheet dynamics*

and sensitivity to subglacial hydrology” (Chapter 5). This work does also reveal that the basal hydrology is not only important for sliding of ice, but also has a significant effect on the temperature of the ice. Higher sliding velocities lead to enhanced advection of cold ice from the surface, decreasing the temperatures and decreasing the fraction of the bed that is at pressure melting point. Models that ignore subglacial hydrology do therefore overestimate temperate areas (Section 5.4.1).

Since the aim of the project was the assessment of the contribution of Greenland to sea level rise under climate change, the next publication “*Simulation of the future sea level contribution of Greenland with a new glacial system model*” (Chapter 6) uses the coupled model of ice dynamics and hydrology to investigate the effect on ice velocities and submarine melt of outlet glaciers. As recited in Chapter 1, the subglacial hydrology in Greenland has observed to have a seasonally evolving hydrology model with efficient channels emerging during summer. This makes the application of a balance flux model, that always assumes the water to move in a thin sheet and the effective pressure to be always zero questionable. However, the long term effects of this mechanism is not yet well understood. Sole et al. (2013) and Moon et al. (2014) show that the seasonal evolution only does not significantly changes the mean ice velocity over multiple years. The use of the hydrology model improves the ability of the ice sheet model to capture fast flow of outlet glaciers.

Subglacial hydrology does also play a role for subglacial melting at the termini of marine-terminated outlet glaciers. The subglacial water discharge generates water plumes which enhance melting of the ice front, leading to enhanced ice flow. The paper “*Modeling the response of Greenland outlet glaciers to global warming using a coupled flowline-plume model*” (Chapter 7) determines the effect of increased subglacial discharge to be comparable to the effect of warmer ocean water in respect to submarine melting. This important effect is often not considered when ice models are coupled with subglacial hydrology. The one-dimensional realization of the glacier flowline models made it necessary to accumulate the subglacial discharge for each glacier, sparking the development of C-IDRE and the procedure to assign discharge to individual glaciers described in Section 3.2.4. In this work, and also for the analysis of subglacial lake in Chapter 5, the hydraulic potential is computed at a higher resolution of 1 km at critical time steps, which proved to be a reasonable approach for ensuring sufficient resolution while keeping the computational cost low.

The use of balance flux methods currently seems to be the best approach for large scale applications, despite its lack of complex physics, simply because at the moment no other type of model is capable of computing periods as large as 280k years in a reasonable time.

10.1.2 EQUIVALENT AQUIFER MODEL

The interactions of subglacial hydrology and ice flow are complex and only recently new models have been able to reproduce melt-induced seasonal speedup as observed in Greenland. Though, there are still questions remaining, especially regarding the long-term effects of increased melt. Hewitt (2013) suggests that increased melt leads to an average increase in ice velocities over the year, while observations by Sole et al. (2013) show that higher summer velocities are correlated with lower winter speeds and that there is no effect on the annual mean. This means that the effects are not yet completely understood and that more work is necessary to comprehend the complex system. For this purpose, models of intermediate complexity can be useful, as they aim to strike a balance of sufficient complexity to capture all essential physics while being simple enough

that they can be applied on large domains. The CUAS model, developed during the course of this thesis and described in the article “*A confined–unconfined aquifer model for subglacial hydrology and its application to the North East Greenland Ice Stream*” (Chapter 8) is such a model. It uses the equivalent aquifer approach, that was introduced in Fleurian et al. (2014) and is described in Section 3.4. It improves the equivalent aquifer approach by allowing for unconfined flow and therefore always ensures physical values for the water pressure and simplifies the system to a single porous layer that is adapted according to water flux and pressure conditions. It is able to reproduce the seasonal evolution of the drainage system for an artificial geometry and is successfully used to compute the effective pressure distribution for the North East Greenland Ice Stream. Using the effective pressure in an ice dynamics model (ISSM) results in notably improved velocities.

The scarcity of observations of the subglacial hydrology make it hard to verify models and the variety of different approaches for modelling the subglacial drainage system complicates the comparison of models. “*SHMIP The Subglacial Hydrology Model Intercomparison Project*” (Chapter 9) is the title of the publication that aims to compare different hydrology models. It does the comparison according to the effective pressure and the discharge, which excludes any balance flux approaches. For the CUAS model this is a great opportunity to assess its performance and see how its results compare to other models. In the context of this thesis, it provides an answer to the question of how well large scale models are able to represent the necessary features that are considered by more complex models and if they lead to comparable results. For the steady state experiments, CUAS matches the results of the reference model by Werder et al. (2013) extremely well, which is remarkable considering its way more simplistic approach. Its results for low water input compare more favorable to the reference than the second equivalent aquifer model (Fleurian et al., 2014), probably due to the incorporation of cavity opening in CUAS. The transient experiments show that CUAS produces similar pressure variations as the other models but a smaller variability in the diurnal case. This shows the importance of storage in the model, which has not been thoroughly studied in CUAS so far. Due to numerical problems with the boundary condition and time constraints, I was unable to complete the experiments E and F. The results give confidence that CUAS is well able to reproduce important features of the subglacial hydrology in steady state cases and for the seasonal evolution of the drainage system, while more work is necessary to study the short time response.

10.2 OUTLOOK AND FUTURE WORK

The two models that have been used in this thesis proved to be able to advance the understanding of subglacial hydrology and the interaction of basal water with ice flow. Now, that they are established and tested, they need to be extended and improved and then applied in future studies as many questions still remain.

While the balance flux method is already well established and used in a number of applications, there is still potential to improve it and its coupling to the ice dynamics. Different schemes on how to distribute the water between neighboring cells have been tested by Le Brocq et al. (2006), but so far the effect of these different schemes on the ice dynamics has not been studied. A major weak point of the method is, that it has no time dependency, all water transport is assumed as instant. Using the formulation in Section 3.2.1, the flux and water storage for each

time step can be computed as a series of efficient matrix multiplications. This could be developed into a flexible framework, allowing differences in flow velocities for individual cells, according to simple rules.

The CUAS model is currently applied to study drainage of supraglacial lakes at 79° North Glacier, where it is used to constrain the drainage paths and timing, revealing possible channel locations. Lake drainage volumes and estimates for the duration are available from digital elevation models. Radar data show subglacial and englacial features which can help to constrain the hydrology model. A manuscript is in preparation.

Currently, the water flux in CUAS is assumed to be laminar and is described via Darcy's law. While this leads to a very well known system of equations, it also precludes the convergence of channels, where larger channels draw away water from smaller channels, leading to an arborescent network. For this instability to appear, it is necessary to assume turbulent flow, which can be expressed by using an exponent $\alpha > 1$ in the flow law (Eq. 3.2)

$$\mathbf{q} = -Kh^\alpha \nabla \phi. \quad (10.1)$$

To avoid a runaway effect which occurs due to the instability (Hewitt, 2011; Walder, 1982), some artificial diffusion has to be added on the opening term. The result of a first test with $\alpha = 1.25$ is shown in Figure 10.1. This should be studied in detail and then implemented in CUAS.

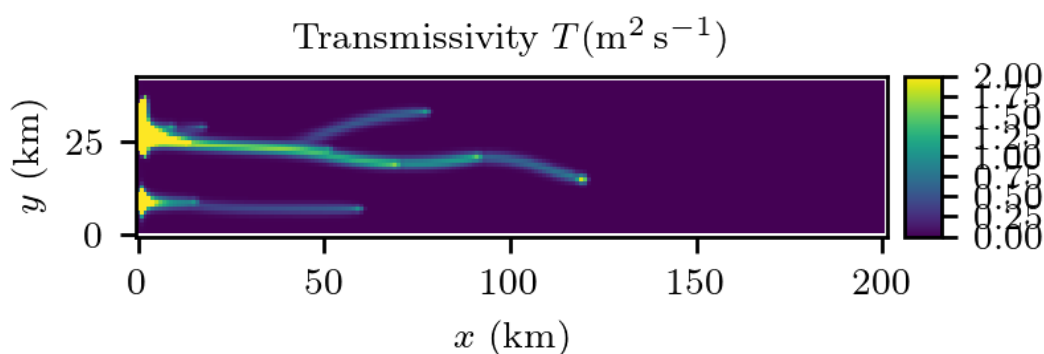


Figure 10.1: Transmissivity computed by CUAS with an adapted flow law. Channels merge together and form an arborescent network.

A number of aspects of CUAS can also be further improved upon; including accounting for anisotropy (flow through channels is anisotropic in the context of a continuum model), using a new parametrizations for the closure term that considers the viscoelastic nature of the overlaying ice and finally, transitioning to a new discretization that uses the finite element method on an unstructured mesh in order to improve resolution in the areas of interest. The next important point is to dynamically couple CUAS to an ice sheet model, possibly ISSM.

Both model approaches could also be adapted to be used for supraglacial hydrology.

For any kind of model it would be great to have more observations to better constrain and calibrate the system.

BIBLIOGRAPHY

- Abyzov, S. S., Mitskevich, I. N., Poglazova, M. N., Barkov, N. I., Lipenkov, V. Y., Bobin, N. E., Koudryashov, B. B., Pashkevich, V. M., and Ivanov, M. V. (2001). "Microflora in the Basal Strata at Antarctic Ice Core above the Vostok Lake". In: *Advances in Space Research* 28.4, pp. 701–706. ISSN: 0273-1177. DOI: 10.1016/S0273-1177(01)00318-0.
- Alley, R. B., Dupont, T. K., Parizek, B. R., and Anandkrishnan, S. (2005a). "Access of Surface Meltwater to Beds of Sub-freezing Glaciers: Preliminary Insights". In: *Annals of Glaciology* 40, pp. 8–14. DOI: 10.3189/172756405781813483.
- Alley, R. B., Clark, P. U., Huybrechts, P., and Joughin, I. (2005b). "Ice-sheet and Sea-level Changes". In: *Science* 310.5747, pp. 456–460. ISSN: 0036-8075. DOI: 10.1126/science.1114613.
- Amundson, J. M. and Carroll, D. (2018). "Effect of Topography on Subglacial Discharge and Submarine Melting during Tidewater Glacier Retreat". In: *Journal of Geophysical Research: Earth Surface* 123.1, pp. 66–79. ISSN: 2169-9003. DOI: 10.1002/2017JF004376.
- Andersen, K. K., Svensson, A., Johnsen, S. J., Rasmussen, S. O., Bigler, M., Röthlisberger, R., Ruth, U., Siggaard-Andersen, M.-L., Steffensen, J. P., and Dahl-Jensen, D. (2006). "The Greenland Ice Core Chronology 2005, 15–42ka. Part 1: Constructing the Time Scale". In: *Quaternary Science Reviews* 25.23-24, pp. 3246–3257. DOI: 10.1016/j.quascirev.2006.08.002.
- Anderson, J. B., Shipp, S. S., Lowe, A. L., Wellner, J. S., and Mosola, A. B. (2002). "The Antarctic Ice Sheet during the Last Glacial Maximum and Its Subsequent Retreat History: A Review". In: *Quaternary Science Reviews* 21.1-3, pp. 49–70. DOI: 10.1016/S0277-3791(01)00083-X.
- Andreassen, K. and Winsborrow, M. (2009). "Signature of Ice Streaming in Bjørnøyrenna, Polar North Atlantic, through the Pleistocene and Implications for Ice-stream Dynamics". In: *Annals of Glaciology* 50.52, pp. 17–26. DOI: 10.3189/172756409789624238.
- Andrews, L. C., Catania, G. A., Hoffman, M. J., Gulley, J. D., Luethi, M. P., Ryser, C., Hawley, R. L., and Neumann, T. A. (2014). "Direct Observations of Evolving Subglacial Drainage beneath the Greenland Ice Sheet". In: *Nature* 514.7520, pp. 80–83. DOI: 10.1038/nature13796.
- Angelen, J. H. van, Lenaerts, J. T. M., Lhermitte, S., Fettweis, X., Kuipers Munneke, P., Broeke, M. R. van den, and Meijgaard, E. van (2012). "Sensitivity of Greenland Ice Sheet Surface Mass Balance to Surface Albedo Parameterization: A Study with a Regional Climate Model". In: *The Cryosphere Discussions* 6.2, pp. 1531–1562. DOI: 10.5194/tcd-6-1531-2012.
- Arakawa, A. and Lamb, V. R. (1977). "Computational Design of the Basic Dynamical Processes of the UCLA General Circulation Model". In: *Methods in Computational Physics Vol. 17*. Ed. by J. Chang. New York, NY, USA: Academic Press, pp. 173–265.

Bibliography

- Arthern, R. J., Winebrenner, D. P., and Vaughan, D. G. (2006). “Antarctic Snow Accumulation Mapped Using Polarization of 4.3-cm Wavelength Microwave Emission”. In: *Journal of Geophysical Research* 111.D06107. DOI: 10.1029/2004JD005667.
- Aschwanden, A., Aðalgeirsdóttir, G., and Khroulev, C. (2013). “Hindcasting to Measure Ice Sheet Model Sensitivity to Initial States”. In: *The Cryosphere* 7.4, pp. 1083–1093. DOI: 10.5194/tc-7-1083-2013.
- Aschwanden, A., Bueller, E., Khroulev, C., and Blatter, H. (2012). “An Enthalpy Formulation for Glaciers and Ice Sheets”. In: *Journal of Glaciology* 58.209, pp. 441–457. DOI: 10.3189/2012JG11J088.
- Aschwanden, A., Fahnestock, M. A., and Truffer, M. (2016). “Complex Greenland Outlet Glacier Flow Captured”. In: *Nature Communications* 7.10524, p. 10524. DOI: 10.1038/ncomms10524.
- Ashmore, D. W., Bingham, R. G., Hindmarsh, R. C. A., Corr, H. F. J., and Joughin I, R. (2014). “The Relationship between Sticky Spots and Radar Reflectivity beneath an Active West Antarctic Ice Stream”. In: *Annals of Glaciology* 55.67, pp. 29–38. DOI: 10.3189/2014A0G67A052.
- Ashmore, D. W. and Bingham, R. G. (2014). “Antarctic Subglacial Hydrology: Current Knowledge and Future Challenges”. In: *Antarctic Science* 26.6, pp. 758–773. DOI: 10.1017/S0954102014000546.
- Bales, R. C., Guo, Q., Shen, D., McConnell, J. R., Du, G., Burkhart, J. F., Spikes, V. B., Hanna, E., and Cappelen, J. (2009). “Annual Accumulation for Greenland Updated Using Ice Core Data Developed during 2000-2006 and Analysis of Daily Coastal Meteorological Data”. In: *J. Geophys. Res.* 114, p. D06116. DOI: 10.1029/2008JD011208.
- Bamber, J. L. (2000). “Widespread Complex Flow in the Interior of the Antarctic Ice Sheet”. In: *Science* 287.5456, pp. 1248–1250. DOI: 10.1126/science.287.5456.1248.
- Bamber, J. L., Griggs, J. A., Hurkmans, R. T.W. L., Dowdeswell, J. A., Gogineni, S. P., Howat, I., Mouginot, J., Paden, J., Palmer, S., Rignot, E., and Steinhage, D. (2013). “A New Bed Elevation Dataset for Greenland”. In: *The Cryosphere* 7.2, pp. 499–510. ISSN: 1994-0416. DOI: 10.5194/tc-7-499-2013.
- Baral, D. R., Hutter, K., and Greve, R. (2001). “Asymptotic Theories of Large-scale Motion, Temperature, and Moisture Distribution in Land-based Polythermal Ice Sheets: A Critical Review and New Developments”. In: *Applied Mechanics Reviews* 54.3, p. 215. DOI: 10.1115/1.3097296.
- Barker, S., Knorr, G., Edwards, R. L., Parrenin, F., Putnam, A. E., Skinner, L. C., Wolff, E., and Ziegler, M. (2011). “800,000 Years of Abrupt Climate Variability”. In: *Science* 334.6054, pp. 347–351. DOI: 10.1126/science.1203580.
- Barnes, R., Lehman, C., and Mulla, D. (2014a). “An Efficient Assignment of Drainage Direction Over Flat Surfaces in Raster Digital Elevation Models”. In: *Computers & Geosciences* 62, pp. 128–135. ISSN: 0098-3004. DOI: 10.1016/j.cageo.2013.01.009.
- Barnes, R., Lehman, C., and Mulla, D. (2014b). “Priority-flood: An Optimal Depression-filling and Watershed-labeling Algorithm for Digital Elevation Models”. In: *Computers & Geosciences* 62.0, pp. 117–127. ISSN: 0098-3004. DOI: 10.1016/j.cageo.2013.04.024.

- Bartholomew, I., Nienow, P., Mair, D., Hubbard, A., King, M. A., and Sole, A. (2010). “Seasonal Evolution of Subglacial Drainage and Acceleration in a Greenland Outlet Glacier”. In: *Nature Geoscience* 3.6, pp. 408–411. DOI: 10.1038/NGE0863.
- Bartholomew, I., Nienow, P., Sole, A., Mair, D., Cowton, T., and King, M. A. (2012). “Short-term Variability in Greenland Ice Sheet Motion Forced by Time-varying Meltwater Drainage: Implications for the Relationship between Subglacial Drainage System Behavior and Ice Velocity”. In: *J. Geophys. Res.* 117.F3, F03002. DOI: 10.1029/2011JF002220.
- Beckmann, J., Perrette, M., and Ganopolski, A. (2018). “Simple Models for the Simulation of Submarine Melt for a Greenland Glacial System Model”. In: *The Cryosphere* 12.1, pp. 301–323. ISSN: 1994-0424. DOI: 10.5194/tc-12-301-2018.
- Bell, R. E., Studinger, M., Shuman, C. A., Fahnestock, M. A., and Joughin, I. (2007). “Large Subglacial Lakes in East Antarctica at the Onset of Fast-flowing Ice Streams”. In: *Nature* 445, pp. 904–907. DOI: 10.1038/nature05554.
- Benn, D. and Evans, D. J. A. (2014). *Glaciers and Glaciation*. Routledge.
- Benn, D. I., Aström, J., Zwinger, T., Todd, J., Nick, F. M., Cook, S., Hulton, N. R. J., and Luckman, A. (2017). “Melt-under-cutting and Buoyancy-driven Calving from Tidewater Glaciers: New Insights from Discrete Element and Continuum Model Simulations”. In: *Journal of Glaciology* 63.240, pp. 691–702. ISSN: 0022-1430. DOI: 10.1017/jog.2017.41.
- Berg, W. J. van de, Broeke, M. R. van den, Reijmer, C. H., and Meijgaard, E. van (2006). “Reassessment of the Antarctic Surface Mass Balance Using Calibrated Output of a Regional Atmospheric Climate Model”. In: *Journal of Geophysical Research* 111. DOI: 10.1029/2005JD006495.
- Bernales, J., Rogozhina, I., Greve, R., and Thomas, M. (2017). “Comparison of Hybrid Schemes for the Combination of Shallow Approximations in Numerical Simulations of the Antarctic Ice Sheet”. In: *The Cryosphere* 11.1, pp. 247–265. DOI: 10.5194/tc-11-247-2017.
- Beyer, S., Kleiner, T., Aizinger, V., Rückamp, M., and Humbert, A. (2017). “A Confined–unconfined Aquifer Model for Subglacial Hydrology and Its Application to the North East Greenland Ice Stream”. In: *The Cryosphere Discussions* 2017, pp. 1–24. DOI: 10.5194/tc-2017-221.
- Bindschadler, R. A., Nowicki, S., Abe-Ouchi, A., Aschwanden, A., Choi, H., Fastook, J., Granzow, G., Greve, R., Gutowski, G., Herzfeld, U. C., Jackson, C., Johnson, J., Khroulev, C., Levermann, A., Lipscomb, W. H., Martin, M. A., Morlighem, M., Parizek, B. R., Pollard, D., Price, S. F., Ren, D., Saito, F., Sato, T., Seddik, H., Seroussi, H., Takahashi, K., Walker, R., and Wang, W. L. (2013). “Ice-sheet Model Sensitivities to Environmental Forcing and Their Use in Projecting Future Sea Level (the SeaRISE Project)”. In: *Journal of Glaciology* 59.214, pp. 195–224. DOI: 10.3189/2013JOG12J125.
- Bjarnadóttir, L. R., Winsborrow, M. C. M., and Andreassen, K. (2014). “Deglaciation of the Central Barents Sea”. In: *Quaternary Science Reviews* 92, pp. 208–226. DOI: 10.1016/j.quascirev.2013.09.012.

- Blatter, H. (1995). "Velocity and Stress Fields in Grounded Glaciers: A Simple Algorithm for Including Deviatoric Stress Gradients". In: *Journal of Glaciology* 41.138, pp. 333–344. DOI: 10.3189/S002214300001621X.
- Bogorodsky, V. V., Bentley, C. R., and Gudmandsen, P. E. (1985). *Radioglaciology*. Iose, Bibliothek: D. Reidel Publishing Company, Dordrecht, Holland.
- Bondzio, J. H., Morlighem, M., Seroussi, H., Kleiner, T., Rückamp, M., Mouginot, J., Moon, T., Larour, E. Y., and Humbert, A. (2017). "The Mechanisms behind Jakobshavn Isbræ's Acceleration and Mass Loss: A 3-d Thermomechanical Model Study". In: *Geophysical Research Letters* 44.12. 2017GL073309, pp. 6252–6260. ISSN: 1944-8007. DOI: 10.1002/2017GL073309.
- Bougamont, M., Christoffersen, P., Hubbard, A. L., Fitzpatrick, A. A., Doyle, S. H., and Carter, S. P. (2014). "Sensitive Response of the Greenland Ice Sheet to Surface Melt Drainage Over a Soft Bed". In: *Nature Comms.* 5. DOI: 10.1038/ncomms6052.
- Box, J. E. and Colgan, W. (2013). "Greenland Ice Sheet Mass Balance Reconstruction. Part Iii: Marine Ice Loss and Total Mass Balance (1840-2010)". In: *J Climate*. DOI: 10.1175/JCLI-D-12-00546.1.
- Box, J. E., Yang, L., Bromwich, D. H., and Bai, L.-S. (2009). "Greenland Ice Sheet Surface Air Temperature Variability: 1840–2007". In: *Journal of Climate* 22.14, pp. 4029–4049. DOI: 10.1175/2009JCLI2816.1.
- Brinkerhoff, D. J., Meyer, C. R., Bueler, E., Truffer, M., and Bartholomäus, T. C. (2016). "Inversion of a Glacier Hydrology Model". In: *Annals of Glaciology* 57.72, pp. 84–95. DOI: 10.1017/aog.2016.3.
- Broeke, M. R. van den, Enderlin, E. M., Howat, I. M., Kuipers Munneke, P., Noël, B. P. Y., Berg, W. J. van de, Meijgaard, E. van, and Wouters, B. (2016). "On the Recent Contribution of the Greenland Ice Sheet to Sea Level Change". In: *The Cryosphere* 10.5, pp. 1933–1946. DOI: 10.5194/tc-10-1933-2016.
- Broeke, M. van den, Box, J., Fettweis, X., Hanna, E., Noël, B., Tedesco, M., As, D. van, Berg, W. J. van de, and Kampenhout, L. van (2017). "Greenland Ice Sheet Surface Mass Loss: Recent Developments in Observation and Modeling". In: *Current Climate Change Reports* 3.4, pp. 1–12. ISSN: 2198-6061. DOI: 10.1007/s40641-017-0084-8.
- Budd, W. F. and Warner, R. C. (1996). "A Computer Scheme for Rapid Calculations of Balance-flux Distributions". In: *Annals of Glaciology* 23, pp. 21–27. DOI: 10.3189/s0260305500013215.
- Bueler, E. and Brown, J. (2009). "Shallow Shelf Approximation As a "sliding Law" in a Thermomechanically Coupled Ice Sheet Model". In: *Journal of Geophysical Research* 114.F3, F03008. DOI: 10.1029/2008JF001179.
- Bueler, E. and Pelt, W. van (2015). "Mass-conserving Subglacial Hydrology in the Parallel Ice Sheet Model Version 0.6". In: *Geoscientific Model Development* 8.6, pp. 1613–1635. DOI: 10.5194/gmd-8-1613-2015.

- Calov, R., Robinson, A., Perrette, M., and Ganopolski, A. (2015). “Simulating the Greenland Ice Sheet under Present-day and Palaeo Constraints Including a New Discharge Parameterization”. In: *The Cryosphere* 9, pp. 179–196. DOI: 10.5194/tc-9-179-2015.
- Calov, R., Beyer, S., Greve, R., Beckmann, J., Willeit, M., Kleiner, T., Rückamp, M., Humbert, A., and Ganopolski, A. (2018). “Simulation of the Future Sea Level Contribution of Greenland with a New Glacial System Model”. In: *The Cryosphere Discussions* 2018, pp. 1–37. DOI: 10.5194/tc-2018-23.
- Calov, R. and Hutter, K. (1996). “The Thermomechanical Response of the Greenland Ice Sheet to Various Climate Scenarios”. In: *Climate Dynamics* 12.4, pp. 243–260. DOI: 10.1007/s003820050106.
- Carroll, D., Sutherland, D. A., Hudson, B., Moon, T., Catania, G. A., Shroyer, E. L., Nash, J. D., Bartholomew, T. C., Felikson, D., Stearns, L. A., Noël, B. P. Y., and Broeke, M. R. van den (2016). “The Impact of Glacier Geometry on Meltwater Plume Structure and Submarine Melt in Greenland Fjords”. In: *Geophysical Research Letters*, pp. 1–10. ISSN: 0094-8276. DOI: 10.1002/2016GL070170.
- Carroll, D., Sutherland, D. a., Shroyer, E. L., Nash, J. D., Catania, G. a., and Stearns, L. a. (2015). “Modeling Turbulent Subglacial Meltwater Plumes: Implications for Fjord-scale Buoyancy-driven Circulation”. In: *Journal of Physical Oceanography*, In press. ISSN: 0022-3670. DOI: 10.1175/JPO-D-15-0033.1.
- Carter, S. P., Blankenship, D. D., Peters, M. E., Young, D. A., Holt, J. W., and Morse, D. L. (2007). “Radar-based Subglacial Lake Classification in Antarctica”. In: *Geochemistry, Geophysics, Geosystems (G3)* 8.3, pp. 1–20. DOI: 10.1029/2006GC001408.
- Celia, M. A., Bouloutas, E. T., and Zarba, R. L. (1990). “A General Mass-conservative Numerical Solution for the Unsaturated Flow Equation”. In: *Water Resources Research* 26.7, pp. 1483–1496. ISSN: 1944-7973. DOI: 10.1029/WR026i007p01483.
- Chandler, D. M., Wadham, J. L., Lis, G. P., Cowton, T., Sole, A., Bartholomew, I., Telling, J., Nienow, P., Bagshaw, E. B., Mair, D., et al. (2013). “Evolution of the Subglacial Drainage System beneath the Greenland Ice Sheet Revealed by Tracers”. In: *Nat. Geosci.* 6.3, pp. 195–198.
- Chauché, N., Hubbard, A., Gascard, J. C., Box, J. E., Bates, R., Koppes, M., Sole, A., Christoffersen, P., and Patton, H. (2014). “Ice-ocean Interaction and Calving Front Morphology at Two West Greenland Tidewater Outlet Glaciers”. In: *Cryosphere* 8.4, pp. 1457–1468. ISSN: 1994-0424. DOI: 10.5194/tc-8-1457-2014.
- Chen, X., Zhang, X., Church, J. A., Watson, C. S., King, M. A., Monselesan, D., Legresy, B., and Harig, C. (2017). “The Increasing Rate of Global Mean Sea-level Rise during 1993-2014”. In: *Nature Climate Change* 7.7, pp. 492–495. ISSN: 1758-678X. DOI: 10.1038/nclimate3325.
- Christianson, K., Jacobel, R. W., Horgan, H. J., Anandakrishnan, S., and Alley, R. B. (2012). “Subglacial Lake Whillans — Ice-penetrating Radar and Gps Observations of a Shallow Active Reservoir beneath a West Antarctic Ice Stream”. In: *Earth and Planetary Science Letters* 331-332, pp. 237–245. ISSN: 0012-821X. DOI: 10.1016/j.epsl.2012.03.013.

Bibliography

- Church, J. A., Clark, P. U., Cazenave, A., Gregory, J. M., Jevrejeva, S., Levermann, A., Merrifield, M. A., Milne, G. A., Nerem, R. S., Nunn, P. D., Payne, A. J., Pfeffer, W. T., Stammer, D., and Unnikrishnan, A. S. (2013). "Sea Level Change". In: *Climate Change 2013: The Physical Science Basis. Contribution of Working Group I to the Fifth Assessment Report of the Intergovernmental Panel on Climate Change*. Ed. by T. F. Stocker, D. Qin, G.-K. Plattner, M. Tignor, S. K. Allen, J. Boschung, A. Nauels, Y. Xia, V. Bex, and P. M. Midgley. Cambridge, United Kingdom and New York, NY, USA: Cambridge University Press, pp. 1137–1216.
- Clarke, G. K. C. (2003). "Hydraulics of Subglacial Outburst Floods: New Insights from the Spring-Hutter Formulation". In: *J. Glaciol.* 49.165, pp. 299–313. DOI: 10.3189/172756503781830728.
- Clarke, G. K. C. (1987). "A Short History of Scientific Investigations on Glaciers". In: *Journal of Glaciology* 33.S1, pp. 4–24. DOI: 10.3189/S0022143000215785.
- Clason, C. C., Applegate, P. J., and Holmlund, P. (2014). "Modelling Late Weichselian Evolution of the Eurasian Ice Sheets Forced by Surface Meltwater-enhanced Basal Sliding". In: *Journal of Glaciology* 60.219, pp. 29–40. DOI: 10.3189/2014jog13j037.
- Claussen, M., Mysak, L. A., Weaver, A. J., Crucifix, M., Fichfet, T., Loutre, M.-F., Weber, S. L., Alcamo, J., Alexeev, V. A., Berger, A., Calov, R., Ganopolski, A., Goosse, H., Lohman, G., Lunkeit, F., Mokhov, I. I., Petoukhov, V., Stone, P., and Wang, Z. (2002). "Earth System Models of Intermediate Complexity: Closing the Gap in the Spectrum of Climate System Models". In: *Clim. Dyn.* 18.7, pp. 579–586. DOI: 10.1007/s00382-001-0200-1.
- Collins, M., Knutti, R., J. Arblaster, J., Dufresne, J.-L., Fichfet, T., Friedlingstein, P., Gao, X., Gutowski, W. J., Johns, T., Krinner, G., Shongwe, M., Tebaldi, C., Weaver, A. J., and Wehner, M. (2013). "Long-term Climate Change: Projections, Commitments and Irreversibility". In: *Climate Change 2013: The Physical Science Basis. Contribution of Working Group I to the Fifth Assessment Report of the Intergovernmental Panel on Climate Change*. Ed. by T. F. Stocker, D. Qin, G.-K. Plattner, M. Tignor, S. K. Allen, J. Boschung, A. Nauels, Y. Xia, V. Bex, and P. M. Midgley. Cambridge, United Kingdom and New York, NY, USA: Cambridge University Press, pp. 1029–1136.
- Comiso, J. C. (2000). "Variability and Trends in Antarctic Surface Temperatures from in Situ and Satellite Infrared Measurements". In: *Journal of Climate* 13.10, pp. 1674–1696. DOI: 10.1175/1520-0442(2000)013<1674:VATIAS>2.0.CO;2.
- Cowton, T., Slater, D., Sole, A., Goldberg, D., and Nienow, P. (2015). "Modeling the Impact of Glacial Runoff on Fjord Circulation and Submarine Melt Rate Using a New Subgrid-scale Parameterization for Glacial Plumes". In: *Journal of Geophysical Research: Oceans* 120.2, pp. 796–812. ISSN: 2169-9275. DOI: 10.1002/2014JC010324.
- Creyts, T. T. and Schoof, C. G. (2009). "Drainage through Subglacial Water Sheets". In: *J. Geophys. Res.* 114.F4, F04008. DOI: 10.1029/2008JF001215.
- Cuffey, K. M. and Paterson, W. S. B. (2010). *The Physics of Glaciers, 4th Edition*. 4th ed. Oxford: Elsevier, Oxford.

- Das, S. B., Joughin, I., Behn, M. D., Howat, I. M., King, M. A., Lizarralde, D., and Bhatia, M. P. (2008). “Fracture Propagation to the Base of the Greenland Ice Sheet during Supraglacial Lake Drainage”. In: *Science* 320.5877, pp. 778–781. ISSN: 0036-8075. DOI: 10.1126/science.1153360.
- Davis, J. L. and Annan, A. P. (1989). “Ground-penetrating Radar Fir High-frequency Mapping of Soil and Rock Stratigraphy”. In: *Geophysical Prospecting* 37, pp. 531–551.
- Dee, D. P., Uppala, S. M., Simmons, A. J., Berrisford, P., Poli, P., Kobayashi, S., Andrae, U., Balmaseda, M. A., Balsamo, G., Bauer, P., Bechtold, P., Beljaars, A. C. M., Berg, L. van de, Bidlot, J., Bormann, N., Delsol, C., Dragani, R., Fuentes, M., Geer, A. J., Haimberger, L., Healy, S. B., Hersbach, H., Hólm, E. V., Isaksen, L., Kållberg, P., Köhler, M., Matricardi, M., McNally, A. P., Monge-Sanz, B. M., Morcrette, J.-J., Park, B.-K., Peubey, C., Rosnay, P. de, Tavolato, C., Thépaut, J.-N., and Vitart, F. (2011). “The ERA-interim Reanalysis: Configuration and Performance of the Data Assimilation System”. In: *Quarterly Journal of the Royal Meteorological Society* 137.656, pp. 553–597. DOI: 10.1002/qj.828.
- Diez, A., Matsuoka, K., Ferraccioli, F., Jordan, T. A., Corr, H. F. J., Kohler, J., Olesen, A. V., and Forsberg, R. (2018). “Basal Settings Control Fast Ice Flow in the Recovery/slessor/bailey Region, East Antarctica”. In: *Geophysical Research Letters* 45.6, pp. 2706–2715. DOI: 10.1002/2017GL076601.
- Dow, C. F., Werder, M. A., Nowicki, S., and Walker, R. T. (2016). “Modeling Antarctic Subglacial Lake Filling and Drainage Cycles”. In: *The Cryosphere* 10.4, pp. 1381–1393. DOI: 10.5194/tc-10-1381-2016.
- Dow, C. F., Karlsson, N. B., and Werder, M. A. (2018). “Limited Impact of Subglacial Supercooling Freeze-on for Greenland Ice Sheet Stratigraphy”. In: *Geophys. Res. Lett.* pp. 1481–1489. DOI: 10.1002/2017GL076251.
- Dow, C. F., Kavanaugh, J. L., Sanders, J. W., Cuffey, K. M., and MacGregor, K. R. (2011). “Sub-surface Hydrology of an Overdeepened Cirque Glacier”. In: *J. Glaciol.* 57.206, pp. 1067–1078. DOI: 10.3189/002214311798843412.
- Dowdeswell, J. A., Evans, J., and Cofaigh, C. O. (2010). “Submarine Landforms and Shallow Acoustic Stratigraphy of a 400 Km-long Fjord-shelf-slope Transect, Kangerlussuaq Margin, East Greenland”. In: *Quaternary Science Reviews* 29.25-26, pp. 3359–3369. ISSN: 0277-3791. DOI: 10.1016/j.quascirev.2010.06.006.
- Downs, J., Johnson, J., Harper, J., Meierbachtol, T., and Werder, M. A. (2018). “Dynamic Hydraulic Conductivity Reconciles Mismatch between Modeled and Observed Winter Subglacial Water Pressure”. In: *J. Geophys. Res.* 123.4, pp. 818–836. DOI: 10.1002/2017JF004522.
- Doyle, S. H., Hubbard, A., Fitzpatrick, A. A. W., As, D. van, Mikkelsen, A. B., Pettersson, R., and Hubbard, B. (2014). “Persistent Flow Acceleration within the Interior of the Greenland Ice Sheet”. In: *Geophys. Res. Lett.* 41.3, pp. 899–905. DOI: 10.1002/2013GL058933.
- Duval (1977). “The Role of the Water Content on the Creep Rate of Polycrystalline Ice”. In: *IAHS Publ* 31.107, pp. 60–62.

Bibliography

- Duval, P. and Lliboutry, L. (1985). “Superplasticity Owing to Grain Growth in Polar Ices”. In: *Journal of Glaciology* 31.107, pp. 60–62. DOI: 10.3189/s002214300005001.
- Edwards, T. L., Fettweis, X., Gagliardini, O., Gillet-Chaulet, F., Goelzer, H., Gregory, J. M., Hoffman, M., Huybrechts, P., Payne, A. J., Perego, M., Price, S., Quiquet, A., and Ritz, C. (2014). “Effect of Uncertainty in Surface Mass Balance–elevation Feedback on Projections of the Future Sea Level Contribution of the Greenland Ice Sheet”. In: *The Cryosphere* 8, pp. 195–208. DOI: 10.5194/tc-8-195-2014.
- Ehlig, C. and Halepaska, J. C. (1976). “A Numerical Study of Confined-unconfined Aquifers Including Effects of Delayed Yield and Leakage”. In: *Water Resources Research* 12.6, pp. 1175–1183. ISSN: 1944-7973. DOI: 10.1029/WR012i006p01175.
- Enderlin, E. M., Howat, I. M., and Vieli, A. (2013). “High Sensitivity of Tidewater Outlet Glacier Dynamics to Shape”. In: *The Cryosphere* 7.3, pp. 1007–1015. ISSN: 1994-0424. DOI: 10.5194/tc-7-1007-2013.
- Enderlin, E. M. and Howat, I. M. (2013). “Submarine Melt Rate Estimates for Floating Termini of Greenland Outlet Glaciers (2000–2010)”. In: *Journal of Glaciology* 59.213, pp. 67–75. ISSN: 0022-1430. DOI: 10.3189/2013JG12J049.
- Enderlin, E. M., Howat, I. M., Jeong, S., Noh, M. J., Van Angelen, J. H., and Van Den Broeke, M. R. (2014). “An Improved Mass Budget for the Greenland Ice Sheet”. In: *Geophysical Research Letters* 41.3, pp. 866–872. ISSN: 1944-8007. DOI: 10.1002/2013GL059010.
- Engelhardt, H. and Kamb, B. (1998). “Basal Sliding of Ice Stream B, West Antarctica”. In: *J. Glaciol.* 44.147, pp. 223–230.
- Ettema, J., Broeke, M. R. van den, Meijgaard, E. van, Berg, W. J. van de, Bamber, J. L., Box, J. E., and Bales, R. C. (2009). “Higher Surface Mass Balance of the Greenland Ice Sheet Revealed by High-resolution Climate Modeling”. In: *Geophys. Res. Lett.* 36, p. L12501. DOI: 10.1029/2009GL038110.
- Evans, J., Dowdeswell, J. A., Cofaigh, C. O., Benham, T. J., and Anderson, J. B. (2006). “Extent and Dynamics of the West Antarctic Ice Sheet on the Outer Continental Shelf of Pine Island Bay during the Last Glaciation”. In: *Marine Geology* 230.1-2, pp. 53–72. DOI: 10.1016/j.margeo.2006.04.001.
- Fahnestock, M., Abdalati, W., Joughin, I., Brozena, J., and Gogineni, P. (2001). “High Geothermal Heat Flow, Basal Melt, and the Origin of Rapid Ice Flow in Central Greenland”. In: *Science* 294.5550, pp. 2338–2342. DOI: 10.1126/science.1065370.
- Farinotti, D., Brinkerhoff, D. J., Clarke, G. K. C., Fürst, J. J., Frey, H., Gantayat, P., Gillet-Chaulet, F., Girard, C., Huss, M., Leclercq, P. W., Linsbauer, A., Machguth, H., Martin, C., Maussion, F., Morlighem, M., Mosbeux, C., Pandit, A., Portmann, A., Rabatel, A., Ramsankaran, R., Reerink, T. J., Sanchez, O., Stentoft, P. A., Singh Kumari, S., Pelt, W. J. J. van, Anderson, B., Benham, T., Binder, D., Dowdeswell, J. A., Fischer, A., Helfricht, K., Kutuzov, S., Lavrentiev, I., McNabb, R., Gudmundsson, G. H., Li, H., and Andreassen, L. M. (2017). “How Accurate Are Estimates of Glacier Ice Thickness Results from ITMIX, the Ice Thickness Models Inter-

- comparison eXperiment”. In: *The Cryosphere* 11.2, pp. 949–970. DOI: 10.5194/tc-11-949-2017.
- Feldmann, J., Albrecht, T., Khroulev, C., Pattyn, F., and Levermann, A. (2014). “Resolution-dependent Performance of Grounding Line Motion in a Shallow Model Compared to a Full-Stokes Model According to the MISIP3d Intercomparison”. In: *Journal of Glaciology* 60.220, pp. 353–360. DOI: 10.3189/2014JOG13J093.
- Ferziger, J. H. and Perić, M. (2002). *Computational Methods for Fluid Dynamics*. 3rd ed. Springer. ISBN: 3-540-42074-6.
- Fettweis, X., Franco, B., Tedesco, M., Van Angelen, J. H., Lenaerts, J. T. M., Van Den Broeke, M. R., and Gallée, H. (2013). “Estimating the Greenland Ice Sheet Surface Mass Balance Contribution to Future Sea Level Rise Using the Regional Atmospheric Climate Model MAR”. In: *The Cryosphere* 7.2, pp. 469–489. ISSN: 1994-0424. DOI: 10.5194/tc-7-469-2013.
- Fleurian, B. de, Gagliardini, O., Zwinger, T., Durand, G., Le Meur, E., Mair, D., and Raback, P. (2014). “A Double Continuum Hydrological Model for Glacier Applications”. In: *The Cryosphere* 8.1, pp. 137–153. DOI: 10.5194/tc-8-137-2014.
- Fleurian, B. de, Morlighem, M., Seroussi, H., Rignot, E., Broeke, M. R. van den, Kuipers Munneke, P., Mouginot, J., Smeets, P. C.J. P., and Tedstone, A. J. (2016). “A Modeling Study of the Effect of Runoff Variability on the Effective Pressure beneath Russell Glacier, West Greenland”. In: *Journal of Geophysical Research: Earth Surface* 121.10, pp. 1834–1848. ISSN: 2169-9011. DOI: 10.1002/2016JF003842.
- Fleurian, B. de, Werder, M. A., Beyer, S., Brinkerhoff, D. J., Delaney, I., Dow, C. F., Downs, J., Gagliardini, O., Hoffman, M. J., Hooke, R. L., Seguinot, J., and Sommers, A. N. (2018a). *Results from the SHMIP Exercise*. ETH Zurich.
- Fleurian, B. de, Werder, M. A., Beyer, S., Brinkerhoff, D. J., Delaney, I., Dow, C. F., Downs, J., Gagliardini, O., Hoffman, M. J., Hooke, R. L., Seguinot, J., and Sommers, A. (2018b). “Shmip the Subglacial Hydrology Model Intercomparison Project”. In: *Journal of Glaciology*. submitted.
- Floricioiu, D., Abdel Jaber, W., and Jezek, K. (2014). “Terrasar-x and Tandem-x Observations of the Recovery Glacier System, Antarctica.” In: *IEEE Xplore. IGARSS 2014, 13-18 July 2014, Quebec, City, QC, Canada*, pp. 4852–4855. DOI: 10.1109/IGARSS.2014.6947581.
- Flowers, G. E., Bjornsson, H., Palsson, F., and Clarke, G. K. C. (2004). “A Coupled Sheet-conduit Mechanism for Jökulhlaup Propagation”. In: *Geophysical Research Letters* 31.5, pp. 1–4. DOI: 10.1029/2003GL019088.
- Flowers, G. E. (2015). “Modelling Water Flow under Glaciers and Ice Sheets”. In: *Proceedings of the Royal Society of London A: Mathematical, Physical and Engineering Sciences* 471.2176, pp. 1–41. ISSN: 1364-5021. DOI: 10.1098/rspa.2014.0907.

Bibliography

- Flowers, G. E. and Clarke, G. K. C. (2002). "A Multicomponent Coupled Model of Glacier Hydrology - 1. Theory and Synthetic Examples". In: *Journal of Geophysical Research: Solid Earth* 107.B11, p. 2287. DOI: 10.1029/2001jb001122.
- Forsberg, R., Sørensen, L., and Simonsen, S. (2017). "Greenland and Antarctica Ice Sheet Mass Changes and Effects on Global Sea Level". In: *Surveys in Geophysics* 38.1, pp. 89–104. ISSN: 1573-0956. DOI: 10.1007/s10712-016-9398-7.
- Forsberg, R., Olesen, A. V., Ferraccioli, F., Jordan, T. A., Matsuoka, K., Zakrajsek, A., Ghidella, M., and Greenbaum, J. S. (2018). "Exploring the Recovery Lakes Region and Interior Dronning Maud Land, East Antarctica, with Airborne Gravity, Magnetic and Radar Measurements". In: *Geological Society, London, Special Publications* 461.1, pp. 23–34. DOI: 10.1144/SP461.17.
- Forsström, P.-L. and Greve, R. (2004). "Simulation of the Eurasian Ice Sheet Dynamics during the Last Glaciation". In: *Global and Planetary Change* 42.1-4, pp. 59–81. DOI: 10.1016/j.gloplacha.2003.11.003.
- Fortuin, J. P. F. and Oerlemans, J. (1990). "The Parameterization of the Annual Surface Temperature and Mass Balance of Antarctica". In: *Annals of Glaciology* 14, pp. 78–84.
- Fountain, A. G. and Walder, J. S. (1998). "Water Flow through Temperate Glaciers". In: *Reviews of Geophysics* 36.3, pp. 299–328.
- Fowler, A. C. (1981). "A Theoretical Treatment of the Sliding of Glaciers in the Absence of Cavitation". In: *Philosophical Transactions of the Royal Society of London. Series A, Mathematical and Physical Sciences* 298.1445, pp. 637–681. ISSN: 0080-4614.
- Fowler, A. C. (1986). "A Sliding Law for Glaciers of Constant Viscosity in the Presence of Subglacial Cavitation". In: *Proceedings of the Royal Society of London. Series A, Mathematical and Physical Sciences* 407.1832, pp. 147–170. ISSN: 0080-4630.
- Fowler, A. C. (1987). "Sliding with Cavity Formation". In: *Journal of Glaciology* 33.115, pp. 255–267. DOI: 10.3189/S0022143000008820.
- Fowler, A. C. (2010). "Weertman, Lliboutry and the Development of Sliding Theory". In: *Journal of Glaciology* 56.200, pp. 965–972. DOI: 10.3189/002214311796406112.
- Fox Maule, C., Purucker, M. E., Olsen, N., and Mosegaard, K. (2005). "Heat Flux Anomalies in Antarctica Revealed by Satellite Magnetic Data". In: *Science* 309.5733, pp. 464–467. DOI: 10.1126/science.1106888.
- Fretwell, P. et al. (2013). "Bedmap2: Improved Ice Bed, Surface and Thickness Datasets for Antarctica". In: *The Cryosphere* 7.1, pp. 375–393. DOI: 10.5194/tc-7-375-2013.
- Fricker, H. A., Scambos, T., Bindschadler, R., and Padman, L. (2007). "An Active Subglacial Water System in West Antarctica Mapped from Space". In: *Science* 315.5818, pp. 1544–1548. DOI: 10.1126/science.1136897.

- Fricker, H. A., Carter, S. P., Bell, R. E., and Scambos, T. (2014). “Active Lakes of Recovery Ice Stream, East Antarctica: A Bedrock-controlled Subglacial Hydrological System”. In: *Journal of Glaciology* 60.223, pp. 1015–1030. ISSN: 1727-5652. DOI: 10.3189/2014jog14j063.
- Fudge, T. J., Harper, J. T., Humphrey, N. F., and Pfeffer, W. T. (2005). “Diurnal Water-pressure Fluctuations: Timing and Pattern of Termination below Bench Glacier, Alaska, USA”. In: *Ann. Glaciol.* 40.1, pp. 102–106.
- Fudge, T. J., Humphrey, N. F., Harper, J. T., and Pfeffer, W. T. (2008). “Diurnal Fluctuations in Borehole Water Levels: Configuration of the Drainage System beneath Bench Glacier, Alaska, USA”. In: *J. Glaciol.* 54.185, pp. 297–306. DOI: 10.3189/002214308784886072.
- Fürst, J. J., Goelzer, H., and Huybrechts, P. (2013). “Effect of Higher-order Stress Gradients on the Centennial Mass Evolution of the Greenland Ice Sheet”. In: *The Cryosphere* 7, pp. 183–199. DOI: 10.5194/tc-7-183-2013.
- Fürst, J. J., Goelzer, H., and Huybrechts, P. (2015). “Ice-dynamic Projections of the Greenland Ice Sheet in Response to Atmospheric and Oceanic Warming”. In: *The Cryosphere* 9.3, pp. 1039–1062. ISSN: 1994-0440. DOI: 10.5194/tc-9-1039-2015.
- Gades, A. M., Raymond, C. F., Conway, H., and Jacobel, R. W. (2000). “Bed Properties of Siple Dome and Adjacent Ice Streams, West Antarctica, Inferred from Radio-echo Sounding Measurements”. In: *Journal of Glaciology* 46.152, pp. 88–94.
- Gagliardini, O. and Werder, M. A. (2018). “Influence of an Increasing Surface Melt Over Decadal Timescales on Land Terminating Outlet Glaciers”. In: *J. Glaciol.* accepted.
- Gagliardini, O., Cohen, D., Råback, P., and Zwinger, T. (2007a). “Correction to “finite-element Modeling of Subglacial Cavities and Related Friction Law””. In: *Journal of Geophysical Research: Earth Surface* 112.F4. DOI: 10.1029/2007JF000911.
- Gagliardini, O., Cohen, D., Råback, P., and Zwinger, T. (2007b). “Finite-element Modeling of Subglacial Cavities and Related Friction Law”. In: *Journal of Geophysical Research: Earth Surface* 112.F2. DOI: 10.1029/2006JF000576.
- Ganopolski, A. and Calov, R. (2011). “The Role of Orbital Forcing, Carbon Dioxide and Regolith in 100 Kyr Glacial Cycles”. In: *Clim. Past* 7, pp. 1415–1425. DOI: 10.5194/cp-7-1415-2011.
- Ghasemizadeh, R., Yu, X., Butscher, C., Hellweger, F., Padilla, I., and Alshawabkeh, A. (2015). “Equivalent Porous Media (epm) Simulation of Groundwater Hydraulics and Contaminant Transport in Karst Aquifers”. In: *PLoS ONE* 10.9, e0138954. ISSN: 1932-6203.
- Gillet-Chaulet, F., Gagliardini, O., Seddik, H., Nodet, M., Durand, G., Ritz, C., Zwinger, T., Greve, R., and Vaughan, D. G. (2012). “Greenland Ice Sheet Contribution to Sea-level Rise from a New-generation Ice-sheet Model”. In: *The Cryosphere* 6.6, pp. 1561–1576. DOI: 10.5194/tc-6-1561-2012.
- Gimbert, F., Tsai, V. C., Amundson, J. M., Bartholomaus, T. C., and Walter, J. I. (2016). “Subseasonal Changes Observed in Subglacial Channel Pressure, Size, and Sediment Transport”. In: *Geophysical Research Letters* 43.8, pp. 3786–3794.

- Glen, J. W. (1955). "The Creep of Polycrystalline Ice". In: *Proceedings of the Royal Society A: Mathematical, Physical and Engineering Sciences* 228.1175, pp. 519–538. DOI: 10.1098/rspa.1955.0066.
- Goelzer, H., Huybrechts, P., Fürst, J. J., Nick, F. M., Andersen, M. L., Edwards, T. L., Fettweis, X., Payne, a.J., and Shannon, S. (2013). "Sensitivity of Greenland Ice Sheet Projections to Model Formulations". In: *Journal of Glaciology* 59.216, pp. 733–749. ISSN: 0022-1430. DOI: 10.3189/2013JOG12J182.
- Goelzer, H., Nowicki, S., Edwards, T., Beckley, M., Abe-Ouchi, A., Aschwanden, A., Calov, R., Gagliardini, O., Gillet-Chaulet, F., Gollledge, N. R., Gregory, J., Greve, R., Humbert, A., Huybrechts, P., Kennedy, J. H., Larour, E., Lipscomb, W. H., Le clec'h, S., Lee, V., Morlighem, M., Pattyn, F., Payne, A. J., Rodehacke, C., Rückamp, M., Saito, F., Schlegel, N., Seroussi, H., Shepherd, A., Sun, S., Wal, R. van de, and Ziemann, F. A. (2017). "Design and Results of the Ice Sheet Model Initialisation Experiments Inimip-greenland: An Ismip6 Intercomparison". In: *The Cryosphere Discussions* 2017, pp. 1–42. DOI: 10.5194/tc-2017-129.
- Gollledge, N. R., Levy, R. H., McKay, R. M., and Naish, T. R. (2017). "East Antarctic Ice Sheet Most Vulnerable to Weddell Sea Warming". In: *Geophysical Research Letters* 44.5. 2016GL072422, pp. 2343–2351. ISSN: 1944-8007. DOI: 10.1002/2016GL072422.
- Gordon, S., Sharp, M., Hubbard, B., Smart, C., Ketterling, B., and Willis, I. (1998). "Seasonal Reorganization of Subglacial Drainage Inferred from Measurements in Boreholes". In: *Hydrol. Process.* 12.1, pp. 105–133. DOI: 10.1002/(SICI)1099-1085(199801)12:1<105::AID-HYP566>3.3.CO;2-R.
- Gorman, M. R. and Siegert, M. J. (1999). "Penetration of Antarctic subglacial lakes by VHF electromagnetic pulses: Information on the depth and Electrical Conductivity of Basal Water Bodies". In: *Journal of Geophysical Research: Solid Earth* 104.B12, pp. 29311–29320. DOI: 10.1029/1999JB900271.
- Gray, L. (2005). "Evidence for Subglacial Water Transport in the West Antarctic Ice Sheet through Three-dimensional Satellite Radar Interferometry". In: *Geophysical Research Letters* 32.3. DOI: 10.1029/2004gl021387.
- Gregory, J. and Huybrechts, P. (2006). "Ice-sheet Contributions to Future Sea-level Change". In: *Philos. Trans. R. Soc. Lond. A* 364, pp. 1709–1731. DOI: 10.1098/rsta.2006.1796.
- Greve, R. (1995). "Thermomechanisches Verhalten Polythermer Eisschilde – Theorie, Analytik, Numerik". Berichte aus der Geowissenschaft, Shaker Verlag, Aachen, Germany. Doctoral thesis. Darmstadt University of Technology, Germany: Department of Mechanics. ISBN: 3-8265-0999-4.
- Greve, R. (2000). "On the Response of the Greenland Ice Sheet to Greenhouse Climate Change". In: *Climatic Change* 46.3, pp. 289–303.
- Greve, R. and Blatter, H. (2016). "Comparison of Thermodynamics Solvers in the Polythermal Ice Sheet Model SICOPOLIS". In: *Polar Science* 10.1, pp. 11–23. DOI: 10.1016/j.polar.2015.12.004.

- Greve, R., Calov, R., and Herzfeld, U. C. (2017). "Projecting the Response of the Greenland Ice Sheet to Future Climate Change with the Ice Sheet Model SICOPOLIS". In: *Low Temperature Science* 75, pp. 117–129. DOI: 10.14943/lowtemsci.75.117.
- Greve, R. (1997). "Application of a Polythermal Three-dimensional Ice Sheet Model to the Greenland Ice Sheet: Response to Steady-state and Transient Climate Scenarios". In: *Journal of Climate* 10.5, pp. 901–918. DOI: 10.1175/1520-0442(1997)010<0901:aoaptd>2.0.co;2.
- Greve, R. and Blatter, H. (2009). *Dynamics of Ice Sheets and Glaciers*. Springer Berlin Heidelberg. ISBN: 978-3-642-03414-5. DOI: 10.1007/978-3-642-03415-2.
- Gudlaugsson, E., Humbert, A., Andreassen, K., Clason, C. C., Kleiner, T., and Beyer, S. (2017). "Eurasian Ice-sheet Dynamics and Sensitivity to Subglacial Hydrology". In: *Journal of Glaciology* 63.239, pp. 556–564. DOI: 10.1017/jog.2017.21.
- Gudlaugsson, E., Humbert, A., Kleiner, T., Kohler, J., and Andreassen, K. (2016). "The Influence of a Model Subglacial Lake on Ice Dynamics and Internal Layering". In: *The Cryosphere* 10.2, pp. 751–760. DOI: 10.5194/tc-10-751-2016.
- Gudmundsson, G. H. (1997a). "Basal-flow Characteristics of a Linear Medium Sliding Frictionless Over Small Bedrock Undulations". In: *Journal of Glaciology* 43.143, pp. 71–79. DOI: 10.3189/S0022143000002823.
- Gudmundsson, G. H. (1997b). "Basal-flow Characteristics of a Non-linear Flow Sliding Frictionless Over Strongly Undulating Bedrock". In: *Journal of Glaciology* 43.143, pp. 80–89. DOI: 10.3189/S0022143000002835.
- Gudmundsson, G. H. (2003). "Transmission of Basal Variability to a Glacier Surface". In: *Journal of Geophysical Research: Solid Earth* 108.B5. DOI: 10.1029/2002jb002107.
- Gulley, J. D., Grabiec, M., Martin, J. B., Jania, J., Catania, G., and Glowacki, P. (2012). "The Effect of Discrete Recharge by Moulins and Heterogeneity in Flow-path Efficiency at Glacier Beds on Subglacial Hydrology". In: *J. Glaciol.* 58.211, pp. 926–940. DOI: 10.3189/2012J0G11J189.
- Hanna, E., Navarro, F. J., Pattyn, F., Domingues, C. M., Fettweis, X., Ivins, E. R., Nicholls, R. J., Ritz, C., Smith, B., Tulaczyk, S., Whitehouse, P. L., and Zwally, H. J. (2013). "Ice-sheet Mass Balance and Climate Change". In: *Nature* 498.7452, pp. 51–59. DOI: 10.1038/nature12238.
- Helm, V., Humbert, A., and Miller, H. (2014). "Elevation and Elevation Change of Greenland and Antarctica Derived from CryoSat-2". In: *The Cryosphere* 8.4, pp. 1539–1559. DOI: 10.5194/tc-8-1539-2014.
- Helsen, M. M., Wal, R. S. W. van de, Broeke, M. R. van den, Berg, W. J. van de, and Oerlemans, J. (2012). "Coupling of Climate Models and Ice Sheet Models by Surface Mass Balance Gradients: Application to the Greenland Ice Sheet". In: *The Cryosphere* 6, pp. 255–272. DOI: 10.5194/tc-6-255-2012, 2012.
- Herron, M. M. and Langway Jr., C. C. (1980). "Firn Densification: An Empirical Model". In: *Journal of Glaciology* 25.93, pp. 373–385.

Bibliography

- Hewitt, I. J. (2011). "Modelling Distributed and Channelized Subglacial Drainage: The Spacing of Channels". In: *J. Glaciol.* 57.202, pp. 302–314.
- Hewitt, I. J. (2013). "Seasonal Changes in Ice Sheet Motion Due to Melt Water Lubrication". In: *Earth and Planetary Science Letters* 371, pp. 16–25. DOI: 10.1016/j.epsl.2013.04.022.
- Hewitt, I. J., Schoof, C., and Werder, M. A. (2012). "Flotation and Free Surface Flow in a Model for Subglacial Drainage. Part 2. Channel Flow". In: *Journal of Fluid Mechanics* 702, pp. 157–187. DOI: 10.1017/jfm.2012.166.
- Hill, E. A., Carr, J. R., and Stokes, C. R. (2017). "A Review of Recent Changes in Major Marine-terminating Outlet Glaciers in Northern Greenland". In: *Frontiers in Earth Science* 4, p. 111. ISSN: 2296-6463. DOI: 10.3389/feart.2016.00111.
- Hindmarsh, R. C. A. (2004). "A Numerical Comparison of Approximations to the Stokes Equations Used in Ice Sheet and Glacier Modeling". In: *Journal of Geophysical Research: Earth Surface* 109.F1. F01012. ISSN: 2156–2202. DOI: 10.1029/2003JF000065.
- Hindmarsh, R. C. A. and Le Meur, E. (2001). "Dynamical Processes Involved in the Retreat of Marine Ice Sheets". In: *J. Glaciol.* 47.157, pp. 271–282.
- Hoffman, M. J., Catania, G. A., Neumann, T. A., Andrews, L. C., and Rumrill, J. A. (2011). "Links between Acceleration, Melting, and Supraglacial Lake Drainage of the Western Greenland Ice Sheet". In: *J. Geophys. Res.* 116, F04035, pp. 1–16. DOI: 10.1029/2010JF001934.
- Hoffman, M. J., Andrews, L. C., Price, S. F., Catania, G. A., Neumann, T. A., Lüthi, M. P., Gulley, J., Ryser, C., Hawley, R. L., and Morriss, B. (2016). "Greenland Subglacial Drainage Evolution Regulated by Weakly Connected Regions of the Bed". In: *Nature Comms.* 7. DOI: 10.1038/ncomms13903.
- Hoffman, M. J., Perego, M., Price, S. F., Lipscomb, W. H., Jacobsen, D., Tezaur, I., Salinger, A. G., Tuminaro, R., and Zhang, T. (2018a). "MPAS-Albany Land Ice (MALI): a Variable Resolution Ice Sheet Model for Earth System Modeling Using Voronoi Grids". In: *Geoscientific Model Development Discussions*, pp. 1–47. DOI: 10.5194/gmd-2018-78.
- Hoffman, M. J., Perego, M., Andrews, L. C., Price, S. F., Neumann, T. A., Johnson, J. V., Catania, G., and Lüthi, M. P. (2018b). "Widespread Moulin Formation during Supraglacial Lake Drainages in Greenland". In: *Geophys. Res. Lett.* 45.2, pp. 778–788. DOI: 10.1002/2017GL075659.
- Hoffman, M. and Price, S. (2014). "Feedbacks between Coupled Subglacial Hydrology and Glacier Dynamics". In: *Journal of Geophysical Research-earth Surface* 119.3, pp. 414–436. DOI: 10.1002/2013JF002943.
- Hooke, R. L., Laumann, T., and Kennett, M. I. (1989). "Austdalsbreen, Norway: Expected Reaction to a 40 M Increase in Water Level in the Lake into Which the Glacier Calves". In: *Cold Regions Science and Technology* 17.2, pp. 113–126. DOI: 10.1016/S0165-232X(89)80002-3.
- Hooke, R. L., Laumann, T., and Kohler, J. (1990). "Subglacial Water Pressure and the Shape of Subglacial Water Conduits". In: *J. Glaciol.* 36.122, pp. 67–71.

- Howat, I. M., Negrete, A., and Smith, B. E. (2014). “The Greenland Ice Mapping Project (gimp) Land Classification and Surface Elevation Data Sets”. In: *The Cryosphere* 8.4, pp. 1509–1518. DOI: 10.5194/tc-8-1509-2014.
- Hubbard, A., Bradwell, T., Golledge, N., Hall, A., Patton, H., Sugden, D., Cooper, R., and Stoker, M. (2009). “Dynamic Cycles, Ice Streams and Their Impact on the Extent, Chronology and Deglaciation of the British-Irish Ice Sheet”. In: *Quaternary Science Reviews* 28.7, pp. 758–776. DOI: 10.1016/j.quascirev.2008.12.026.
- Hubbard, B. P., Sharp, M. J., Willis, I. C., NIELSEN, M. K. t, and Smart, C. C. (1995). “Borehole Water-level Variations and the Structure of the Subglacial Hydrological System of Haut Glacier D’arolla, Valais, Switzerland”. In: *Journal of Glaciology* 41.139, pp. 572–583.
- Huss, M., Bauder, A., Werder, M., Funk, M., and Hock, R. (2007). “Glacier-dammed Lake Outburst Events of Gornersee, Switzerland”. In: *J. Glaciol.* 53.181, pp. 189–200.
- Hutter, K. (1983). *Theoretical Glaciology; Material Science of Ice and the Mechanics of Glaciers and Ice Sheets*. Dordrecht, The Netherlands: D. Reidel Publishing Company.
- Huybrechts, P. and Wolde, J. de (1999). “The Dynamic Response of the Antarctic and Greenland Ice Sheets to Multiple-century Climatic Warming”. In: *J. Climate* 12.8, pp. 2169–2188. DOI: 10.1175/1520-0442(1999)012<2169:TDR0TG>2.0.CO;2.
- Huybrechts, P. (1990). “A 3-d Model for the Antarctic Ice Sheet: A Sensitivity Study on the Glacial-interglacial Contrast”. In: *Climate Dynamics* 5.2, pp. 79–92. DOI: 10.1007/BF00207423.
- Iken, A. and Bindschadler, R. A. (1986). “Combined Measurements of Subglacial Water Pressure and Surface Velocity of Findelengletscher, Switzerland: Conclusions about Drainage System and Sliding Mechanism”. In: *J. Glaciol.* 32.110.
- Iken, A. and Truffer, M. (1997). “The Relationship between Subglacial Water Pressure and Velocity of Findelengletscher, Switzerland, during Its Advance and Retreat”. In: *J. Glaciol.* 43.144, pp. 328–338.
- Iken, A., Echelmeyer, K., Harrison, W., and Funk, M. (1993). “Mechanisms of Fast Flow in Jakobshavn-Isbræ, West Greenland. 1. Measurements of Temperature and Water-level in Deep Boreholes”. In: *J. Glaciol.* 39.131, pp. 15–25.
- Iken, A. (1981). “The Effect of the Subglacial Water Pressure on the Sliding Velocity of a Glacier in an Idealized Numerical Model”. In: *Journal of Glaciology* 27.97, pp. 407–421. DOI: 10.3189/S0022143000011448.
- Inall, M. E., Murray, T., Cottier, F. R., Scharrer, K., and Boyd, T. J. (2014). “Oceanic Heat Delivery Via Kangerdlugssuaq Fjord to the South-east Greenland Ice Sheet”. In: *Journal of Geophysical Research : Oceans*, pp. 631–645. DOI: 10.1002/2013JC009295. Received.
- IPCC (2013). *Climate Change 2013: The Physical Science Basis. Contribution of Working Group I to the Fifth Assessment Report of the Intergovernmental Panel on Climate Change*. Cambridge, United Kingdom and New York, NY, USA: Cambridge University Press, p. 1535. ISBN: ISBN 978-1-107-66182-0. DOI: 10.1017/CB09781107415324.

Bibliography

- Jackson, R. H., Shroyer, E. L., Nash, J. D., Sutherland, D. A., Carroll, D., Fried, M. J., Catania, G. A., Bartholomaus, T. C., and Stearns, L. A. (2017). "Near-glacier Surveying of a Subglacial Discharge Plume: Implications for Plume Parameterizations". In: *Geophysical Research Letters*. ISSN: 0094-8276. DOI: 10.1002/2017GL073602.
- Jackson, R. H., Straneo, F., and Sutherland, D. A. (2014). "Externally Forced Fluctuations in Ocean Temperature at Greenland Glaciers in Non-summer Months". In: *Nature Geoscience* 7.7, pp. 503–508. ISSN: 1752–0894. DOI: 10.1038/ngeo2186.
- Jacobel, R. W., Lapo, K. E., Stamp, J. R., Youngblood, B. W., Welch, B. C., and Bamber, J. L. (2010). "A Comparison of Basal Reflectivity and Ice Velocity in East Antarctica". In: *The Cryosphere* 4.4, pp. 447–452. DOI: 10.5194/tc-4-447-2010.
- Jenkins, A. (2011). "Convection-driven Melting near the Grounding Lines of Ice Shelves and Tide-water Glaciers". In: *Journal of Physical Oceanography* 41.12, pp. 2279–2294. ISSN: 0022-3670. DOI: 10.1175/JPO-D-11-03.1.
- Jezek, K. C. (1999). "Glaciological Properties of the Antarctic Ice Sheet from Radarsat-1 Synthetic Aperture Radar Imagery". In: *Annals of Glaciology* 29, pp. 286–290. DOI: 10.3189/172756499781820969.
- Johnson, J. and Fastook, J. L. (2002). "Northern Hemisphere Glaciation and Its Sensitivity to Basal Melt Water". In: *Quaternary International* 95-96, pp. 65–74. DOI: 10.1016/S1040-6182(02)00028-9.
- Joughin, I., Fahnestock, M., MacAyeal, D., Bamber, J. L., and Gogineni, P. (2001). "Observation and Analysis of Ice Flow in the Largest Greenland Ice Stream". In: *Journal of Geophysical Research: Atmospheres* 106.D24, pp. 34021–34034.
- Joughin, I., Smith, B. E., Howat, I. M., Scambos, T., and Moon, T. (2010). "Greenland Flow Variability from Ice-sheet-wide Velocity Mapping". In: *Journal of Glaciology* 56.197, pp. 415–430.
- Kageyama, M., Braconnot, P., Bopp, L., Caubel, A., Foujols, M.-A., Guilyardi, E., Khodri, M., Lloyd, J., Lombard, F., Mariotti, V., Marti, O., Roy, T., and Woillez, M.-N. (2013). "Mid-holocene and Last Glacial Maximum Climate Simulations with the IPSL Model—part I: Comparing IPSL_CM5a to IPSL_CM4". In: *Climate Dynamics* 40.9-10, pp. 2447–2468. DOI: 10.1007/s00382-012-1488-8.
- Kamb, B. (1970). "Sliding Motion of Glaciers: Theory and Observation". In: *Reviews of Geophysics* 8.4, pp. 673–728. DOI: 10.1029/RG008i004p00673.
- Kamb, B. (1987). "Glacier Surge Mechanism Based on Linked Cavity Configuration of the Basal Water Conduit System". In: *Journal of Geophysical Research: Solid Earth* 92.B9, pp. 9083–9100. DOI: 10.1029/JB092iB09p09083.
- Kavanagh, M. and Tarasov, L. (2017). "BrAHMs V1.0: A Fast, Physically-based Subglacial Hydrology Model for Continental-scale Application". In: *Geoscientific Model Development Discussions* 2017, pp. 1–20. DOI: 10.5194/gmd-2017-275.

- Kessler, M. A. and Anderson, R. S. (2004). “Testing a Numerical Glacial Hydrological Model Using Spring Speed-up Events and Outburst Floods”. In: *Geophys. Res. Lett.* 31.18, pp. 1–5. DOI: 10.1029/2004GL020622.
- Khan, S. a., Kjaer, K. H., Bevis, M., Bamber, J. L., Wahr, J., Kjeldsen, K. K., Bjork, A. a., Korsgaard, N. J., Stearns, L. a., Broeke, M. R. van den, Liu, L., Larsen, N. K., and Muresan, I. S. (2014). “Sustained Mass Loss of the Northeast Greenland Ice Sheet Triggered by Regional Warming”. In: *Nature Climate Change* 4.4, pp. 292–299. ISSN: 1758-678X. DOI: 10.1038/nclimate2161.
- Kleiner, T. and Humbert, A. (2014). “Numerical Simulations of Major Ice Streams in Western Dronning Maud Land, Antarctica, under Wet and Dry Basal Conditions”. In: *Journal of Glaciology* 60.220, pp. 215–232. DOI: 10.3189/2014jog13j006.
- Kolditz, O., Nagel, T., Shao, H., Wang, W., and Bauer, S. (2015). *Thermo-hydro-mechanical-chemical Processes in Fractured Porous Media: Modelling and Benchmarking*. Ed. by O. Kolditz, H. Shao, W. Wang, and S. Bauer. Springer.
- Koziol, C. P. and Arnold, N. (2018). “Modelling Seasonal Meltwater Forcing of the Velocity of Land-terminating Margins of the Greenland Ice Sheet”. In: *The Cryosphere* 12.3, pp. 971–991. DOI: 10.5194/tc-12-971-2018.
- Kusahara, K., Sato, T., Oka, A., Obase, T., Greve, R., Abe-Ouchi, A., and Hasumi, H. (2015). “Modelling the Antarctic Marine Cryosphere at the Last Glacial Maximum”. In: *Annals of Glaciology* 56.69, pp. 425–435. DOI: 10.3189/2015A0G69A792.
- Langley, K., Kohler, J., Matsuoka, K., Sinisalo, A., Scambos, T. A., Neumann, T., Muto, A., Winther, J.-G., and Albert, M. (2011). “Recovery Lakes, East Antarctica, Radar Assessment of Subglacial Water Extent”. In: *Geophysical Research Letters* 38.L05501. DOI: 10.1029/2010GL046094.
- Langley, K., Tinto, K., Block, A., Bell, R., Kohler, J., and Scambos, T. (2014). “Onset of Fast Ice Flow in Recovery Ice Stream, East Antarctica: A Comparison of Potential Causes”. In: *Journal of Glaciology* 60.223, pp. 1007–1014. DOI: 10.3189/2014JG14J067.
- Larour, E., Seroussi, H., Morlighem, M., and Rignot, E. (2012). “Continental Scale, High Order, High Spatial Resolution, Ice Sheet Modeling Using the Ice Sheet System Model (issm)”. In: *Journal of Geophysical Research: Earth Surface* 117.F01022. ISSN: 2156-2202. DOI: 10.1029/2011JF002140.
- Le Brocq, A. M., Hubbard, A., Bentley, M. J., and Bamber, J. L. (2008). “Subglacial Topography Inferred from Ice Surface Terrain Analysis Reveals a Large Un-surveyed Basin below Sea Level in East Antarctica”. In: *Geophysical Research Letters* 35.16. DOI: 10.1029/2008GL034728.
- Le Brocq, A. M., Payne, A. J., Siegert, M. J., and Alley, R. B. (2009). “A Subglacial Water-flow Model for West Antarctica”. In: *Journal of Glaciology* 55.193, pp. 879–888. DOI: 10.3189/002214309790152564.
- Le Brocq, A. M., Payne, A. J., and Siegert, M. J. (2006). “West Antarctic Balance Calculations: Impact of Flux-routing Algorithm, Smoothing Algorithm and Topography”. In: *Computers & geosciences* 32.10, pp. 1780–1795. DOI: 10.1016/j.cageo.2006.05.003.

Bibliography

- Le clec'h, S., Fettweis, X., Quiquet, A., Dumas, C., Kageyama, M., Charbit, S., Wyard, C., and Ritz, C. (2017). "Assessment of the Greenland Ice Sheet – Atmosphere Feedbacks for the Next Century with a Regional Atmospheric Model Fully Coupled to an Ice Sheet Model". In: *The Cryosphere Discussions* 2017, pp. 1–31. DOI: 10.5194/tc-2017-230.
- Le Meur, E. and Huybrechts, P. (1996). "A Comparison of Different Ways of Dealing with Isostasy: Examples from Modelling the Antarctic Ice Sheet during the Last Glacial Cycle". In: *Annals of Glaciology* 23, pp. 309–317. DOI: 10.3189/s0260305500013586.
- Leuschen, C., Gogineni, P., Rodriguez-Morales, F., Paden, J., and Allen, C. (2010, updated 2017). *Icebridge Mcords L2 Ice Thickness (antarctica 2011/12, 2012/13)*. Tech. rep. Boulder, Colorado USA: NASA National Snow and Ice Data Center Distributed Active Archive Center. DOI: 10.5067/GDQ0CUCVTE2Q.
- Leysinger Vieli, G. J.-M. C., Hindmarsh, R. C. A., and Siegert, M. J. (2007). "Three-dimensional Flow Influences on Radar Layer Stratigraphy". In: *Annals of Glaciology* 46, pp. 22–28.
- Leysinger Vieli, G. J.-M. C., Hindmarsh, R. C. A., Siegert, M. J., and Sun, B. (2011). "Time-dependence of the Spatial Pattern of Accumulation Rate in East Antarctica Deduced from Isochronic Radar Layers Using a 3-d Numerical Ice Flow Model". In: *Journal of Geophysical Research: Earth Surface* 116.F2. DOI: 10.1029/2010JF001785.
- Lister, H. and Pratt, G. (1959). "Geophysical Investigations of the Commonwealth Trans-Antarctic Expedition". In: *The Geographical Journal* 125.3/4, pp. 343–354. ISSN: 00167398, 14754959.
- Livingstone, S. J., Clark, C. D., Woodward, J., and Kingslake, J. (2013). "Potential Subglacial Lakes and Meltwater Drainage Pathways beneath the Antarctic and Greenland Ice Sheets". In: *The Cryosphere* 7, pp. 1721–1740.
- Livingstone, S. J., Clark, C. D., Piotrowski, J. A., Tranter, M., Bentley, M. J., Hodson, A., Swift, D. A., and Woodward, J. (2012). "Theoretical Framework and Diagnostic Criteria for the Identification of Palaeo-subglacial Lakes". In: *Quaternary Science Reviews* 53, pp. 88–110. DOI: 10.1016/j.quascirev.2012.08.010.
- Livingstone, S. J., Storrar, R. D., Hillier, J. K., Stokes, C. R., Clark, C. D., and Tarasov, L. (2015). "An Ice-sheet Scale Comparison of Eskers with Modelled Subglacial Drainage Routes". In: *Geomorphology* 246, pp. 104–112. DOI: 10.1016/j.geomorph.2015.06.016.
- Lliboutry, L. (1968). "General Theory of Subglacial Cavitation and Sliding of Temperate Glaciers". In: *Journal of Glaciology* 7.49, pp. 21–58. DOI: 10.3189/s0022143000020396.
- Lliboutry, L. and Duval, P. (1985). "Various Isotropic and Anisotropic Ices Found in Glaciers and Polar Ice Caps and Their Corresponding Rheologies." In: *Ann. Geophys.* 3, pp. 207–224.
- Lliboutry, L. (1958a). "Contribution à La Théorie Du Frottement Du Glacier Sur Son Lit". In: *Comptes rendus hebdomadaires des séances de l'Académie des sciences* 247.3, pp. 318–320.
- Lliboutry, L. (1958b). "Frottement Sur Le Lit Et Mouvement Par Saccades D'un Glacier". In: *Comptes rendus hebdomadaires des séances de l'Académie des sciences* 247.2, pp. 328–330.

- MacAyeal, D. R. (1989). “Large-scale Ice Flow Over a Viscous Basal Sediment: Theory and Application to Ice Stream B, Antarctica”. In: *Journal of Geophysical Research: Solid Earth* 94.B4, pp. 4071–4087.
- MacGregor, J. A., Winebrenner, D. P., Conway, H., Matsuoka, K., Mayewski, P. A., and Clow, G. D. (2007). “Modeling Englacial Radar Attenuation at Siple Dome, West Antarctica, Using Ice Chemistry and Temperature Data”. In: *Journal of Geophysical Research: Earth Surface* 112, F03008. DOI: 10.1029/2006JF000717.
- MacGregor, J. A., Fahnestock, M. A., Catania, G. A., Aschwanden, A., Clow, G. D., Colgan, W. T., Gogineni, S. P., Morlighem, M., Nowicki, S. M. J., Paden, J. D., Price, S. F., and Seroussi, H. (2016). “A Synthesis of the Basal Thermal State of the Greenland Ice Sheet”. In: *J. Geophys. Res.* 121, pp. 1328–1350. DOI: 10.1002/2015JF003803.
- Matsuoka, K., Morse, D., and Raymond, C. F. (2010). “Estimating Englacial Radar Attenuation Using Depth Profiles of the Returned Power, Central West Antarctica”. In: *Journal of Geophysical Research: Earth Surface* 115.F2. DOI: 10.1029/2009JF001496.
- Matsuoka, K., MacGregor, J. A., and Pattyn, F. (2012). “Predicting Radar Attenuation within the Antarctic Ice Sheet”. In: *Earth and Planetary Science Letters* 359-360, pp. 173–183. DOI: 10.1016/j.epsl.2012.10.018.
- McMillan, M., Nienow, P., Shepherd, A., Benham, T., and Sole, A. (2007). “Seasonal Evolution of Supra-glacial Lakes on the Greenland Ice Sheet”. In: *Earth and Planetary Science Letters* 262.3, pp. 484–492. ISSN: 0012-821X. DOI: 10.1016/j.epsl.2007.08.002.
- Meierbachtol, T., Harper, J., and Humphrey, N. (2013). “Basal Drainage System Response to Increasing Surface Melt on the Greenland Ice Sheet”. In: *Science* 341.6147, pp. 777–779. DOI: 10.1126/science.1235905.
- Mernild, S. H. and Liston, G. E. (2012). “Greenland Freshwater Runoff. Part II: Distribution and Trends, 1960–2010”. In: *Journal of Climate* 25.17, pp. 6015–6035. DOI: 10.1175/JCLI-D-11-00592.1.
- Moon, T., Joughin, I., Smith, B., and Howat, I. (2012). “21st-century Evolution of Greenland Outlet Glacier Velocities”. In: *Science* 336.6081, pp. 576–578. DOI: 10.1126/science.1219985.
- Moon, T. and Joughin, I. (2008). “Changes in Ice Front Position on Greenland’s Outlet Glaciers from 1992 to 2007”. In: *Journal of Geophysical Research: Earth Surface* 113.F2, F02022. DOI: 10.1029/2007JF000927.
- Moon, T., Joughin, I., Smith, B., Broeke, M. R., Berg, W. J., Noël, B., and Usher, M. (2014). “Distinct Patterns of Seasonal Greenland Glacier Velocity”. In: *Geophysical Research Letters* 41.20, pp. 7209–7216. DOI: 10.1002/2014GL061836.
- Morland, L. W. (1984). “Thermomechanical Balances of Ice Sheet Flows”. In: *Geophysical and Astrophysical Fluid Dynamics* 29, pp. 237–266.

Bibliography

- Morland, L. W. (1987). "Unconfined Ice-shelf Flow". In: *Dynamics of the West Antarctic Ice Sheet*. Ed. by C. J. van der Veen and J. Oerlemans. Dordrecht, The Netherlands: D. Reidel Publishing Company, pp. 99–116.
- Morlighem, M., Seroussi, H., Larour, E., and Rignot, E. (2013). "Inversion of Basal Friction in Antarctica Using Exact and Incomplete Adjoints of a Higher-order Model". In: *J. Geophys. Res.* 118.3, pp. 1746–1753. DOI: 10.1002/jgrf.20125.
- Morlighem, M., Bondzio, J., Seroussi, H., Rignot, E., Larour, E., Humbert, A., and Rebuffi, S. (2016). "Modeling of Store Gletscher's Calving Dynamics, West Greenland, in Response to Ocean Thermal Forcing". In: *Geophysical Research Letters* 43.6, pp. 2659–2666. ISSN: 0094-8276. DOI: 10.1002/2016gl067695.
- Morlighem, M., Rignot, E., Mouginot, J., Seroussi, H., and Larour, E. (2014). "Deeply Incised Submarine Glacial Valleys beneath the Greenland Ice Sheet". In: *Nature Geoscience* 7.6, pp. 418–422. ISSN: 1752-0894. DOI: 10.1038/ngeo2167.
- Mortensen, J., Bendtsen, J., Motyka, R. J., Lennert, K., Truffer, M., Fahnestock, M., and Rysgaard, S. (2013). "On the Seasonal Freshwater Stratification in the Proximity of Fast-flowing Tidewater Outlet Glaciers in a Sub-arctic Sill Fjord". In: *Journal of Geophysical Research: Oceans* 118.3, pp. 1382–1395. ISSN: 2169-9291. DOI: 10.1002/jgrc.20134.
- Murray, T., Scharrer, K., James, T. D., Dye, S. R., Hanna, E., Booth, A. D., Selmes, N., Luckman, A., Hughes, A. L. C., Cook, S., and Huybrechts, P. (2010). "Ocean Regulation Hypothesis for Glacier Dynamics in Southeast Greenland and Implications for Ice Sheet Mass Changes". In: *Journal of Geophysical Research: Earth Surface* 115.F3. F03026. ISSN: 2156-2202. DOI: 10.1029/2009JF001522.
- Nghiem, S. V., Hall, D. K., Mote, T. L., Tedesco, M., Albert, M. R., Keegan, K., Shuman, C. A., DiGirolamo, N. E., and Neumann, G. (2012). "The Extreme Melt across the Greenland Ice Sheet in 2012". In: *Geophysical Research Letters* 39.20. DOI: 10.1029/2012GL053611.
- Nick, F. M., Vieli, A., Andersen, M. L., Joughin, I., Payne, A., Edwards, T. L., Pattyn, F., and Wal, R. S. W. van de (2013). "Future Sea-level Rise from Greenland's Main Outlet Glaciers in a Warming Climate". In: *Nature* 497.7448, pp. 235–238. ISSN: 0028-0836. DOI: 10.1038/nature12068.
- Nienow, P. W., Sole, A. J., Slater, D. A., and Cowton, T. R. (2017). "Recent Advances in Our Understanding of the Role of Meltwater in the Greenland Ice Sheet System". In: *Current Climate Change Reports*, pp. 330–344. ISSN: 2198-6061. DOI: 10.1007/s40641-017-0083-9.
- Nixdorf, U., Steinhage, D., Meyer, U., Hempel, L., Jenett, M., Wachs, P., and Miller, H. (1999). "The Newly Developed Airborne Res-system of the Awi As a Glaciological Tool". In: *Annals of Glaciology* 29, pp. 231–238.
- Nowicki, S., Bindschadler, R. A., Abe-Ouchi, A., Aschwanden, A., Bueler, E., Choi, H., Fastook, J., Granzow, G., Greve, R., Gutowski, G., Herzfeld, U., Jackson, C., Johnson, J., Khroulev, C., Larour, E., Levermann, A., Lipscomb, W. H., Martin, M. A., Morlighem, M., Parizek, B. R., Pollard, D., Price, S. F., Ren, D., Rignot, E., Saito, F., Sato, T., Seddik, H., Seroussi, H., Taka-

- hashi, K., Walker, R., and Wang, W. L. (2013). “Insights into Spatial Sensitivities of Ice Mass Response to Environmental Change from the Searise Ice Sheet Modeling Project I: Antarctica”. In: *Journal of Geophysical Research: Earth Surface* 118.2, pp. 1002–1024. ISSN: 2169-9011. DOI: 10.1002/jgrf.20081.
- Nye, J. F. (1969). “A Calculation on the Sliding of Ice Over a Wavy Surface Using a Newtonian Viscous Approximation”. In: *Proceedings of the Royal Society of London A: Mathematical, Physical and Engineering Sciences* 311.1506, pp. 445–467. ISSN: 0080-4630. DOI: 10.1098/rspa.1969.0127.
- Nye, J. F. (1970). “Glacier Sliding without Cavitation in a Linear Viscous Approximation”. In: *Proceedings of the Royal Society of London A: Mathematical, Physical and Engineering Sciences* 315.1522, pp. 381–403. ISSN: 0080-4630. DOI: 10.1098/rspa.1970.0050.
- Nye, J. F. (1973). “Water at the Bed of a Glacier”. In: *Symposium at Cambridge 1969 - Hydrology of Glaciers* 95, pp. 189–194.
- Nye, J. F. (1976). “Water Flow in Glaciers: Jökulhlaups, Tunnels and Veins”. In: *Journal of Glaciology* 17.76, pp. 181–207.
- O’Leary, M. and Christoffersen, P. (2013). “Calving on Tidewater Glaciers Amplified by Submarine Frontal Melting”. In: *The Cryosphere* 7.1, pp. 119–128. DOI: 10.5194/tc-7-119-2013.
- Oswald, G. K. A. and Gogineni, S. P. (2008). “Recovery of Subglacial Water Extent from Greenland Radar Survey Data”. In: *Journal of Glaciology* 54.184, pp. 94–106.
- Paterson, W. S. B. and Budd, W. F. (1982). “Flow Parameters for Ice Sheet Modeling”. In: *Cold Regions Science and Technology* 6.2, pp. 175–177. DOI: 10.1016/0165-232x(82)90010-6.
- Pattyn, F. (2010). “Antarctic Subglacial Conditions Inferred from a Hybrid Ice Sheet/ice Stream Model”. In: *Earth and Planetary Science Letters* 295.3-4, pp. 451–461. DOI: 10.1016/j.epsl.2010.04.025.
- Pattyn, F. (2017). “Sea-level Response to Melting of Antarctic Ice Shelves on Multi-centennial Timescales with the Fast Elementary Thermomechanical Ice Sheet Model (f.ETISH V1.0)”. In: *The Cryosphere* 11.4, pp. 1851–1878. DOI: 10.5194/tc-11-1851-2017.
- Pattyn, F. (2003). “A New Three-dimensional Higher-order Thermomechanical Ice Sheet Model: Basic Sensitivity, Ice Stream Development, and Ice Flow across Subglacial Lakes”. In: *Journal of Geophysical Research: Solid Earth* 108.B8. DOI: 10.1029/2002JB002329.
- Pattyn, F. (2008). “Investigating the Stability of Subglacial Lakes with a Full Stokes Ice-sheet Model”. In: *Journal of Glaciology* 54.185, pp. 353–361. DOI: 10.3189/002214308784886171.
- Pattyn, F., De Smedt, B., and Souchez, R. (2004). “Influence of Subglacial Vostok Lake on the Regional Ice Dynamics of the Antarctic Ice Sheet: A Model Study”. In: *Journal of Glaciology* 50.171, pp. 583–589. DOI: 10.3189/172756504781829765.
- Paxman, G. J. G., Jamieson, S. S. R., Ferraccioli, F., Bentley, M. J., Forsberg, R., Ross, N., Watts, A. B., Corr, H. F. J., and Jordan, T. A. (2017). “Uplift and Tilting of the Shackleton Range in

Bibliography

- East Antarctica Driven by Glacial Erosion and Normal Faulting”. In: *Journal of Geophysical Research: Solid Earth* 122.3, pp. 2390–2408. DOI: 10.1002/2016JB013841.
- Payne, A. J. and Baldwin, D. J. (1999). “Thermomechanical Modelling of the Scandinavian Ice Sheet: Implications for Ice-stream Formation”. In: *Annals of Glaciology* 28, pp. 83–89. DOI: 10.3189/172756499781821733.
- Payne, A. J., Huybrechts, P., Abe-Ouchi, A., Calov, R., Fastook, J. L., Greve, R., Marshall, S. J., Marsiat, I., Ritz, C., Tarasov, L., and Thomassen, M. P. A. (2000). “Results from the EISMINT Model Intercomparison: The Effects of Thermomechanical Coupling”. In: *J. Glaciol.* 46.153, pp. 227–238.
- Peano, D., Colleoni, F., Quiquet, A., and Masina, S. (2017). “Ice Flux Evolution in Fast Flowing Areas of the Greenland Ice Sheet Over the 20th and 21st Centuries”. In: *J. Glaciol.* 63.239, pp. 499–513. DOI: 10.1017/jog.2017.12.
- Peters, M. E., Blankenship, D. D., and Morse, D. L. (2005). “Analysis Techniques for Coherent Airborne Radar Sounding: Application to West Antarctic Ice Streams”. In: *Journal of Geophysical Research: Solid Earth* 110.B6. DOI: 10.1029/2004JB003222.
- Pimentel, S. and Flowers, G. E. (2010). “A Numerical Study of Hydrologically Driven Glacier Dynamics and Subglacial Flooding”. In: *Proceedings of the Royal Society of London A: Mathematical, Physical and Engineering Sciences* 467.2126, pp. 537–558. ISSN: 1364-5021. DOI: 10.1098/rspa.2010.0211.
- Poinar, K., Joughin, I., Das, S. B., Behn, M. D., Lenaerts, J., and Broeke, M. R. (2015). “Limits to Future Expansion of Surface-melt-enhanced Ice Flow into the Interior of Western Greenland”. In: *Geophys. Res. Lett.* 42.6, pp. 1800–1807.
- Pollard, D. and DeConto, R. M. (2007). “A Coupled Ice-sheet/ice-shelf/sediment Model Applied to a Marine-margin Flowline: Forced and Unforced Variations”. In: *Glacial Sedimentary Processes and Products*. Ed. by M. J. Hambrey, P. Christoffersen, N. F. Glasser, and B. Hubbard. Oxford, UK.: Blackwell Publishing Ltd., pp. 37–52. DOI: 10.1002/9781444304435.ch4.
- Pollard, D. and DeConto, R. M. (2012). “Description of a Hybrid Ice Sheet-shelf Model, and Application to Antarctica”. In: *Geoscientific Model Development* 5.5, pp. 1273–1295. DOI: 10.5194/gmd-5-1273-2012.
- Price, S. F., Payne, A. J., Howat, I. M., and Smith, B. E. (2011). “Committed Sea-level Rise for the Next Century from Greenland Ice Sheet Dynamics during the Past Decade”. In: *PNAS* 108.22, pp. 8978–8983. DOI: 10.1073/pnas.1017313108.
- Purucker, M. (2012a). personal communication with Ralf Greve, accessible via www.sicopolis.net.
- Purucker, M. (2012b). “Geothermal Heat Flux Data Set Based on Low Resolution Observations Collected by the Champ Satellite between 2000 and 2010, and Produced from the Mf-6 Model Following the Technique Described in Fox Maule Et Al. (2005)(<http://websrv.cs.umt.edu/isis/index.php/antarctica> update.

- Quinn, P. F. B. J., Beven, K., Chevallier, P., and Planchon, O. (1991). "Prediction of Hillslope Flow Paths for Distributed Hydrological Modelling Using Digital Terrain Models". In: *Hydrological processes* 5.1, pp. 59–79. DOI: 10.1002/hyp.3360050106.
- Rada, C. and Schoof, C. (2018). "Subglacial Drainage Characterization from Eight Years of Continuous Borehole Data on a Small Glacier in the Yukon Territory, Canada". In: *The Cryosphere Discussions* 2018, pp. 1–42. DOI: 10.5194/tc-2017-270.
- Rae, J. G. L., Aðalgeirsdóttir, G., Edwards, T. L., Fettweis, X., Gregory, J. M., Hewitt, H. T., Lowe, J. A., Lucas-Picher, P., Mottram, R. H., Payne, A. J., Ridley, J. K., Shannon, S. R., Berg, W. J. van de, Wal, R. S. W. van de, and Broeke, M. R. van den (2012). "Greenland Ice Sheet Surface Mass Balance: Evaluating Simulations and Making Projections with Regional Climate Models". In: *The Cryosphere* 6.6, pp. 1275–1294. DOI: 10.5194/tc-6-1275-2012.
- Ridley, J., Gregory, J. M., Huybrechts, P., and Lowe, J. (2010). "Thresholds for Irreversible Decline of the Greenland Ice Sheet". In: *Climate Dynamics* 35.6, pp. 1049–1057. DOI: 10.1007/s00382-009-0646-0.
- Rietbroek, R., Brunnabend, S.-E., Kusche, J., Schröter, J., and Dahle, C. (2016). "Revisiting the Contemporary Sea-level Budget on Global and Regional Scales". In: *Proceedings of the National Academy of Sciences* 113.6, pp. 1504–1509. DOI: 10.1073/pnas.1519132113.
- Rignot, E. and Mouginot, J. (2012). "Ice Flow in Greenland for the International Polar Year 2008–2009". In: *Geophysical Research Letters* 39.11, p. L11501. DOI: 10.1029/2012GL051634.
- Rignot, E., Box, J. E., Burgess, E., and Hanna, E. (2008a). "Mass Balance of the Greenland Ice Sheet from 1958 to 2007". In: *Geophys. Res. Lett.* 35, p. L20502. DOI: 10.1029/2008GL035417.
- Rignot, E., Bamber, J. L., Boroeke, M. R. van den, Davis, C., Li, Y., Berg, W. J. van de, and Meijgaard, E. van (2008b). "Recent Antarctic Ice Mass Loss from Radar Interferometry and Regional Climate Modelling". In: *Nature Geoscience* 1, pp. 106–110. DOI: 10.1038/ngeo102.
- Rignot, E., Velicogna, I., Broeke, M. R. van den, Monaghan, A., and Lenaerts, J. T. M. (2011a). "Acceleration of the Contribution of the Greenland and Antarctic Ice Sheets to Sea Level Rise". In: *Geophysical Research Letters* 38.5. DOI: 10.1029/2011GL046583.
- Rignot, E., Mouginot, J., and Scheuchl, B. (2011b). "Ice Flow of the Antarctic Ice Sheet". In: *Science* 333.6048, pp. 1427–1430. DOI: 10.1126/science.1208336.
- Rignot, E., Fenty, I., Xu, Y., Cai, C., and Kemp, C. (2015). "Undercutting of Marine-terminating Glaciers in West Greenland". In: *Geophysical Research Letters* 42.14, pp. 5909–5917. ISSN: 1944-8007. DOI: 10.1002/2015GL064236.
- Rignot, E., Fenty, I., Xu, Y., Cai, C., Velicogna, I., Cofaigh, C., Dowdeswell, J. A., Weinrebe, W., Catania, G., and Duncan, D. (2016). "Bathymetry Data Reveal Glaciers Vulnerable to Ice-ocean Interaction in Uummannaq and Vaigat Glacial Fjords, West Greenland". In: *Geophysical Research Letters* 43.6, pp. 2667–2674. ISSN: 1944-8007. DOI: 10.1002/2016GL067832.

Bibliography

- Rippin, D., Bamber, J. L., Siegert, M. J., Vaughan, D. G., and Corr, H. F. J. (2006). "Basal Conditions beneath Enhanced-flow Tributaries of Slessor Glacier, East Antarctica". In: *Journal of Glaciology* 52.179, pp. 481–490.
- Ritz, C., Rommelaere, V., and Dumas, C. (2001). "Modeling the Evolution of Antarctic Ice Sheet Over the Last 420,000 Years: Implications for Altitude Changes in the Vostok Region". In: *Journal of Geophysical Research: Atmospheres* 106.D23, pp. 31943–31964. DOI: 10.1029/2001JD900232.
- Robin, G. d. Q., Evans, S., and Bailey, J. T. (1969). "Interpretation of Radio Echo Sounding in Polar Ice Sheets". In: *Philosophical Transactions of the Royal Society London Series A* 265, pp. 437–505.
- Robinson, A., Calov, R., and Ganopolski, A. (2011). "Greenland Ice Sheet Model Parameters Constrained Using Simulations of the Eemian Interglacial". In: *Clim. Past* 7, pp. 381–396. DOI: 10.5194/cp-7-381-2011.
- Robinson, A., Calov, R., and Ganopolski, A. (2012). "Multistability and Critical Thresholds of the Greenland Ice Sheet". In: *Nature Climate Change* 2, pp. 429–432. DOI: 10.1038/NCLIMATE1449.
- Rogozhina, I., Petrunin, A. G., Vaughan, A. P. M., Steinberger, B., Johnson, J. V., Kaban, M. K., Calov, R., Rickers, F., Thomas, M., and Koulakov, I. (2016). "Melting at the Base of the Greenland Ice Sheet Explained by Iceland Hotspot History". In: *Nat Geosci* 9, pp. 366–369. DOI: 10.1038/NGE02689.
- Ross, N., Bingham, R. G., Corr, H. F. J., Ferraccioli, F., Jordan, T. A., Le Brocq, A., Rippin, D. M., Young, D., Blankenship, D. D., and Siegert, M. J. (2012). "Steep Reverse Bed Slope at the Grounding Line of the Weddell Sea Sector in West Antarctica". In: *Nature Geoscience*, pp. 393–396. DOI: 10.1038/ngeo1468.
- Röthlisberger, H. (1972). "Water Pressure in Intra- and Subglacial Channels". In: *Journal of Glaciology* 11.62, pp. 177–203. DOI: 10.3189/s0022143000022188.
- Röthlisberger, H. and Lang, H. (1987). *Glacio-fluvial Sediment Transfer: An Alpine Perspective*. New York, NY, USA: John Wiley and Sons.
- Röthlisberger, H. (1969). "Water Pressure in Subglacial Channels". In: *Union Géodésique et Géophysique Internationale. Association Internationale d'Hydrologie Scientifique. Commission de Neiges et Glaces. Symposium on the hydrology of Glaciers, Cambridge, 7*, p. 97.
- Saha, S. et al. (2010). "The NCEP Climate Forecast System Reanalysis". In: *Bulletin of the American Meteorological Society* 91.8, pp. 1015–1058. DOI: 10.1175/2010bams3001.1.
- Saito, F., Abe-Ouchi, A., Takahashi, K., and Blatter, H. (2016). "Searise Experiments Revisited: Potential Sources of Spread in Multi-model Projections of the Greenland Ice Sheet". In: *The Cryosphere* 10.1, pp. 43–63. DOI: 10.5194/tc-10-43-2016.
- Scanlon, B. R., Mace, R. E., Barrett, M. E., and Smith, B. (2003). "Can We Simulate Regional Groundwater Flow in a Karst System Using Equivalent Porous Media Models Case Study, Barton Springs Edwards Aquifer, Usa". In: *Journal of Hydrology* 276.1, pp. 137–158. ISSN: 0022-1694. DOI: 10.1016/S0022-1694(03)00064-7.

- Schaffer, J., Timmermann, R., Erik Arndt, J., Savstrup Kristensen, S., Mayer, C., Morlighem, M., and Steinhage, D. (2016). “A Global, High-resolution Data Set of Ice Sheet Topography, Cavity Geometry, and Ocean Bathymetry”. In: *Earth System Science Data* 8.2, pp. 543–557. ISSN: 1866-3516. DOI: 10.5194/essd-8-543-2016.
- Schaffer, J., Appen, W. J. von, Dodd, P. A., Hofstede, C., Mayer, C., Steur, L. de, and Kanzow, T. (2017). “Warm Water Pathways toward Nioghalvfjærdsfjorden Glacier, Northeast Greenland”. In: *Journal of Geophysical Research: Oceans* 122.5, pp. 4004–4020. ISSN: 2169-9291. DOI: 10.1002/2016JC012462.
- Schoof, C. (2005). “The Effect of Cavitation on Glacier Sliding”. In: *Proceedings of the Royal Society of London A: Mathematical, Physical and Engineering Sciences* 461.2055, pp. 609–627. ISSN: 1364-5021. DOI: 10.1098/rspa.2004.1350.
- Schoof, C. (2010a). “Coulomb Friction and Other Sliding Laws in a Higher-order Glacier Flow Model”. In: *Mathematical Models and Methods in Applied Sciences* 20.01, pp. 157–189. DOI: 10.1142/S0218202510004180.
- Schoof, C. (2010b). “Ice-sheet Acceleration Driven by Melt Supply Variability”. In: *Nature* 468.7325, pp. 803–806. ISSN: 0028-0836. DOI: 10.1038/nature09618.
- Schoof, C., Hewitt, I. J., and Werder, M. A. (2012). “Flotation and Free Surface Flow in a Model for Subglacial Drainage. Part I: Distributed Drainage”. In: *Journal of Fluid Mechanics* 702, pp. 126–156. DOI: 10.1017/jfm.2012.165.
- Schwanghart, W. and Scherler, D. (2014). “Short Communication: Topotoolbox 2 – Matlab-based Software for Topographic Analysis and Modeling in Earth Surface Sciences”. In: *Earth Surface Dynamics* 2.1, pp. 1–7. DOI: 10.5194/esurf-2-1-2014.
- Schwanghart, W. and Kuhn, N. J. (2010). “Topotoolbox: A Set of Matlab Functions for Topographic Analysis”. In: *Environmental Modelling & Software* 25.6, pp. 770–781. ISSN: 1364-8152. DOI: 10.1016/j.envsoft.2009.12.002.
- Sciascia, R., Straneo, F., Cenedese, C., and Heimbach, P. (2013). “Seasonal Variability of Submarine Melt Rate and Circulation in an East Greenland Fjord”. In: *Journal of Geophysical Research: Oceans* 118.5, pp. 2492–2506. ISSN: 2169-9275. DOI: 10.1002/jgrc.20142.
- Seddik, H., Greve, R., Zwinger, T., Gillet-Chaulet, F., and Gagliardini, O. (2012). “Simulations of the Greenland Ice Sheet 100 Years into the Future with the Full Stokes Model Elmer/Ice”. In: *J. Glaciol.* 58.209, pp. 427–440. DOI: 10.3189/2012JG11J177.
- Shannon, S. R., Payne, A. J., Bartholomew, I. D., Broeke, M. R. van den, Edwards, T. L., Fettweis, X., Gagliardini, O., Gillet-Chaulet, F., Goelzer, H., Hoffman, M. J., Huybrechts, P., Mair, D. W. F., Nienow, P. W., Perego, M., Price, S. F., Smeets, C. J. P. P., Sole, A. J., Wal, R. S. W. van de, and Zwinger, T. (2013). “Enhanced Basal Lubrication and the Contribution of the Greenland Ice Sheet to Future Sea-level Rise”. In: *Proceedings of the National Academy of Sciences of the United States of America* 110.35, pp. 14156–14161. DOI: 10.1073/pnas.1212647110.

Bibliography

- Shapiro, N. M. and Ritzwoller, M. H. (2004). “Inferring Surface Heat Flux Distributions Guided by a Global Seismic Model: Particular Application to Antarctica”. In: *Earth and Planetary Science Letters* 223, pp. 213–224. DOI: 10.1016/j.epsl.2004.04.011.
- Shepherd, A., Hubbard, A., Nienow, P., King, M., McMillan, M., and Joughin, I. (2009). “Greenland Ice Sheet Motion Coupled with Daily Melting in Late Summer”. In: *Geophysical Research Letters* 36.1. DOI: 10.1029/2008GL035758.
- Shepherd, A., Ivins, E. R., Geruo, A., Barletta, V. R., Bentley, M. J., Bettadpur, S., Briggs, K. H., Bromwich, D. H., Forsberg, R., Galin, N., Horwath, M., Jacobs, S., Joughin, I., King, M. A., Lenaerts, J. T. M., Li, J., Ligtenberg, S. R. M., Luckman, A., Luthcke, S. B., McMillan, M., Meister, R., Milne, G., Mouginot, J., Muir, A., Nicolas, J. P., Paden, J., Payne, A. J., Pritchard, H., Rignot, E., Rott, H., Sørensen, L. S., Scambos, T. A., Scheuchl, B., Schrama, E. J. O., Smith, B., Sundal, A. V., Angelen, J. H. van, Berg, W. J. van de, Broeke, M. R. van den, Vaughan, D. G., Velicogna, I., Wahr, J., Whitehouse, P. L., Wingham, D. J., Yi, D., Young, D., and Zwally, H. J. (2012). “A Reconciled Estimate of Ice-sheet Mass Balance”. In: *Science* 338.6111, pp. 1183–1189. ISSN: 0036-8075. DOI: 10.1126/science.1228102.
- Shoemaker, E. M. (1986). “Subglacial Hydrology for an Ice Sheet Resting on a Deformable Aquifer”. In: *Journal of Glaciology* 32.110, pp. 20–30. DOI: 10.1017/s0022143000006833.
- Shreve, R. L. (1972). “Movement of Water in Glaciers”. In: *Journal of Glaciology* 11.62, pp. 205–214. DOI: 10.3189/s002214300002219x.
- Siclen, V. and Clinton, D. (2002). “Equivalent Channel Network Model for Permeability and Electrical Conductivity of Fracture Networks”. In: *Journal of Geophysical Research: Solid Earth* 107.B6, ECV 1–1–ECV 1–10. ISSN: 2156-2202. DOI: 10.1029/2000JB000057.
- Siegert, M. (2004). “Numerical Reconstructions of the Eurasian Ice Sheet and Climate during the Late Weichselian”. In: *Quaternary Science Reviews* 23.11-13, pp. 1273–1283. DOI: 10.1016/j.quascirev.2003.12.010.
- Siegert, M. J. and Bamber, J. L. (2000). “Subglacial Water at the Heads of Antarctic Ice-stream Tributaries”. In: *Journal of Glaciology* 46.155, pp. 702–703. DOI: 10.3189/172756500781832783.
- Siegert, M. J. and Ridley, J. K. (1998). “Determining Basal Ice-sheet Conditions in the Dome C Region of East Antarctica Using Satellite Radar Altimetry and Airborne Radio-echo Sounding”. In: *Journal of Glaciology* 44.146, pp. 1–8. DOI: 10.3189/s00221430000229x.
- Siegert, M. J., Dowdeswell, J. A., Gorman, M. R., and McIntyre, N. F. (1996). “An Inventory of Antarctic Sub-glacial Lakes”. In: *Antarctic Science* 8.03. DOI: 10.1017/s0954102096000405.
- Siegert, M. J., Ross, N., Corr, H. F. J., Smith, B., Jordan, T., Bingham, R. G., Ferraccioli, F., Rippin, D. M., and Le Brocq, A. (2014). “Boundary Conditions of an Active West Antarctic Subglacial Lake: Implications for Storage of Water beneath the Ice Sheet”. In: *The Cryosphere* 8.1, pp. 15–24. DOI: 10.5194/tc-8-15-2014.
- Siegert, M. J., Ross, N., and Le Brocq, A. M. (2016a). “Recent Advances in Understanding Antarctic Subglacial Lakes and Hydrology”. In: *Philosophical Transactions of the Royal Society A:*

- Mathematical, Physical and Engineering Sciences* 374.2059, p. 12. DOI: 10.1098/rsta.2014.0306.
- Siegert, M. J., Ross, N., Li, J., Schroeder, D. M., Rippin, D., Ashmore, D., Bingham, R., and Gogineni, P. (2016b). “Subglacial Controls on the Flow of Institute Ice Stream, West Antarctica”. In: *Annals of Glaciology* 57.73, pp. 19–24. DOI: 10.1017/aog.2016.17.
- Slater, D. A., Nienow, P. W., Cowton, T. R., Goldberg, D. N., and Sole, A. J. (2015). “Effect of Near-terminus Subglacial Hydrology on Tidewater Glacier Submarine Melt Rates”. In: *Geophysical Research Letters* 42.8, pp. 2861–2868. ISSN: 1944-8007. DOI: 10.1002/2014GL062494.
- Slater, D., Nienow, P., Sole, A., Cowton, T. O. M., Mottram, R., Langen, P., and Mair, D. (2017). “Spatially Distributed Runoff at the Grounding Line of a Large Greenlandic Tidewater Glacier Inferred from Plume Modelling”. In: *Journal of Glaciology*, pp. 1–15. ISSN: 0022-1430. DOI: 10.1017/jog.2016.139.
- Smith, B. E., Fricker, H. A., Joughin, I. R., and Tulaczyk, S. (2009). “An Inventory of Active Subglacial Lakes in Antarctica Detected by Icesat (2003–2008)”. In: *Journal of Glaciology* 55.192, pp. 573–595. DOI: 10.3189/002214309789470879.
- Smith, L. C., Yang, K., Pitcher, L. H., Overstreet, B. T., Chu, V. W., Rennermalm, Å. K., Ryan, J. C., Cooper, M. G., Gleason, C. J., Tedesco, M., Jeyaratnam, J., As, D. van, Broeke, M. R. van den, Berg, W. J. van de, Noël, B., Langen, P. L., Cullather, R. I., Zhao, B., Willis, M. J., Hubbard, A., Box, J. E., Jenner, B. A., and Behar, A. E. (2017). “Direct Measurements of Meltwater Runoff on the Greenland Ice Sheet Surface”. In: *Proceedings of the National Academy of Sciences* 114.50, E10622–E10631. DOI: 10.1073/pnas.1707743114.
- Smith, W. and Wessel, P. (1990). “Gridding with Continuous Curvature Splines in Tension”. In: *Geophysics* 55.3, pp. 293–305.
- Sole, A., Nienow, P., Bartholomew, I., Mair, D., Cowton, T., Tedstone, A., and King, M. A. (2013). “Winter Motion Mediates Dynamic Response of the Greenland Ice Sheet to Warmer Summers”. In: *Geophysical Research Letters* 40.15, pp. 3940–3944. ISSN: 1944-8007. DOI: 10.1002/grl.50764.
- Sommers, A., Rajaram, H., and Morlighem, M. (2018). “Shakti: Subglacial Hydrology and Kinetic Transient Interactions V1.0”. In: *Geoscientific Model Development Discussions*, pp. 1–23. DOI: 10.5194/gmd-2018-58.
- Spring, U. and Hutter, K. (1982). “Conduit Flow of a Fluid through Its Solid Phase and Its Application to Intraglacial Channel Flow”. In: *International Journal of Engineering Sciences* 20, pp. 327–363.
- Stearns, L. A. and Veen, C. J. van der (2018). “Friction at the Bed Does Not Control Fast Glacier Flow”. In: *Science*. ISSN: 0036-8075. DOI: 10.1126/science.aat2217.
- Stearns, L. A., Smith, B. E., and Hamilton, G. S. (2008). “Increased Flow Speed on a Large East Antarctic Outlet Glacier Caused by Subglacial Floods”. In: *Nature Geoscience* 1.12, pp. 827–831. DOI: 10.1038/ngeo356.

Bibliography

- Stevens, L. A., Behn, M. D., McGuire, J. J., Das, S. B., Joughin, I., Herring, T., Shean, D. E., and King, M. A. (2015). "Greenland Supraglacial Lake Drainages Triggered by Hydrologically Induced Basal Slip". In: *Nature* 522, p. 73. DOI: 10.1038/nature14480.
- Stone, E. J., Lunt, D. J., Annan, J. D., and Hargreaves, J. C. (2013). "Quantification of the Greenland Ice Sheet Contribution to Last Interglacial Sea Level Rise". In: *Clim. Past* 9, pp. 621–639. DOI: 10.5194/cp-9-621-2013.
- Straneo, F., Curry, R. G., Sutherland, D. A., Hamilton, G. S., Cenedese, C., Våge, K., and Stearns, L. A. (2011). "Impact of Fjord Dynamics and Glacial Runoff on the Circulation near Helheim Glacier". In: *Nature Geoscience* 4.5, pp. 322–327. ISSN: 1752-0894. DOI: 10.1038/ngeo1109.
- Straneo, F., Hamilton, G. S., Stearns, L. A., and Sutherland, D. A. (2016). "Connecting the Greenland Ice Sheet and the Ocean: A Case Study of Helheim Glacier and Sermilik Fjord". In: *Oceanography* 29. DOI: 10.5670/oceanog.2016.97.
- Straneo, F. and Heimbach, P. (2013). "North Atlantic Warming and the Retreat of Greenland's Outlet Glaciers." In: *Nature* 504.7478, pp. 36–43. ISSN: 1476-4687. DOI: 10.1038/nature12854.
- Straneo, F., Sutherland, D. a., Holland, D., Gladish, C., Hamilton, G. S., Johnson, H. L., Rignot, E., Xu, Y., and Koppes, M. (2012). "Characteristics of Ocean Waters Reaching Greenland's Glaciers". In: *Annals of Glaciology* 53.60, pp. 202–210. ISSN: 0260-3055. DOI: 10.3189/2012AoG60A059.
- Sundal, A. V., Shepherd, A., Nienow, P., Hanna, E., Palmer, S., and Huybrechts, P. (2009). "Evolution of Supra-glacial Lakes across the Greenland Ice Sheet". In: *Remote Sensing of Environment* 113, pp. 2164–2171. DOI: 10.1016/j.rse.2009.05.018.
- Sundal, A. V., Shepherd, A., Nienow, P., Hanna, E., Palmer, S., and Huybrechts, P. (2011). "Melt-induced Speed-up of Greenland Ice Sheet Offset by Efficient Subglacial Drainage". In: *Nature* 469, p. 521. DOI: 10.1038/nature09740.
- Survey, B. A. (2004). *Antarctic Digital Database*. 4th ed. Scientific committee on Antarctic Research. lose.
- Sutherland, D. A. and Straneo, F. (2012). "Estimating Ocean Heat Transports and Submarine Melt Rates in Sermilik Fjord, Greenland, Using Lowered Acoustic Doppler Current Profiler (LADCP) Velocity Profiles". In: *Annals of Glaciology* 53.60, pp. 50–58. ISSN: 0260-3055. DOI: 10.3189/2012AoG60A050.
- Svendsen, J. (2004). "Late Quaternary Ice Sheet History of Northern Eurasia". In: *Quaternary Science Reviews* 23.11-13, pp. 1229–1271. DOI: 10.1016/j.quascirev.2003.12.008.
- Svendsen, J. I., Gataullin, V., Mangerud, J., and Polyak, L. (2004). "The Glacial History of the Barents and Kara Sea Region". In: *Developments in Quaternary Sciences*. Elsevier, pp. 369–378. DOI: 10.1016/S1571-0866(04)80086-1.
- Syvitski, J. P. M., Andrews, J. T., and Dowdeswell, J. (1996). "Sediment Deposition in an Iceberg-dominated Glacimarine Environment, East Greenland: Basin Fill Implications". In: *Global and Planetary Change* 12.1-4, pp. 251–270. ISSN: 0921-8181. DOI: 10.1016/0921-8181(95)00023-2.

- Talpe, M. J., Nerem, R. S., Forootan, E., Schmidt, M., Lemoine, F. G., Enderlin, E. M., and Landerer, F. W. (2017). "Ice Mass Change in Greenland and Antarctica between 1993 and 2013 from Satellite Gravity Measurements". In: *J. Geod.* 91.11, pp. 1283–1298. DOI: 10.1007/s00190-017-1025-y.
- Tarboton, D. G. (1997). "A New Method for the Determination of Flow Directions and Upslope Areas in Grid Digital Elevation Models". In: *Water Resources Research* 33.2, pp. 309–319. DOI: 10.1029/96WR03137.
- Tedstone, A. J., Nienow, P. W., Gourmelen, N., Dehecq, A., Goldberg, D., and Hanna, E. (2015). "Decadal Slowdown of a Land-terminating Sector of the Greenland Ice Sheet Despite Warming". In: *Nature* 526.7575, pp. 692–695. DOI: 10.1038/nature15722.
- Tedstone, A. J., Nienow, P. W., Sole, A. J., Mair, D. W. F., Cowton, T. R., Bartholomew, I. D., and King, M. A. (2013). "Greenland Ice Sheet Motion Insensitive to Exceptional Meltwater Forcing". In: *Proceedings of the National Academy of Sciences* 110.49, pp. 19719–19724. ISSN: 0027-8424. DOI: 10.1073/pnas.1315843110.
- Teutsch, G. and Sauter, M. (1991). "Groundwater Modeling in Karst Terranes: Scale Effects, Data Acquisition and Field Validation". In: *Third Conference on Hydrogeology, Ecology, Monitoring, and Management of Ground Water in Karst Terranes. National Ground Water Association, Dublin, Ohio*, pp. 17–35.
- Tsai, V. C. and Rice, J. R. (2010). "A Model for Turbulent Hydraulic Fracture and Application to Crack Propagation at Glacier Beds". In: *J. Geophys. Res.* 115.F3, F03007.
- Tulaczyk, S. and Hossainzadeh, S. (2011). "Antarctica's Deep Frozen "lakes"". In: *Science* 331.6024, pp. 1524–1525. ISSN: 0036-8075. DOI: 10.1126/science.1202888.
- Tulaczyk, S., Kamb, W. B., and Engelhardt, H. F. (2000a). "Basal Mechanics of Ice Stream B, West Antarctica: 1. Till Mechanics". In: *Journal of Geophysical Research: Solid Earth* 105.B1, pp. 463–481. DOI: 10.1029/1999jb900329.
- Tulaczyk, S., Kamb, W. B., and Engelhardt, H. F. (2000b). "Basal Mechanics of Ice Stream B, West Antarctica: 2. Undrained Plastic Bed Model". In: *Journal of Geophysical Research: Solid Earth* 105.B1, pp. 483–494. DOI: 10.1029/1999JB900328.
- Uppala, S. M., Kållberg, P. W., Simmons, A. J., Andrae, U., Bechtold, V. D. C., Fiorino, M., Gibson, J. K., Haseler, J., Hernandez, A., Kelly, G. A., Li, X., Onogi, K., Saarinen, S., Sokka, N., Allan, R. P., Andersson, E., Arpe, K., Balmaseda, M. A., Beljaars, A. C. M., Berg, L. V. D., Bidlot, J., Bormann, N., Caires, S., Chevallier, F., Dethof, A., Dragosavac, M., Fisher, M., Fuentes, M., Hagemann, S., Hólm, E., Hoskins, B. J., Isaksen, I., Janssen, P. A. E. M., Jenne, R., McNally, A. P., Mahfouf, J.-F., Morcrette, J.-J., Rayner, N. A., Saunders, R. W., Simon, P., Sterl, A., Trenberth, K. E., Untch, A., Vasiljevic, D., Viterbo, P., and Woollen, J. (2005). "The ERA-40 Re-analysis". In: *Quarterly Journal of the Royal Meteorological Society* 131.612, pp. 2961–3012. DOI: 10.1256/qj.04.176.
- Vallelonga, P., Christianson, K., Alley, R. B., Anandkrishnan, S., Christian, J. E. M., Dahl-Jensen, D., Gkinis, V., Holme, C., Jacobel, R. W., Karlsson, N. B., Keisling, B. A., Kipfstuhl, S., Kjær,

Bibliography

- H. A., Kristensen, M. E. L., Muto, A., Peters, L. E., Popp, T., Riverman, K. L., Svensson, A. M., Tibuleac, C., Vinther, B. M., Weng, Y., and Winstrup, M. (2014). "Initial Results from Geophysical Surveys and Shallow Coring of the Northeast Greenland Ice Stream (NEGIS)". In: *The Cryosphere* 8.4, pp. 1275–1287. DOI: 10.5194/tc-8-1275-2014.
- Veen, C. J. van der (2002). "Calving Glaciers". In: *Progress in Physical Geography: Earth and Environment* 26.1, pp. 96–122. DOI: 10.1191/0309133302pp327ra.
- Veen, C. J. van der (2007). "Fracture Propagation As Means of Rapidly Transferring Surface Meltwater to the Base of Glaciers". In: *Geophysical Research Letters* 34.1. DOI: 10.1029/2006GL028385.
- Velicogna, I. and Wahr, J. (2005). "Greenland Mass Balance from GRACE". In: *Geophysical Research Letters* 32.18. L18505. DOI: 10.1029/2005GL023955.
- Vizcaino, M., Mikolajewicz, U., Ziemann, F., Rodehacke, C. B., Greve, R., and Broeke, M. R. van den (2015). "Coupled Simulations of Greenland Ice Sheet and Climate Change up to A.d. 2300". In: *Geophysical Research Letters* 42.10. 2014GL061142, pp. 3927–3935. ISSN: 1944-8007. DOI: 10.1002/2014GL061142.
- Von Hippel, A. R. (1958). *Dielectric Materials and Applications*. Ed. by A. Hippel. 2nd ed. Iose: The Technology Press of M.I.T. Cambridge, Massachusetts, and John Wiley & Sons, Inc. New York.
- Wal, R. S. W. van de, Boot, W., Broeke, M. R. van den, Smeets, C. J.P. P., Reijmer, C. H., Donker, J. J. A., and Oerlemans, J. (2008). "Large and Rapid Melt-induced Velocity Changes in the Ablation Zone of the Greenland Ice Sheet". In: *Science* 321.5885, pp. 111–113. ISSN: 0036-8075. DOI: 10.1126/science.1158540.
- Wal, R. S. W. van de, Smeets, C. J.P. P., Boot, W., Stoffelen, M., Kampen, R. van, Doyle, S. H., Wilhelms, F., Broeke, M. R. van den, Reijmer, C. H., Oerlemans, J., and Hubbard, A. (2015). "Self-regulation of Ice Flow Varies across the Ablation Area in South-west Greenland". In: *The Cryosphere* 9.2, pp. 603–611. DOI: 10.5194/tc-9-603-2015.
- Walder, J. S. and Fowler, A. (1994). "Channelized Subglacial Drainage Over a Deformable Bed". In: *J. Glaciol.* 40.134, pp. 3–15.
- Walder, J. S. (1982). "Stability of Sheet Flow of Water beneath Temperate Glaciers and Implications for Glacier Surging". In: *Journal of Glaciology* 28.99, pp. 273–293. DOI: 10.3189/S0022143000011631.
- Walder, J. S. (1986). "Hydraulics of Subglacial Cavities". In: *Journal of Glaciology* 32.112, pp. 439–445. DOI: 10.3189/S0022143000012156.
- Walker, R. T., Werder, M. A., Dow, C. F., and Nowicki, S. M. J. (2017). "Determining Ice-sheet Uplift Surrounding Subglacial Lakes with a Viscous Plate Model". In: *Frontiers in Earth Science* 5, p. 103. DOI: 10.3389/feart.2017.00103.
- Weatherall, P., Marks, K. M., Jakobsson, M., Schmitt, T., Tani, S., Arndt, J. E., Rovere, M., Chayes, D., Ferrini, V., and Wigley, R. (2015). "A New Digital Bathymetric Model of the World's Oceans". In: *Earth and Space Science* 2.8, pp. 331–345. DOI: 10.1002/2015ea000107.

- Weertman, J. (1957). “On the Sliding of Glaciers”. In: *Journal of Glaciology* 3.21, pp. 33–38. DOI: 10.3189/S0022143000024709.
- Weertman, J. (1962). “Catastrophic Glacier Advances”. In: *Union Géodésique et Géophysique Internationale, Association Internationale d’Hydrologie Scientifique. Colloque d’Obergurgl 10–18 Sept 1962*, pp. 31–39.
- Weertman, J. (1966). “Effect of a Basal Water Layer on the Dimensions of Ice Sheets”. In: *Journal of Glaciology* 6.44, pp. 191–207. DOI: 10.1017/S0022143000019213.
- Weertman, J. (1972). “General Theory of Water Flow at the Base of a Glacier or Ice Sheet”. In: *Reviews of Geophysics* 10.1, pp. 287–333. ISSN: 1944-9208. DOI: 10.1029/rg010i001p00287.
- Weikusat, I., Jansen, D., Binder, T., Eichler, J., Faria, S. H., Wilhelms, F., Kipfstuhl, S., Sheldon, S., Miller, H., Dahl-Jensen, D., and Kleiner, T. (2017). “Physical Analysis of an Antarctic Ice Core—towards an Integration of Micro- and Macrodynamics of Polar Ice”. In: *Philosophical Transactions of the Royal Society of London A: Mathematical, Physical and Engineering Sciences* 375.2086. DOI: 10.1098/rsta.2015.0347.
- Werder, M. A. (2016). “The Hydrology of Subglacial Overdeepenings: A New Supercooling Threshold Formula”. In: *Geophys. Res. Lett.* 43.5, pp. 2045–2052. DOI: 10.1002/2015GL067542.
- Werder, M. A., Schuler, T. V., and Funk, M. (2010). “Short Term Variations of Tracer Transit Speed on Alpine Glaciers”. In: *The Cryosphere* 4, pp. 381–396. DOI: 10.5194/tc-4-381-2010.
- Werder, M. A., Hewitt, I. J., Schoof, C. G., and Flowers, G. E. (2013). “Modeling Channelized and Distributed Subglacial Drainage in Two Dimensions”. In: *Journal of Geophysical Research-earth Surface* 118.4, pp. 2140–2158. DOI: 10.1002/jgrf.20146.
- Wessem, J. M. van, Reijmer, C. H., Morlighem, M., Mouginot, J., Rignot, E., Medley, B., Joughin, I., Wouters, B., Depoorter, M. A., Bamber, J. L., Lenaerts, J. T. M., Berg, W. J. van de, Broeke, M. R. van den, and Meijgaard, E. van (2014). “Improved Representation of East Antarctic Surface Mass Balance in a Regional Atmospheric Climate Model”. In: *Journal of Glaciology* 60.222, pp. 761–770. DOI: 10.3189/2014J0G14J051.
- Winkelmann, R., Martin, M. A., Haseloff, M., Albrecht, T., Bueler, E., Khroulev, C., and Levermann, A. (2011). “The Potsdam Parallel Ice Sheet Model (PISM-PIK) – Part 1: Model Description”. In: *The Cryosphere* 5.3, pp. 715–726. DOI: 10.5194/tc-5-715-2011.
- Winsborrow, M. C. M., Andreassen, K., Corner, G. D., and Laberg, J. S. (2010). “Corrigendum to “deglaciation of a Marine-based Ice Sheet: Late Weichselian Palaeo-ice Dynamics and Retreat in the Southern Barents Sea Reconstructed from Onshore and Offshore Glacial Geomorphology” [quat. Sci. Rev. 29 (2010) 424–442]”. In: *Quaternary Science Reviews* 29.11-12, p. 1501. DOI: 10.1016/j.quascirev.2010.03.009.
- Wolff, E. W., Chappellaz, J., Blunier, T., Rasmussen, S. O., and Svensson, A. (2010). “Millennial-scale Variability during the Last Glacial: The Ice Core Record”. In: *Quaternary Science Reviews* 29.21-22, pp. 2828–2838. DOI: 10.1016/j.quascirev.2009.10.013.

Bibliography

- Wright, A. P., Young, D. A., Roberts, J. L., Schroederm, D. M., Bamberg, J. L., Dowdeswell, J. A., Young, N. W., Le Brocq, A. M., Warner, R. C., Payne, A. J., Blankenship, D. D., Ommen, T. D. van, and Siegert, M. J. (2012). “Evidence of a Hydrological Connection between the Ice Divide and Ice Sheet Margin in the Aurora Subglacial Basin, East Antarctica”. In: *Journal of Geophysical Research: Earth Surface* 117.F1. DOI: 10.1029/2011JF002066.
- Wright, A. P., Young, D. A., Bamber, J. L., Dowdeswell, J. A., Payne, A. J., Blankenship, D. D., and Siegert, M. J. (2014). “Subglacial Hydrological Connectivity within the Byrd Glacier Catchment, East Antarctica”. In: *Journal of Glaciology* 60.220, pp. 345–352. DOI: 10.3189/2014JG13J014.
- Wright, A. and Siegert, M. (2012). “A Fourth Inventory of Antarctic Subglacial Lakes”. In: *Antarctic Science* 24.6, pp. 659–664. DOI: 10.1017/S095410201200048X.
- Wright, P. J., Harper, J. T., Humphrey, N. F., and Meierbachtol, T. W. (2016). “Measured Basal Water Pressure Variability of the Western Greenland Ice Sheet: Implications for Hydraulic Potential”. In: *J. Geophys. Res.* 121.6, pp. 1134–1147. DOI: 10.1002/2016JF003819.
- Xie, J., Bertino, L., Knut, L., and Sakov, P. (2017). “Quality Assessment of the Topaz4 Reanalysis in the Arctic Over the Period 1991-2013”. In: *Ocean Science* 13.1, pp. 123–144. ISSN: 1812-0792. DOI: 10.5194/os-13-123-2017.
- Xu, Y., Rignot, E., Fenty, I., Menemenlis, D., and Flexas, M. M. (2013). “Subaqueous Melting of Store Glacier, West Greenland from Three-dimensional, High-resolution Numerical Modeling and Ocean Observations”. In: *Geophysical Research Letters* 40.17, pp. 4648–4653. ISSN: 0094-8276. DOI: 10.1002/grl.50825.
- Yin, J., Overpeck, J. T., Griffies, S. M., Hu, A., Russell, J. L., and Stouffer, R. J. (2011). “Different Magnitudes of Projected Subsurface Ocean Warming around Greenland and Antarctica”. In: *Nature Geoscience* 4.8, pp. 524–528. DOI: 10.1038/ngeo1189.
- Zirizzotti, A., Cafarella, L., Baskaradas, J. A., Tabacco, I. E., Urbini, S., Mangialetti, M., and Bianchi, C. (2010). “Dry—wet Bedrock Interface Detection by Radio Echo Sounding Measurements”. In: *Geoscience and Remote Sensing, IEEE Transactions on* 48.5, pp. 2343–2348. DOI: 10.1109/TGRS.2009.2038900.
- Zwally, H. J., Abdalati, W., Herring, T., Larson, K., Saba, J., and Steffen, K. (2002). “Surface Melt-induced Acceleration of Greenland Ice-sheet Flow”. In: *Science* 297.5579, pp. 218–222. ISSN: 0036-8075. DOI: 10.1126/science.1072708.